Establishment of 3D hiPSC cardiac differentiation platforms to investigate congenital heart disease

by

Morgan Elizabeth Ellis

A dissertation submitted to the Graduate Faculty of
Auburn University
in partial fulfillment of the
requirements for the Degree of
Doctor of Philosophy

Auburn, Alabama
May 1st, 2021

Keywords: Congenital heart disease, hiPSCs, biomaterials, direct cardiac differentiation, engineered cardiac tissue

Approved by

Elizabeth A. Lipke, Chair, Mary and John H. Sanders Professor, Department of Chemical Engineering
Maria L. Auad, W. Allen and Martha Reed Endowed Professor, Associate Dean for Graduate Studies and Faculty Development
Virginia A. Davis, Alumni Professor, Department of Chemical Engineering
Thomas S. Denney, Mr. & Mrs. Bruce Donnellan & Family Endowed Professor, Department of Electrical and Computer Engineering
Anne A. Wooldridge, Professor of Equine Internal Medicine, Department of Clinical Sciences

Abstract

Cardiac tissue engineering shows great potential for alleviating some of the immense burden of cardiovascular disease. The introduction of human induced pluripotent stem cells (hiPSCs) in 2007 led to a paradigm shift in cardiac tissue engineering, providing a reliable and patient-specific cell source for producing cardiomyocytes *in vitro*. However, standard methods for producing 3D engineered cardiac tissue often combine pre-differentiated cardiomyocytes with biomaterials, which does not fully recapitulate 3D cardiac development and prohibits the ability to study congenital heart diseases that initiate during development. This work demonstrated the ability to directly differentiate hiPSCs in 3D hydrogel microenvironments using multiple biomaterials and tissue geometries and deployed our direct differentiation platform to study a drug-induced and a genetic cause of congenital heart disease.

Expanding on a previously established 3D direct differentiation platform, the first study utilized new hybrid biomaterial, gelatin methacryloyl (GelMA), to produce GelMA human engineered cardiac tissues (GEhECTs). GelMA is a tunable biomaterial that provided a soft (<1kPa) 3D microenvironment which supported cell growth and cardiac differentiation. Resulting GEhECTs displayed appropriate changes in cell morphology, gene expression, and contractility over time. The next study investigated the impact of encapsulation geometry on tissue homogeneity and functionality by introducing two new encapsulation geometries, square and rectangle, in comparison to the previously established microisland geometry. All tissue geometries displayed similar cardiac differentiation efficiencies (~ 65%) and temporal changes in gene expression. However, rectangular tissues had a significantly higher degree of homogeneity across the tissue

volume and anisotropic contraction compared to microisland and square tissues. Additionally, square and rectangular tissues displayed more mature ultrastructural features including aligned Z-bands and organized myofibers.

To study both drug-induced and genetic causes of congenital heart disease, two studies were performed, one involving a known teratogen, thalidomide, and another utilizing left ventricular noncompaction (LVNC) patient-derived hiPSC line. First, to determine if the established 3D direct differentiation platform was sensitive enough to detect thalidomide-induced changes in tissue functionality, 3D engineered cardiac tissues were exposed to 0, 10, and 70 μM thalidomide throughout differentiation and long-term culture. Thalidomide-treated tissues showed decrease cardiac differentiation efficiency, changes in extracellular matrix composition, and reduced electrophysiological function. Finally, to investigate a genetic congenital heart disease *in vitro*, a 3D direct differentiation platform was used with LVNC patient-derived hiPSCs to produce 2D LVNC cardiac monolayers and 3D LVNC cardiac microspheres. Both 2D LVNC cardiac monolayers and 3D LVNC cardiac microspheres exhibited decreased contraction velocity and calcium handling capabilities compared to control tissues.

Overall, the findings from these studies improved and expanded this 3D direct cardiac differentiation platform and demonstrated its applicability in studying both drug-induced and genetic causes of congenital heart diseases. This 3D direct differentiation platform shows great potential for being used in preclinical testing and future disease modeling studies.

Acknowledgments

The years I have spent here in Auburn have been some of the most challenging yet rewarding times of my life. There are so many people who made this possible. First, I would like to thank Dr. Elizabeth Lipke for her guidance throughout the five past years. I would like to thank all of the members of the Lipke Lab specifically, Ferdous Finklea, Yuan Tian, Iman Hassani, Benny Anbiah, Nicole Habbit, Mohammadjafar Hashemi, Mayra Paez, Justin Harvell, and Petra Kerscher. You all have been incredibly supportive, and I have learned so much from each of you. I would like to thank all of the undergraduate students that helped with these projects including Bryana Harris, Hannah Brien, Emma Hicks, Michaela Bush, and Eric Wang. Furthermore, I would like to thank my committee members Dr. Maria Auad, Dr. Virginia Davis, Dr. Thomas Denney, and Dr. Anne Wooldridge for their time and feedback during this process.

Thank you to Brian Schweiker for fixing everything I ever broke and teaching me how to solder, and to Georgetta Dennis for solving every stipend problem I threw at you. Thank you to Dr. Greene for your guidance on gene expression experiments, and Allison Church-Bird for your flow cytometry expertise.

I would like to thank my family and friends for their steadfast support throughout this process. Special thank you to my husband, Tucker Ellis, for your unwavering love and support. There is no way I could have done this without you.

Table of Contents

List of Tables

List of Figures

List of Abbreviations

ANOVA	analysis of variance
ARVC	arrhythmogenic right ventricular cardiomyopathy
AV	atrioventricular
BSA	bovine serum albumin
CHD	congenital heart disease
CMs	cardiomyocytes
CPVT	catecholaminergic polymorphic ventricular tachycardia
Ct	threshold cycle
cTnT	cardiac troponin T
CVD	cardiovascular disease
Cx43	connexin 43
DAD	delayed afterdepolarizations
DAPI	4’,6-diamidino-2-phenyl-indole
DCM	dilated cardiomyopathy
DoF	degree of functionalization
EB	embryoid body
ECM	extracellular matrix
ES	embryonic stem cells
FBS	fetal bovine serum
FHF	first heart field

FN	fibrinogen
GEhECTs	GelMA human engineered cardiac tissues
GelMA	gelatin methacryloyl
GFP	green fluorescent protein
HCM	hypertrophic cardiomyopathy
hiPSCs	human induced pluripotent stem cells
HLHS	hypoplastic left heart syndrome
$I_{Ca,\ L}$	L-type Ca^{2+} channel current
$I_{Ca,T}$	T-type Ca^{2+} channel current
I_f	funny current
I_K	delayed rectifying current
I_{K1}	inward rectifying current
I_{Kr}	rapid delayed rectifying current
I_{Ks}	slow delayed rectifying current
I_{Kur}	ultra-rapid delayed rectifying current
I_{Na}	sodium current
iPSC CMs	induced pluripotent stem cell derived cardiomyocytes
Iso	isoproterenol
I_{to}	transient outward current
LQTS	long QT syndrome
LQTS1	long QT syndrome type 1
LQTS2	long QT syndrome type 2
LQTS3	long QT syndrome type 3

LQTS8	long QT syndrome type 8
LVHT	left ventricular hypertrabeculation
LVNC	left ventricular noncompaction
MA	methacrylic anhydride
MEA	multielectrode array
MEA	multielectrode array
MLC2a	myosin light chain 2 atrial
MLC2V	myosin light chain 2 ventricular
MRI	magnetic resonance imaging
NE	norepinephrine
NVP	N-vinylpyrrolidone
PBS	phosphate buffer solution
PDMS	polydimethylsiloxane
PEG	polyethylene glycol
PEGDA	poly ethylene glycol diacrylate
PEG-FN	polyethylene glycol fibrinogen
Prop	propranolol
RGD	arginine-glycine-aspartic acid
RI	rock inhibitor
RT-qPCR	Reverse Transcription Quantitative PCR
SA	sinoatrial
SHF	second heart field
TA	triggered arrhythmias

TCEP-HCL	tris (2-carboxyethyl) phosphine hydrochloride
TEM	transmission electron microscopy
TEOA	triethanolamine
TGF-β1	transforming growth factor beta1
TNNT2	cardiac troponin T gene
TS	Timothy Syndrome
UV	ultraviolent
WHO	World Health Organization
α-SA	alpha sarcomeric actinin
αMHC	alpha myosin heavy chain
βMHC	beta myosin heavy chain

Chapter 1: Introduction and Motivation

Cardiovascular disease is the leading cause of death worldwide, mostly due to the heart's inability to regenerate itself after injury. It has been shown that only 1% of cardiomyocytes turnover each year up until age 25 with a reduction to 0.45% by the age of 75 (Bergmann et al. 2009). When the body develops post-gastrulation, most of the cells in heart are terminally differentiated, meaning they are permanently cardiomyocytes (CMs). Cells that experience trauma undergo apoptosis, or cell death, and because of this limited regenerative capacity, there are a minimal number of cells that can work to regenerate this damaged region.

For example, when a myocardial infarction (heart attack) occurs, nearly one billion cells die. The heart sends fibroblasts and growth factors to the injury site for repair. However, this process is often insufficient and results in changes to the muscular architecture, which leads to chronic heart failure (Pfeffer and Braunwald 1990). In addition to physiological trauma, many prescribed medications are cardiotoxic, especially those used in chemotherapy. While treating various diseases, these medications can also have long term effects on the heart, resulting in clinical heart failure.

Currently, the bulk of cardiac research focuses on 2D monolayer cardiac sheets, pre-differentiated CMs for 3D tissues, or animal models. While these models have provided some insight to potential regeneration therapies and drug testing platforms, each have major drawbacks when it comes to translating research to clinical applications. For example, 2D monolayers show how individual cardiomyocytes behave but do not accurately recapitulate the 3D structure, cell-to-cell interactions, and electrophysiology in the human heart. The use of pre-differentiated CMs to form 3D cardiac tissues presents

many challenges; the tissue formation process disrupts important cell-cell junctions and prohibits the ability to study cardiac development in 3D. While animal models give some insight into heart function and abnormalities, they frequently cannot accurately recapitulate human cardiac development, drug response, and disease processes. Therefore, a robust 3D platform must be established to create uniform 3D human cardiac tissues that can be used to study cardiac development and drug response.

The ability to use patient-derived human induced pluripotent stems cells (hiPSC) has led to a paradigm shift in the study of cardiac disease mechanisms. However, current methods involving the use of 2D monolayer or pre-differentiated patient-derived hiPSC-CMs prohibit the exploration of cardiac development and more specifically, the mechanisms of congenital heart disease (CHD), in 3D. Therefore, a platform must be established where cardiac differentiation can occur in 3D to provide insight on disease development and potential therapies. Accordingly, the aims of this dissertation are two-fold. First, an existing 3D direct differentiation platform was expanded to a new biomaterial, gelatin methacryloyl, to demonstrate the robust nature of the system and improved resulting cardiac tissue functionality by changing the initial encapsulation geometry. Second, the direct differentiation platform was utilized to study both nongenetic (thalidomide-induced CHD) and genetic (left ventricular noncompaction) CHDs. Using this 3D direct differentiation platform, we are able to gain knowledge about CHD manifestation and progression that was not previously possible using current methods.

Chapter 2: Background

2.1 Cardiovascular System

2.1.1 Cardiovascular Anatomy

The cardiovascular system is one of the hardest working systems in the human body. Its functions include transporting nutrient-rich blood throughout the body, removing metabolites, and controlling certain components of hemostasis including body temperature regulation, nutrient requirements, and hormonal and immunity response in the body. This system is made up of two parts: the heart and the blood vessels. The heart is a four-chambered, bifunctional pump that is responsible for systemic circulation, sending blood around the body, and pulmonary circulation, sending blood to the lungs for gas exchange from carbon dioxide to oxygen (Robert M. Berne 1997). The blood vessels, made up of veins and arteries, carry the estimated five liters of blood along the roughly 100,000-mile path of adult vasculature. Deoxygenated blood flows into the right atrium of the heart via the superior and inferior vena cava. Upon initiation of contraction, the tricuspid valve opens allowing blood to move into the right ventricle. When the right ventricle becomes full, the tricuspid valve closes, and the pulmonic valve opens allowing for blood flow through the pulmonary artery to the lungs for re-oxygenation. Returning from the lungs, the oxygen-rich blood flows into the left atrium and into the left ventricle through the mitral (bicuspid) valve. As the contraction comes to completion, the blood leaves the heart through the aortic valve and is systemically spread throughout the body via the aorta (Gray and Lewis 1918).

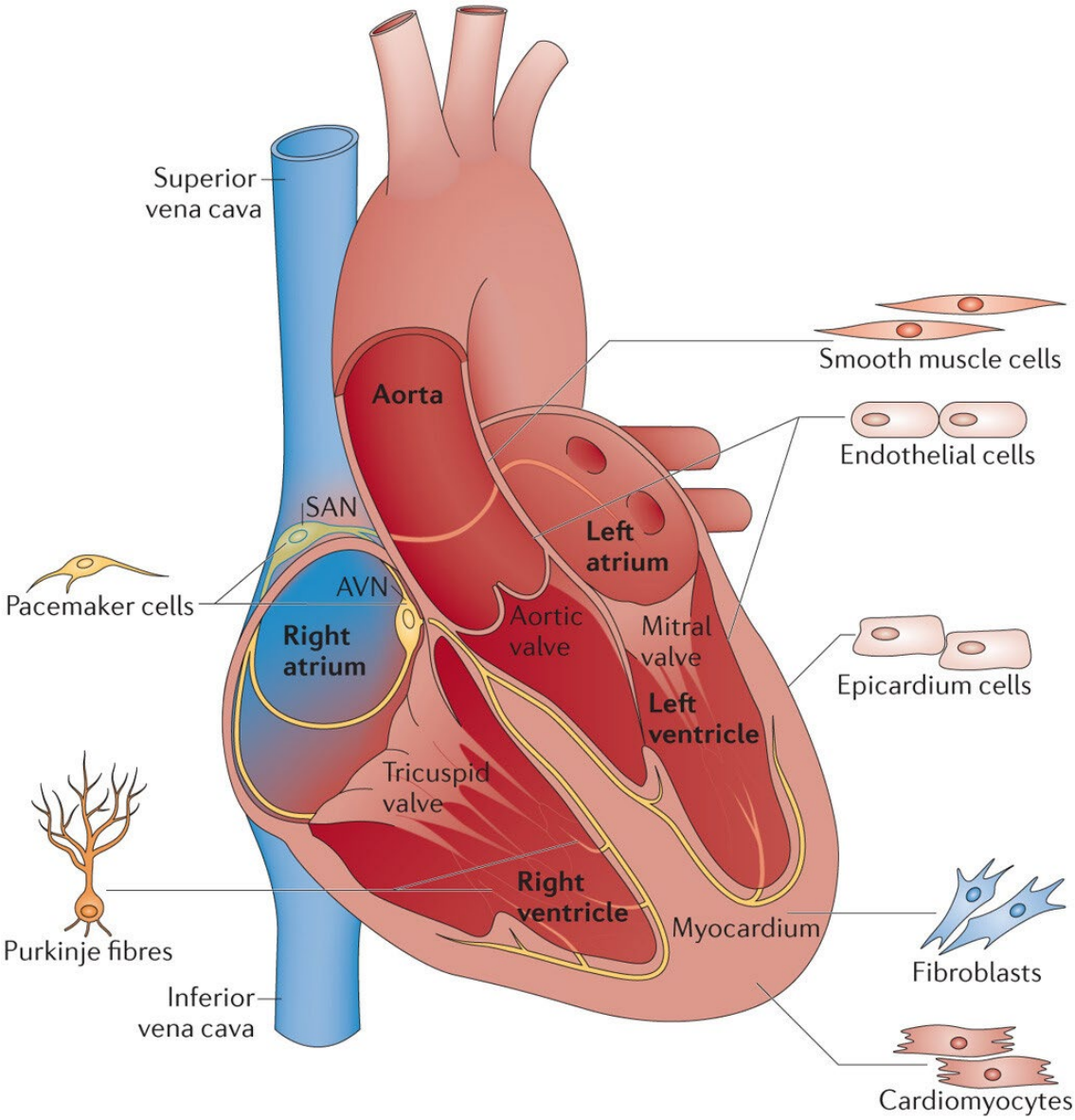

Figure 2.1 The four-chambered heart consists of different cell types.

These cell types contribute to structural, biochemical, mechanical, and electrical properties of the functional heart. Reprinted by permission from Springer Nature permission: Mending broken hearts: cardiac development as a basis for adult heart regeneration and repair. Xin *et al*. *Nature Reviews Molecular Cell Biology.* Copyright 2013;14: 529-541 (Xin, Olson, and Bassel-Duby 2013a)

The heart is an exceedingly complex organ consisting of multiple highly specialized cell types that work together to convert electrical signal into contractile motion. These cell types include cardiomyocytes, fibroblasts, epicardium cells, endothelial cells, smooth muscle cells, pacemaker cells and Purkinje fibers, as seen in Figure 2.1 (Xin, Olson, and Bassel-Duby 2013b). Cardiomyocytes can be categorized as atrial or ventricular based on their location in the heart. These cells consist of myofibrils that contain sarcomeres, which act as the contractile units in the cells that create the muscular wall of the each of the chambers in the heart (Robert M. Berne 1997). Cardiac fibroblasts make up 50% of the cells in the heart and play a major role in extracellular matrix production and immune response after injury (Brown et al. 2005; Xin, Olson, and Bassel-Duby 2013b). The epicardial cells are the outermost layer of the heart and have the potential to differentiate into multiple cell types including endothelial cells, smooth muscle cells and fibroblasts (P.R. Riley 2008). Endothelial cells form the inner lining of the of the heart and blood vessels (Xin, Olson, and Bassel-Duby 2013b). Smooth muscle cells control the flow of blood throughout the body by regulating resistance in the vasculature (Robert M. Berne 1997). Lastly, pacemaker cells and Purkinje fibers are responsible for the intricate electrical activity of the heart (Robert M. Berne 1997).

2.1.2 Cardiovascular Development

The heart is among the first organs to form during the development of the human body. The process is wildly intricate and complex, consisting of a series of specifically timed molecular and developmental steps, each critical to the proper formation of the

heart (C. Gao and Wang 2014). While the order of structural development in the heart has been known for quite some time (Srivastava and Olson 2000), current studies are focused on the genes responsible for controlling heart formation and mutations that lead to heart disease (Table 2.1).

An overview for cardiac development can be seen in Figure 2.2. Gastrulation occurs between days 7-10 of pregnancy, resulting in three germ layers that make up all of the tissues in the body: the endoderm, ectoderm, and mesoderm. Cardiac development begins in the mesoderm around Day 15 of gestation (Moore and Persaud 1998). Differentiation of mesodermal stem cells occurs in the anterior lateral mesoderm in response to growth factors secreted by the endoderm (Schultheiss, Xydas, and Lassar 1995). The cardiomyocytes migrate to the lateral and anterior positions, forming the first heart field (FHF) and second heart field (SHF) (Buckingham, Meilhac, and Zaffran 2005). Around day 21 of human development, the two layers of the myocardium move to the midline and fuse to form a linear heart tube. At this stage in development, the heart begins to beat and circulate blood, forming the first functional organ system in the developing human body (Moore and Persaud 1998). The linear heart tube is composed of four layers, endocardium, cardiac jelly, myocardium, and epicardium that each serve a different function in the developed heart. It is segmented along the vertical axis into the aortic sac, conotruncal segment, atrioventricular (AV) node, right ventricle, left ventricle, and the atria. From days 22-28, the linear heart tube loops to the right, and early chamber formation is initiated (Iaizzo 2005).

Between weeks 4-8 of development, the cardiovascular system undergoes extensive remodeling of the vasculature and four chambers. Previously bilaterally

symmetrical, the vasculature is remodeled so the inflow of blood occurs in the right atrium. The outflow tract begins to rotate and separates into the aorta and pulmonary trunk, with outflow tract cushions forming in the cardiac jelly (Iaizzo 2005). At the same time, the septum develops between the right and left atria. A shunt is formed between the right and left atria to allow oxygenated blood from the mother to by-pass the under-developed pulmonary system. In addition, cells from the right and left ventricles begin to form the septum between the two chambers. The septum will remain partially open until development is finished (Bruneau 2008). Finally, the coronary arteries begin to develop from the epicardium layer of the looping heart tube via vasculogenesis (Iaizzo 2005).

From the 11th week of pregnancy onward, the heart grows via cell division, matures in contractile function, and changes in cardiac muscle composition. At birth, the umbilical cord is cut, removing the oxygen supply to the baby from the mother. With the baby's first breath, the shunt between the arteries is closed, and full septation is achieved (Iaizzo 2005). After this final event, the cardiovascular system is fully developed. Although this structural development is well defined and understood, the regulatory mechanisms that control this development are somewhat unknown.

Genetic mutations that result in loss-of-function phenotypes often provide insights in the role that specific genetic information plays in cardiac development. However, this does not always guarantee that the same mutation will result in the same functional losses. Development is highly complex with several genes controlling the activation and deactivation of downstream genes. Also, there are multiple negative and positive feedback loops controlling the release of transcription factors during development. For example, Nkx2.5 plays a role in several cardiac developmental events throughout heart

formation. A mutation in this gene can cause a plethora of defects including atrial septal defect, ventricular septal defect, hypoplastic left heart, teratology of Fallot, coarctation of the aorta, and others (Fahed et al. 2013). Table 2.1 shows some of the confirmed genes that play a role in various aspects of human cardiovascular development.

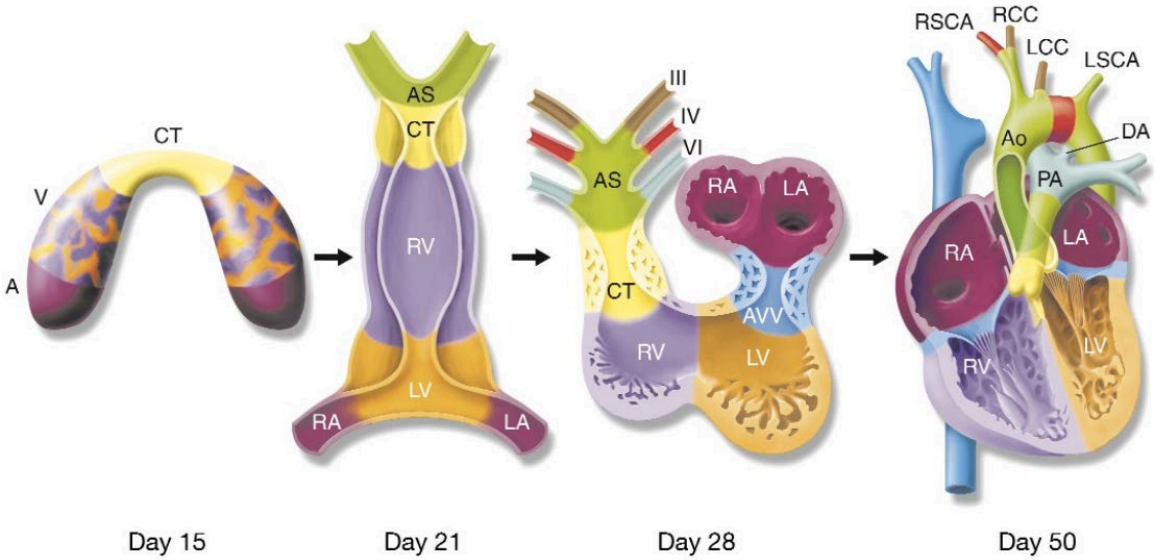

Figure 2.2 Schematic of cardiac morphogenesis.

A, atrium; Ao, aorta; DA, ductus arteriosus; LA, left atrium; LCC, left common carotid; LSCA, left subclavian artery; LV, left ventricle; PA, pulmonary artery; RA, right atrium; RCC, right common carotid; RSCA, right subclavian artery; RV, right ventricle; V, ventricle. Reprinted with permission from Springer Nature: A genetic blueprint for cardiac development. Srivastava & Olson. Nature. 2000; 407: 221-226 (Srivastava and Olson 2000).

Table 2.1 A table of developmental events and associated genetic factors.

Developmental Events	*Factors Contributing to Formation*	*References*
Cardiomyocytes		
Cardiac Differentiation	*NKX2.5* *BMP* *MEF2*	(Harvey 1996) (Schultheiss, Burch, and Lassar 1997)

	GATA4	(Gajewski et al. 1997) (Durocher et al. 1997)
Heart tube		
Linear Heart Tube Formation	*GATA4* *GATA5*	(Molkentin et al. 1997) (Reiter et al. 1999)
Looping	*SMAD2* *NODAL* *LEFTY* *PITX2*	(Nomura and Li 1998) (Nomura and Li 1998) (Meno et al. 1996) (Kioussi et al. 2002)
Conduction system		
Purkinje Cells	*ET-1* *NG-1*	(Gourdie et al. 2003) (Gourdie et al. 2003)
Atria		
Formation	*COUP-TFII* *HRT1*	(Pereira et al. 1999) (Nakagawa et al. 1999)
Septation	*NKX2.5* *TBX5* *GATA4* *TBX20* *MYH6*	(Schott et al. 1998) (Basson et al. 1997) (Garg et al. 2003) (Kirk et al. 2007) (Ching et al. 2005)
Valves		
	NF-ATC *MADH6* *TGF-β* *NOTCH1*	(Ranger et al. 1998) (Galvin et al. 2000) (Galvin et al. 2000) (Timmerman et al. 2004)
Ventricles		
Right Ventricle	*dHAND* *MEF2C* *VERSICAN*	(P. Riley, Anson-Cartwright, and Cross 1998) (Lin et al. 1997) (Henderson and Copp 1998)
Left Ventricle	*TBX5* *TBX20* *EHAND*	(Basson et al. 1997) (Kirk et al. 2007) (P. Riley, Anson-Cartwright, and Cross 1998)
Septation	*TBX1* *TBX5* *TBX20* *GATA4* *NKX2.5*	(Xu et al. 2004) (Basson et al. 1997) (Kirk et al. 2007) (Garg et al. 2003) (Schott et al. 1998)
Maturation	*IRX4* *HRT2*	(Bao et al. 1999) (Xin et al. 2007)

	RXRA *N-MYC* *NEUREGULIN*	(Gruber et al. 1996) (Sawai et al. 1993) (W.Z. Zhu et al. 2010)

2.1.3 Cardiovascular Electrophysiology

Cardiac action potentials are the direct result of cell membrane permeability allowing for an exchange of ions. Ion channels have two major properties: permeation, which accounts for the selectivity of a specific ion to a specific channel, and gating, which accounts for the opening and closing of the channels due to stimuli (Grant 2009). When an action potential transpires in the heart, electrical signals are converted to mechanical motion allowing the heart to contract and relax. The action potentials that occur are categorized into two categories: slow response and fast response.

Slow response and fast response cells undergo different ion exchanges to achieve an action potential. The slow response action potentials are seen in the pacemaker cells which reside in both the sinoatrial (SA) node and the atrioventricular (AV) node. The SA node is responsible for driving an electrical signal that results in a heartbeat. The AV node transfers the electrical signal from the atria to the ventricles (Robert M. Berne 1997). From here, the signal is conducted along the left and right bundle branches to the Purkinje fibers and eventually to the myocardium. As seen in Figure 2.3A, the slow response cardiac tissue has a higher resting membrane potential than fast response tissue and a longer duration of phase 0. At the start of the slow response action potential, spontaneous depolarization occurs after reaching the threshold of the funny current (I_f) at around -40mV (Klabunde 2017). The I_f current brings the membrane potential up to the threshold required for the T-type Ca^{2+} channel current ($I_{Ca,T}$) which continues to

depolarize the cell to reach the L-type Ca^{2+} channel current ($I_{Ca,\ L}$) threshold (phase 0). The cells begin repolarizing via the Na^{+}/Ca^{2+} exchanger, where Ca^{2+} is pumped out of the cell, and Na^{+} is pumped into the cell. The cells experience further repolarization to the pseudo-resting potential through the delayed rectifying K channels (I_K) and acetylcholine-activated K^{+} current (phase 3) (Grant 2009). After this cycle, the cells begin to experience the effects of $I_{f,}$ and the action potential cycle starts again.

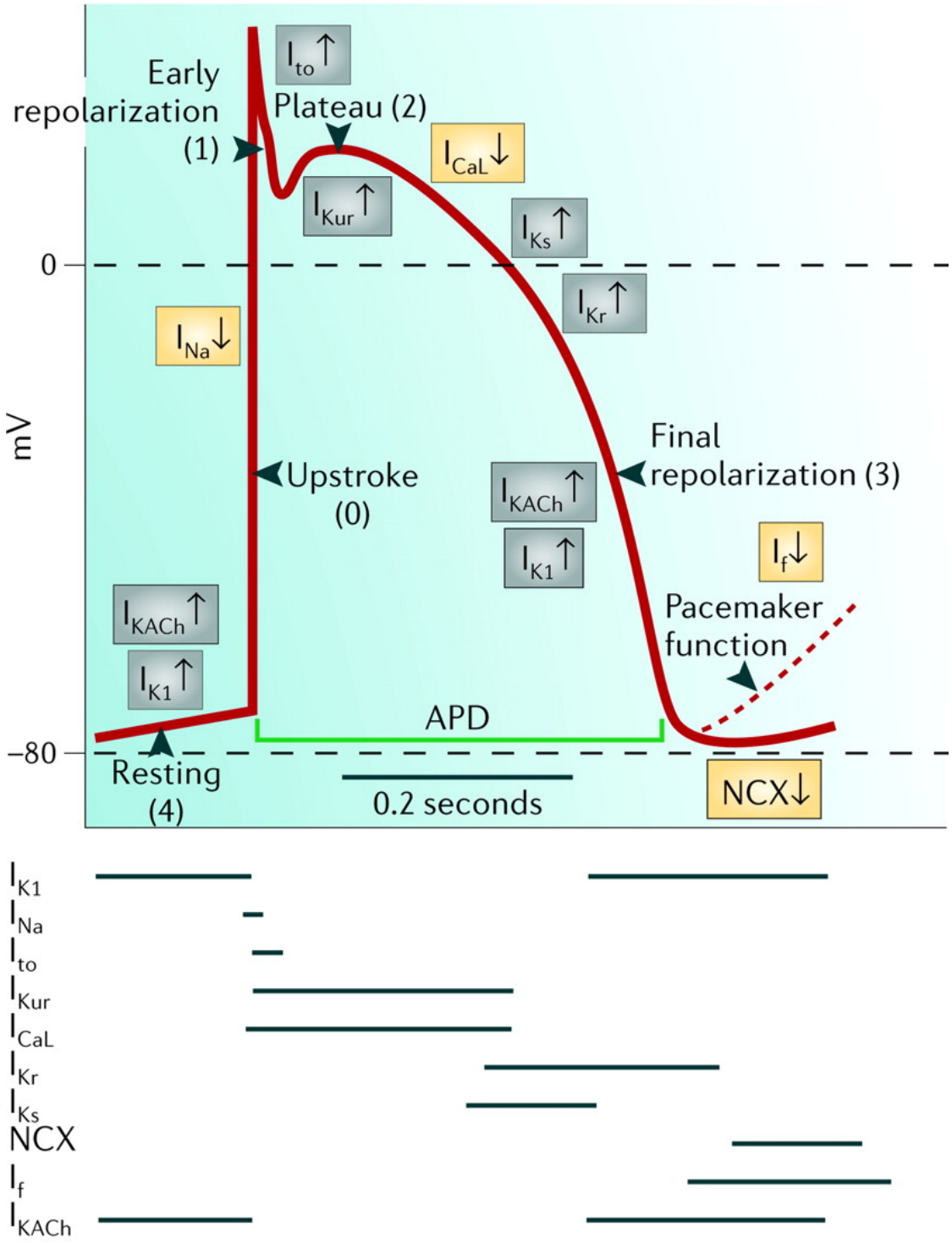

Figure 2.3 Action potential phases of fast response tissues.

Reprinted by permission from Springer Nature, Nat Rev Drug Discov, Innovative approaches to anti-arrhythmic drug therapy. Nattel, S., Carlsson, L., Copyright 2006 (Nattel and Carlsson 2006)

The fast response action potential comes from the atrial and ventricular cardiomyocytes and the Purkinje fibers (Klabunde 2017). The fast response cells experience different ion exchange sequences, with a more negative resting membrane potential and sharper upstroke of cell depolarization. As seen in Figure 2.3B, the resting membrane potential hovers around -90mV. At this point, the cell is experiencing a small K^+ leak and is being influenced by the K^+ leakage from surrounding cells. The action potential is initiated (phase 0) when the membrane potential increases to about -70mV. The fast Na^+ and the slow L-type Ca^{2+} channels open, allowing the sodium current (I_{Na}) and $I_{Ca,L}$ to enter the cell, resulting in positive membrane potential (Klabunde 2017). At the peak of the upstroke, a small repolarization occurs due to the transient outward current (I_{to}) which involves the intracellular K^+ ions moving out of the cells (phase 1) (Grant 2009). The I_{to} does not affect the $I_{Ca,L}$ allowing the Ca^{2+} ions to continue entering the cell thereby maintaining a balance of positive and negative ion exchange in the cells (phase 2). Eventually, the L-type Ca^{2+} channels begin to close, and the delayed rectifier currents (I_{Kur}, I_{Ks}, and I_{Kr}) slowly send K^+ ions out of the cell, returning the cell to a negative membrane potential (Robert M. Berne 1997). Lastly, the inward rectifying current (I_{K1}) returns the cell to its negative resting membrane potential (phase 4) (Grant 2009).

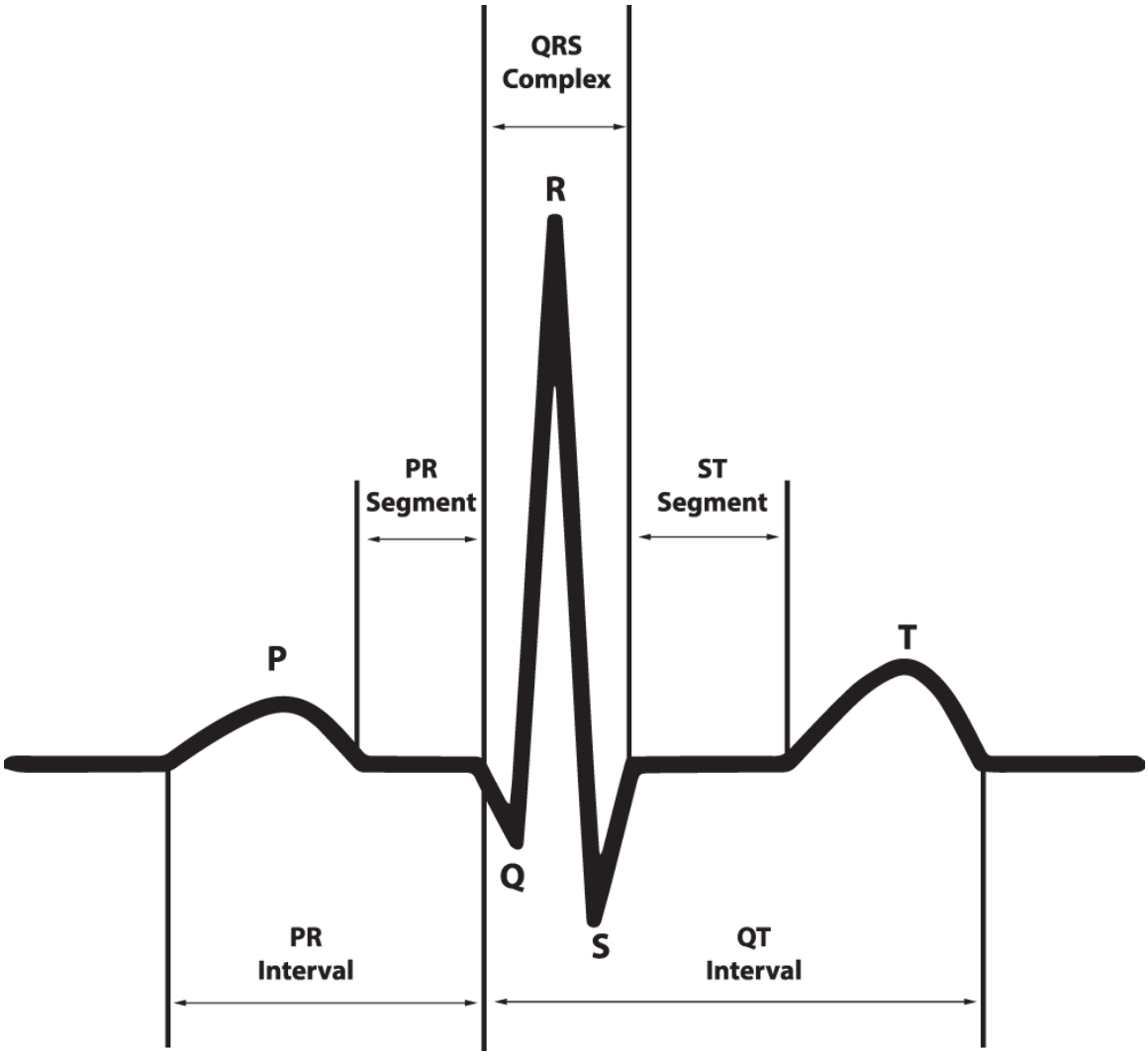

Figure 2.4 A labeled ECG waveform.

Reprinted with permission from Springer Nature and the Creative Commons CC BY license Open Access: A 12-lead electrocardiogram database for arrhythmia research covering more than 10,000 patients. Zheng, J., Zhang, J., Danioko, S. et al. Sci Data 7, 48 (2020). (Zheng et al. 2020)

Slow and fast response action potentials, while very different, work in conjunction to pump blood through the heart. The action potentials in the slow and fast response cells coordinate to create a systematic contraction that pumps blood into and out

of the heart. As seen in Figure 2.4, the contraction begins with a P wave when the electrical signal is sent from the SA node and the right and left atria contracting in succession (Khan 1997). There is a brief pause between the P wave and the QRS complex known as the PR interval, which allows the blood in the atria to fully empty into the ventricles before refilling. The AV node is responsible for this delay. Next, the electrical signal is propagated down to the bundle of His to the bundle branches and through the Purkinje fibers until it reaches the left and right ventricles. This wave propagation is responsible for the QRS complex and maintains a depolarized state through the ST interval (Klabunde 2017). Lastly, the T wave represents the ventricular repolarization. The QT interval is the time that it takes for the ventricles to initiate depolarization and fully repolarize.

The electrophysiology of the heart is complex with multiple cell types controlling various aspects of contractility. Each of these features must work in a synchronous manner to efficiently pump blood into and out of the heart to keep the body oxygenated. Any deviations from regularity can have devastating impacts including cardiac arrhythmias, myocardial infarction, and death.

2.1.4 Cardiovascular Disease

Cardiovascular disease (CVD) is the leading cause of death worldwide in both men and women. According to the World Health Organization (WHO), CVD accounted for over 17.7 million deaths worldwide, representing 31% of all deaths in 2016. Globally, CVD prevalence has declined in high income countries but remains significantly higher in lower income areas (Benjamin et al. 2017). In the United States

alone, it is estimated that 92.1 million adults are living with at least one type of CVD. In 2012-2013, Americans paid $316.1 billion for CVD related healthcare and work time loss. This value is expected to rise to $918 billion by 2030 (Writing Group et al. 2016).

CVD disease is an umbrella term that encompasses many different diseases relating to cardiovascular health. Some of these diseases include coronary heart disease, stroke, congenital heart disease, arrhythmias, atherosclerosis, heart failure, valvular disease, and peripheral arterial disease (Writing Group et al. 2016). Causes of CVD disease are widespread and originate from lifestyle, genetic, and medicinal factors. Lifestyle choices like smoking, physical activity, obesity, and diet all contribute to overall heart health (Writing Group et al. 2016). With only 50% of adults reaching the recommended amount of physical activity and only 0.6% of adults eating an ideal healthy diet, it is not surprising that CVD is so prevalent in the United States (Benjamin et al. 2017). These poor lifestyle choices often lead to additional health concerns including high cholesterol, high blood pressure, and diabetes (Writing Group et al. 2016). While occurrence of these lifestyle risk factors has, for the most part, decreased since 2012, heart disease remains the leading cause of death in the United States.

CVD disease is so widespread due to the heart's inability to regenerate after suffering injury or disease. Cardiomyocytes lose their proliferative capacity after birth; therefore, when these cells die, they are not replaced with cardiomyocytes but rather other cell types including myofibroblast and endothelial cells, which cannot recapitulate the cardiomyocyte's functionality (Leoni and Soehnlein 2018). Over time a reduction in cardiac functionality leads to further complications and chronic heart problems. The field

of cardiac tissue engineering was established to investigate new therapeutic options for regenerating cardiac tissue and to study cardiac development and disease progression.

2.2 Congenital Heart Disease

Congenital heart disease (CHD) is the most common type of congenital anomaly in newborns, representing 28% of all major congenital disease cases (Dolk et al. 2011). Annually, 1.35 million babies are born with a CHD (Fahed et al. 2013). In North America, the frequency of CHD is roughly 8 per 1000 live births (Reller et al. 2008). Due to late onset of symptoms during late infancy and childhood, the true prevalence of CHD may surpass these estimates.

Previously, almost half of CHD-related deaths occurred during infancy. With significant advances in the medical field, now 76% of children who survive the first year make it to adulthood (Gilboa et al. 2010). Currently, the number of adults with CHD has exceeded the number of children with CHD to an estimated 21 million adults living with CHD (Fahed et al. 2013) (van der Bom et al. 2011). As the number of CHD patients living into adulthood increases, the financial, physiological and emotional burdens associated with disease also increase (van der Linde et al. 2011).

The causes of CHD are variable and incompletely studied. It is said that only about 15% of CHD cases can be linked to a known cause (van der Bom et al. 2011). The causes of CHD can be grouped into two broad classifications, nongenetic and genetic. Causes of nongenetic CHD involve maternal exposures, including drugs and alcohol, environmental teratogens, including dioxins and pesticides, and infectious agents,

including rubella and hepatitis (Fahed et al. 2013). Genetic causes of CHD have only recently been studied due to advancements in genomics (van der Bom et al. 2011). This classification of causes is significantly understudied due to the complexities and unknown mechanisms of cardiac development. CHD is a heterogeneous disease, with a complicated diagnosis and response based upon the type of genetic mutations involved. A single genetic mutation can cause to a plethora of different malformations. Additionally, multiple different genetic mutations can all lead to identical malformations. Currently, over 40 different genes have been shown to play a role in cardiac development, however, the interaction of these genes in CHD development has not been fully elucidated (Wessels and Willems 2010). A mutation in any one of the genes can result in a trickling effect in cardiac development that causes a genetic CHD.

It is imperative that CHD disease continues to be studied worldwide. With a growing population of adult patients with genetic CHD looking to start families, an understanding of disease etiology is crucial to develop a strategy for disease prevention. As knowledge in human genomics, patient derived stem cells, and tissue engineering increases, predictive models of genetic CHD and developmental biology are more attainable. This dissertation focuses on thalidomide-induced defects and left ventricular noncompaction.

2.2.1 Thalidomide Syndrome

In the late 1950s thalidomide was released by a German pharmaceutical company, Chemie-Grunenthal, as an anti-emetic and marketed to treat morning sickness in pregnant women. Roughly four years later the drug was pulled from the market after independent

researchers determined that it caused severe birth defects in multiple systems in the body. The release and subsequent withdrawal of thalidomide forever change the way drugs were tested in pre-clinical settings (Vargesson 2015).

At the time of its release, thalidomide had been tested in mice and showed no detrimental side effects. By 1964, it was determined that thalidomide could impact nearly every human tissue but primarily impacted limb development, facial features, and internal organs including the heart (McCredie 2009). The disease phenotype and severity varied widely between victims, mostly like due to the timing and dosage of thalidomide during pregnancy. For most women, it was prescribed from week 4 to 12 of pregnancy when morning sickness is more prevalent; this timing coincides with major developmental events in all tissues including cardiogenesis, further magnifying the negative outcomes of thalidomide exposure (Vargesson 2015). In the heart, thalidomide syndrome often presents as ventricular or atrial septal defects, or pulmonary stenosis.

The exact mechanism that causes thalidomide syndrome has been widely studied but remains vague. Researchers have hypothesized impact multiple mechanisms including DNA replication and transcription, cell proliferation, and the synthesis, function, and interplay of growth factors (Zhou et al. 2013). Thalidomide syndrome is often compared to Holt-Oran syndrome (HOS) due to the similar disease phenotype and progression; moreover, thalidomide is capable of binding to directly to the TBX5 gene, which is the site of the genetic mutation causing HOS (Khalil et al. 2017).

2.2.2 Left Ventricular Noncompaction Disease

Left Ventricular Noncompaction (LVNC), also known as left ventricular hypertrabeculation (LVHT), is a CHD that affects the structure of the left ventricle (Sarma, Chana, and Elkayam 2010). LVNC occurs when the left ventricle does not undergo proper compaction, leaving large trabeculations or deep recesses in the ventricular walls as seen in Figure 2.5 (Captur and Nihoyannopoulos 2010). There are several classifications for LVNC mostly due to the ambiguity regarding disease etiology. This disease can be inherited, presenting *in utero* as a congenital cardiomyopathy, or be acquired over time after birth (Finsterer, Stollberger, and Towbin 2017). LVNC can be genetic, with wide phenotypic variety within one family (Johnson et al. 2006). Non isolated LVNC is determined by the presence of abnormalities in conjunction with trabeculations, while the absence of additional abnormalities is diagnosed as isolated LVNC (Sarma, Chana, and Elkayam 2010). While LVNC has been widely studied, disease prevalence is unclear due to inconsistencies in diagnosis criteria and delayed onset of symptoms into adulthood (Finsterer, Stollberger, and Towbin 2017).

The mechanism for LVNC is widely debated in the literature. Congenital LVNC is thought to be the result of a disruption of the trabeculation compaction that occurs between weeks 5-8 of gestation (Captur and Nihoyannopoulos 2010). The epicardial layer compacts to a dense layer while the endocardial layer stays as trabeculation creating a “spongy” layer (Goud and Padmanabhan 2016). The noncompaction prevents the left ventricle from properly pumping blood out of the heart through the aorta often leading to heart failure, cardiac arrhythmias and conduction problems involving electrical signal blockage in AV nodes and bundle branches (Captur and Nihoyannopoulos 2010). The

onset symptoms of LVNC are highly variable and can appear as early as infancy or as late as adulthood, with some patients not knowing they have the disease until undergoing routine physicals and screenings (Sarma, Chana, and Elkayam 2010).

Diagnosis of LVNC is exceedingly complicated, with no universally accepted criteria for disease confirmation. LVNC is often diagnosed using transthoracic echocardiogram to image the moving heart using ultrasound (Weiford, Subbarao, and Mulhern 2004). However, criterion like the ratio of compacted to noncompacted layers, number of trabeculations, distance between peaks of trabeculation and compacted epicardial layers, and timing of echocardiogram make this assessment highly variable based on image quality and location (Stollberger et al. 2013). Other methods for diagnosing LVNC include cardiac MRI, ventriculography, electrocardiography, endomyocardial biopsy, and genetic testing, but each comes with various drawbacks (Finsterer, Stollberger, and Towbin 2017). Patients with LVNC are treated with beta blockers, diuretics, and ACE inhibitors to combat cardiac dysfunction and are recommended not to participate in strenuous physical activities (Goud and Padmanabhan 2016). The mortality rate for LVNC ranges from 13% to 23% for children and 5% to 12% for adults with death occurring due to heart failure or ventricular tachycardia (Finsterer, Stollberger, and Towbin 2017).

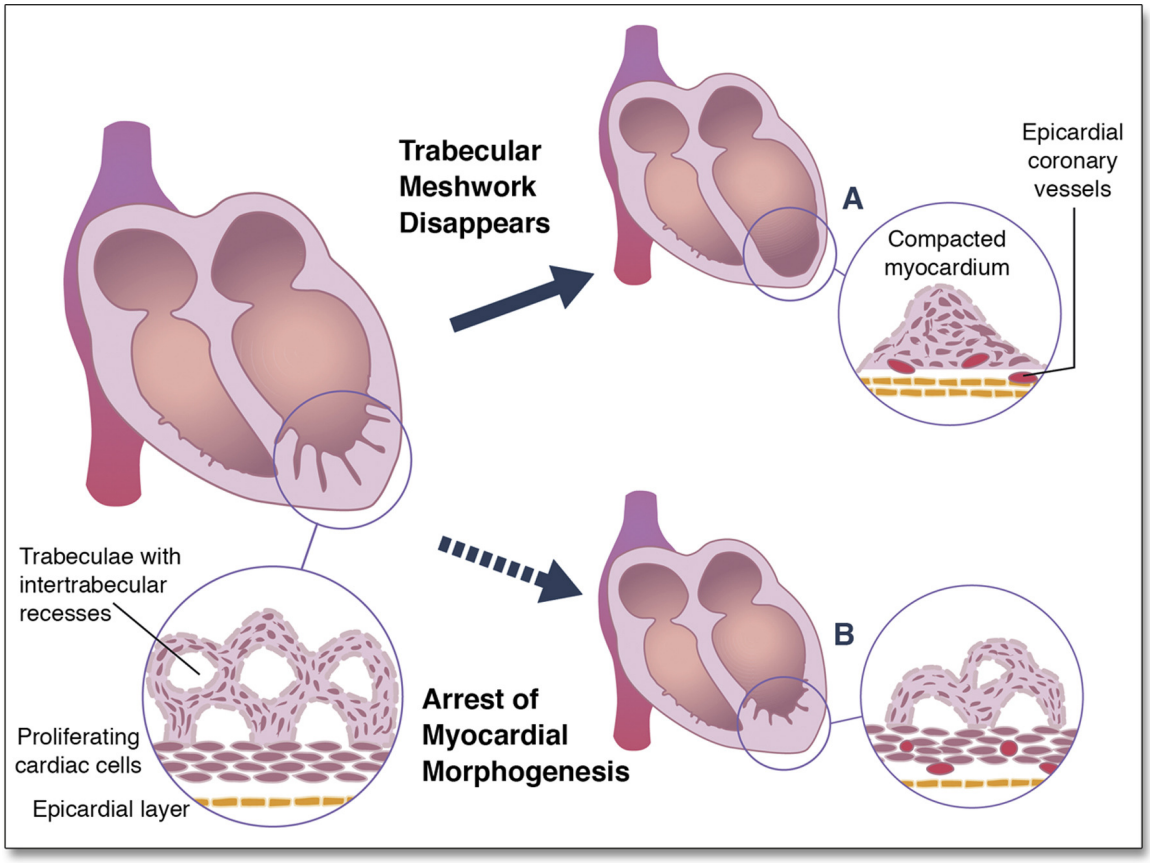

Figure 2.5 A schematic of left ventricular noncompaction disease.

Reprinted from JACC: Cardiovascular Imaging. Vol 7 No. 12. Adult Left Ventricular Noncompaction: Reappraisal of Current Diagnostic Imaging Modalities, Sabiha Gati, Ronak Rajani, Gerald S. Carr-White, and John B. Chambers, 1266-1275, Copyright 2014, with permission from Elsevier (Gati et al. 2014)

2.3 Patient-Derived Human Induced Pluripotent Stem Cells

Studying CVD *in vitro* presents many inherent challenges since cardiomyocytes are terminally differentiated cells that cannot be cultured outside of the body long term. For decades, researchers utilized cell types from other species which often lacked

translational specificity, or human embryonic stem cells (hESCs) which come with significant ethical concerns. In 2006, the ability to reprogram differentiated somatic cells back to a pluripotent state represented a paradigm shift in tissue engineering. After testing a combination for 24 factors, Takahashi and Yamanaka, discovered four transcription factors capable of reprogramming somatic cell via retrovirus-mediated transfection. The four defined factors were Oct3/4, Sox2, c-Myc, and Klf4. The newly reprogrammed cells were designated induced pluripotent stem cells (iPSCs). When compared to ESCs they displayed similar morphology, growth patterns, and gene expression. When implanted, the iPSCs could differentiate into all three germ layers, similar to their ES counterparts (Takahashi and Yamanaka 2006). Since this discovery, significant progress has been made in reprogramming technology. Increased reprogramming efficiency and new, easily accessible somatic cell sources allow for iPSC application in disease modeling and drug screening.

With this novel technology comes the ability to study disease models in a way that was not previously possible. Now, iPSCs can be derived from patients afflicted with disease of known genetic or environmental origins and can be differentiated into any tissue type in order to study disease manifestation in these tissues. Genetic mutations are maintained during reprogramming thereby maintaining disease phenotype. Several studies have shown that differentiation of patient-derived iPSCs shows characteristics of disease *in vitro* (Yazawa et al. 2011; Moretti et al. 2010b; Itzhaki et al. 2011; Davis, Casini, van den Berg, Hoekstra, Remme, Dambrot, Salvatori, Ward-van Oostwaard, et al. 2012; Jiang et al. 2014b; Jung et al. 2012; Novak et al. 2012; Sun et al. 2012b). With this

platform, personalized therapeutic and regenerative medicine are no longer a thing of the future (Wu and Hochedlinger 2011).

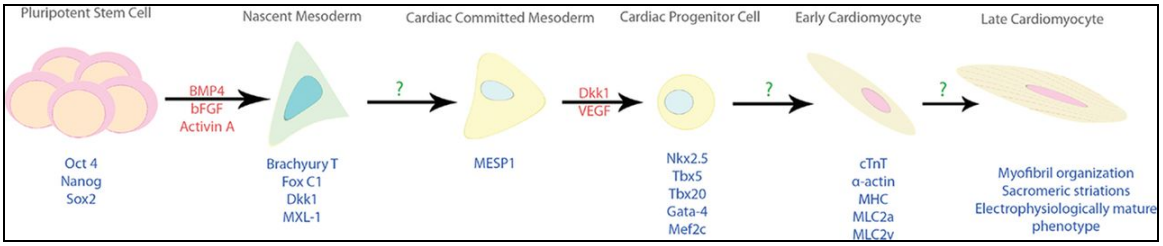

Figure 2.6 Cardiac transcription factors and exogenous control of pluripotent stem cell differentiation.

The differentiation of PSC to CMs is sequential distinguished by the expression of various combinations of transcription factors. There are several different differentiation methods, but a specific set of exogenous factors are still needed to force PSCs down the cardiac lineage. The timing to introduce these factors is very important. In general, initial introduction of Gsk3 inhibitor will start the directed differentiation and later introduction of a Wnt signal inhibitor (Dkk1), and vascular endothelial growth factor (VEGF) will help to push the cells further to form CMs. cTnT, cardiac troponin T; Dkk1, dickkopf homolog 1; FoxC1, forkhead box C1; Gata-4, Gata binding protein 4; MESP1, mesoderm posterior 1 homolog; MHC, major histocompatibility complex; MLC, myosin light chain; Sox2, SRY (sex determining region Y)-box 2. Reprinted from The Biochemical Journal. Vol 434 Issue 1. Cardiomyocyte differentiation of pluripotent stem cells and their use as cardiac disease models, Cheryl Dambrot, Robert Passier, Douwe Atsma, Christine L. Mummery, 25-35, Copyright 2011, with permission from Portland Press LTD.(Dambrot et al. 2011b)

HiPSC technology has given scientists the ability to study human cardiomyocytes (CMs) *in vitro*, which could not be done with postnatal CMs due to low regenerative

capacity and viability outside the body. Researchers in the cardiac tissue engineering field have developed a variety of differentiation protocols for directing iPSCs to the cardiac linage including embryoid body differentiation (Kurosawa 2007a) and 2D monolayer differentiation (Lian et al. 2013). These protocols often consist of media changes with the addition of growth factors and small molecules at various time points and eventually cardiac maintenance media for CMs to mature (Lian et al. 2013; Burridge et al. 2014; Burridge et al. 2011; Kuo et al. 2020). Figure 2.6 shows the series of events that occur in transforming iPSCs into iPSC CMs (Dambrot et al. 2011a). Efficient cardiac differentiation that drives CMs toward maturation will be exceedingly useful in studying developmental cardiac biology and heart disease, as well as drug tests for new therapeutics and cardiotoxicities.

2.4 Current Scaffold-Free CVD Models in Cardiac Tissue Engineering

Current methods in cardiac tissue engineering used for studying CVD range in complexity and applicability from single cell studies to *in vivo* models. With every increase in complexity comes a more physiologically relevant product; however, increased complexity is not always necessary or applicable especially in industrial practices where widespread implementation and reproducibility is required. Each of the current methods presented here have resulted in significant increases in our understanding of cardiac development and regeneration. Additionally, these models can be used in conjunction with patient-derived hiPSCs to study disease development, progression, and treatment (Hoes, Bomer, and van der Meer 2019).

2.4.1 2D Monolayer Disease Models

2D monolayer hiPSC differentiation is often used for creating *in vitro* human cardiac tissue models due to its relative simplicity compared to other methods. Monolayer differentiation involves seeding a single layer of hiPSCs at a high seeding density onto a substrate, which then undergo cardiac differentiation using established protocols to form a contracting cardiac sheet. This method of differentiation has been shown to generate a higher differentiation efficiency than embryoid body differentiation (Lian et al. 2013). 2D monolayer hiPSC differentiation has been deployed to study a broad range of CVDs.

Left ventricular noncompaction (LVNC) occurs when the left ventricle does not undergo compaction, leaving a spongy, left ventricular wall that is not capable of effectively pumping blood out of the heart. To study LVNC, Kodo *et al.* derived hiPSC from patients with a Tbx20 mutation. Using an iPSC derived CM monolayer, they showed that the Tbx20 gene is responsible for downstream activation of TGF-β signaling, which is important for ventricular development. Mutations in the TBX20 caused abnormal TGF-β signaling and interrupted crucial interactions with other cardiac transcription factors that control CM proliferation and compaction. TGF-β inhibitors and corrected genetic sequences showed a restoration of CM proliferation and function (Kodo et al. 2016a).

Hypertrophic cardiomyopathy (HCM) was investigated by Birket *et al.* using monolayer differentiation with an hiPSC line containing a MYBPC3 non-sense mutation. In this study, hiPSC-CM containing the mutation displayed a decrease in force generation compared to control. This finding was further validated in an hiPSC MYBPC3

knockdown model where similar effects were observed. Together, the results of this model suggest decreased force generation as an early predictor of HCM (Birket et al. 2015).

A 2D cardiac monolayer was employed to study laminin A/C (LNMA) -related cardiomyopathy by Lee *et al*. HiPSC lines were generated and differentiated from patients with LMNA genetic mutations to study potential therapeutic targets. LMNA-related cardiomyopathy was induced in the hiPSC-CMs using electrical stimulation, and researchers found that certain mutations responded to the therapeutic treatment which lessened nuclear senescence, stopped apoptosis, and enhanced excitation-contraction coupling. Other mutations did not respond in the same manner, indicating a need for mutation specific treatment and the potential for 2D cardiac monolayers to predict the probability of success for a given treatment (Y.K. Lee et al. 2017).

2D cardiac monolayers have been used to study a variety of CVDs that present with proliferative, mechanical and electrophysiology phenotypes. These models impart valuable information on the cellular level and are appropriate for studies involving single cell assays. However, 2D monolayers lack the complexity required for studying tissue level disease mechanisms such as structural abnormalities or extracellular matrix irregularities.

2.4.2 Embryoid Bodies

Embryoid bodies (EBs) have been used for decades to differentiate embryonic stem cells into the three germ layers, largely because they mimic the structure of the developing embryo. After somatic cell reprograming was discovered in 2006, EBs

became increasingly popular for differentiating patient-specific cell lines into functional disease models (Takahashi and Yamanaka 2006). There are a variety of ways to create EBs with the three most basic methods being hanging droplets, methylcellulose semisolid culture media, and liquid suspension in bacterial-grade dishes (Kurosawa 2007a). Several EBs models have been created to study CVD *in vitro* using patient-derived iPSCs.

To study long QT syndrome type 1 (LQTS1), Moretti *et al*. infected two lines of fibroblast from patients in the same family with defined transcription factors to reprogram the cells into iPSCs. The iPSCs maintained the R190Q missense mutation in the KCNQ1 gene, which controls the alpha subunit of the slow potassium rectifying current (I_{Ks}) . The iPSCs were differentiated into the cardiac lineage in embryoid bodies and dissociated into single cells for analysis after the initiation of spontaneous contractions. The ventricular and atrial iPSC-CMs showed delayed repolarization and extended action potentials. Single cell patch clamp analysis showed a reduction in the K^+ current by about 75% and the presence of arrhythmias and early afterdepolarization events when treated with isoproterenol. Each of these responses recapitulated disease phenotype associated with LQTS-1 (Moretti et al. 2010b).

Itzhaki *et al.* investigated long QT syndrome type-2 (LQTS2) using reprogrammed fibroblasts from a patient with a A614V missense mutation in the KCNH2 gene, responsible for controlling the rapid potassium rectifying current (I_{Kr}). This study showed that LQTS2 iPSC-CMs in EBs had prolonged action potentials and lower repolarization velocity compared to control iPSC CMs. The LQTS2 iPSC CM showed a higher occurrence of arrhythmias and early afterdepolarization events (Itzhaki et al. 2011).

Long QT syndrome type 3 (LQTS3), the cardiac phenotype of Brugada Syndrome, was examined by Davis *et al*. This loss of function disease resulted from mutations in the SCN5A gene that encodes for the alpha subunit of the I_{Na}. iPSC CMs differentiated in EBs were dissociated and analyzed using patch clamp techniques. The result showed a decreased I_{Na} density by about 46% and prolonged action potential duration compared to control iPSC CMs (Davis, Casini, van den Berg, Hoekstra, Remme, Dambrot, Salvatori, Ward-van Oostwaard, et al. 2012).

Jiang *et al.* examined hypoplastic left heart syndrome (HLHS) using two hiPSC clones derived from a patient. The researchers observed unorganized sarcomeric alignment and decrease contractile rates in HLHS-IPSC-derived CM EBs. These observations suggested that differentiation of multiple cardiac lineages is impaired in patients with HLHS, preventing cardiac wall formation and maturation (Jiang et al. 2014b).

To explore the dominant form of catecholaminergic polymorphic ventricular tachycardia (CPVT), Jung *et al.* reprogrammed patient fibroblast containing S406L missense mutation of RYR2 gene into iPSCs. This disease normally presents with abnormal Ca^{2+} release in response to stress leading to life-threatening arrhythmias. Using EB differentiation, areas of contracting cardiomyocytes were excised for single cell analysis. Calcium handling studies showed a higher percentage of CPVT iPSCs CMs with abnormal Ca^{2+} handling with varying arrhythmogenicity compared to control. To emulate stress, the β-adrenergic agonist isoproterenol was added to single cells and the response was measured. CPVT iPSC CMs showed elevated Ca^{2+} levels in response to stress, suggesting a leak in the RYR2 channels where the mutation occurs. Next,

dantrolene, a drug that is thought to stabilize the mutated RYR2 channel, was added to the cells under basal conditions. Drug treatment alleviated the phenotypic impact of the mutation and restored normal Ca^{2+} function. Lastly, the effect of the unprompted release of Ca^{2+} on the Na^{+}/Ca^{2+} exchanger was investigated by measuring membrane potentials after electrical pacing. Delayed afterdepolarizations (DADs) and triggered arrhythmias (TAs) were observed in CPVT iPSC CMs but not in control CMs. Upon treatment with dantrolene, DADs and TAs were eradicated, suggesting a potential therapeutic effect for CPVT (Jung et al. 2012).

The autosomal recessive form of catecholaminergic polymorphic ventricular tachycardia (CPVT) was studied by Novak *et al*. using two patient-derived iPSC lines with a missense mutation D307H in the CASQ2 gene, the gene responsible for the excitation contraction coupling process. iPSCs were differentiated to the cardiac lineage in EBs, and areas of contracting cardiomyocytes were removed and further cultured. The frequency of contraction was significantly lower in CPVT iPSC CMs than in control iPSC CMs. TEM images showed more mature myofibrils and a higher number of caveolae in control iPSC CMs compared to CPVT iPSC CMs. Treatment with isoproterenol resulted in DADs and TAs in CPVT iPSC CMs with an increase in diastolic Ca^{2+} density. Lastly, action potential durations at 20% and 50% were significantly longer in CPVT iPSC CMs (Novak et al. 2012).

One of the many genetic etiologies of dilated cardiomyopathy (DCM) was studied by Sun *et al*. using four patient-derived iPSC lines from the same family with a R173W missense mutation in the cardiac troponin T gene (TNNT2), which controls sarcomeric activity, contraction, and force production in CMs. Contracting EBs showed no

differences in onset of spontaneous contraction, contraction frequency, and action potential duration between the patient and control cell lines. To study the organization of the myofibrils, contracting EBs were dissociated into clusters and single cells then labeled with various cardiac markers including cardiac troponin T (cTnT), sarcomeric α-actinin (αSA), and myosin light chain 2a (MLC2a). DCM iPSCs CMs showed a punctate distribution of αSA, signifying decreased sarcomere integrity with probable degeneration compared to control iPSCs CMs. TEM images showed less aligned Z-lines in DCM iPSCs CMs compared to control iPSCs CMs, consistent with the previously αSA staining of single CMs. To study how positive inotropic reagents expedite the disease phenotype, EBs were treated with norepinephrine (NE) for one week and examined using MEA and TEM. NE treatment resulted in 80-90% of DCM iPSCs CMs with punctate αSA and decrease force of contraction. This was not observed in control iPSCs-CMs. Single cell patch clamping showed no significant difference between control and DCM iPSCs CMs action potential durations and resting potentials at baseline. To study the excitation-contraction coupling, fluorescent Ca^{2+} imaging was used. This experiment showed significantly smaller Ca^{2+} amplitudes in both baseline and caffeine treated DCM iPSCs CMs, probably due to decreased sarcoplasmic reticulum Ca^{2+} storage or altered function of release channels. Lastly, atomic force microscopy measured decreased force of contraction in DCM iPSCs CMs compared to control iPSCs CMs (Sun et al. 2012b).

Hypertrophic cardiomyopathy (HCM) was investigated by Lan *et al.* using five patient iPSCs lines with a missense mutation R663H on the β-myosin heavy chain gene. Control and patient iPSCs were differentiated in EBs, where they presented with spontaneous contractions and were positive for cardiac markers. Dissociation of single

cells showed cellular enlargement, multinucleation, and increased myofibril content in immunostained HCM iPSC CMs compared to control iPSC CMs. To test the significance of the calcineurin-NFAT pathway, which can cause hypertrophy, blockade treatments were used, and a 40% reduction in hypertrophy was observed. To examine the electrophysiology of the CMs, whole cell patch clamping was used. The control and HCM iPSCs CMs showed similar action potentials, contraction frequencies and resting potentials up until Day 30, while the HCM iPSCs CMs began to have arrhythmias and DADs. Calcium handling experiments showed anomalies in calcium transients in HCM iPSCs CMs, which confirmed what was observed in previous whole cell patch clamping studies. Lastly, therapeutic drugs were tested to try to alleviate HCM phenotypes. The calcium channel blockers verapamil, nifedipine, and diltiazem all had a therapeutic effect towards abolishing HCM abnormalities (Lan et al. 2013).

The cardiac phenotype of LEOPARD syndrome, an autosomal dominant developmental disorder, was studied by Carvajal-Vergara *et al.* using two patient-derived iPSCs lines with a T468M missense mutation in the PTPN11 gene, which encodes SHP2 phosphatase. The major phenotypic response for LEOPARD syndrome is HCM. iPSCs were differentiated in EBs, then dissociated and plated in dishes. Single cell analysis showed LEOPARD syndrome iPSC CMs had significantly larger surface areas, increased sarcomere assembly and higher nuclear calcineurin-NFAT localization compared to control iPSCs CMs, all consistent with the HCM disease phenotype (Carvajal-Vergara et al. 2010).

Ma *et al.* explored arrhythmogenic right ventricular cardiomyopathy (ARVC) which is caused by a L614P missense mutation in the PKP2 gene, which encodes for

desmosomal proteins. The hallmark symptom of ARVC is fatty infiltration of the myocardium. Control and ARVC iPSCs lines were differentiated in EBs and dissociated for single cell patch clamping, laser confocal calcium transients, gene expression, TEM, and immunostaining analyses. Gene expression showed decreased levels of the desmosomal protein PKP2 in ARVC iPSCs CMs compared to control iPSCs CMs. This was confirmed via immunostaining for PKP2. TEM images showed significantly larger cell widths, less organized Z-bands, and less dense desmosomes in ARVC iPSCs CMs. To determine the adipogenic potential, CMs were culture in adipogenic media for two weeks, and lipid droplets were visualized by immunostaining with Oil O Red. Dense positive staining for lipid droplets was seen in the ARVC iPSCs CMs compared to a sparse positive staining in the control iPSCs CMs (D. Ma et al. 2013).

Yazawa *et al.* demonstrated the ability to use patient-derived iPSCs to create contracting embryoid bodies (EB) that express the disease phenotype, long QT syndrome 8 (LQT8), associated with Timothy Syndrome. They observed decreased and irregular contraction frequency in TS EBs compared to control EBs. After dissociating the EBs into single cells, this platform was used to test the drug roscovitine as a method of restoring normal action potential and preventing arrhythmias using whole cell patch clamping techniques (Yazawa et al. 2011).

While each of these EB models provides valuable knowledge about human disease manifestation, they lack necessary cell-to-cell junctions, uniform structure, and cardiomyocyte functionality required for applicable therapeutic testing. In each of the studies described, contracting CMs were removed from the bulk EB for long-term culture on cover slips. This shows that EBs do not result in synchronously contracting constructs,

but rather sporadic areas of functionality that do not mimic the native tissue. In addition, each of these EB studies perform single cell analyses like whole cell patch clamping and individual cell calcium handling experiments. While this gives perspective as to what is happening on the cellular level, it does not show what is happening on a tissue level or how cell-to-cell interaction plays a role in disease manifestation.

2.4.3 In Vivo Animal Models

In vivo animal models are often used after cardiac monolayers or EB models to further elucidate disease mechanisms. These models provide researchers with 3D, systemic platforms that are similar to humans on a physiological and anatomical level. Animal models provide higher complexity and demonstrate the interaction between multiple organ systems during disease progression and treatment.

To study left ventricular noncompaction (LVNC) *in vivo*, Kodo *et al*. created several transgenic and knockout mouse models. The first model was a transforming growth factor-beta (TGF-β1) overexpressing transgenic mouse model which sought to emulate the abnormal presence of TGF-β1 in early development. These murine models did not live past day 11.5, confirming the hindrance of TGF-β1 to cardiac development. The next developed transgenic mouse model was a hybrid between the TGF-β1 model and a Nkx2.5 activated green fluorescent protein (GFP) labeled model, which helped to visualize the thickness of the cardiac layer and the decreased presence of proliferative cardiomyocytes. The final transgenic mouse model was used to test the viability and proliferative capacity of doxycycline treated TGF-β1 activated cardiomyocytes (CMs). This model showed fewer CMs in the left ventricle, further supporting the TGF-β1

hypothesis. Finally, to determine the sequence of events that occur with Tbx20 mutation, gene expression was performed on a knockout mouse and compared to LVNC induced pluripotent stem cell derived cardiomyocytes (iPSC-CMs). The resulting genetic profile showed some similarities between human and mouse CMs including the upregulation of TGF-β1 (Kodo et al. 2016a).

Basso *et a*l. examined genetic arrhythmogenic right ventricular cardiomyopathy (ARVC) in boxer dogs to determine if it was suitable as an animal model for humans. Of the 23 diseased dogs, death occurred due to sudden cardiac death (9), right-sided congestive heart failure (3), rapid hypotension (6), and noncardiac causes (5). Premature ventricular complexes were present in 89% of the animals, due to blockages in the left bundle branch morphology causing irregular heartbeats. Pathological findings showed histopathological lesions and replacement of CMs with adipose or fibrous tissue in ARVC dogs compared to control dogs, similar to human patient responses. Myocarditis in the right and left ventricle was identified in 61% and 70% of ARVC dogs, respectively, and was present in each of the nine dogs that died of sudden cardiac death. CM death occurred in 39% of ARVC dogs but not in controls. Overall, the study concludes that the boxer dogs model of ARVC is a suitable model for mimicking the pathological features of the human disease (Basso et al. 2004).

A mouse model of hypertrophic cardiomyopathy (HCM) was developed by Georgakopoulos *et al.* in mice with a R403Q missense mutation in the α-cardiac myosin heavy chain. Control mice were compared to both younger and older mutant mice. Pressure –volume loops showed 30-40% decreased cardiac output in older mutant mice compared to control mice. Ventricular pressure tracings displayed the development of

systolic pressure gradients between the aorta and mid-cavity, as seen in humans with HCM. The end-systolic elastance, which measures chamber stiffness after systole, was nearly 300% higher in older mutant mice compared to younger mutant mice but similar to younger control mice, showing the late onset of HCM in mutant mice. Older mutant mice showed increase chamber stiffness, reduced stroke volume, and systolic hyper injection, which was not seen in the younger mutant or control mice, but are all hallmarks of HCM in humans (Georgakopoulos et al. 1999).

Brunner *et al*. studied both long QT syndrome type 1 and type 2 (LQTS1, LQTS2) in a transgenic rabbit model presenting the mutations Y315S in the KCNQ1 gene (I_{Ks}) and G628S in the KCHN2 gene (I_{Kr}), respectively. The mutations in these genes showed prolonged action potential durations. The elimination of rapid potassium rectifier current (I_{Kr}), which controls cell repolarization, in LQTS2 rabbits showed significant prolonged action potential duration and increased arrhythmogenicity and sudden cardiac death. Two of the seven LQTS2 rabbits died of spontaneous polymorphic ventricular tachycardia compared to none for control and LQTS1 rabbits. Current densities for remaining K^+ rectifying currents, I_{Kr} in LQTS1 patients and I_{Ks} in LQTS2, were decreased compared to control rabbits, suggesting that the other currents are not able to compensate for the loss due to mutation. Finally, optical mapping showed increased spatial dispersion of repolarization leading to early afterdepolarization and arrhythmias, similar to human patients with LQTS (Brunner et al. 2008).

While animal models have provided significant insights into disease processes, they cannot accurately recapitulate human disease development. Cardiac development and maturation occur differently in most animals compared to humans. For example, the

gestational period for a mouse is 18 to 22 days, while the gestational period for a human is 40 weeks (Krishnan et al. 2014). In addition, cardiac electrophysiology is different between various animal models and humans. Rats and mice are commonly used to model cardiac disease, but their action potentials are much shorter than humans, and their heartrates are five to ten time faster (Bers 2001). Also, mice possess different potassium channels for repolarization compared to humans (Nerbonne 2004). Overall, a more accurate model for studying human diseases is required to develop therapeutics that are clinically relevant.

2.5 Biomaterials in Cardiac Tissue Engineering

2.5.1 Introduction to Biomaterials: Natural, Synthetic, Hybrid

Biomaterials are widely used in tissue engineering to mimic *in vivo* environments. Biomaterials can provide mechanical, electrical, and bioactive cues that support tissue formation and development. These materials must be biocompatible, support cell adhesion, differentiation, and proliferation, and avoid immune responses upon implantation. Degradation of biomaterials must coincide with tissue regeneration and replacement occurring inside the body (E.J. Lee, Kasper, and Mikos 2014a). There are several different types of biomaterials, each with specific characteristics that make them well suited for various applications in tissue engineering (Hubbell 1995). Each of these can be characterized as natural, synthetic, or a hybrid of both types. These materials are made of polymers, ceramics, composites, bioglass and metals (Eisenbarth 2007).

Biomaterials used in cardiac tissue engineering require a specific set of constraints for creating tissues that can appropriately integrate into the native tissue without causing arrhythmias or further tissue damage. These materials are required to withstand contractile motion and electrical signaling between cells while being easily vascularized to prevent tissue ischemia (Radisic 2015). Cardiac biomaterials must support cell differentiation, encourage cardiomyocyte maturation, and promote wound healing at injury sites (Q.Z. Chen et al. 2008). These constraints make it difficult to create a viable cardiac tissue engineering product for clinical application. Some successful biomaterials for cardiac tissue engineering include: polycaprolactone, poly-L-lactic acid, chitosan-hyaluronan/silk patches, alginate, collagen, Matrigel, poly (N-isopropyl acrylamide), polyethylene glycol fibrinogen, and gelatin methacryloyl.

2.5.2 Polyethylene Glycol Fibrinogen

Polyethylene glycol fibrinogen (PEG-fibrinogen) is a polymeric biomaterial used in tissue engineering to support tissue formation. This material is composed of both a synthetic and a biological component to create a hybrid biomaterial. The synthetic component is polyethylene glycol (PEG), which is biocompatible and tunable but does not support cell adhesion. The natural component is fibrinogen, which is abundant in the extracellular matrix of human tissue and provides biologically active sites for cell adhesion (Almany and Seliktar 2005a).

PEG has a unique set of characteristics that makes it widely applicable in tissue engineering. First, PEG is highly versatile. It is available in a variety of molecular weights, is linear or branched, and can be manipulated with a variety of functional

groups based on the application (J.M. Zhu 2010). Second, PEG is biocompatible. The surface does not allow for cell or protein adhesion and it does not illicit an immune response or harm other cells or proteins when injected into the body (Alcantar, Aydil, and Israelachvili 2000). Third, PEG can be used to form 3D hydrogels that resemble soft tissue. Photoinitiators combined with PEG undergo photopolymerization using visible or ultraviolet light to turn the polymeric liquid into a 3D hydrogel via free radical polymerization (K.T. Nguyen and West 2002).

Fibrinogen is often used in tissue engineering for its bifunctionality. This glycoprotein is naturally found circulating in the blood and is synthesized by the body in response to injury to help form blood clots (Herrick et al. 1999). Its structure is made up of two half chains with an enzymatically cleavable middle chain. In tissue engineering, fibrinogen is utilized for its bioactivity and cell adhesion sites. The cleavable middle chain allows adhered cells to degrade the biomaterial as they form their own extracellular matrix (ECM) (J.M. Zhu 2010). Additionally, it has been shown that fibrinogen and its cleavage products enhance angiogenesis, cell proliferation, and cell migration (Bootle-Wilbraham et al. 2001).

PEG-fibrinogen is synthesized via a Michael-type addition reaction between PEG-diacrylate (DA) and fibrinogen. The reaction forms an ester bond between the acrylate end groups of the PEG-DA and the free thiols on located in the fibrinogen cysteines (Lutolf and Hubbell 2003). Photoinitiators and co-initiators are added to the synthesized PEG-fibrinogen and the solution is exposed to visible or ultraviolet light to form the 3D hydrogel network as seen in Figure 2.7.

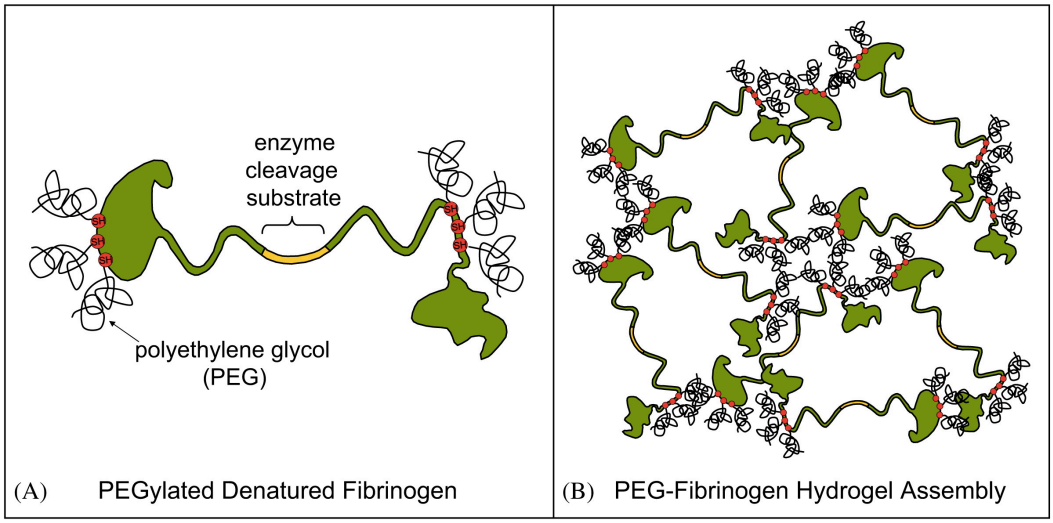

Figure 2.7 Schematic illustration of the PEG-fibrinogen hydrogel assembly.

PEGylated fibrinogen fragments (A) contain a natural protease cleavage site (yellow) and multiple unpaired thiols (red) for covalent conjugation of functionalized PEG by Michael-type addition reaction. PEG-fibrinogen hydrogel assembly (B) is accomplished by photoinitiation of unreacted PEG-DA, resulting in a hydrogel network of PEGylated fibrinogen. Reprinted from Biomaterials, Vol 26 Issue 15, Liora Almany and Dror Seliktar, Biosynthetic hydrogel scaffolds made from fibrinogen and polyethylene glycol for 3D cell cultures, 2467-2477, Copyright 2005, with permission from Elsevier (Almany and Seliktar 2005b)

Overall, PEG-fibrinogen has been successfully used as a biomaterial in a variety of tissue engineering fields including cardiovascular (Kerscher, Turnbull, et al. 2016), orthopedic (Peled et al. 2007), and cancer modeling (Pradhan et al. 2017). Currently, a PEG-fibrinogen hydrogel product, GelrinC, is in phase III clinical trials for treatment of cartilage defects in the knee (Ltd. 2016).

2.5.3 Gelatin Methacryloyl

Gelatin Methacryloyl (GelMA) is a hybrid biomaterial composed of a modified natural component, gelatin, functionalized with methacryloyl groups to form a polymer precursor suitable for 3D hydrogel formation (Nichol et al. 2010). When combined, these materials create a highly tunable polymeric solution containing cell adhesion sites and structural support for tissue formation (Y.C. Chen et al. 2012).

Gelatin is derived from naturally abundant collagen found in cartilage, bones, skin and is formed when the collagen triple helix is destabilized and broken to form soluble gelatin coils. Two different types of gelatin, Type A and Type B, can be formed based on the acidic or basic pre-treatment methods (Gomez-Guillen et al. 2011). Derived from the ECM protein collagen, gelatin maintains several arginine-glycine-aspartic acid (RGD) sequences that support cell attachment. When compared to collagen, gelatin has a better solubility and a lesser chance of eliciting an immune response (Yue et al. 2015).

Methacryloyl groups are used to functionalize pure gelatin, altering the mechanical properties of the tissue engineered product. These groups allow photocrosslinking to occur in the presences of a photoinitiator, to form a 3D hydrogel (Lutolf and Hubbell 2003). The degree of gelatin functionalization directly correlates with the crosslinking density. A larger degree of functionalization (DoF) increases the mechanical properties and decreases the porosity of the hydrogel (Van Den Bulcke et al. 2000).

The methacryloyl groups are added to the gelatin via substitution of free amine groups of the gelatin backbone, as seen in Figure 2.8 (Nichol et al. 2010). The reaction is performed in dark conditions at 50 ºC under vigorous stirring. The degree of

functionalization can be controlled by reaction time, temperature, and mass ratio of gelatin to methacrylic anhydride (Loessner et al. 2016).

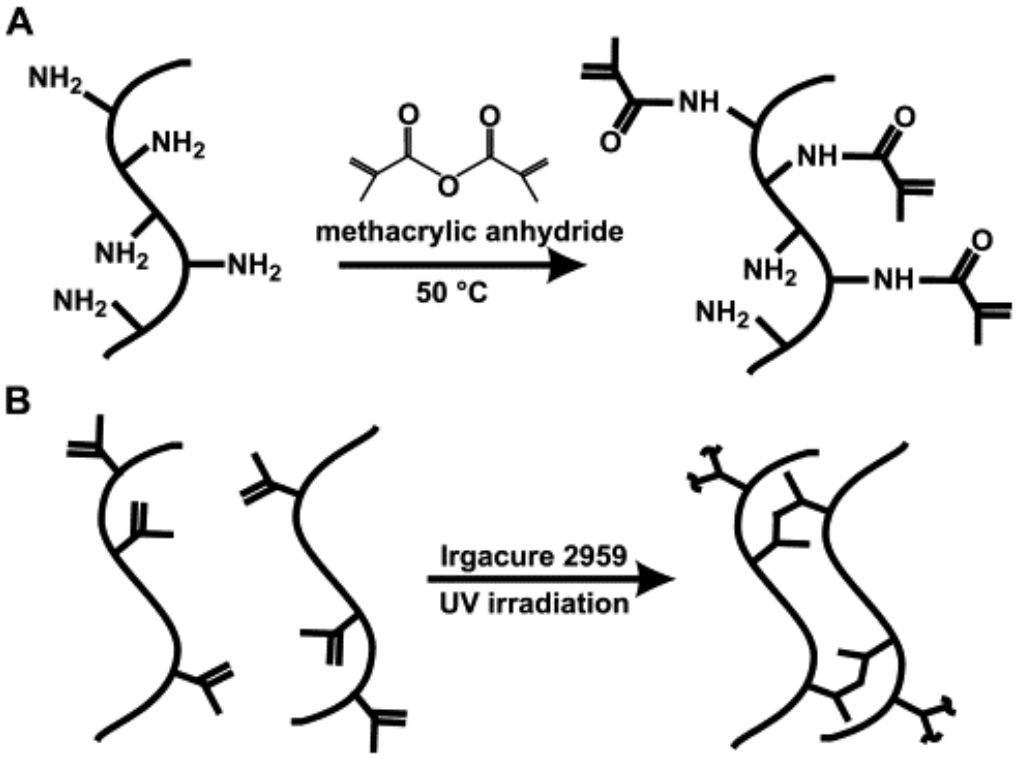

Figure 2.8 Synthesis of methacrylated gelatin.

Gelatin macromers containing primary amine groups were reacted with methacrylic anhydride (MA) to add methacrylate pendant groups (A). To create a hydrogel network, the methacrylated gelatin was crosslinked using ultraviolet irradiation in the presence of a photoinitiator (B). Reprinted from Biomaterials Vol 31 Issue 21. Cell-laden microengineered gelatin methacrylate hydrogels, Jason W. Nichol, Sandeep T. Koshy, Hojae Bae, Chang M. Hwang, Seda Yamanlar, Ali Khademhosseini, 5536-5544, Copyright 2010, with permission from Elsevier (Nichol et al. 2010)

GelMA has a wide variety of applications in tissue engineering mostly due to its highly tunable nature. It has been used as a suitable biomaterial in cardiovascular

(Kerscher, Kaczmarek, et al. 2016a), skin (Zhao et al. 2016), and cartilage (Schuurman et al. 2013) engineering, among several others. Currently, GelMA is not a part of any ongoing clinical trials.

Chapter 3: Direct Production of Human Cardiac Tissues by Pluripotent Stem Cell Encapsulation in Gelatin Methacryloyl

3.1 Introduction

Cardiovascular disease has been and continues to be the leading cause of death accounting for over 31% of deaths worldwide in 2016 (Benjamin *et al.* 2017). The high mortality rate is mostly due to the hearts inability to heal itself after injury and disease, leaving patients in dire need of a heart transplant (Bergmann *et al.* 2009). The demand for transplants greatly outweighs the number of viable donor hearts. Therefore, there is a great necessity for an *in vitro* platform for generating functional cardiac tissues that can be used for regenerative medicine, developing new therapeutics to treat heart disease, and studying the cardiac development and disease processes (Wu and Hochedlinger 2011). With the discovery of human induced pluripotent stem cells (hiPSCs) (Takahashi and Yamanaka 2006) and advancements in highly efficient differentiation protocols (Lian et al. 2013), there is great potential for cardiac tissue regeneration. To produce a clinically relevant developing cardiac tissue, it is important to mimic the extracellular matrix and cell to cell interactions of the native heart environment. Using biomimetic materials to encapsulate hiPSCs provides an appropriate microenvironment for maintaining cell viability and proliferation, driving differentiation, and encouraging cellular function (E.J. Lee, Kasper, and Mikos 2014a). Hydrogel constructs provide a suitable biomimetic environment for achieving scalable tissue production.

Most protocols for creating three-dimensional cardiac tissues involve encapsulation of pre-differentiated stem cells (D.C. Nguyen et al. 2014; Turnbull et al.

2014), or tissue samples taken directly from heart tissues (Bian et al. 2014; Shapira-Schweitzer and Seliktar 2007). Forming engineered cardiac tissues from pre-differentiated stem cell requires contracting cardiomyocyte (CM) aggregates to be dissociated and then encapsulated in a 3D hydrogel biomaterial. The dissociation of contracting aggregates has a negative impact on cell viability and disrupts important cell-cell junctions that are required for cardiac tissue development and functionality. A better option for engineering cardiac tissues is the direct encapsulation of hiPSCs in a biomimetic material, which then undergoes direct differentiation to the cardiac lineage (Kerscher, Turnbull, et al. 2016). This single cell-handling step encapsulation technique to produce 3D cardiac tissue using hiPSCs has been successfully employed using the hybrid biomaterial, poly (ethylene glycol)- fibrinogen (PEG-fibrinogen), as the extracellular matrix (ECM) for hiPSC encapsulation and differentiation, to create 3D developing human engineered cardiac tissues (3D-dhECTs) (Kerscher, Turnbull, et al. 2016). Translating this technique to additional hydrogel biomaterials for engineering cardiac tissues is important for future applications in tissue engineering.

When searching for additional hydrogel materials, it was important to consider the native cardiac tissue. Collagen is a naturally abundant ECM protein of in the adult heart (Gomez-Guillen *et al.* 2011), making it a potential matrix material suitable for direct differentiation of hiPSCs into 3D-dhECTs. However, collagen alone presents many challenges due to immunogenicity, batch to batch variability, and the inability to form mechanically tunable hydrogels using visible light (V.A. Kumar et al. 2014). To avoid these setbacks, while still mimicking the native heart ECM and supporting hiPSC differentiation to CMs, we selected biomaterial gelatin methacryloyl (GelMA), for this

study. GelMA is a hybrid biomaterial composed of gelatin, denatured collagen, functionalized with methacryloyl groups. A wide variety of structural and functional characteristics can be achieved depending on the degree of functionalization (Nichol *et al.* 2010). Most notably, GelMA can be combined with photoinitiators and can be photo-crosslinked with visible light to form soft 3D hydrogels, which are necessary for hiPSC survival.

In this study, we show for the first time the ability to successfully produce GelMA human engineered cardiac tissues (GEhECTs) using a one cell-handling step hiPSC encapsulation and direct differentiation in soft GelMA hydrogels. We began by synthesizing GelMA with 22% substitution of methacryloyl groups and test acellular hydrogels for biodegradability. Next, we formed cell-laden GelMA hydrogels by mixing hiPSCs with a GelMA precursor solution and photo-crosslinking with visible light for less than one minute. HiPSC viability was confirmed using a live/dead assay and cardiac differentiation efficiency was verified using flow cytometry. Onset of spontaneous contraction was observed in isolated areas by day 8 with synchronous whole tissue contractions occurring by day 14. Cells in the hydrogel constructs remodeled their environment and transitioned from round stem cell morphology to elongated cardiac muscle morphology. Temporal differentiation of cells formed a contracting tissue that increased in frequency and velocity and showed appropriate gene expression changes over time. GEhECTs-CMs were immunostained with α-sarcomeric actinin to visualize aligned sarcomere. Lastly, CM functionality was validated with appropriate response to pacing and drug treatment. Overall, our results show that GelMA is a suitable biomaterial for differentiating hiPSC to form a GEhECTs.

3.2 Materials and Methods

3.2.1 HiPSC Culture

Two hiPSC cell lines, IMR-90 Clone 1and 19-9-11 (WiCell), were cultured in mTeSR-1 medium (Stem Cell Technologies) on hESC qualified Matrigel (BD Biosciences) coated well plates. HiPSCs were passaged about every 5 days using Versene (Life Technologies) for about 4.5 minutes at 37 ºC into mTeSR-1 medium supplemented with 5μM ROCK inhibitor (RI) (Y-27632, Stem Cell Technologies).

3.2.2 PDMS Mold Preparation

Polydimethylsiloxane (PDMS) molds were made using the Sylgrad Elastkit (Fisher Scientific). Briefly, Sylgard 184 silicone elastomer and Sylgard 184 curing agent were combined at a 10:1 ratio and placed under vacuum to remove all bubbles. The mixture was poured between two pieces of glass separated by 650 μm spacers and cured for two hours at 70 ºC. After curing, the PDMS sheet was peeled off and a cork borer was used to cut molds with four circular holes (4mm in diameter). PDMS molds were sterilized by sonication in 70% ethanol and exposed to UV light 12 hours prior to encapsulation. For encapsulation, the molds were transferred to the bottom of a 6-well plate.

3.2.3 Gelatin Methacryloyl Synthesis and Precursor Preparation

All chemicals were purchased from Sigma-Aldrich unless otherwise specified. GelMA was synthesized with modifications of previously established protocols (Nichol

et al. 2010; Van Den Bulcke *et al.* 2000). Bovine gelatin Type B was dissolved at 5% (w/v) into phosphate-buffered saline (PBS, Gibco) at 50 ºC while stirring until fully dissolved, approximately 20 minutes. The pH was measured and adjusted to 7 using 1M NaOH if necessary. Methacrylic anhydride (MA) was slowly added to the gelatin mixture (15%w/v) over 10 minutes and reacted for 2 hours at 50 ºC. The reaction was stopped with a 5X dilution using PBS and the reaction mixture was placed in dialysis tubing. The mixture was dialyzed against distilled water at 40 ºC for 7 days with three water changes per day and lyophilized for 5 days. Lyophilized GelMA was dissolved in deuterium oxide (Fischer Scientific) for NMR analysis. ^{1}HNMR spectra were collected using a Bruker NMR spectrometer.

The GelMA precursor solution was prepared by dissolving lyophilized GelMA into PBS at 80 ºC at a concentration of 15mg/mL. After being dissolved, 1.5v/v% triethanolamine (TEOA), 3.96 µL/mL N-vinylpyrrolidone (NVP) and 0.1 mM eosin Y (Fischer Scientific) photoinitiator was combined with the GelMA solution (Franco, Price, and West 2011). Acellular hydrogels were made to test the degradation of GelMA in the presence of an enzyme. For this study, acellular GelMA hydrogels (20µL) were crosslinked for 60 seconds and incubated in PBS or 5U/mL collagenase Type 2 (Worthington) at 37 ºC. Hydrogel weight measurements were taken at 0, 3, and 6 hours (n=3 hydrogels).

3.2.4 Fabrication of GelMA Human Engineered Cardiac Tissues

To form GelMA tissues, hiPSCs were dissociated using Versene for 4.5 minutes at 37 ºC, collected in a 15-mL centrifuge tube, and centrifuged for 5 minutes at 200 g.

The supernatant was removed, and the cell pellet was resuspended in GelMA at a concentration of 26± 4.1*10^6 hiPSCs/mL GelMA. The GelMA cell suspension was pipetted into one circular mold (8 µL each) and photo-crosslinked using visible light (203 mW/cm^2) for 40 seconds (Figure 4.1a). After crosslinking, the PDMS molds were removed and the tissues were suspended in mTeSR-1 medium supplemented with 5 µM RI for 24 hours (day -3, 4 tissues per well). For the next two days (day -2, day -1) mTeSR-1 medium was changed daily. Cardiac differentiation was initiated on the third day after encapsulation (day 0).

Cardiac differentiation was initiated on day 0 using a well-established protocol (Lian et al. 2013; Kerscher, Turnbull, et al. 2016). mTeSR-1 medium was replaced with RPMI/B27 without insulin (Invitrogen) medium supplemented with 12µM CHIR99021 (Stem Cell Technologies). Exactly 24 hours later (day 1) the medium was replaced with 4 mL of RPMI/B27 minus insulin. Exactly 48 hours later (day 3) 2mL of the old day 1 media was combined with 2mL of fresh RPMI/B27 minus insulin supplemented with 5µM IWP2 (Stem Cell Technologies). After 48 hours (day 5) the media was replaced with 4 mL of RPMI/B27 minus insulin. On day 7, the media was replaced with RPMI/B27 and replaced every 3 days thereafter.

3.2.5 Parallel Plate Mechanical Testing

Acellular and cellular GelMA hydrogels were crosslinked for 40 seconds, cultured according to the above protocol, and tested for their mechanical properties on days -2, 7 and 19 using a mechanical testing system (MicroSquisher, CellScale). The force was calculated using a cantilever beam deflection in response to a user defined

distance of compression. All samples were tested in PBS at 35 ºC with a tungsten cantilever beam with a diameter of 558.8µm. Stress-strain characteristics of each tissue was used to determine the elastic modulus using the linear 5-20% portion of the strain curve (n=3 samples).

3.2.6 Tissue Dissociation and Replating

For assays requiring dissociated cells, tissues were incubated in a collagenase type 2 (1 mg/ml, Worthington) dissociation solution. The dissociation solution was made by dissolving 120 mM NaCl, 5.4 mM KCl, 5 mM $MgSO_4$, 5 mM Na-pyruvate, 20 mM glucose, 20 mM taurine, and 10 mM HEPES in ultrapure water supplemented with 30µM $CaCl_2$. Tissues were incubated in the dissociation solution for 2 hours at 37 ºC, centrifuged for 5minutes at 200 g, and resuspended in 0.25% trypsin EDTA (Mediatech) for 5 minutes at 37 ºC. Cells were centrifuged and resuspended in RPMI20 medium (RPMI 1640 medium with 20% FBS, Atlanta Biologicals) supplemented with 5µM RI and seeded on fibronectin (25µg/mL)-coated coverslips or MEA.

3.2.7 Viability and Immunofluorescent Visualization

A LIVE/DEAD viability kit (Molecular Probes) was used to evaluate hiPSC viability 24 hours after encapsulation (day -2). Staining was performed according to the manufactures protocol. Fluorescent z-stacks were taken at random locations within each tissue. The live and dead cells in each Z-stack were counted to determine the percent of live cells. Viability stain was performed on day 8 following differentiation.

Protein expression in GelMA tissues was visualized through immunofluorescence staining. Whole GEhECTs were stained with Alexa Fluor 568 phalloidin (actin filaments,

Invitrogen) on day 0 and day 22. Dissociated GEhECT-CMs attached to fibronectin coated PDMS-coated glass coverslips and whole GEhECTs were stained on Day 23 with either the cardiac marker α-sarcomeric actinin (αSA, Mouse IgG1) or cardiac troponin T (cTnT, Mouse IgG1, Thermo Scientific) and for connexin 43 (Cx43, Rabbit IgG). Dissociated cells and whole tissues were fixed using either 4% paraformaldehyde (Electron Microscopy Sciences) at room temperature or 50:50 acetone: ethanol for Cx43 at -20 ºC for 20 minutes. Cells were permeabilized with PBS-T (PBS with 1% bovine serum albumin (BSA) and 0.2% Triton X-100) and blocked with 3% FBS in PBS blocking buffer overnight. The samples were incubated successively in primary antibody (1:200) and then secondary antibody (Alexa Fluor 568 and 488, 1:200) overnight at 4 ºC. The samples were counterstained with 4',6-diamidino-2-phenyl-indole (DAPI, Molecular Probes). Samples were visualized with a Nikon Alsi confocal microscope.

Nuclear circularities and cross-sectional areas from cells inside the GEhECTs were analyzed on day 0 and day 22 using ImageJ by manually outlining DAPI-stained nuclei. Sarcomere spacing and alignment from dissociated GEhECT-CMs were analyzed using ImageJ plugins. Sarcomere spacing was determined by drawing a perpendicular line through the sarcomeres and obtaining an intensity profile to observe the intersecting sarcomere locations. A second line was drawn on top of each sarcomere one at a time and the angle between the two lines was recorded for at least five sarcomeres per cell (n=36 CMs).

3.2.8 Early GEhECT Growth

To track early tissue growth, phase contrast images of whole tissues were taken daily from day -2 to day 7 of differentiation to measure changes in tissue surface area (Ti Eclipse, Nikon equipped with an Andor Luca S camera). Tissue edges were traced, and the surface area was quantified using ImageJ plugins (n=3). Changes in tissue thickness overtime was measured on days -2, 7, and 19 using the MicroSquisher side-view images.

3.2.9 Contraction Analysis of GEhECTs

Contractions of GEhECTs were measured using motion-tracking software (Huebsch et al. 2015b). Videos of contraction GEhECTs were recorded on days 14, 17, and 40 (n=3 tissues per time point). Each video was converted to a series of tiff files and the motion between the images was calculated. The "DataEvaluation" interface was used to plot the average maximum contraction and relaxation velocities and to determine the frequency of contraction.

3.2.10 Flow Cytometry

On day 27, the cells were prepared for flow cytometry. The tissues were dissociated as described above. The cells were resuspended in 4% paraformaldehyde and incubated for 20 minutes at room temperature. The cells were centrifuged, resuspended in 90% cold methanol, and incubated for 15 minutes at 4 ºC. The fixed cells were blocked with 5% BSA in PBS for 5 minutes, centrifuged and washed two more times. The cells were labeled using 100 µL of primary antibody (cTnT, Thermo Scientific; Ki67, AbCam; CD90, AbCam) diluted in 0.5% BSA and 0.1% Triton X-100 PBS. Cells were incubated overnight and then washed with 0.5% BSA and 0.1% Triton X-100 PBS two more times

before adding 100 µL of secondary antibody (Alexa Fluor 488/647, Invitrogen) diluted in 0.5% BSA and 0.1% Triton X-100 PBS. The samples were washed again and analyzed using a BD Accuri C6 (BD Biosciences).

3.2.11 Reverse Transcription Quantitative PCR (RT-qPCR)

RNA was isolated using a Nucleospin RNA kit (Macherey-Nagel) from GEhECTs on days 10, 22 and 73 (n= 3 different tissues per time point). The RNA concentration was determined using a NanoDrop 1000 UV-Spectrophotometer (Thermo Fisher Scientific). SuperScript III Platinum One-Step RT-qPCR kit was used with 25ng of sample in 12.5 µL of reaction volume. RT-qPCR was run with one cycle at 50 ºC for 15 minutes, one cycle at 95 ºC for 3 minutes, 45 cycles at 95 ºC for 15 seconds each and 55 ºC for 30 seconds each. Gene expression was determined using Taqman probes with forward and reverse primers.

MLC2v: F = GGGCGGAGTGTGGAATTCTT, R = CCCGGCTCTCTTCTTTGCTT, P = /56-FAM/AGTGCTGGG/ZEN/TCCTTTCCACCAT/3IABkFQ/; αMHC: F = ACCAACCT-GTCCAAGTTCCG, R = TTGCTTGGCACCAATGTCAC, P = /56FAM/AGCATGAGC/ZEN/-TGGATGAGGCAGAG/3IABkFQ/; βMHC: F = CACAGCCATGGGAGATTCGG, R = CAGGCACG-AAGACATCCTTCT, P = /56-FAM/CCTACCTGC/ZEN/GCAAGTCAGAGAA-GG/3IABkFQ/; Cx43: F = TGAGCAGTCTGC-CTTTCGTT, R = CCAGAAGCGCACAT-GAGAGA, P =/56FAM/ACACTCAGC/ZEN/AACCTGGTTGTG-AAA/3IABkFQ/. Each data point is averaged from technical duplicates of three biological replicates. A fold change in gene

expression is calculated from $2^{-(\Delta Ct),}$ where ΔCt is the difference from the Ct value of the day 10 sample.

3.2.12 Electrophysiological Characterization and Drug Response

Day 30 GEhECTs was dissociated as previously described and seeded on a 60pMEA200/30iR-Ti (Multichannel Systems) in RPMI20 medium supplemented with 5 μM RI. After 24 hours, the MEA was perfused with Tyrode's solution (1.8 mM $CaCl_2$, 5 mM glucose, 5 mM HEPES, 1 mM $MgCl_2$, 5.4 mM KCl, 135 mM NaCl, and 0.33 mM NaH_2PO_4, pH 7.4) at 37ºC. The MEA was used in a setup with a 1060-Inv-BC preamplifier with STG4002 stimulus generator. Field potential recording were acquired at a sampling frequency of 10 kHz. Samples were exogenously paced from 0.5-3.0 Hz using a rectangular pulse pattern at ±4000 mV and a pulse duration of 10 ms.

Drug treatments were tested using MEA. The β-adrenergic agonist isoproterenol and antagonist propranolol (Molecular Devices) were introduced to the spontaneously contracting GEhECTs-CMs and their response were recorded using video analysis. Isoproterenol at 1 μM was first added to the samples followed by the addition of 1 μM propranolol. Next, the drugs were washed out and baseline contractions were restored.

To visualized propagating calcium waves across the GEhECTs, whole tissues were incubated with the calcium dye Rhod-2 (Invitrogen) and recorded using optical mapping. The calcium dye was prepared using 5 μL of 100 μM Rhod-2 and 5 μL of Pluronic F-127 (4% w/v in DMSO) in 1 mL of Tyrode's solution containing blebbistatin (50 μM). GEhECTs were incubated in the dye for 2 hours at room temperature and then

rinsed with Tyrode's for 15 minutes. Videos of propagating calcium waves were taken as previously described (Spearman *et al.* 2015).

3.2.13 Statistics

Minitab 17 was used to analyze the results and the mean ± standard deviation was reported of all replicates. After testing for normal distribution, one-way analysis of variance (ANOVA) using Tukey's test was used for all studies with equal variance and equal sample size. If the variance was not normally distributed, the Games-Howell test was used. $P < 0.05$ denoted statistically significant differences.

3.3 Results

3.3.1 GelMA Forms Photo-crosslinked Hydrogels That Enzymatically Degrade

In this study, we show the ability to successfully encapsulate hiPSCs in GelMA hydrogels and directly differentiate these cell laden constructs into uniformly contracting cardiac tissues. GelMA has been shown to be suitable biomaterial for a variety of tissue engineering applications (Zhao *et al.* 2016; Schuurman *et al.* 2013). Previous GelMA studies show that a low degree of functionalization (~ 20% methacrylation) forms soft hydrogels, while a high degree of functionalization (~80% methacrylation) forms stiffer hydrogels (Nichol *et al.* 2010). Based on our previous studies with PEG-fibrinogen, we chose to synthesize GelMA with a low degree of functionalization to form soft hydrogels that would be appropriate for forming GEhECTs. Synthesized GelMA was analyzed using ^{1}HNMR to determine the degree of functionalization. A 22% degree of

functionalization (Figure 3.1b) was determined using dividing methacryloyl group peaks (5.3 and 5.5 ppm) by gelatin's free amine group peaks.

Preliminary studies showed that GelMA hydrogels could be formed using the photoinitiator eosin Y by photo-crosslinking with visible light. GelMA hydrogels were enzymatically degradable supporting the cell migration, proliferation, ECM replacement. To validate this, acellular hydrogels were incubated in PBS or collagenase type 2 solution at 37 ºC and weighed at 0, 3, and 6 hours. Hydrogels placed in PBS maintained their mass over the 6-hour period after initially swelling as expected. Hydrogels placed in the enzymatic solution decreased in mass over the same time period, confirming GelMA degradation (Figure 3.1c). After 24 hours, the hydrogels placed in the collagenase were completely degraded. This experiment showed the ability of GelMA to be degraded via enzymatic degradation using enzymes naturally secreted by the cells for remodeling their microenvironments.

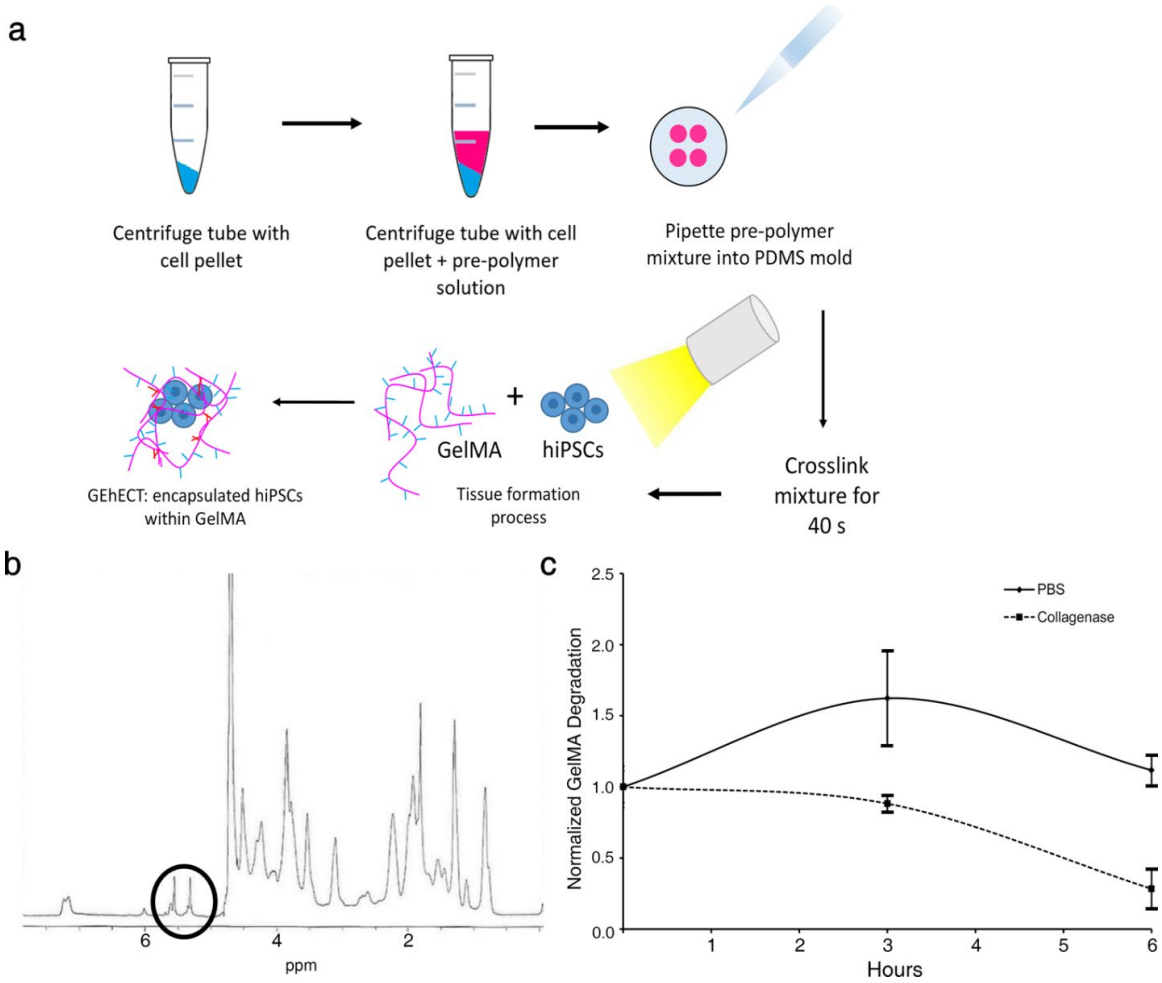

Figure 3.1 Successful use of GelMA hydrogels to produce GEhECTs.

(a) HiPSCs were collected and combined with a liquid GelMA precursor solution; this mixture was then added into a circular PDMS mold and photo-cross-linked for 40 s using visible light. (b) NMR spectrum showed synthesized GelMA with a methacryloyl substitution degree of 22% (signals of methacrylate double bonds at 5.3 and 5.5 ppm). (c) Photo-cross- linked GelMA hydrogels initially swelled in the presence of PBS and degraded when incubated in collagenase, with over 50% mass loss by 6 h (n = 3 hydrogels). Figure courtesy of Petra Kerscher.

3.3.2 GelMA Hydrogels Support hiPSC Survival, Growth and Cardiac Differentiation

To form cell-laden hydrogels, hiPSCs were suspended in polymer precursor solution, pipetted into 8 μL molds, and crosslinked with visible light for less than 1 minute. To verify that soft GelMA hydrogels were formed, mechanical testing was performed on acellular and cellular hydrogels (Figure 3.2a). Acellular hydrogels were much stiffer than cellular hydrogels with an elastic modulus of 660 ± 307 Pa (n=4 tissues). Cellular hydrogels initially decreased in stiffness with the onset of differentiation from 219 ±140 Pa (n=3 tissues) on day -2 (24 h after encapsulation) to 90 ± 8.4 Pa (n=3 tissues) on day 7. As cardiac differentiation progressed, the stiffness of the GEhECTs increased to 248 ± 109 Pa (n= 3 tissues) by day 19.

Following hiPSC encapsulation, morphology and viability assays were performed to analyze cell distribution (Figure 3.2b) and survival (Figure 3.2c). Phase contrast imaging showed uniformly distributed hiPSC colonies throughout the GelMA hydrogels. Viability assays showed > 75% of hiPSCs survived the encapsulation process. Three days post-encapsulation, hiPSCs began to grow outside the original hydrogel construct (Figure 3.2d) resulting in an increase of lateral surface area. As the hiPSC proliferated, they maintained a round cell morphology, visualized by F-actin staining (Figure 3.2e), through the start of differentiation (day 0).

Cell proliferation and growth are most pronounced around the circumference of the GEhECTs prior to and during differentiation (Figure 3.2 and 3.3a), visualized by subsequent darkening of phase contrast images due to increased cell density and tissue area. GEhECTs lateral tissue surface area increased by 13.1 ± 1.7 % between day -2 and day 5 of differentiation. From day 5 to day 7, lateral surface decreased by 2.8% (Figure

3.3b, n =3 tissues), followed by the onset of spontaneous contraction on day 8. GEhECT thickness remained constant between day -2 and day 7. A significant increase in tissue thickness was observed by day 19 (Figure 3.3.c). Successful cardiac differentiation of encapsulated hiPSCs was verified by flow cytometry on day 27 of differentiation. GEhECTs contained 70.4 ± 1.6% CMs (cTnT+), with 10.6 ± 2.6% being proliferating CMs (cTnT +, Ki67+), and 8.4 ± 0.3% fibroblast (CD90+, Figure 3.3d, n=3 tissues). Immunostaining with cardiac marker cTnT and functional protein Cx43 showed expression throughout whole GEhECTs. Appropriate temporal changes in cardiac and functional gene expression verified progressive maturation of GEhECTs. Expression of ventricular cardiac markers MLC2v was significantly upregulated on days 20 and 70 compared to day 10, with a downward trend between days 20 and 70 (Figure 3.3e). Alpha myosin heavy-chain (αMHC) decreased from days 10 and 20 to day 70 (Figure 3.3f). Beta myosin heavy-chain (βMHC) showed a significant increase between days 10 and 20 to day 70, indicative of temporal maturation (Figure 3.3g). The functional gene connexin 43 (Cx43) increased between day 10, 20 and 70, suggesting an increase in cardiac functionality over time (Figure 3.3h)

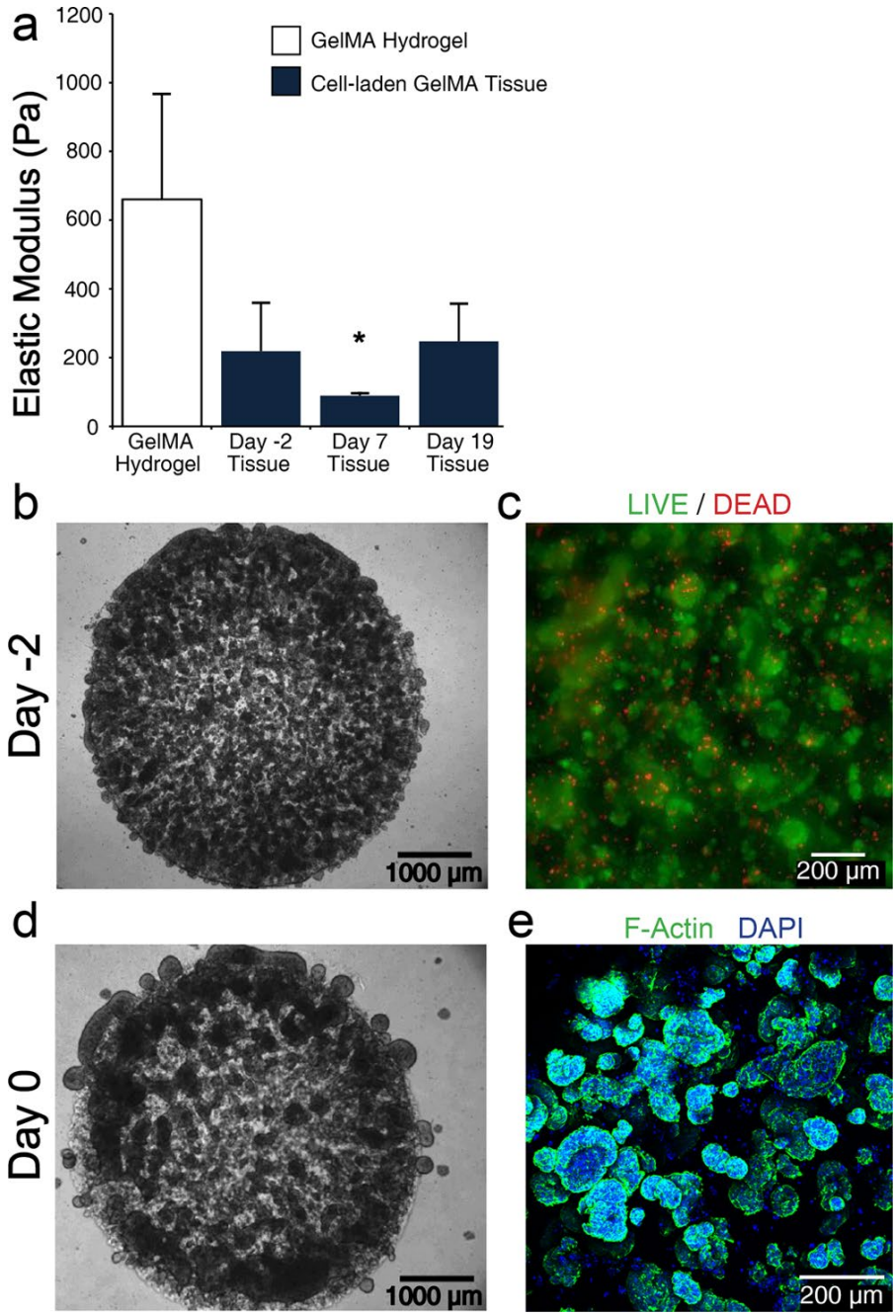

Figure 3.2 GelMA encapsulated hiPSCs form soft, cell-laden hydrogels with hiPSCs surviving the encapsulation process to produce GEhECTs.

(a) Acellular GelMA hydrogels exhibited an elastic modulus of 660 ± 307 Pa; in comparison, cellular GelMA tissues 24 h after encapsulation (day −2) were softer, with an elastic modulus of 219 ± 140 Pa. Elastic modulus of the GEhECTs decreased to 90 ± 8.4 Pa by day 7. Later in the

cardiac differentiation process (day 19), GEhECT elastic modulus was again higher at 248 ± 109 Pa. n = 3 tissues per group. Mean ± s.d. ANOVA $P < 0.05$, *vs GelMA hydrogel. (b) Phase contrast image showed circular 3D cell-laden hydrogel 24 h after encapsulation (day −2) with (c) the majority of hiPSCs surviving the encapsulation process (green = viable, red = dead). (d) Three days after encapsulation (day 0), hiPSCs formed growing clusters, (e) displaying a round cell morphology (F-actin filaments visualized by phalloidin, green) with cells expanding beyond the original boundary of the hydrogel. Images courtesy of Petra Kerscher.

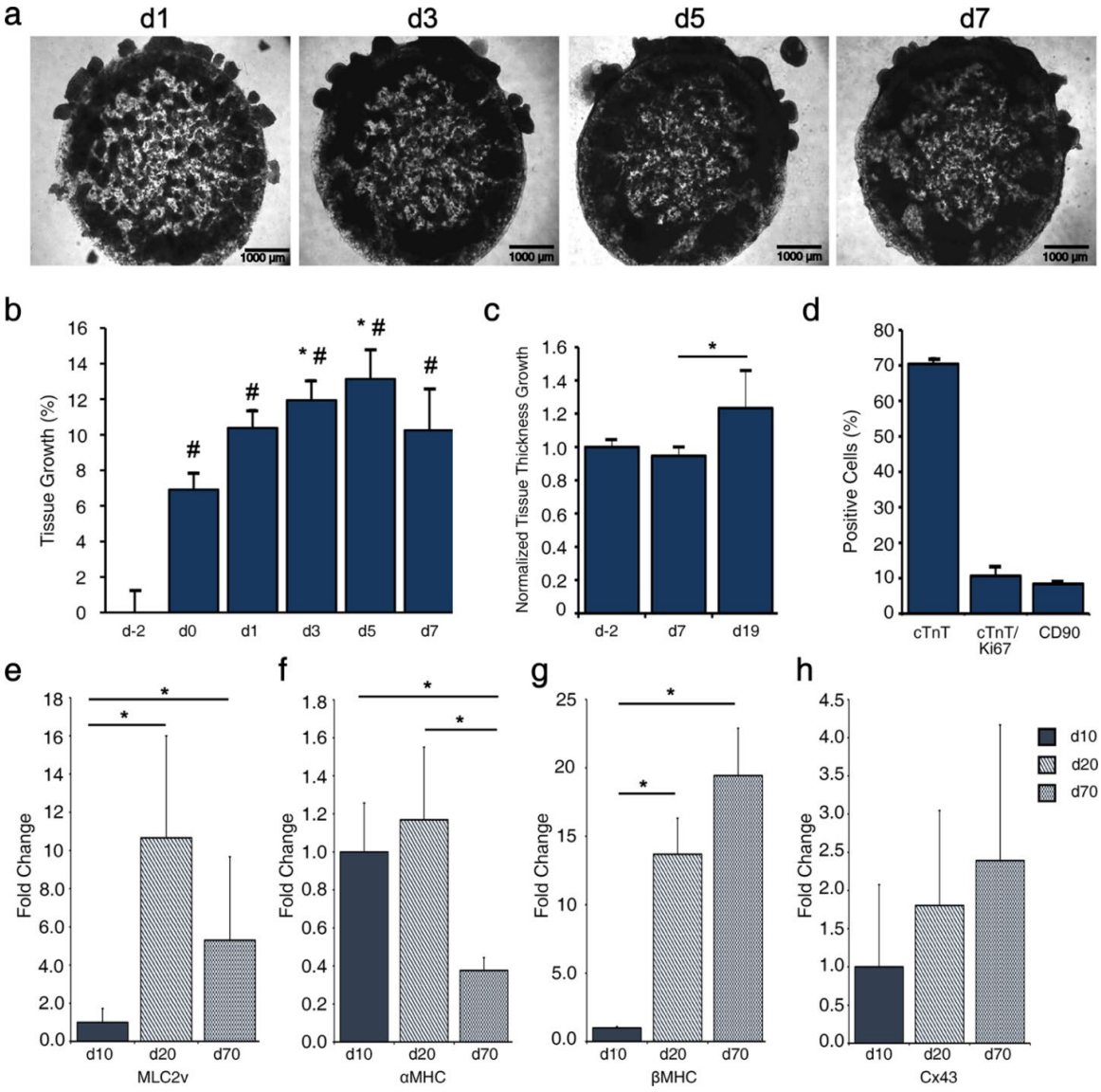

Figure 3.3 Growth and differentiation of encapsulated hiPSCs form a continuous tissue over time.

(a) After the onset of cardiac differentiation (day 0), cells continued to grow within the original GelMA construct, forming a more connected tissue over time. (b) Circular surface area of tissues increased by 13.1 ± 1.7% by day 5 and decreased somewhat thereafter to form a dense tissue by day 7, immediately prior to the onset of contraction, observed consistently on day 8. n = 3 tissues per group. Mean ± s.d. ANOVA $P < 0.05$, $^{\#}$vs day −2, *vs day 0. (c) Tissue thickness was similar on day −2 and day 7 but increased by day 19 of differentiation. n = 3 tissues per group. Mean ±

s.d. ANOVA P < 0.05, *vs day 7. (d) On day 17, GEhECTs contained approximately 70.4 ± 1.6% CMs (cTnT+), of which 10.6 ± 2.6% were proliferating (cTnT+, Ki67+), and 8.4 ± 0.3% fibroblasts (CD90+) (n = 3 tissues). (e) Gene expression of the cardiac markers MLC2v, αMHC, and βMHC on day 10, 20, and 70 GEhECTs showed temporal changes expected of maturing SC-CMs during culture. Cx43 gene expression in GEhECTs trended upward suggesting developing cell−cell coupling (n = 3 GEhECTs). Mean ± s.d. ANOVA *P < 0.05. Data courtesy of Petra Kerscher.

3.3.3 Uniformly Contracting GEhECTs Showed Increased Frequency and Velocity of Contraction Over Time.

GEhECTs consistently showed onset of spontaneous contraction on day 8 of differentiation, with more areas initiating contraction over time. Uniformly contracting tissues were seen by day 14. Once isolated areas joined and began contracting uniformly, frequency and average maximum contraction and relaxation velocity increased over time (Figure 3.4). Video recording show visual deforming between contraction and relaxation states. Sarcomeres and functional proteins were visualized through immunostaining whole tissues (Figure 3.4a). The frequency of contraction significantly increased from day 14 (0.3 Hz) to day 40 (0.9Hz, Figure 3.4b). The maximum contraction velocity increased between days 14 and 40 from 120 ±48 μm/s to 597 ± 127 μm/s (Figure 3.4c). The maximum relaxation velocity followed the same trend increasing from 86 ±58 mm/s on day 14 to 564 ± 107 mm/s on day 40 (Figure 3.4d). These increases in frequency and velocity correlate to video recordings showing stronger tissue contraction over time.

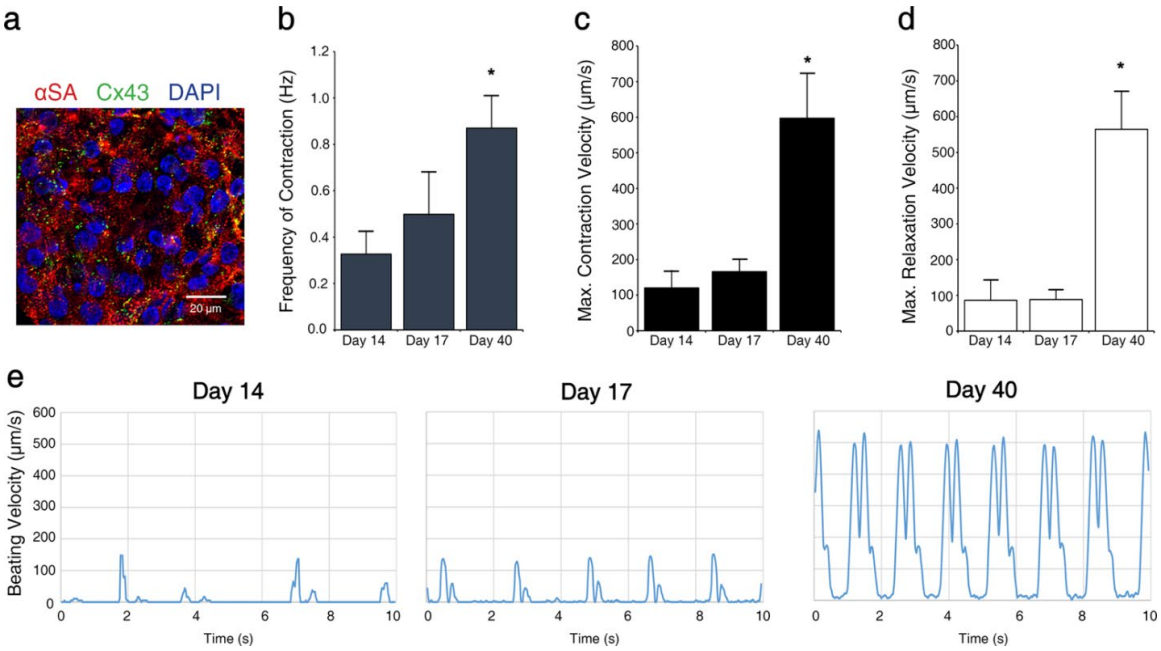

Figure 3.4 Increase in frequency of spontaneous contraction and contractile velocity with GEhECTs culture time.

(a) Whole tissue staining of day 23 GEhECTs displayed striation (αSA, red) and gap junctions (Cx43, green). (b) GEhECTs formed uniformly contracting tissues by day 14, with frequencies of spontaneous contraction increasing significantly between days 14 and 40. (c, d) In addition to the increase in contraction frequency, average maximum contraction and relaxation velocities also increased from day 14 to day 40 of differentiation. This increase in contraction and relaxation velocity corresponded with visual observations of stronger contracting tissues (Supplementary Movies 3 and 4). (e) Representative analyzed traces showing progression over time. n = 3−5 tissues. Mean ± s.d. ANOVA $P < 0.05$, *vs days 14, 17.

3.3.4 Cellular Remodeling and Development of CMs in GEhECTs

Changes in actin filament morphology and nuclei size and morphology between days 0 and 22 of differentiation indicate intracellular and microenvironment remodeling

to form a connective and uniformly contracting tissue. Confocal imaging of F-actin and DAPI staining on day 0 (Figure 3.2e) show encapsulated cells with round (0.8 ± 0.1 circularity, Figure 3.2b) and small (91.2 ± 30 μm^2 , Figure 3.2c) cell nuclei. On day 22 after differentiation, GEhECTs showed elongated actin filaments (Figure 3.5a) with slightly more elongated (0.7 ± 0.1 circularity, Figure 4.5b) and bigger (149 ± 52.4 μm^2, Figure 3.5c) nuclei of differentiated cells.

In addition to the previously described results, immunostaining of dissociated GEhECTs CMs confirmed successful differentiation. Whole GEhECTs were dissociated and replated on a 2D surface where they reestablished synchronous contractions. Dissociated CMs showed well-defined (Figure 3.5d) and aligned (Figure 3.5e, n=36) sarcomeres, spaced at 1.85 ± 0.1 μm (n = 20 cells).

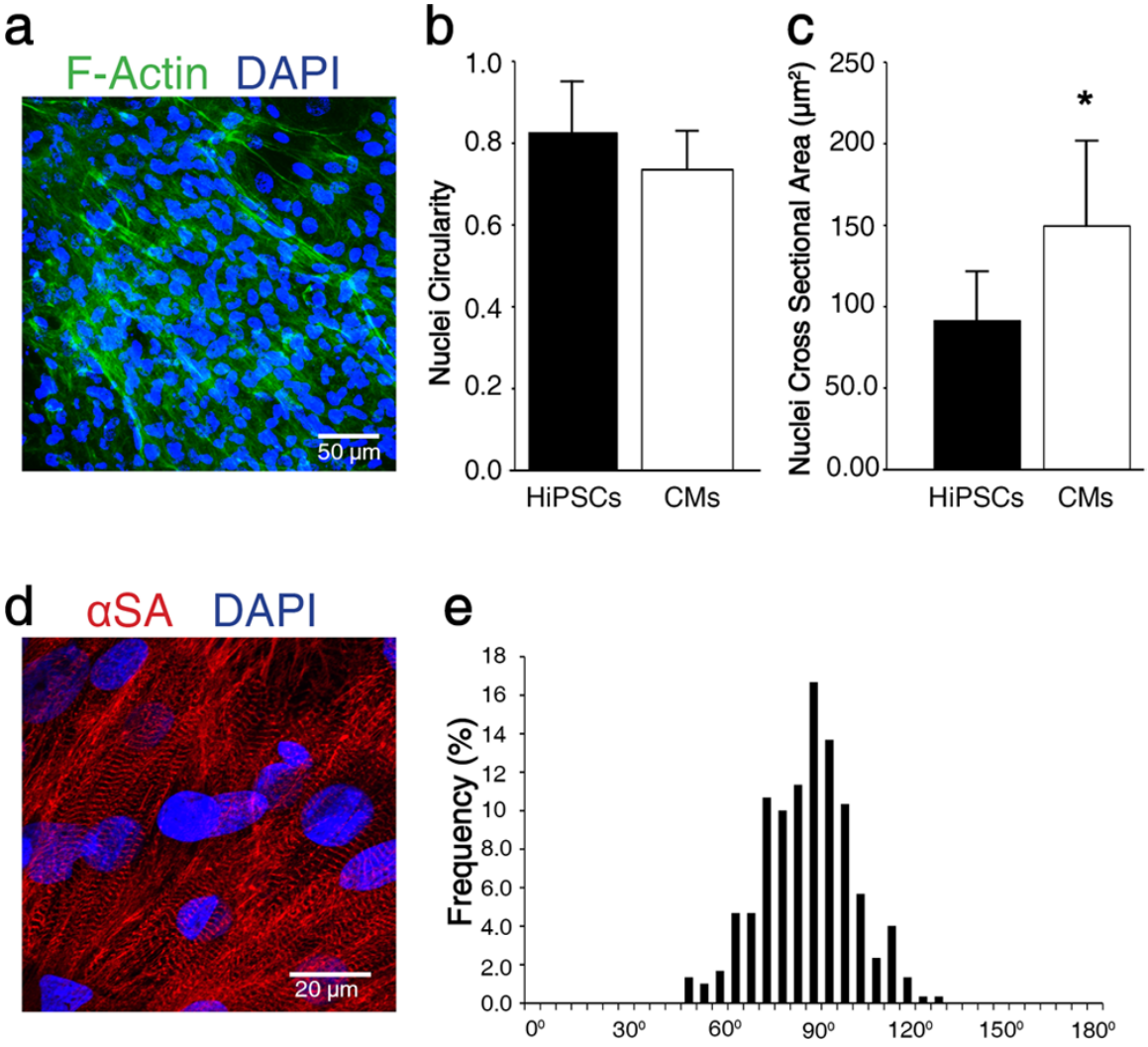

Figure 3.5 GEhECT CMs remodel their microenvironment and show morphological differences expected from differentiated cells.

(a) Day 22 tissues contained areas of high cell density primarily on the edges of GEhECTs where cells showed elongated F-actin filaments (phalloidin, green). (b, c) Day 0 (hiPSCs) encapsulated cells displayed more circular and smaller nuclei compared to day 22 (CMs) cells. n = 30 nuclei per condition. Mean ± s.d. ANOVA $P < 0.05$, *vs HiPSC. (d) Following tissue dissociation, GEhECT-dissociated CMs continued to spontaneously contract (Supplementary Movie 5) and locally self- aligned with each other, displaying defined sarcomeres (αSA, red) with (e) high intracellular alignment (n = 36). Data courtesy of Petra Kerscher.

3.3.5 GEhECT CMs Responded to Extrinsic Stimuli

Spontaneous calcium wave propagation was visualized in whole GEhECTs. The functionality of CMs was evaluated by pharmacological and electrical stimulation to evaluate the potential of GEhECTs CMs to be used for clinical applications. Contracting GEhECTs were treated with the β-adrenergic agonist isoproterenol (1 μM), which resulted in an increase in frequency (~ 0.2 Hz), as expected. Successively, the β-adrenergic antagonist was added to the contracting GEhECTs which caused an expected decrease in contraction frequency (~ 0.36 Hz, Figure 3.6a, n = 3 tissues). Changes in frequency of contraction were consistent across two cells lines and multiple tissues. GEhECTs were dissociated, seeded on an MEA chip (Figure 3.6b), and electrically paced from 0.5 to 3.0 Hz. Field potential recording responded appropriately to outside pacing (Figure 3.6c).

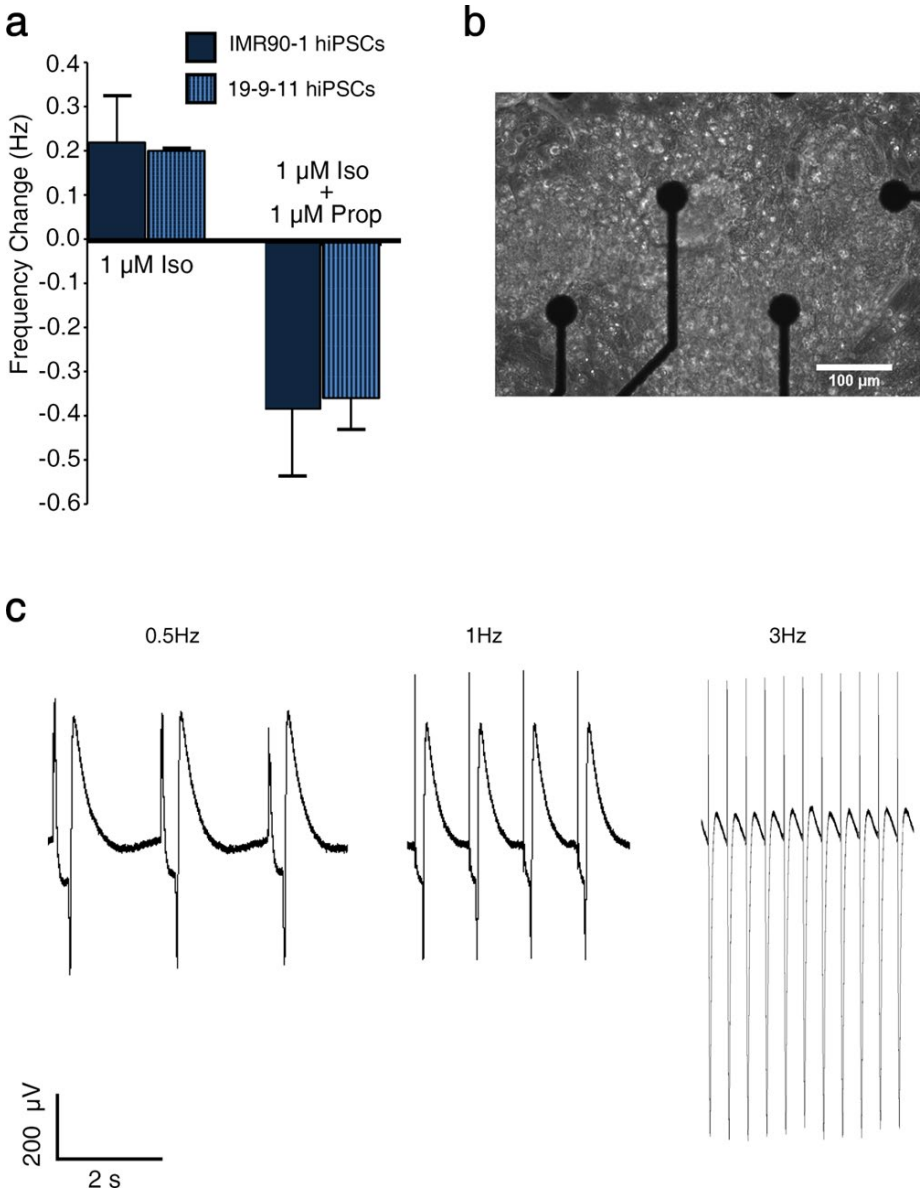

Figure 3.6 Response of cardiac tissues to drug treatment and outside pacing. (a) GEhECTs produced with IMR90-1 and 19-9-11 hiPSC lines responded to the β-adrenergic agonist isoproterenol (Iso) and β- adrenergic antagonist propranolol (Prop); 1 µM Iso increased the frequency of spontaneous contraction, the subsequent addition of 1 µM Prop slowed down the contraction. (b) Day 30 GEhECT- dissociated CMs (from IMR90-1 hiPSCs) were cultured on MEA (Supplementary Movie 7) and (c) extrinsically paced. GEhECT- dissociated CMs responded to outside pacing frequencies up to 3.0 Hz. Data Courtesy of Petra Kerscher.

3.4 Discussion

In the present study, we show that GelMA is a fitting biomaterial for direct cardiac differentiation of hiPSCs to form GelMA human engineered cardiac tissues (GEhECTs). GelMA is a hybrid biomaterial composed of the denatured ECM protein collagen. GelMA is a biomimetic material that encourages cellular enzymatic degradation and remodeling of the microenvironment. The stiffness of GelMA can be changed by altering the degree of functionalization, exposure time, and light intensity (Loessner et al. 2016). Soft GelMA hydrogels were produced using by encapsulating hiPSCs in GelMA with a 22% degree of functionalization. During mechanical testing, acellular hydrogels were much stiffer than cellular hydrogels at all time points but remained under 1 kPA. GelMA with high degrees of functionalization was not chosen for this project due to the tendency of stiffer materials to prevent cell spreading and change cell morphology (Frisman, Seliktar, and Bianco-Peled 2011). Compared to other studies with similar degrees of functionalization, our synthesized GelMA hydrogels were softer. This could be the result of difference in photoinitiator or crosslinking time.

Identifying successful biomaterials for producing functional developing human heart tissues using a single hiPSC handling step is challenging. Creating a successful tissue engineering product depends on a variety of parameters including but not limited to, mechanical properties, rate, and mode of degradation, hiPSC seeding density, cell culture and differentiation processes. Biomaterials designed for cardiac tissue engineering are the subject of significant research efforts (Radisic 2015). Incorporating

additional mechanical and electrical cues may further enhance GEhECT functionality and maturation (Shin *et al.* 2013). In previous studies, natural biomaterials like collagen, Matrigel, or fibrin have been used to create cardiac tissues because they mimic native ECM proteins (Nunes et al. 2013; Radisic et al. 2004b; Ye, Sullivan, and Black 2011). While these materials are biocompatible and biodegradable, they often have batch to batch variability and are not tunable. Purely synthetic materials have been used in tissue engineering applications for their precise control and tunable nature (Loessner *et al.* 2010). However, these materials often lack cell adhesion and bioactive sites necessary to support cell viability, motility, and proliferation.

Based on the limitations of each category of biomaterials alone, hybrid and modified natural biomaterials are becoming more widely used in tissue engineering. Hybrid and biosynthetic materials are tunable and possess the necessary mechanical, biological, and physical characteristics required for cell survival, adhesion, and proliferation (E.J. Lee, Kasper, and Mikos 2014a). Therefore, PEG-fibrinogen and GelMA are advantageous choices for producing developing cardiac tissues. Recently, we showed that PEG-fibrinogen is a suitable biomaterial for direct cardiac differentiation of hiPSCs (Kerscher, Turnbull, et al. 2016). PEG-fibrinogen has been successfully used as a biomaterial in a variety of tissue engineering fields including cardiovascular (Kerscher, Turnbull, et al. 2016), orthopedic (Peled *et al.* 2007), and cancer modeling (Pradhan *et al.* 2017). In addition, a PEG-fibrinogen hydrogel product, GelrinC, is in phase III clinical trials for treatment of cartilage defects in the knee (Ltd. 2016). Although PEG-fibrinogen is widely successful, it has not yet been used in bioprinting applications, which is critical for transitioning from benchtop studies to biomanufacturing. GelMA has been used as a

suitable biomaterial in cardiovascular (Kerscher, Kaczmarek, et al. 2016a), skin (Zhao *et al.* 2016), and cartilage (Schuurman *et al.* 2013) engineering, among several others. Furthermore, GelMA has been used for bioprinting 3D tissues (Kolesky et al. 2014; Y.F. Ma, Ji, et al. 2015).

Bioprinting allows for fast production of various 3D cell configurations with high reproducibility and production speed. Bioprinting with hiPSCs presents a few challenges due to the delicate nature of the cell type. Nonetheless, hiPSCs have been printed with high viability and cell quality (Faulkner-Jones *et al.* 2015). Printing hiPSCs in hybrid biomaterials followed by direct differentiation to the cardiac lineage has not been investigated to our knowledge. Based on our results, GelMA could have a high potential for bioprinting hiPSCs for cardiac differentiation.

Function and mechanical contractions are an easily monitored physical characteristic of healthy cardiac tissues that can be seen throughout *in vitro* development and maturation. Using video analysis of whole GEhECTs, changes in contraction frequency and velocity showed significant increases over time. GEhECTs were maintain in suspension culture without constraints. Contraction and relaxation velocities of whole GEhECTs at day 14 matched those of other 2D culture hiPSC-CMs (Huebsch et al. 2015b). By day 17, GEhECTs developed stronger cell-cell connections, with tissues contracting faster and with greater deformation. Increased contraction and relaxation velocity were seen through at least day 40 of differentiation. Although GEhECTs increased their contraction frequency over time, the rate of contractions was slower than previously established *in vitro* models cultured with an applied mechanical(Tulloch et al. 2011). GEhECTs showed regular contraction patterns with uniform frequency which has

previously been linked to uniform distribution and cell alignment (Tsang *et al.* 2015). Overall, the *in vitro* functionality of these developing tissues is important for future applications in drug testing and regenerative medicine.

3.5 Conclusions

In recent years, significant research has been performed to produce functional human induced pluripotent stem cell-derived cardiomyocytes. The interactions between the cells and the materials have been widely studied but determining appropriate materials to facilitate these interactions has been challenging. In this study, we have shown for the first time that the printable biomaterials gelatin methacryloyl (GelMA) can be successfully used to encapsulate and directly differentiation hiPSCs to form GelMA human engineered cardiac tissues (GEhECTs). GelMA with a low degree of functionalization supports cell viability, microenvironment remodeling, and high-efficiency cardiac differentiation. We showed that GEhECTs increased in frequency and velocity of contraction over time and GEhECTs-CMs presented with well aligned sarcomeres and responded appropriate to drug treatment and external pacing. Our results show the potential for GelMA to be translated toward a bioprinting application for manufacturing reproducible human cardiac tissues.

Chapter Adapted with permission from Petra Kerscher, Jennifer A. Kaczmarek, Sara E. Head, Morgan E. Ellis, Wen J. Seeto, Joonyul Kim, Subhrajit Bhattacharya, Vishnu Suppiramaniam, and Elizabeth A. Lipke. ACS Biomaterials Science & Engineering 2017

3 (8), 1499-1509. DOI: 10.1021/acsbiomaterials.6b00226. Copyright 2016 American Chemical Society

Chapter 4: Initial HiPSC Encapsulation Geometry Impacts 3D Developing Human Engineered Cardiac Tissue Functionality

Cardiac tissue engineering has been working to alleviate the immense burden of cardiovascular disease for several decades. To improve cardiac tissue homogeneity and cardiomyocyte (CM) maturation, here we investigated altering initial encapsulation geometry in a 3D direct cardiac differentiation platform. Traditional engineered cardiac tissue production utilizes pre-differentiated CMs to produce 3D cardiac tissue and often involves various cell selection and exogenous stimulation methods to promote CM maturation. Starting tissue formation directly with human induced pluripotent stem cells (hiPSCs), rather than pre-differentiated CMs, simplifies the engineered cardiac tissue formation process making it more applicable for widespread implementation and scale-up. Here, hiPSCs were encapsulated in PEG-fibrinogen in three tissue geometries (disc-shaped microislands, squares, and rectangles) and subjected to established cardiac differentiation protocols. Resulting 3D engineered cardiac tissues (3D-ECTs) from each geometry displayed similar CM populations (~ 65%) and gene expression over time. Notably, rectangular tissues displayed less tissue heterogeneity and more advanced features of maturing CMs including myofibrillar alignment and Z-line formation. Additionally, rectangular tissue showed significantly higher anisotropic contractile properties compared to square and microisland tissues (MI 0.28 ± 0.03, SQ 0.35 ± 0.05, RT 0.79 ± 0.04). This study demonstrates a straightforward method for simplifying and improving 3D-ECT production without the use of exogenous mechanical or electrical pacing and can be extended in bioprinting and drug testing applications.

4.1 Introduction

Heart disease is the leading cause of death worldwide in both men and women of nearly all ethnicities (Organization 2017). With limited regenerative capacity, diseased cardiac tissue is not able to fulfill its electrical and mechanical roles, including electrical signal propagation and blood circulation, often leading to arrhythmias and sudden cardiac death. Heart transplants remain the standard of care for treating heart failure, but as a result of the highly limited supply of organs for transplant, this costly and invasive option is not always available (Bernstein 2011). Cardiac tissue engineering provides the potential to create functional replacement tissues for use in cardiac regenerative medicine and as an *in vitro* platform for testing new therapeutics.

With the discovery of human induced pluripotent stem cells (hiPSCs) in 2007 (Takahashi et al. 2007), employing hiPSC-derived cardiomyocytes (hiPSC-CMs) has become customary in the field of cardiac tissue engineering. HiPSCs are differentiated down the cardiac lineage using a series of small molecules and growth factors, often in the form of embryoid bodies (L. Yang et al. 2008; Kattman et al. 2011) or monolayers (Burridge et al. 2011; Lian et al. 2013). Extensive research is being conducted using hiPSC-CMs to recapitulate the native tissue functionality, but there are major challenges in producing cells that mature to the adult CM phenotype, in particular with respect to cell morphology and alignment, electrophysiological function, calcium handling, and gap junction distribution (Feric and Radisic 2016; H.S. Chen, Kim, and Mercola 2009).

One of the key components of cardiac maturation *in vivo* is the alignment of CMs to form highly aligned myofibers, which are important for contraction (Black et al. 2009) and electrophysiological function (Chung, Bien, and Entcheva 2007). In the native myocardium, the CMs orient themselves longitudinally to allow for electric coupling through intercalated discs at the ends of the rod-shaped cells, where most of the gap junctions reside, resulting in anisotropic action potential propagation (Kleber and Rudy 2004). The organization and distribution of gap junctions in neighboring cells determines the current resistance, and therefore electrical function of the tissue (Severs 2000). *In vivo*, anisotropic action potential results in faster propagation in the longitudinal direction than in the transverse direction (Trantidou et al. 2015). This orientation allows for the individual cardiomyocytes to function together as a single contractile tissue for proper cardiac function. *In vitro*, engineered cardiac tissues often contain fetal-like CMs with randomly dispersed gap junctions, resulting in isotropic action potential propagation (Feric and Radisic 2016). Improving *in vitro* CM morphology and alignment, thereby promoting CM maturation, is critical for applicability in therapeutic testing and disease modeling.

Several techniques have been employed to improve cell organization *in vitro*, including micro- and nano-patterning (D.H. Kim et al. 2010; McDevitt et al. 2002b). However, these experiments often required specialized equipment and are performed in 2D monolayers rather than 3D tissues. Additionally, many of these platforms require pre-differentiated CMs which prevents us from studying CM alignment throughout development. We have previously shown the ability to encapsulate hiPSCs in poly (ethylene glycol) fibrinogen (PEG-fibrinogen) to form 3D human engineered cardiac

tissues (3D-ECTs) in a “microisland” disc-shaped geometry. While this study was highly successful, resulting in 3D-ECTs that presented with T-tubules adjacent to Z-lines, a key component of functional maturation (Kerscher, Turnbull, et al. 2016), contraction often propagated in a circular direction along the edges of the microisland, which is not typical of contracting human myocardium.

In this study, we investigated the promotion of cardiac tissue maturation on the macro-scale by changing the initial hiPSC encapsulation geometry. To do this, we compared three different tissue geometries: a rectangular tissue with a 5:1 length to width ratio, a square tissue with a 1:1 length to width ratio, and our established microisland geometry. The square geometry was selected to mimic the microislands while providing a straight outer edge for alignment. The rectangular geometry was designed to simulate a linear representation of the dense tissue ring that we saw in previous studies. Here we show that the rectangular geometry resulted in less tissue heterogeneity and improved cardiac tissue maturation resulting in the tissues more closely mimicking the native myocardium. The knowledge gained in this study will impact future production of engineered cardiac tissue for studying disease mechanisms and cardiac developmental biology.

4.2 Materials and Methods

All materials were purchased from Sigma-Aldrich unless otherwise stated.

4.2.1 Glass Acrylation and PDMS Mold Preparation

Tissues were immobilized on acrylated glass coverslips to accurately track tissue development. Circular glass coverslips (21 mm, No.1 Fischer Scientific) were sterilized in 70% sulfuric acid (H2SO4) and 30 % hydrogen peroxide (H2O2) for approximately 30 minutes, rinsed with ethanol, and dried overnight in an oven at 40°C. Sterilized cover slips were added to acrylation solution containing 0.26 % (v/v) glacial acetic acid, 2.64% (v/v) distilled water, 0.48% (v/v) 3-(Trimethoxysilyl) propyl methacrylate, and 97% (v/v) ethanol for 12 hours at room temperature. After acrylation, coverslips were rinsed with ethanol, dried, and stored at 4 ºC.

Polydimethylsiloxane (PDMS) molds were created using the Sylgard Elastometer Kit (Fisher Scientific) (Supplementary Figure 4.1). The Sylgard 184 curing agent was mixed with the Sylgard 184 silicone elastomer at a 1:10 ratio and placed under vacuum to remove bubbles. The mixture was poured into 3D printed negative castings of the desired tissue geometries and cured for 48 hours at room temperature. After curing, the molds were peeled off the castings, sonicated in 70% ethanol solutions, and sterilized under ultraviolet light before use. For encapsulations, the PDMS molds were placed on top of an acrylated glass coverslip.

3D-printed cast were designed using SolidWorks software. Cast were printed using acrylonitrile butadiene styrene filament. The basic design was a round wafer shape with raised areas representing the negative volume of the desired tissue geometries. Square molds had a tissue 1:1 length to width ratio. Rectangular molds had a tissue 5:1 length to width ratio.

4.2.2 HiPSC Culture

IMR90 clone 1 (WiCell) hiPSCs were cultured in mTeSR medium (Stem Cell Technologies) on six-well plates coated with hESC qualified Matrigel (BD Biosciences) at 37 ºC, 5% CO_2, and 85% relative humidity. HiPSCs were passaged approximately every 4 days using Versene for 4.5 minutes at 37 ºC into mTeSR supplemented with 10 µM ROCK inhibitor (RI, Y-27632, Stem Cell Technologies) for 24 hours after passaging.

4.2.3 Synthesis of PEG-fibrinogen and Preparation of Precursor Solution

Poly (ethylene glycol) diacrylate (PEGDA) and poly (ethylene glycol) fibrinogen (PEG-fibrinogen) were synthesized as previously described (DeLong, Moon, and West 2005; Plotkin et al. 2014).

Briefly, acryloyl chloride was reacted with PEG (molecular weight: 10 kDa) in a 4:1 molar ratio in anhydrous dichloromethane with trimethylamine at 1:2 molar ratio under argon overnight at 25 ºC. The reacted PEGDA mixture was purified by phase separation using 2M K_2CO_3. The synthesize PEGDA was dried using anhydrous $MgSO_4$ and filtered. Lastly, the PEGDA was precipitated in diethyl ether, filtered, and dried at room temperature overnight. The PEGDA was stored at -20 ºC. ^{1}H NMR was used to calculate the degree of acrylation.

PEG-fibrinogen was synthesized by covalently coupling bovine fibrinogen to PEGDA. Bovine fibrinogen (7 mg/ml) was dissolved in 10 mM PBS containing 8 M urea solution. Tris (2-carboxyethyl) phosphine hydrochloride (TCEP-HCl) was added to the above solution in a 1.5:1 molar ratio of TCEP to fibrinogen cysteines. The pH was adjusted to 8.0. The synthesized PEGDA was dissolved in 8M urea-PBS solution at 280

mg/ml, centrifuged to form a clear solution, and added to the fibrinogen solution. The reaction proceeded for three hours in the dark at 25 ºC and stopped by diluting the solution with an equal volume of 8M urea-PBS buffer. The reaction products were precipitated in acetone at a 4:1 volumetric ratio of acetone to product solution. After settling, the precipitate was centrifuged, and the supernatant was removed. The remaining product was weighed and dissolved in 8M urea-PBS buffer at a concentration of 2.2 mL of buffer/ gram of precipitate. Finally, the product was dialyzed against 1L of PBS at 4 ºC in the dark overnight and stored at -80 ºC. PEG-fibrinogen protein content was measured using Pierce™ BCA Protein Assay Kit (Thermo Fisher Scientific). Relative PEGDA content was determined by aliquoting PEG-fibrinogen solution into glass vials, lyophilizing, and calculating the net weight of the dry solid.

The PEG-fibrinogen polymer precursor solution was made using PEG-fibrinogen at a final protein concentration of 10 mg/ml in PBS. The PEG-fibrinogen was combined with 1.5v/v% triethanolamine (TEOA), 0.39 v/v% N-vinylpyrrolidone (NVP) and 0.1 mM eosin Y (Fischer Scientific) photoinitiator.

4.2.4 3D-ECT formation

HiPSCs were dissociated using Versene for 4.5 minutes at 37 ºC. HiPSCs were resuspended in mTeSR medium and centrifuged for 5 minutes at 200g. The supernatant was removed leaving a cell pellet which was resuspended in polymer precursor solution at a concentration of 60 million hiPSCs/ml of precursor solution using a wide orifice pipet. Eight microliters of cell suspension was pipetted into each tissue geometry mold on acrylated glass coverslips. The solution was crosslinked using visible light for 30

seconds. The PDMS mold was carefully removed and the attached tissues were placed in a 6-well plate with 3 mL of mTeSR medium supplemented with 10 μM RI (Day -3). On the following two days (Day -2, Day -1) the spent media was replaced with 3 mL of fresh mTeSR media. On Day 0, cardiac differentiation was initiated using established protocols (Lian et al. 2013) where 12 μM CHIR was added to RPMI B27 minus insulin (Thermo Fisher Scientific). Exactly 24 hours later (Day 1), the media was replaced with fresh RPMI B27 minus insulin. Exactly 48 hours later (Day 3), half of the spent media was combined with an equal amount of fresh RPMI B27 minus insulin supplemented with 5 μM IWP2. Exactly 48 hours later (Day 5), spent media was replaced with fresh RPMI B27 minus insulin. On Day 7 and every 3 days thereafter, 3D engineered cardiac tissues (3D-ECTs) were fed with RMPI B27.

4.2.5 Viability and Immunofluorescent Visualization

A viability assay was performed using Live/Dead Viability kit (Thermo Fisher Scientific). Whole 3D-ECTs were stained with calcein AM, ethidium homodimer-1, and Hoechst 33342 and visualized using a Nikon A1R laser-scanning confocal microscope. Confocal Z-stacks with 5 μm steps were taken at the edge and in the middle of each tissue geometry and projected to a single image.

4.2.6 Early 3D-ECT Growth

Low magnification (2X) phase contrast images were taken of 3D-ECTs throughout differentiation on days -2, -1, 0, 2, and 7 using a Ti Eclipse Nikon equipped with an Andor Luca S camera. Images were processed using ImageJ. To quantify tissue area growth over time, ($n \geq 3$ encapsulations per time point for each geometry) tissue area

was calculated for each tissue and normalized to itself on day -2. Regions of heterogeneity were quantified by subtracting the void regions from the total tissue area.

4.2.7 Tissue Dissociation

3D-ECTs were dissociated using collagenase type B (Worthington) and 0.025% trypsin (Corning). Tissues were washed with PBS and placed in collagenase type B with 0.5 mg/mL DNAse solution for roughly 10 minutes in a 37°C water bath with periodic shaking. The samples were spun down, the supernatant was removed, and the cell pellets were resuspended in 0.025% trypsin for 2 minutes in a 37°C water bath. The trypsin solution was neutralized with three times the volume of RPMI20. The suspension was centrifuged, supernatant was removed, and cells were resuspended in PBS or media for further characterization.

4.2.8 Flow Cytometry

On day 10, 3D-ECTs (n = 3, 2 tissues per encapsulation for 3 encapsulations for each geometry) were dissociated as described above. Resulting cell pellets were washed with PBS before being labeled with the viability marker Zombie Green (Biolegends) for 30 minutes. Cells were washed with 10% FBS with 1% BSA blocking buffer. The cells were centrifuged, the supernatant was removed, and the cells were resuspended in FoxP3 (Thermo Fisher Scientific) for fixation overnight at 4°C. The following day cells were permeabilized in Permeabilization Buffer (Thermo Fisher Scientific). Next, the cells were blocked and permeabilized using FACS buffer containing 10% FBS and 1% BSA in Permeabilization Buffer. Cell suspensions were filtered using 40 μm flow filters and split for primary staining. Cells were labeled with primary antibody MF 20 (Developmental

Studies Hybridoma Bank) and cardiac troponin T (cTnT, Thermo Fisher Scientific) for one hour at room temperature and washed 3 times with Permeabilization Buffer. Cells were then incubated with secondary antibody for 45 minutes at room temperature, washed three times with Permeabilization Buffer, and resuspended in blocking buffer for analysis. Samples were analyzed using a Cytoflex LX and FlowJo software. Data presented represents all live, single cells.

4.2.9 Immunostaining and sarcomere length

To visualize differences in cardiac tissue formation and sarcomere length between geometries, immunostaining was performed using alpha-sarcomeric actinin (αSA, Sigma A7811), connexin 43 (Cx43, Sigma C6219), and Hoechst 33342 . Whole tissues from each geometry were fixed with 2% paraformaldehyde, permeabilized using PBS-T, and blocked using 10% FBS with 1% BSA blocking buffer. Next tissues were incubated with primary antibodies at 4°C overnight, washed with PBS-T, and incubated with secondary antibodies for 2 hours at room temperature. Immunostained tissue were imaged using Nikon A1R laser-scanning confocal microscope at 20X with 5 μm steps.

Dissociated cardiomyocytes were plated on fibronectin coated glass coverslips and immunostained with alpha-sarcomeric actinin (α-SA), connexin 43 (Cx43), and Hoechst 33342 to quantify sarcomere length. Images were taken at 40X magnification and sarcomere length was measured using ImageJ.

4.2.10 Contraction and directionality analysis of 3D-ECTs

Videos of spontaneously contracting 3D-ECTs were recorded with a Nikon Ti Eclipse phase contrast microscope fitted with an Andor Luca S camera. The contraction

videos were converted into TIFF image files using NIS Elements and analyzed with optical flow MATLAB software (Huebsch et al. 2015a). Macroblocks were assigned to the pixels in the image files to track the motion between frames. This motion was calculated regionally on days 20 and 41 (n = 6 encapsulations for each geometry; analysis was performed on 4 tissues of each geometry per encapsulation and results were averaged). Regions of interest (ROIs) of the microisland and square geometries were analyzed as quadrants, while the rectangular geometry had two ROIs along the longitudinal axis. The values from each ROI for each tissue were averaged to calculate whole-tissue averages. Individual value plots of average contraction velocity, average relaxation velocity, frequency, and time interval between contraction and relaxation were generated. Each data point represents the averaged ROI values for one whole tissue.

The expanded TIFF image files obtained from the contraction videos were used for directionality analysis. The motion between frames was analyzed using the open-source MATLAB code (Huebsch et al. 2015a), and a directional movie was generated. The center of beating was determined, and the software produced a motion vector field around this point. The maximum contraction and relaxation motion frames were determined from the vector fields, and these individual frames were analyzed with an ImageJ Directionality plug in. A histogram for the angles of each motion vector from -90° to 90° was generated, and the goodness of fit values for these histograms were compared, where a goodness of 0 corresponds to no uniform directionality and a goodness of 1 corresponds to a single directionality.

4.2.11 Reverse Transcription Quantitative PCR (RT-qPCR)

Two-step RT-qPCR was performed on tissue samples (n=3 tissues of each geometry from independent differentiations) from days 10, 20, and 40. First, total RNA was isolated using a NucleoSpin RNA isolation kit (Machery-Nagel) and RNA yield was quantified using a Nanodrop (Thermo Fisher Scientific). cDNA was synthesized using a SuperScript™ IV First-Strand Synthesis System (Thermo Fisher Scientific).

RT-qPCR was performed using either TaqMan™ Fast Advanced Master Mix or Power SYBR™ Green PCR Master Mix (Thermo Fisher Scientific) based on previously design primers (Kerscher, Kaczmarek, et al. 2016b; Kerscher, Turnbull, et al. 2016) or new KiCqStart® SYBR® Green Primers (Sigma Aldrich) (Supplementary Table 1) using a QuantStudio™ 3. Each Taqman reaction was ran in duplex with GAPDH and contained 5ng cDNA, 200 nM forward and reverse primer (GAPDH and Gene of interest), and 100nM probe (HEX and FAM), and was run at an annealing temperature of 55°C. Each SYBR Green reaction contained 5ng cDNA and 500 nM forward and reverse primers, and was run at an annealing temperature of 58°C. All gene expression levels were normalized using GAPDH and quantified using the 2(-ΔΔCt) method. Primers are listed in Supplementary Table 4.1.

4.2.12 TEM Imaging

Day 140 3D-ECTs of each geometry (n=3 tissues of each geometry from 3 independent differentiations) were fixed in 3% glutaraldehyde (Electron Microscopy Science) and shipped at room temperature to the Pathology Electron Microscopy Core facility at the Icahn School of Medicine at Mount Sinai, NY. 3D-ECTs were sectioned

(60 nm ultrathin sections), stained with uranyl acetate-lead citrate solution, and imaged using a transmission electron microscope (H-7650, Hitachi High Technologies).

4.2.13 Statistics

All statistics were performed using Minitab 19. All numerical data is presented as the mean ± the standard deviation unless otherwise stated. Data was subjected to General Linear Model or Mixed Model Effects analysis depending on data acquisition and quantification to evaluate significant differences with a $p < 0.05$.

4.3 Results

HiPSCs were encapsulated in three tissue geometries prior to cardiac differentiation.

In this study, we demonstrate that initial encapsulation geometry of hiPSCs impacts the functionality of resulting 3D-ECTs. Building on prior work, molds were designed to ascertain whether a straight edge and shorter edge to middle distance would promote CM alignment and maturation. The microisland geometry served as the control, with an edge to middle distance of 2 mm and tissue thickness of 700-800 μm. The square geometry design incorporated straight edges while maintaining the 2 mm edge to middle distance. The rectangular geometry design aimed to mimic a straightened version of the outer ring that formed throughout the microisland differentiation, with an edge to middle distance of 0.75 to 1 mm at any given point along the length of the rectangle. Custom PDMS molds in microisland, square, and rectangular geometries were produced using 3D printed positive casts (Supplementary Figure 4.1). HiPSCs were encapsulated at 60

million cells per mL in PEG-fibrinogen (Figure 4.1) in each geometry similar to previously established methods (Kerscher, Turnbull, et al. 2016; Kerscher, Kaczmarek, et al. 2016b) via free radical polymerization using the photoinitiator Eosin Y and visible light. On Day -2 (24 h post encapsulation), hiPSC colonies appeared evenly distributed throughout in all tissue geometries (Figure 4.1).

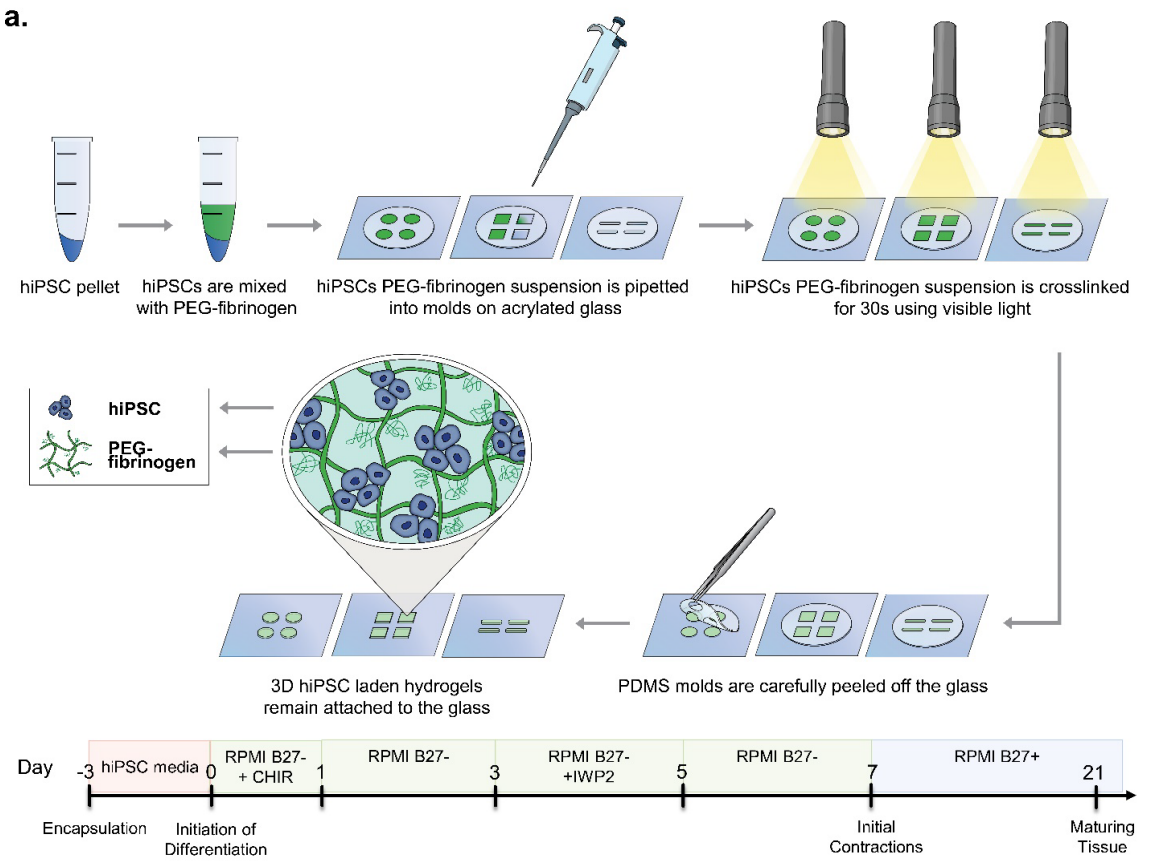

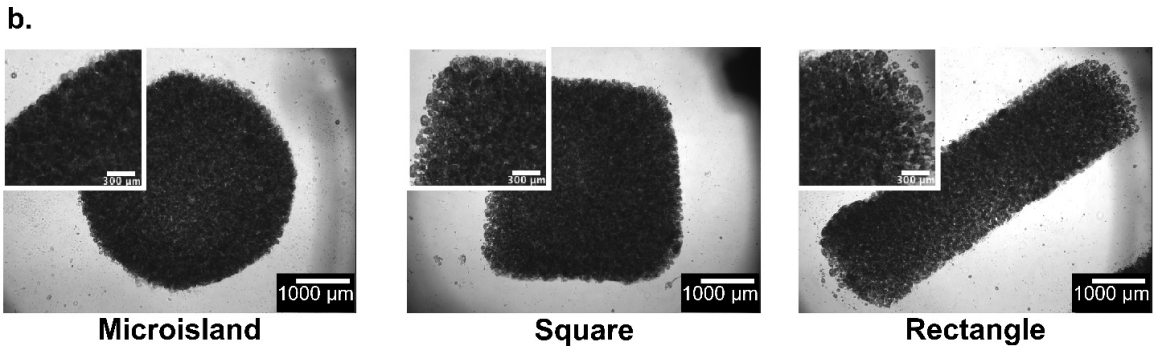

Figure 4.1 HiPSCs were encapsulated and differentiated in microisland, square, and rectangular geometries.

(a) To immobilize tissues hiPSCs were encapsulated in PEG-fibrinogen hydrogels on acrylated glass coverslips. Maintaining equivalent volume and thickness, three tissue geometries were produced using custom microisland, square, and rectangle PDMS molds. (b) HiPSC colonies were evenly distributed throughout each tissue geometry as shown in Day -2 phase contrast

images. Resulting tissues were cultured in stem cell media for three days prior to cardiac differentiation beginning on Day 0.

HiPSCs remained viable throughout encapsulation and differentiation.

Cell viability was monitored throughout differentiation in regions on the edge and middle of each tissue. On Day -2 (24 hours post encapsulation), viable cell density appeared uniform both within and between each tissue geometry (Figure 4.4.2a and Supplementary Figure 4.4.3). At the onset of differentiation on Day 0, viable cell colonies both on the edge and in the middle increased in size for all tissue geometries as hiPSCs proliferated in the 3D PEG-fibrinogen microenvironment; PEG-fibrinogen can be degraded and remodeled by encapsulated cells (Dikovsky, Bianco-Peled, and Seliktar 2006). By Day 7 of differentiation, viable cell density was similarly uniformly distributed around the edges of each tissue geometry; however, this uniform distribution of viable cells was not maintained in the middle regions of microisland and square tissues (Supplementary Figure 4.4.3). Rectangular tissues showed a more homogenous regional cell viability throughout differentiation. Tissue area for each geometry increased comparably (MI 31.0 ± 3.3%, SQ 28.4 ± 4.5%, RT 27.5 ± 2.9%) throughout differentiation from Day -2 to Day 7 (Figure 4.2b).

Engineered cardiac tissue geometry does not impact cardiac differentiation.

On Day 10 of differentiation, cell population was analyzed by dissociating 3D-ECTs and performing flow cytometry using a fixable viability dye and cardiac markers, cTnT and MF20. All tissue geometries showed similar percentages of cTnT+ cells (cTnT:

MI 59.5 ± 10.1%, SQ 61.4 ± 5.8%, RT 66.7± 4.6%; MF20 MI 57.9 ± 10.2%, SQ 61.7± 6.1%, RT 67.0± 5.3%) (Figure 4.4.3a-d,f) as expected for this differentiation protocol without the use of cardiomyocyte selection (Kerscher, Kaczmarek, et al. 2016b; Kerscher, Turnbull, et al. 2016).

Cardiac development was also assessed using a variety of genes that influence electrophysiology, calcium handling, contractility, and extracellular matrix production. 3D-ECTs from each geometry showed temporally appropriate changes in gene expression (Figure 4.3 e, g , Supplementary Figure 4.4). No significant differences were observed between tissue geometries at each time point, which is somewhat expected; the outer rings of the microisland and edges of the square tissues, which is where the majority of the cells are located, develop and mature similarly to the rectangular tissues throughout differentiation. Cardiac gene MYH7 (β-myosin heavy chain, β-MHC) expression increased over time with a subsequent temporal decrease of MYH6 (α-myosin heavy chain, α-MHC) expression, revealing a transition from fetal isoform α-MHC to the adult isoform β-MHC (Supplementary Figure 4.4e, f). Additionally, MLY2 (ventricular myosin light chain 2, MLC2v) expression increased over culture time as expected based on previous studies (Supplementary Figure 4.4g) (Kerscher, Turnbull, et al. 2016). All geometries showed increased expression of GJA5 (connexin 40, CX40) and COL3A1 (Collagen Type III Alpha 1 Chain) over time (Supplementary Figure 4.4d, k). Microisland and square geometries showed an upregulation of MYL7 (atrial myosin light chain 2, MLC2a) expression from Day 20 to 40 which was not apparent in rectangular tissues (Supplementary Figure 4.4h).

a.

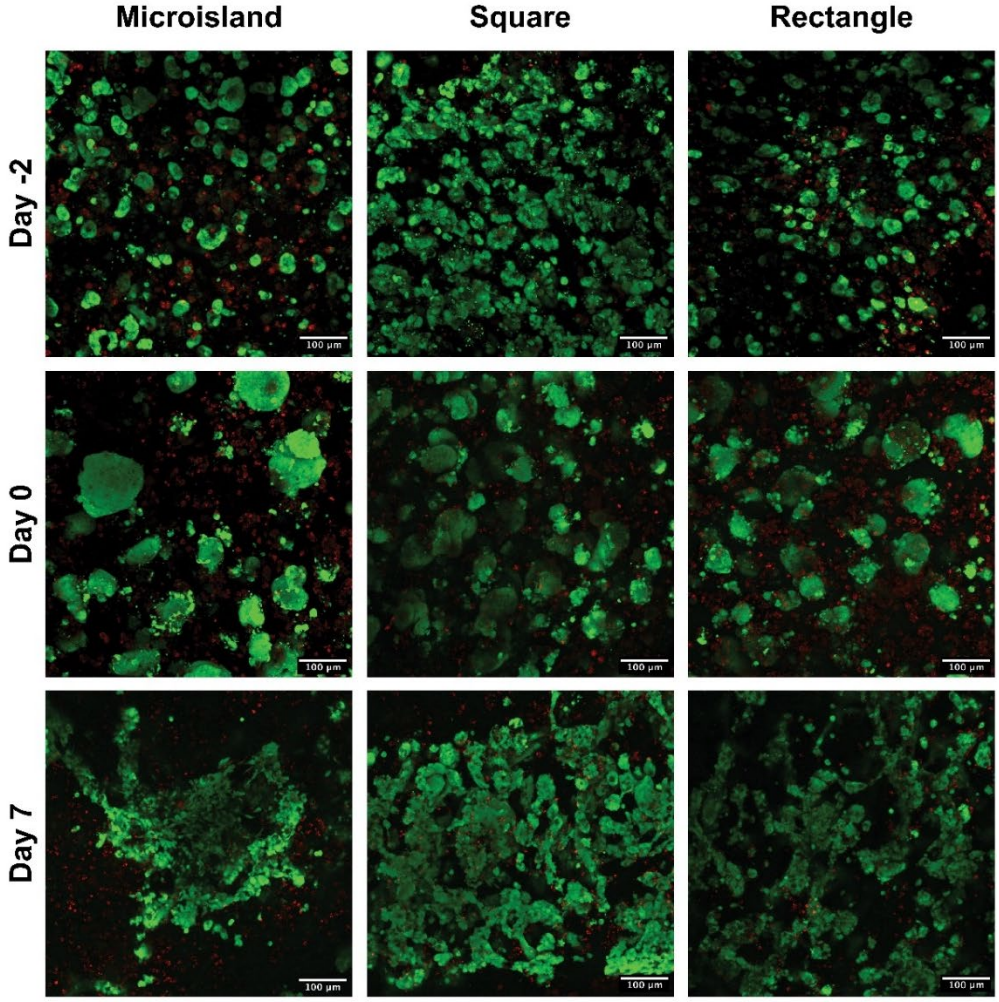
Microisland
Square
Rectangle
Day -2
Day 0
Day 7
100 µm

b.

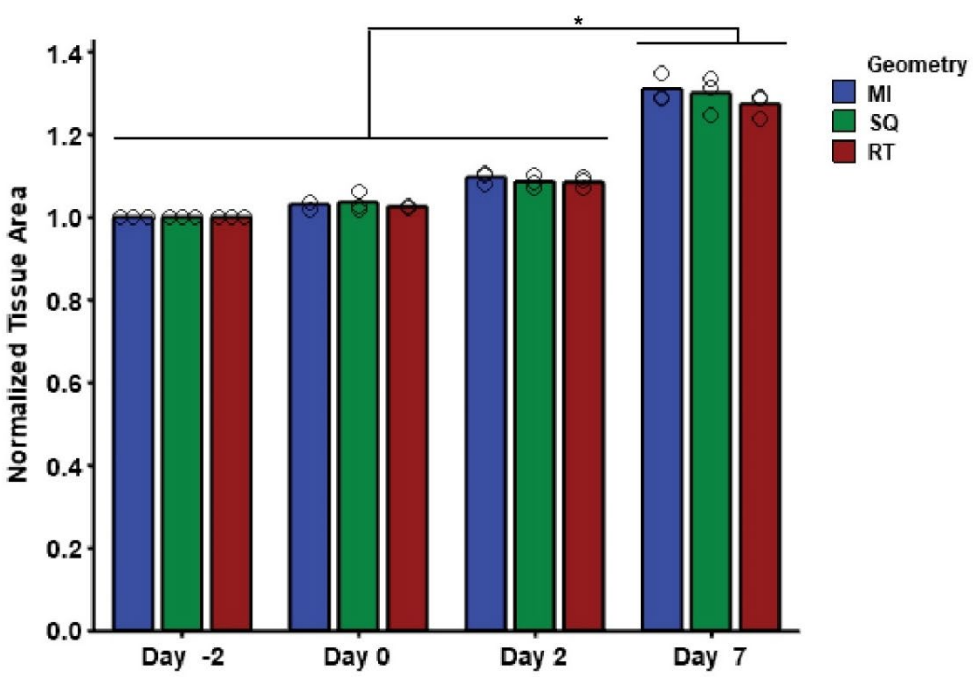
*
Normalized Tissue Area
1.4
1.2
1.0
0.8
0.6
0.4
0.2
0.0
Day -2
Day 0
Day 2
Day 7
Geometry
MI
SQ
RT

Figure 4.2 HiPSC colonies remained viable and grew in the 3D microenvironment post encapsulation.

(a) Viable cell density was evenly distributed throughout the tissue edge in all geometries on Day -2. From Day -2 to the onset of differentiation on Day 0, viable cell colonies increased in size and maintained an even distribution. By Day 7 of differentiation, viable cell colonies localized toward the edge of both microisland and square tissue geometries (Supplementary Figure 4.3), while maintaining a nearly even distribution throughout the rectangular tissues. (b) 3D-ECTs from all geometries maintained a similar size throughout differentiation with all tissue types increasing by 30% by Day 7 ($n = 3$ encapsulations containing 4 tissues each from each geometry per timepoint, circles represent an average of 4 tissues per encapsulation and bar reports mean for 3 encapsulations, * $p < 0.05$)

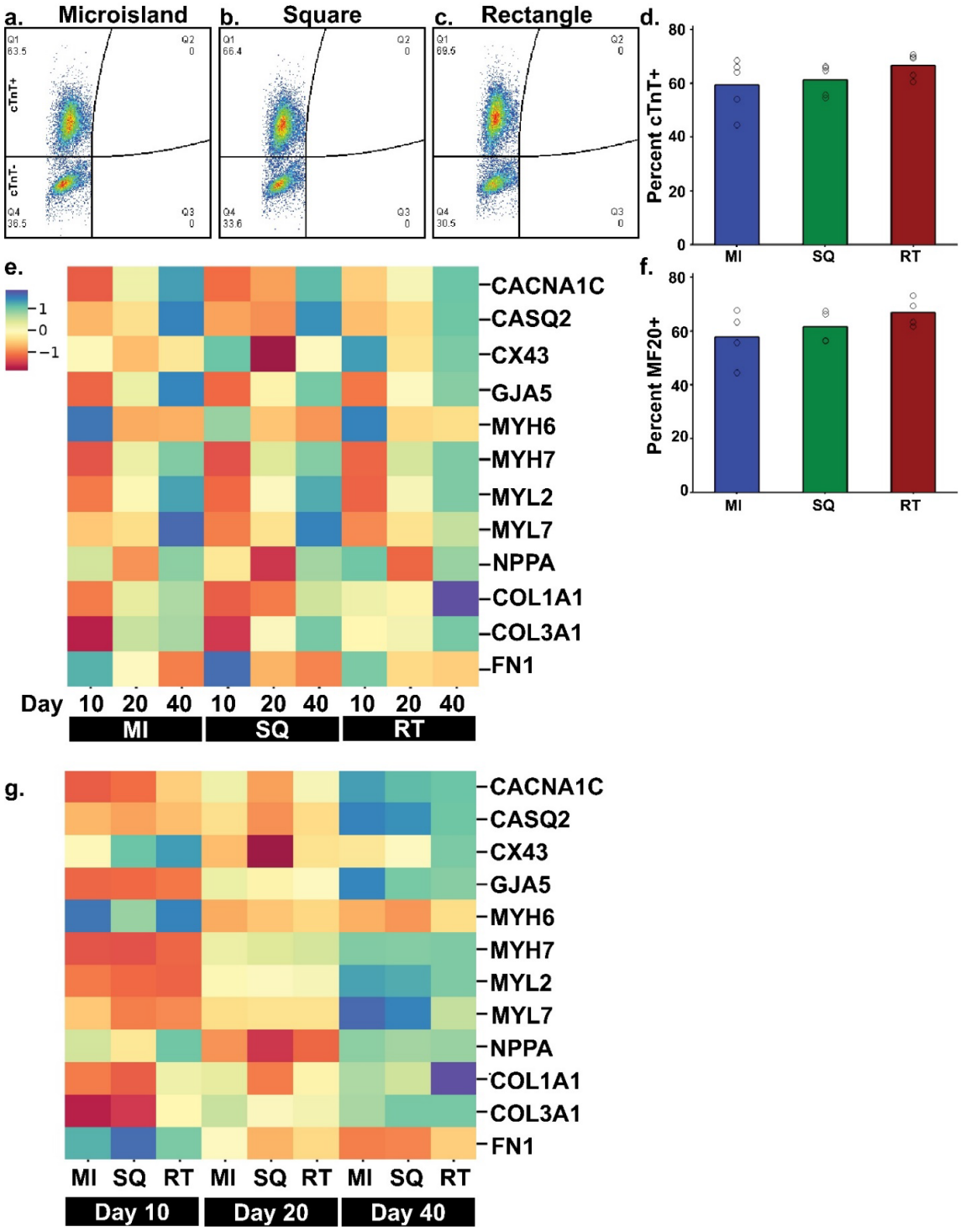

Figure 4.3 HiPSCs differentiated in all tissue geometries and showed temporally appropriate changes in gene expression.

(a-c) Representative dot-plots show live single cells gated for cTnT+. (d,f) Microisland, square, and rectangular tissues contained 59.5%, 61.4%, and 66.7% cTnT positive populations and 57.9%, 61.7%, and 67.0% MF20 positive populations respectively (n = 3 encapsulations, 2 tissues from each encapsulation for each geometry, mean ± s.d.). Heat maps compare various cardiac maturation and ECM-related genes for (e) each geometry overtime and (f) each geometry at each timepoint. (n = 3 samples per geometry per timepoint, data is normalized to GAPDH, blue colors correspond to an upregulation, red colors correspond to a downregulation, individual gene data in Supplementary Figure 4.4).

Rectangular tissues show less heterogeneity compared to microisland and square tissues.

By Day 40 post differentiation, an outer tissue ring formed on both microisland and square tissue edges leaving the middle of the tissues less dense, while rectangles showed minimal areas of low cell density (Figure 4.4a). To visualize the features the CMs inside the ECTs, whole tissue immunostaining was performed using alpha sarcomeric actinin (αA), connexin 43 (Cx43), and Hoechst (Figure 4.4b). Tissues from each geometry displayed similar bulk tissue characteristics on the tissue edge. To quantify the heterogenous fraction in each tissue geometry, total tissue area was manually measured from phase contrast images on Day 20 and 40. Next, the heterogenous region inside the tissue was measured and divided by the total tissue area resulting in a fraction from 0 to 1. Rectangular tissues showed less regional heterogeneity on Day 20 compared to their time-matched microisland tissue and on Day 40 compared to square tissues (Day

20: MI 0.4 ± 0.2 , SQ 0.32 ± 0.11, RT 0.20 ± 0.10; Day 40 MI 0.24 ± 0.11 , SQ 0.27 ± 0.08, RT 0.17 ± 0.09) (Figure 4.4c).

.

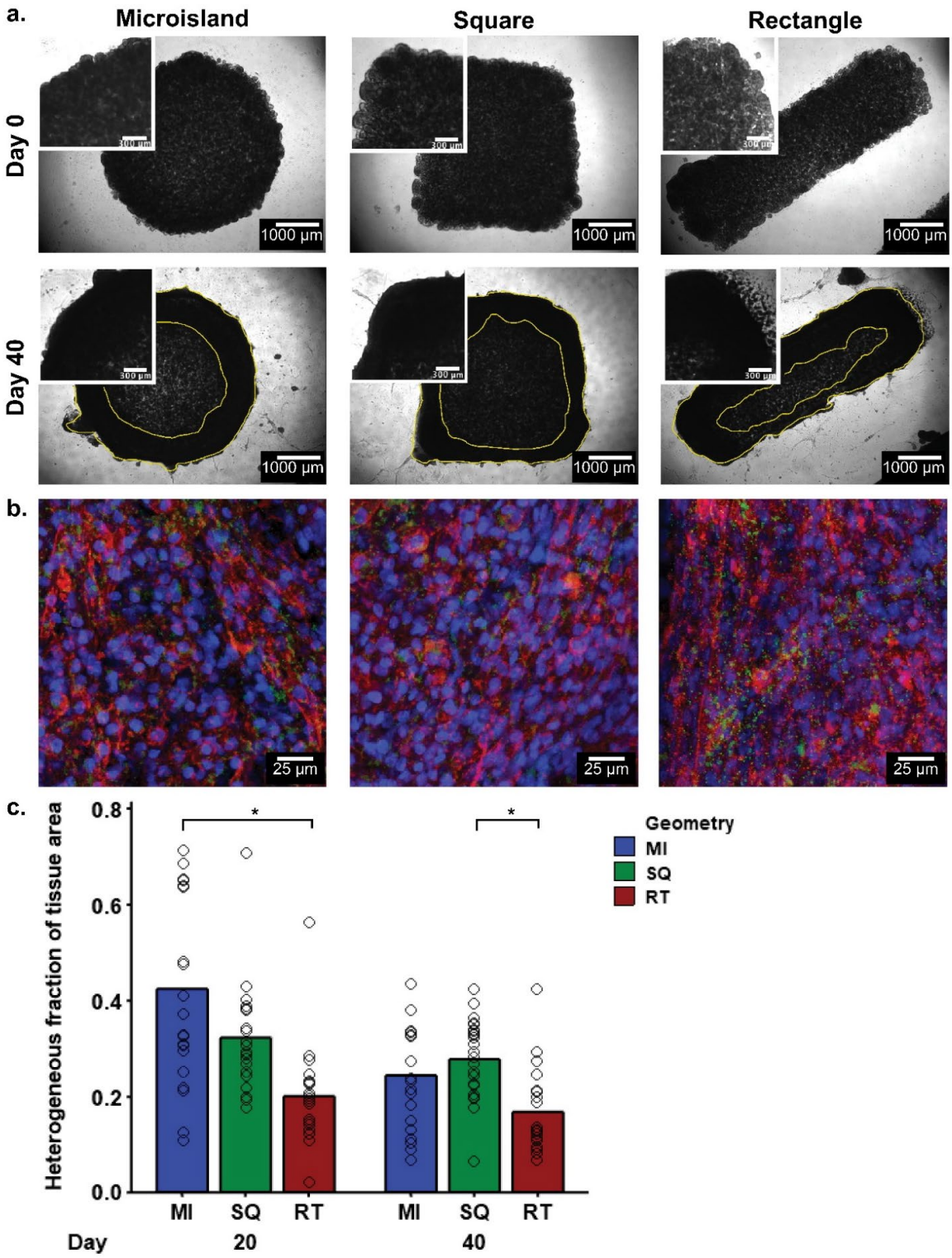

Figure 4.4 HiPSCs in 3D-dECTs underwent successful cardiac differentiation and remodeled their microenvironment over time.

(a) HiPSC encapsulation resulted in homogenous cell distribution on Day 0. After differentiation, dense outer rings formed on microisland and square geometries, which were less apparent in rectangular tissues (outlined in yellow). (b) Whole 3D-ECTs samples from each geometry show the high incidence of cardiomyocytes with positively stained sarcomeres (αSA) and gap junction protein, connexin 43 (Cx43) on the edge of each tissue. (c) Regions of tissue heterogeneity were identified and measured with Image J, and then divided by total tissue area to calculate the heterogenous fraction of tissue area. Rectangular tissues show significantly less heterogeneity compared to microislands on Day 20 and squares on Day 40 (circles indicate individual tissues, bar indicates average, n> 15 tissue per geometry at each timepoint, * $p < 0.05$).

All tissue geometries contract at similar frequencies and velocities at late timepoints

Spontaneous contraction was recorded on Days 20 and 40 and were analyzed using an open-source MATLAB code (Huebsch et al. 2015a). Whole tissue averages were calculated by taking the average of several regions per tissue in each geometry. Frequency of contraction increased for all geometries from Day 20 to Day 40 (Figure 4.5a). The time interval between contraction and relaxation was significantly longer in square and rectangular tissues on both Day 20 and 40 (Figure 4.5b). On Day 20, contraction and relaxation velocity was significantly slower in rectangles compared to microislands (Figure 4.5 c, d), but these differences were not apparent by Day 40. On Day 40, the frequency, contraction velocity, and relaxation velocity increased for all geometries as expected with prolonged culture time.

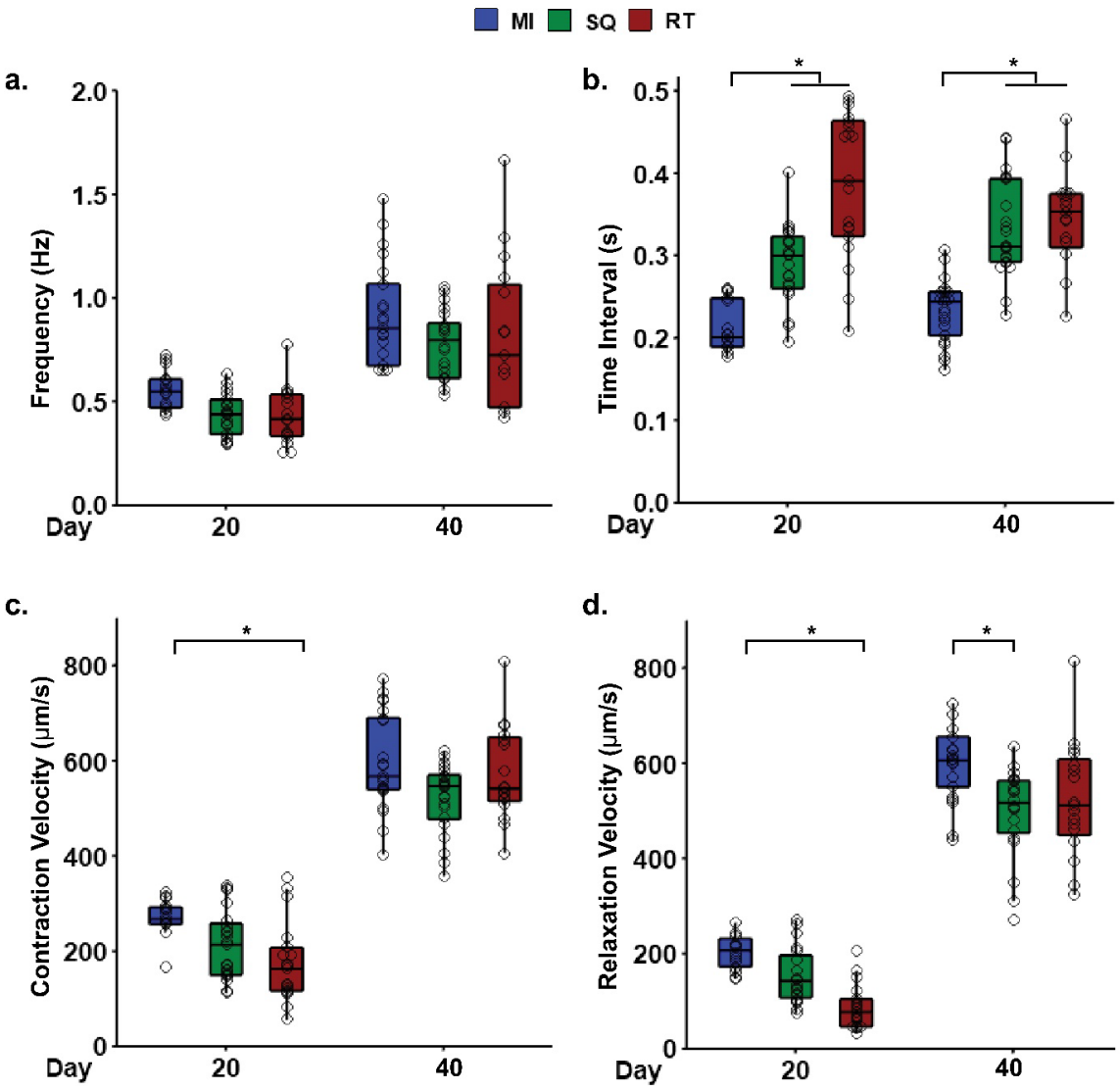

Figure 4.5 ECTs exhibited an increase in contraction velocity with tissue development in all geometries.

(a, c, d) Contraction analysis of ECTs indicated an increase of contraction frequency, contraction velocity, and relaxation velocity with culture time for all geometries. (b) Time interval between contraction and relaxation was significantly higher in square and rectangular tissue compared to microislands at each time point. Each data point represents the average value of multiple regions of interest per 3D-ECT. (n = 5 encapsulations, 4 tissue per encapsulation per geometry, * $p < 0.05$)

Rectangular tissues show unidirectional contraction.

While tissue geometries contracted at similar velocities, the qualitative videos showed differences in the way the different geometries contracted (Supplementary Movies 1, 2, 3). Microisland and square tissues contracted from the dense outer band inward towards the center of the tissue in all directions. The rectangular tissues contracted along their longitudinal axis. To quantify this, velocity vectors of spontaneous contraction were analyzed on Day 40. Frames of a maximum contraction and maximum relaxation were superimposed with their vector fields (Figure 4.6a, red lines). These images were then used to create histograms for the frequency of each angle. Histograms for microisland and square geometries showed no major peaks corresponding to a single directionality (Figure 4.6c). Rectangular geometries demonstrated a single peak at 45° which corresponded with the longitudinal length of the tissue. Goodness of fit values for each histogram confirmed that the rectangular geometry had significantly more uniform contraction directionality compared to both microisland and square geometries (MI 0.28 ± 0.03, SQ 0.35 ± 0.05, RT 0.79 ± 0.04), where 0 represents no fit and 1 represents a perfect fit (Figure 4.6b). Similar to the native myocardium, the rectangular tissue showed anisotropic contraction along the longitudinal axis.

Square and Rectangular 3D-dECTs show more mature structural features.

3D-ECTs were dissociated and plated on fibronectin coated coverslips for single cell analysis. To visualize sarcomeres and gap junction proteins, dissociated cells were stained with αSA, Cx43, and Hoechst (Figure 4.7a). Sarcomeres were ~1.8 μm in length,

agreeing with literature values for hiPSC-CMs (Feric and Radisic 2016), and showed no significant difference between tissue geometries. To further visualize ultrastructural features, TEM imaging was performed on Day 140 samples (Figure 4.7b). These images revealed signs of higher maturation in square and rectangular tissues including sarcomeres with regularly spaced Z bands and adjacent mitochondria compared to microisland tissue which presented with an immature arrangement of myofibrils and mitochondria with rudimentary sarcomere structures containing Z bodies.

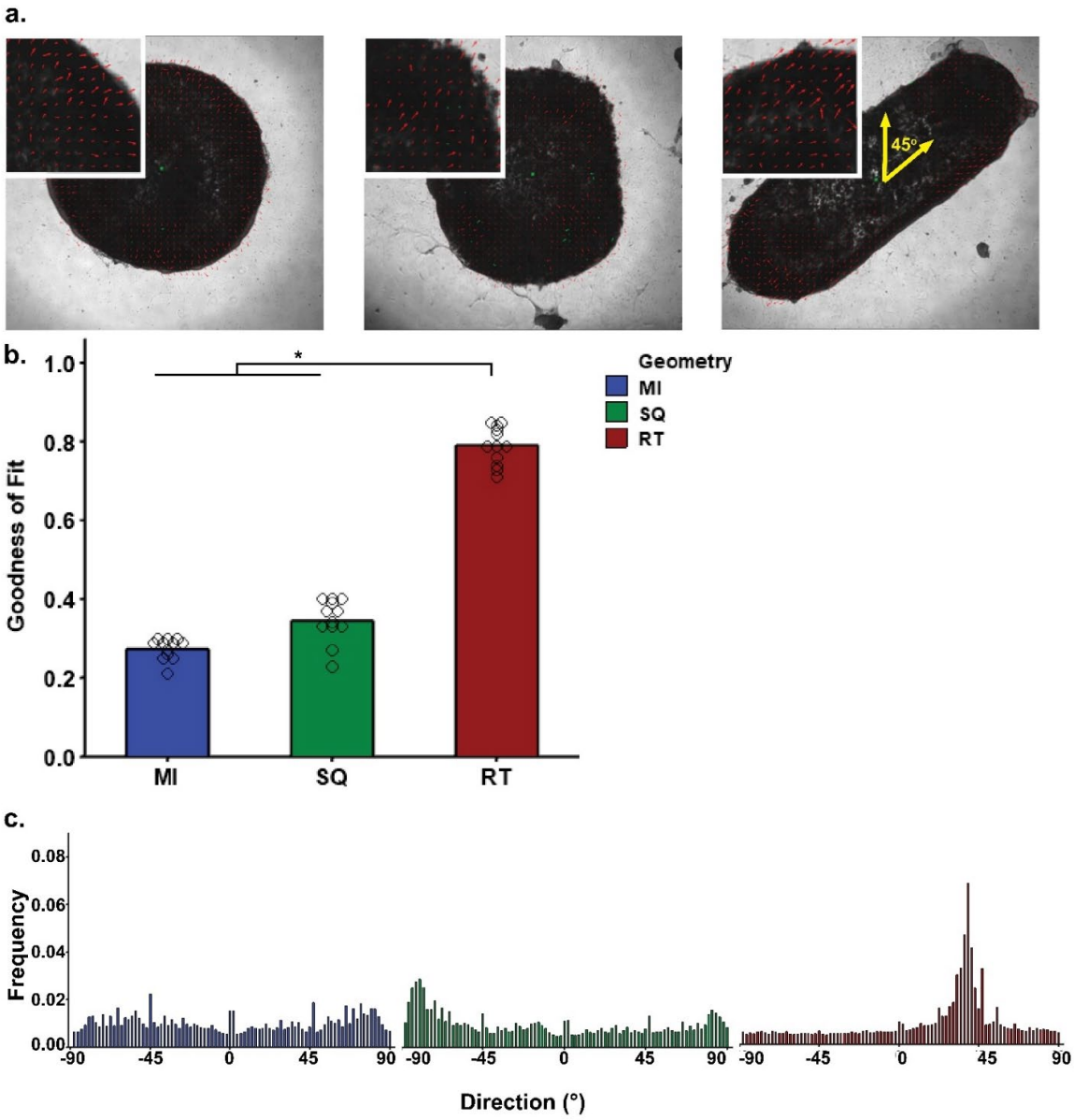

Figure 4.6 Rectangular ECTs exhibited anisotropic contraction along a longitudinal axis whereas the other geometries did not.

(a) ECT velocity vector (red lines) fields were analyzed to give frequencies of contraction vectors at angles from -90º to 90º. (c) Microisland and square geometries had roughly zero directionality around the center of beating, while rectangular geometries exhibited a peak of contraction at 45º, corresponding to the longitudinal axis. (b) Goodness of fit values show microisland and square geometries had significantly lower directionality, where 0 represents no single directionality and

1 represents a single directionality. (n = 5 encapsulations, 4 tissues per encapsulation per geometry, for each geometry at each timepoint, mean ± s.d., $p < 0.05$)

.

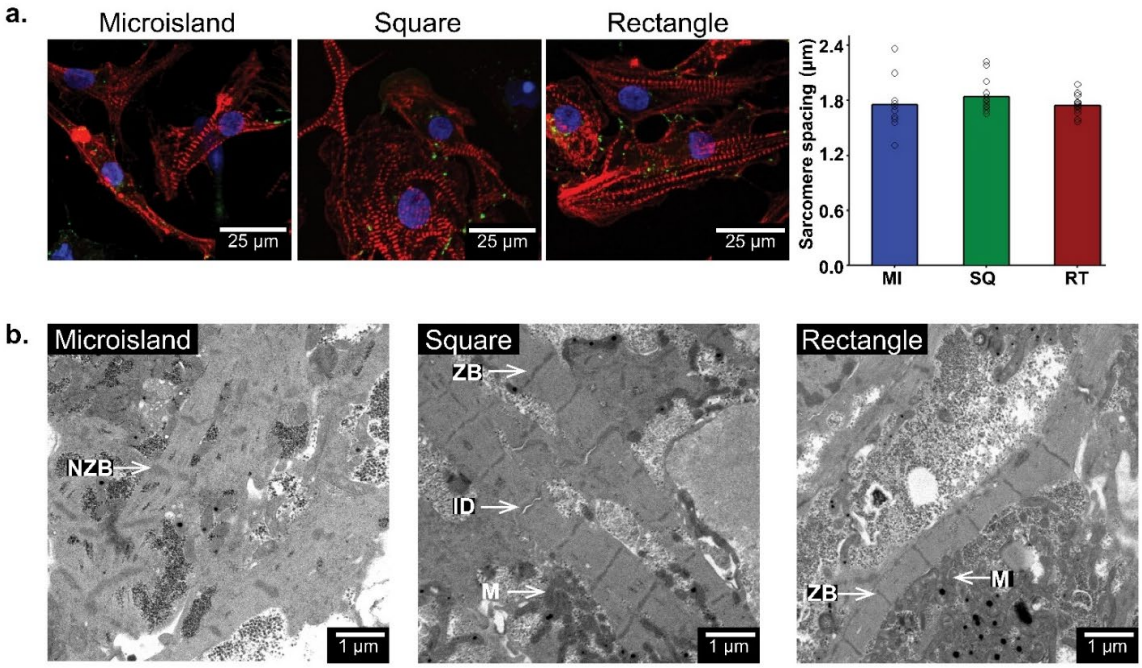

Figure 4.7 Rectangle and square 3D-ECTS show features of advancing maturity compared to microislands.

3D-ECTs from each geometry were dissociated, plated on coverslips, and immunostained for sarcomere quantification. (a) No significant difference in sarcomere length was observed between the three geometries with average lengths of 1.75, 1.84, and 1.74 microns for CMs from microislands, squares, and rectangles, respectively. (n >10 CMs per geometry, mean ± s.d., $p < 0.05$) (b) TEM images from late timepoint 3D-ECTs show poorly organized nascent z-bodies in microisland tissue compared to regularly spaced Z bands in square and rectangular tissues (n= 3 tissue per geometry, NZB: nascent Z band, ZB: Z-bands, ID: intercalated disc, M: mitochondria).

4.4 Discussion

In this work, we produced 3D-ECTs in three tissue geometries and investigated the impact of initial tissue geometry on cardiac differentiation, maturation, and functionality. The hybrid biomaterial, PEG-fibrinogen, was selected to provide the 3D microenvironment based on its relevance in clinical trials (Fuoco et al. 2012) and previously published work. Previous microisland studies using both PEG-fibrinogen (Kerscher, Turnbull, et al. 2016) and GelMA (Kerscher, Kaczmarek, et al. 2016b) produced functional cardiac tissues that presented with adultlike ultrastructural features including T-tubules adjacent to Z lines and appropriate responses to external stimuli. While these studies were successful, the microisland tissue geometry (diameter ~ 4 mm) resulted in a dense outer ring of contracting tissue with a less viable tissue center.

To alleviate regional tissue heterogeneity and improve cardiac tissue maturation, here two new encapsulation geometries were investigated. The square geometry provided a straight edge for cell alignment while maintaining similar edge to center (roughly 4x4 mm) distances as the microisland. The rectangular geometry was designed to mimic a straightened version of the dense outer ring formed in the microisland tissues (1.5x5 mm). HiPSCs were encapsulated in PEG-fibrinogen in each of the three initial tissue geometries on acrylated glass coverslips and differentiated, forming spontaneously contracting 3D-ECTs by day 7. The similarities in differentiation efficiency, gene expression, and contraction velocity between geometries were well supported by the observation that each of these characterization methods is primarily assessing the properties of the dense outer band of cardiac tissue, which contains many more cells than the middle of the microisland and square 3D-ECTs. Early timepoint characterization

including day 10 cardiac differentiation efficiency and gene expression showed that initial encapsulation geometry does not impact whether successful cardiac differentiation occurs. Rather, the important differences in cardiac tissue maturation and functionality were observed at later timepoints when tissues were cultured long term (30-150 days) as evidenced by reduced tissue heterogeneity and enhanced myofibrillar organization.

The enhanced maturation seen in rectangular tissues is critical for applications in pharmaceutical development and regenerative medicine. Unfortunately, most engineered cardiac tissue never progresses beyond the fetal developmental milestones, limiting its applicability in preclinical studies and cell therapy. Several methods of varying complexity have been utilized to enhance maturation, including but not limited to, altering substrate stiffness, micropatterning, electrical and mechanical stimulation (X. Yang, Pabon, and Murry 2014). Plating CMs on stiffer substrates (up to 10kPa) has been shown to increase CM force generation and improve calcium handling (Jacot, McCulloch, and Omens 2008). Similarly, seeding CMs on micropatterned surfaces has been shown to improve myofibrillar alignment and CM function (McDevitt et al. 2002a). While these methods are applicable to pre-differentiated CM monolayers, they are not relevant for 3D engineered cardiac tissue maturation that is composed of several layers of CMs. Introduction of intermittent electrical (Tandon et al. 2009) and/or mechanical (Ge et al. 2009; Gelmi et al. 2016) stimulation post differentiation has been shown to improve cardiac electrophysiology and increase myofibril alignment over time in 3D engineered tissues. However, these methods sacrifice simplicity for enhanced maturation which may not be applicable for widespread acceptance in cardiac tissue engineering and pharmaceutical testing applications. Using the methods described here, cardiac

maturation can be improved by simply using a rectangular tissue geometry during the single cell-handling encapsulation step, rather than implementing cell selection or tedious post-differentiation manipulation.

Overall increased tissue homogeneity was consistently seen in the rectangular geometry compared to the microisland and square geometries. During initial stages of cardiac differentiation, we saw a change in viable cell density distribution from Day -2 to Day 7. On Day -2, all tissue geometries showed uniform viable cell density distribution at both the edge and middle of hiPSC laden hydrogels. By Day 0, hiPSCs colonies increased in size and remained evenly distributed throughout the hydrogels. After cardiac differentiation on Day 7, there were regional differences in viable cell density for all tissue geometries. The exact causes of regional viable cell distributions are unknown; cells in the center may have died or migrated to the outer edge where they have greater access to nutrients and waste removal (Radisic et al. 2006). Due to the inherent nature of the rectangular geometry, where the middle is never as far from the edge compared to square and microisland geometries, regions of low viable cell density were smaller resulting in more homogenous cardiac tissues over time. Tissue homogeneity is important for studying the impact of therapeutics on cardiac electrophysiology, where anomalies in cardiac tissue can result in unwanted arrhythmias and disruptions in electrical signal propagation. To further refine tissue production and alleviate these areas of low viable cell density, additional testing could be performed to produce tissues with smaller dimensions to avoid nutrient diffusion limitations, or vasculature could be incorporated to improve oxygen and nutrient distribution and waste removal (Radisic et al. 2004a).

Throughout long term culture, tissue contraction progressed from initially localized areas of spontaneous beating to strong synchronous beating as the cardiac tissue became more interconnected in late-stage differentiation and maturation. Significant increases in contraction frequency and velocity were quantified from Day 20 and Day 40. While ECTs from each geometry contracted at similar speeds, the directionality of propagation was significantly different between geometries. Microisland and square ECTs contracted form their outer edges inward, toward the center of the tissue, potentially indicating CM alignment from the periphery into the middle of the tissue. Conversely, rectangular ECTs propagated along the longitudinal axis, indicating anisotropic CM alignment and action potential propagation. In addition, TEM imaging revealed higher myofibrillar organization and Z line formation in rectangular tissues compared to microislands. Taken together, these findings demonstrate that encapsulating and differentiating hiPSCs in a rectangular geometry will result in more mature ECTs, with contractile and structural properties that more closely mimic native myocardium.

The approach presented here is relatively straight-forward to implement and has several advantages for producing 3D ECTs *in vitro*. However, making more intricate tissue geometries or utilizing additional cell types requires more complex solutions like bioprinting. First, the ability to 3D print positive casts for producing custom made PDMS molds allows for virtually unlimited design options for PDMS mold preparation. However, we are currently limited in tissue complexity by pipetting the polymer precursor solution by hand. Rudimentary geometries like microisland, squares, and rectangles are easily pipetted by hand, but achieving even polymer precursor distribution and tissue thickness in complex geometries is challenging. Bioprinting of 3D ECTs

shows great potential for solving this problem where tissue can be printed with sub-millimeter resolution (Kupfer et al. 2020). Second, while encapsulating hiPSCs on acrylated glass coverslips enables ease of characterization and is likely important in the observed improved cardiac maturation, it adds a limitation for tissue size and thickness. The acrylated coverslip prevents nutrient and waste diffusion from the bottom surface area of the tissue; this most likely contributes to the low viability in the center of microisland and square tissues.

4.5 Conclusions

In this study, we demonstrate the ability to impact cardiac tissue functionality by changing the initial encapsulation geometry of hiPSCs in hydrogel biomaterials. Rectangular 3D-ECTs displayed increased tissue uniformity with unidirectional contraction and evenly spaced and aligned sarcomeres, which are hallmarks of native adult myocardium. This robust yet simple encapsulation platform can be extended to a range of applications including cardiac drug development and cardiotoxicity analysis.

4.6 Supplementary Information

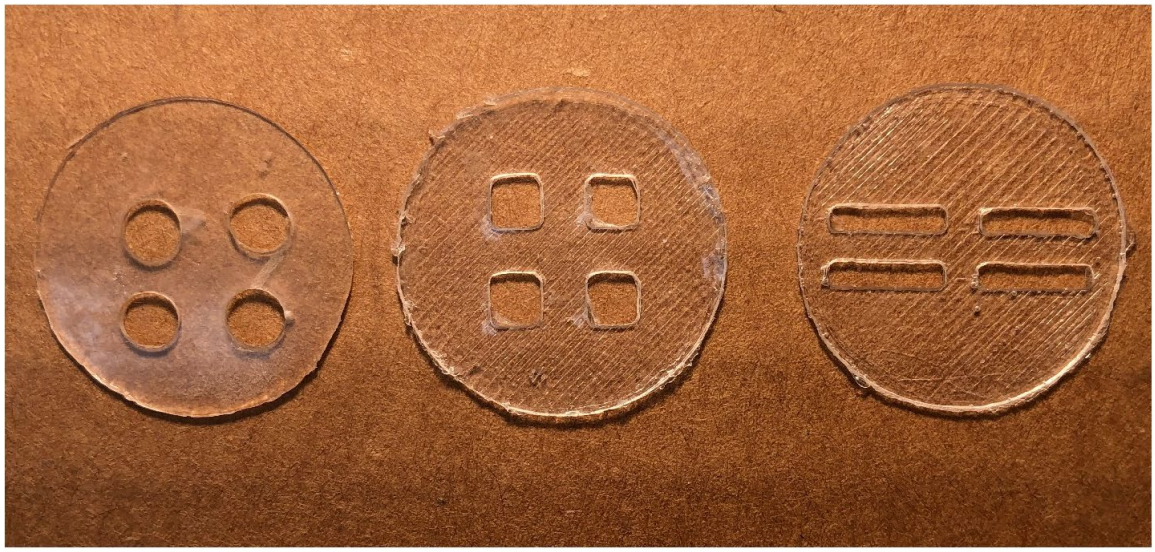

Supplementary Figure 4.1 Custom PDMS molds

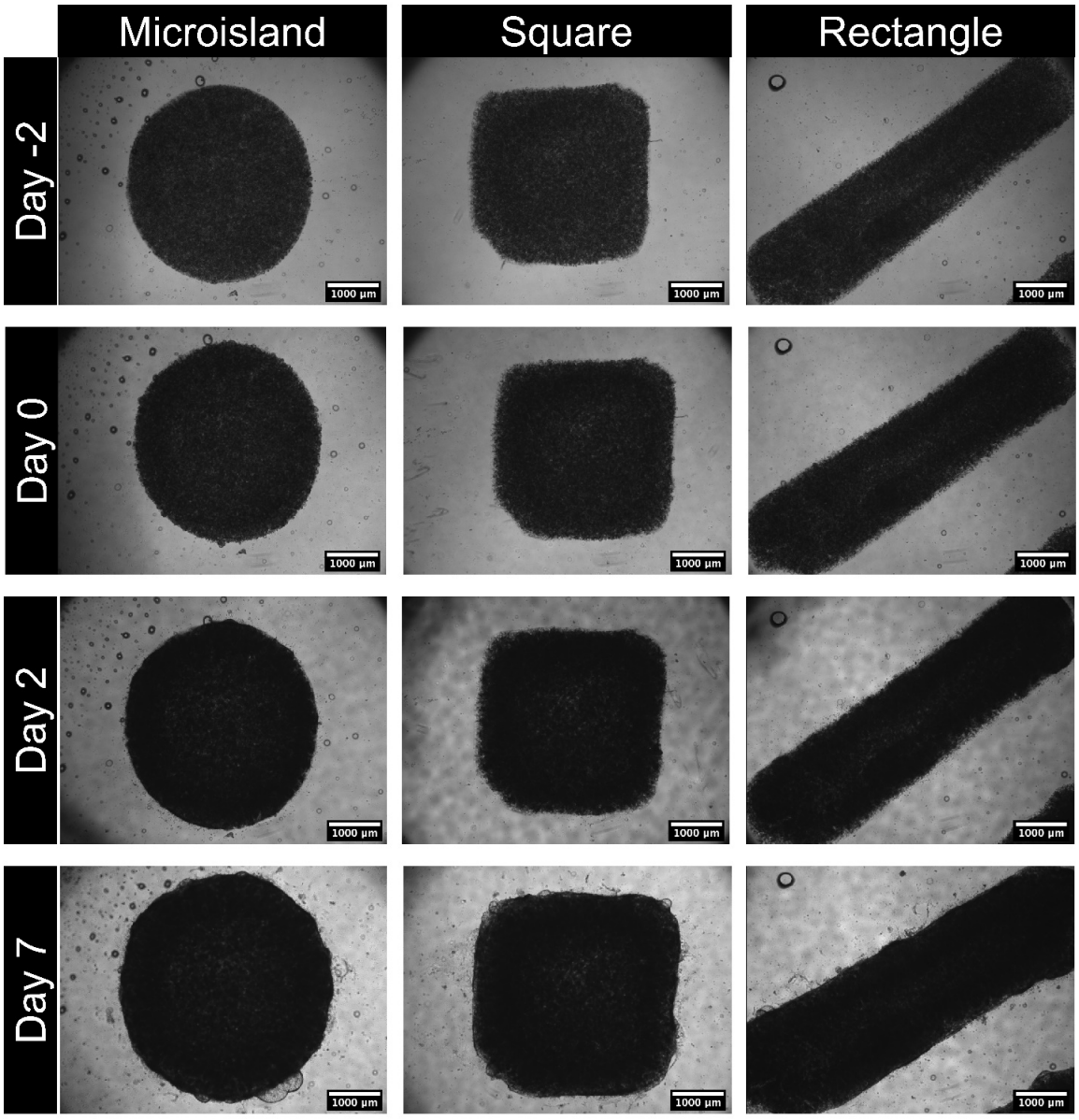

Supplementary Figure 4.2 Representative images of each geometry throughout cardiac differentiation.

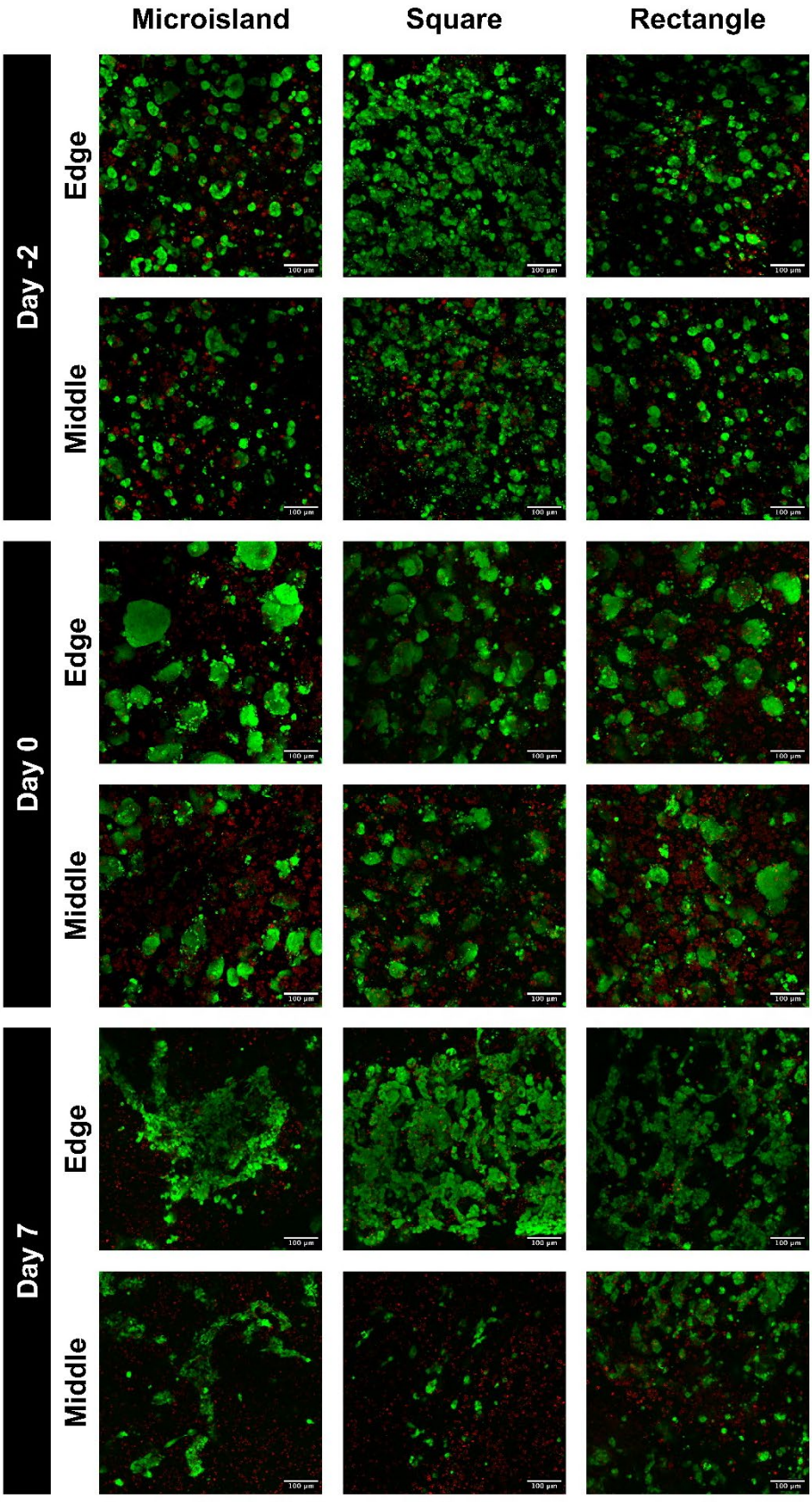
Microisland
Square
Rectangle
Day -2
Edge
Middle
Day 0
Edge
Middle
Day 7
Edge
Middle

Supplementary Figure 4.3 Confocal images show variation of viable cell distribution between the between edge and middle regions in microisland and square geometries by Day 7 of cardiac differentiation (live: green, dead: red)

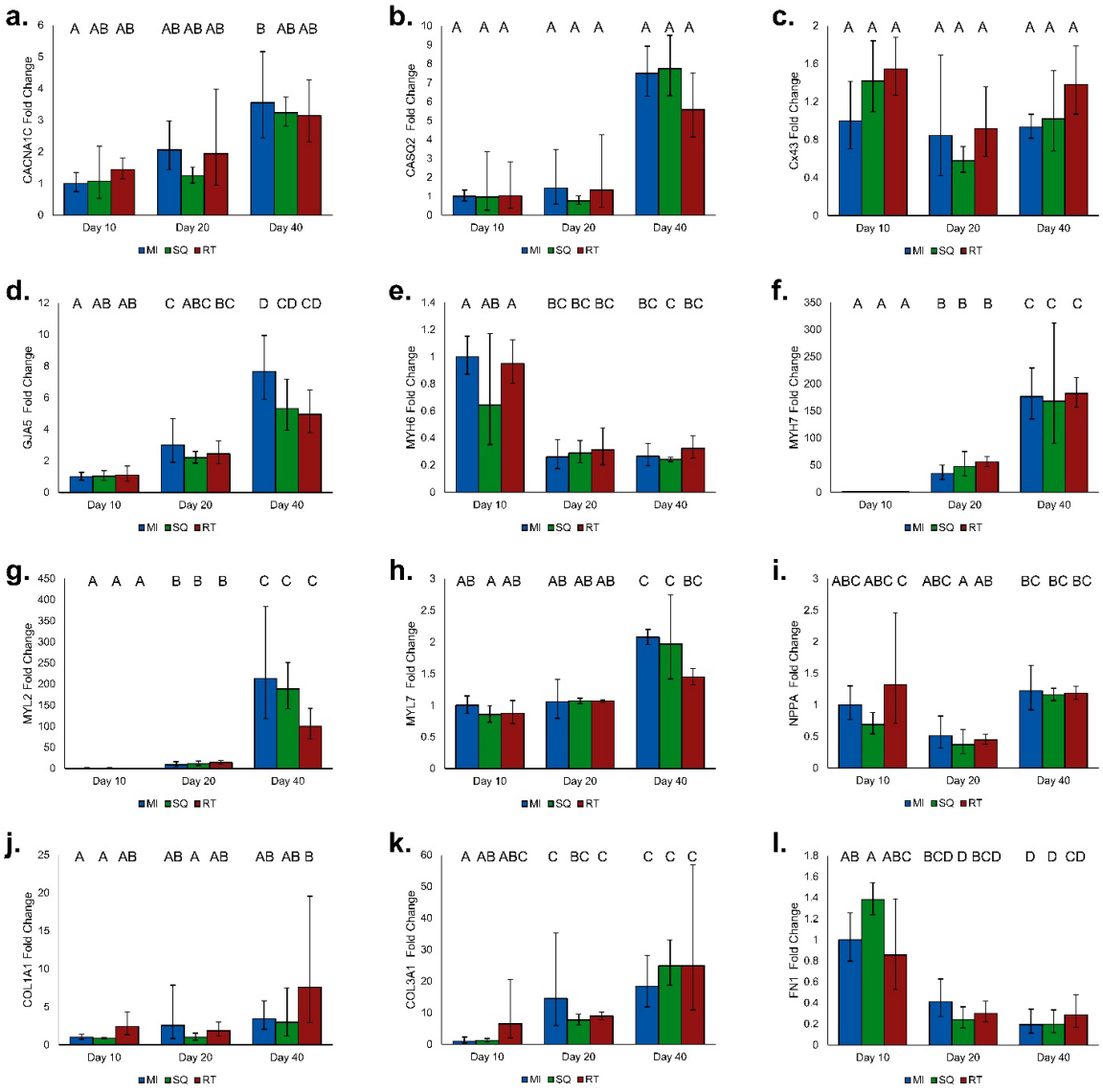

Supplementary Figure 4.4 Individual gene expression data for each gene displayed in Figure 4.3.

Data is presented as fold change (2-ΔΔCt) normalized to GAPDH and microisland sample on day 10 (n = 3 samples per treatment group per timepoint, error bars are the fold change of the s.d. of

ΔΔCt, statistics calculated based on ΔCt values, bars that do not share a letter are significantly different, $p < 0.05$).

Supplementary Table 4.1 Primers used for qPCR

Gene (Product)	Primers, F:Forward, R:Reverse, Pr:Probe (Taqman primers only)
CACNA1C (CaV1.2)	F: GGTCTTGATTTCAGAAGGAC R: CAGTTCACAAAGGGTAAGAG
CASQ2 (Calsequestrin 2)	F: GATCTAATTGAAGACCCAGTG R: CACTCTTGAAAAAGCCAATG
COL1A1 (Collagen Type I alpha 1 chain)	F: GCTATGATGAGAAATCAACCG R: TCATCTCCATTCTTTCCAGG
COL3A1 (Collagen Type III alpha 1 chain)	F: ATTCACCTACACAGTTCTGG R: TGCGTGTTCGATATTCAAAG
GJA1 (Cx43)	F: TGAGCAGTCTGCCTTTCGTT R: CCAGAAGCGCACATGAGAGA Pr: /56-FAM/ACACTCAGC/ZEN/AACCTGGTTGTGAAA/3IABkFQ/
FN1 (Fibronectin)	F: CCATAGCTGAGAAGTGTTTTG R: CAAGTACAATCTACCATCATCC
GAPDH for SYBR Green	F: TCGGAGTCAACGGATTTG R: CAACAATATCCACTTTACCAGAG
GAPDH for Taqman	F: CCCCTTCATTGACCTCAACTACA R: TTGCTGATGATCTTGAGGCTGT P: /5Cy5/AAATCCCATCACCATCTTCCAGGAGC/3IAbRQSp/
GJA5 (Cx40)	F: CCTCTACCCAGTATACGAAG R: GCTGGTATGTAGAGAGAGAG
MYH6 (αMHC)	F: ACCAACCTGTCCAAGTTCCG R: TTGCTTGGCACCAATGTCAC Pr: /56-FAM/AGCATGAGC /ZEN/TGGATGAGGCAGAG /3IABkFQ/
MYH7 (βMHC)	F: CACAGCCATGGGAGATTCGG R: CAGGCACGAAGACATCCTTCT Pr: /56-FAM/CCTACCTGC /ZEN/GCAAGTCAGAGAAGG /3IABkFQ/
MYL2 (MLC2v)	F: GGGCGGAGTGTGGAATTCTT R: CCCGGCTCTCTTCTTTGCTT Pr: /56-FAM/AGTGCTGGG /ZEN/TCCTTTCCACCAT

	/3IABkFQ/
MYL7 (MLC2a)	F: GTTCTTCCAACGTCTTTTCC R: ATCACGATTCTGGTCGATAC
NPPA (NPPA)	F: GTACTGAAGATAACAGCCAG R: GATGTGAGAAGTGTTGACAG

Chapter 5: 3D Human Pluripotent Stem Cell Differentiation to Study Thalidomide-Induced Congenital Heart Defects

Tissue engineering approaches have shown promise for studying cardiotoxicity and congenital heart defect formation, particularly in the presence of teratogenic compounds. Traditional models utilize pre-differentiated CMs differentiated in monolayers; however, this does not allow for investigation of drug-induced changes to cardiac tissue during heart development. Previously, we established a novel 3D cardiac differentiation system to generate 3D developing human engineered cardiac tissues (3D-dECTs) directly differentiated from biomaterial encapsulated pluripotent stem cells; building on this, here we demonstrate the utilization of the direct differentiation platform for studying drug induced changes to cardiac tissue formation and differentiation. In this proof-of-concept study, human induced pluripotent stem cells (hiPSCs) were encapsulated in PEG-fibrinogen microislands and differentiated in the presence of thalidomide at 0 μM (drug carrier), 10 μM, and 70 μM beginning on day 1 and continuing throughout the time course of differentiation and 3D-dECT culture. Thalidomide treatment impacted tissue formation and growth in a dose-dependent matter and was accompanied by a subsequent increase in cell debris. The percentage of CMs was significantly lower in thalidomide treated samples compared to the control. Furthermore, there were differences in electrophysiology, gene expression, and extracellular matrix composition between the thalidomide treated samples and the control. These results indicate that utilizing a 3D direct differentiation platform to

establish *in vitro* cardiotoxicity models provides advantages for studying the cumulative effect of teratogens on cardiac tissue development and formation.

5.1 Introduction

Congenital heart defects (CHDs) are the most common type of birth defect worldwide (Gelb, Brueckner, Chung, Goldmuntz, Kaltman, Kaski, Kim, Kline, Mercer-Rosa, Porter, Roberts, Rosenberg, Seiden, Seidman, Sleeper, Tennstedt, Kaltman, Schramm, Burns, Pearson, and Rosenberg 2013), with occurrences between 2.4 and 13.7 per 1000 live births (Virani et al. 2020). Moreover, CHDs are the leading cause of infant deaths (Dean, Udelsman, and Breuer 2012). However, the underlying causes are only partially understood, particularly those caused by drug-induced mutations during organ development. Although great progress has been shown, many cardiac defects, like ventricular septal defects (VSDs), must be repaired by open heart surgery (Limperopoulos et al. 1999), or in severe cases, with pediatric heart transplantation. Even when treated, CHDs can cause developmental delays, long-term cardiac complications, shortened life expectancy, and increased risk for certain cancers (Mandalenakis et al. 2019; Mussatto et al. 2015).

In 1957, Thalidomide ((±)2-(2,6-Dioxo-3-piperidinyl)-1H-isoindole-1,3(2H)-dione) (N. Kumar et al. 2012), a sedative drug prescribed for morning sickness in pregnant women, was launched in many European countries. Originally, thalidomide was considered a “wonder drug” due to its non-lethal effects when overdosing in mice and was publicized immediately after small animal experimentations (Smithells and Newman 1992). Insufficient testing of thalidomide prior to its release led to formation of birth

defects in more than 10,000 children (Smithells and Newman 1992). Although thalidomide exposure caused a variety of birth defects, this drug is primarily affiliated with symmetrical limb deformation (Therapontos et al. 2009). Approximately 6% of affected infants had CHDs including VSDs and atrial septic defects (ASDs). 30-40% of those affected died due to severe defects (Smithells and Newman 1992), and an unknown number of miscarriages occurred in the aftermath of thalidomide treatment (Ito, Ando, and Handa 2011). Studies now show that thalidomide's interactions during organogenesis are species-dependent, bringing awareness to obstacles for effectively screening candidate drugs (Parman, Wiley, and Wells 1999; Stephens 1988).

The thalidomide incident revealed the need for more thorough testing of candidate pharmaceuticals and led to significant changes in the testing required for the regulatory approval process, particularly for drugs prescribed during pregnancy. However, current methods for developmental toxicity studies primarily focus on small animal models, which do not fully recapitulate human heart development and can result in false information on the safety and efficacy of potential, new pharmaceuticals on the developing organ. Attempts have been made to incorporate *in vitro* assays with *in vivo* animal models for pharmaceutical testing, but current state-of-the-art drug-screening platforms for identification of teratogenic compounds continue to primarily employ animal subjects, which are expensive and time-consuming, and can result in misleading outcomes due to interspecies variability (T.W. Kim, Che, and Yun 2019; Grimm et al. 2018; Caspi et al. 2009; Meseguer-Ripolles et al. 2018). Furthermore, due to the fact that adult cardiomyocytes (CMs) cannot be cultured long-term *in vitro*, these studies are carried out using other cell types. The preclinical assays for determining cardiac side-

effects typically only involve the use of immortalized cell lines with an overexpression of a particular ion channel. However, recent advances in stem cell differentiation provide the ability to mimic human developmental processes *in vitro* to better understand heart development and enhance drug discovery and toxicology (Caspi et al. 2009; Grimm et al. 2018). *In vitro* specification and differentiation of cardiac cells from human induced pluripotent stem cells (hiPSCs) follow pathways analogous to those seen in *in vivo* heart development (van den Heuvel et al. 2014). Stem cell biologists have drawn upon developmental biology to establish high-efficiency protocols for cardiac differentiation of hiPSCs (Lian et al. 2013; Burridge et al. 2014; Burridge et al. 2011; Kuo et al. 2020), which can now be employed to mimic development and better predict cardiac toxicity of pharmaceuticals. Small molecule-based differentiation using Wnt/β-catenin signaling has proven efficient, resulting in mesoderm formation and cardiogenesis (Lian et al. 2012)**.** Human induced pluripotent stem cell derived CMs (hiPSC-CMs) provide a powerful option to enhance preclinical testing and developmental toxicity screening by providing CM cell source, while simultaneously overcoming the interspecies variations (Adler et al. 2008).

Currently, there are no established *in vitro* assays to assess the effect of compounds on human 3D developing heart tissues; *in vitro* cardiac toxicity screening with PSCs has been focused on the use of pre-differentiated hiPSC-derived CMs, which has limitations for use in mechanistic studies and in screening of potential cardiac teratogens. Although existing 2D differentiation systems are highly effective for CM production, they provide limited ability to study mechanical, structural, and functional properties of cardiac tissue development; previously published work suggests 3D

biomaterial encapsulation and subsequent differentiation is advantageous for mesoderm teratogen screening (Belair et al. 2020). Mechanical and structural cues, provided primarily by the 3D microenvironment of surrounding cells and matrix material, are important in guiding embryogenesis. Without recapitulation of the 3D microenvironment present during development, even basic questions concerning the impact of teratogen exposure or genetic variants on developing human cardiac tissue properties, particularly extracellular matrix (ECM) composition and tissue function, cannot be investigated.

Previously, our group established the first 3D platform for direct cardiac differentiation of hiPSCs encapsulated within a biomaterial matrix (Kerscher, Kaczmarek, et al. 2016b; Kerscher, Turnbull, et al. 2016), and the objective of this study was to determine if these 3D developing engineered cardiac tissues (3D-dECT) could be used to identify drug-induced congenital heart defects with thalidomide treatment during and after cardiac differentiation. Starting directly with human induced pluripotent stem cells (hiPSCs), rather than pre-differentiated cardiomyocytes, a 3D-dECT model enables investigation of cardiac tissue properties both in the early stages of cardiac specification and in later stages of cardiac differentiation. Here, hiPSCs were encapsulated in hybrid biomaterial PEG-fibrinogen on day -3 and were allowed to adjust to their new microenvironment prior to initiation of cardiac differentiation on day 0. Prior to drug treatment, we first verified that there were no changes to short term hiPSC viability, proliferation, and mitochondria distribution after thalidomide exposure. Beginning on day 1 of cardiac differentiation, thalidomide was administered to 3D-dECTs at 0 μM (drug solvent), 10 μM, and 70 μM. In our 3D-dECT model, we detected changes in tissue architecture and efficiency of cardiac differentiation. Differences in mitochondria

distribution and sarcomere alignment were visualized in thalidomide-treated CMs compared to control CMs. Importantly, we studied functional properties of the 3D-dECT and saw thalidomide induced changes in ECM composition and gene expression. Overall, our findings show that our 3D-dECT model of the developing heart is a robust 3D model that can be used to detect drug-induced changes during development.

5.2 Materials and Methods

5.2.1 HiPSC culture

Human induced pluripotent stem cells (hiPSCs, IMR-90 Clone 1, WiCell) were cultured on hESC qualified Matrigel (Corning) using mTeSR-1 medium (Stem Cell Technologies). HiPSCs were passaged using Versene (Life Technologies) and cultured in mTeSR-1 medium supplemented with 5 μM ROCK inhibitor (Y-27632, Stem Cell Technologies) for 24 h after passaging.

5.2.2 Cell viability and immunofluorescence staining

HiPSC viability and proliferation were assessed 24 h after thalidomide addition using a LIVE/DEAD viability kit (Molecular Probes) and immunofluorescence staining with proliferating cell nuclear antigen (PCNA, Millipore) and 4',6-diamidino-2-phenylindole (DAPI, Molecular Probes) (Supplementary Figure 5.1, $n = 3$ per condition). The percentages of viable and proliferating cells were calculated as the number of viable and PCNA positive cells divided by total cell number.

5.2.3 2D monolayer formation

For 2D monolayer differentiations, hiPSCs were dissociated using Accutase (Innovative Cell Technologies) and seeded on Matrigel coated PDMS coverslips in a 12-well plate (0.5×10^6 hiPSCs per well). Cells were cultured in mTeSR-1 medium supplemented with 5 μM ROCK inhibitor for 24 h (day -4), followed by a daily mTeSR-1 medium exchange until the initiation of cardiac differentiation on day 0.

5.2.4 3D developing engineered cardiac tissue (3D-dECT) formation process

All chemicals were purchased from Sigma-Aldrich unless reported otherwise. PEG-fibrinogen was synthesized as previously described (Almany and Seliktar 2005b). In short, tris (2-carboxyethyl) phosphine (TCEP, Acros Organics) was mixed with 7 mg/ml fibrinogen in 8 M urea-PBS. Next, PEGDA was reacted with fibrinogen for 3 h, precipitated in acetone, and dissolved in 8M urea-PBS. The reacted PEG-fibrinogen was dialyzed in PBS for 24 h at 4 °C.

For 3D encapsulation, hiPSCs were dissociated with Versene, and the cell pellet was combined with liquid PEG-fibrinogen precursor solution containing 1.5% (v/v) triethanolamine (TEOA), 0.39% (v/v) N-vinyl pyrrolidone (NVP), and 0.1 mM Eosin Y (Fisher Scientific) at a cell density of $55 \pm 8.5 \times 10^6$ hiPSCs/ml of PEG-fibrinogen. 8 μl of this mixture was transferred into a circular PDMS mold on acrylated glass (Kerscher, Turnbull, et al. 2016) and photocrosslinked with visible light (203 mW/cm^2) for 30 s. Following photocrosslinking, the PDMS mold was removed, and cell-laden hydrogels attached to the acrylated glass were cultured in mTeSR-1 medium supplemented with 5

μM ROCK inhibitor for 24 h. On day -2 and day -1, mTeSR-1 medium was changed daily.

5.2.5 Cardiac differentiation and thalidomide treatment

Media components and timeline of cardiac differentiation followed the previously published protocol (Lian et al. 2013). Briefly, on day 0 of differentiation, media of 2D monolayers and 3D-dECTs was changed to RPMI/B27 without insulin (Life Technologies) + 12 μM CHIR99021 (Stem Cell Technologies) for 24 h. Media was exchanged with RPMI/B27 without insulin for an additional 48 h. On day 3 of differentiation, an equal volume of old media was combined with RPMI/B27 without insulin and supplemented with 5 μM IWP2 (Stem Cell Technologies) for 48 h. On day 5, the media was exchanged with fresh RPMI/B27 without insulin. On day 7, media was replaced with RPMI/B27 (Life Technologies); the media was changed every three to four days with RPMI/B27.

Thalidomide (MP Biomedicals) was dissolved in dimethyl siloxane (DMSO) and stored at 4 ºC. To determine the effect of thalidomide on cardiac differentiation, the drug vehicle (0 μM), 10 μM, and 70 μM thalidomide were added to the media beginning on day 1 of differentiation (Figure 5.1A).

5.2.6 Early growth progression of differentiating 3D-dECTs

Low magnification images of whole tissues from day -2 to day 7 were acquired using an Andor Luca S camera attached to a phase contrast microscope (Ti Eclipse, Nikon). The lateral surface area of control, 10 μM, and 70 μM thalidomide treated 3D-dECTs were analyzed using ImageJ software with standard analysis plugins (n = 9 tissues

per condition). Each tissue was normalized to its area on day 1 of differentiation (the first day of thalidomide treatment).

5.2.7 Enzymatic cardiac tissue dissociation

Tissues were dissociated with collagenase Type 2 (1 mg/mL, Worthington) in dissociation solution supplemented with 30 μM $CaCl_2$ and 5 μM ROCK inhibitor at 37 ºC for 2 h. Dissociation solution was composed of 120 mM NaCl, 5.4 mM KCl, 5 mM $MgSO_4$, 5 mM Na-pyruvate, 20 mM glucose, 20 mM taurine, and 10 mM HEPES in PBS (pH 6.9). Cells were further dissociated with 0.25% Trypsin EDTA (Corning) at 37ºC for 5 min. All cells were resuspended in RPMI20 medium (RPMI 1640 medium (Gibco) with 20% fetal bovine serum (FBS, Atlanta Biologics)) supplemented with 5 μM ROCK inhibitor and plated onto fibronectin coated PDMS glass coverslips.

5.2.8 Flow Cytometry

On day 15 of differentiation, control (0 μM), 10 μM, and 70 μM 3D-dECTs were dissociated into single cells as described above. Singularized cells were transferred to RPMI20 media (RPMI + 20% FBS) and centrifuged at 200 g for 5 min. Cells were prepared for cell counting using flow cytometry, using previously described methods (Kerscher, Turnbull, et al. 2016).

5.2.9 Immunocytochemistry and sarcomere length quantification

Following dissociation and seeding on coverslips, hiPSCs and dissociated tissues were fixed using 4% paraformaldehyde (Electron Microscopy Sciences), permeabilized using PBS-T (PBS with 1% bovine serum albumin (BSA) and 0.2% Triton X-100) and

blocked in 3% FBS in PBS (blocking buffer). Primary antibody α-sarcomeric actinin (αSA) and secondary antibody Alexa Fluor 488 (Invitrogen) were then added consecutively. All samples were counterstained with DAPI and visualized using a Nikon A1R laser-scanning confocal microscope.

On day 38 of differentiation, dissociated 3D-dECTs were labeled with αSA for quantification of sarcomere length. Images were acquired using a 60X plan apochromat oil-immersion objective on the confocal microscope. All images were imported to Image J, where fast Fourier transform (FFT) and intensity profiles of drawn paths along well-defined, in-plane sarcomeres were collected. Data from intensity profiles were used to perform FFT. A minimum of ten sarcomeres per treatment group were selected based on continuity of sarcomeres in the field of view.

5.2.10 Mitochondria localization and analysis of thalidomide-treated hiPSCs and 3D-dECT CMs

The mitochondria in HiPSCs and dissociated 3D-dECT cells for all treatment groups were visualized using MitoTracker Red (Invitrogen) diluted to a final concentration of 1 nM in cell culture media. The MitoTracker Red working solution was added to all wells and incubated at 37 °C for 30 min. Cells were rinsed with PBS, fixed, permeabilized, and blocked with blocking buffer. 3D-dECT cells were also stained with αSA to identify mitochondria of CMs, and samples were counterstained with DAPI. The number and area of mitochondria per CM were quantified using Mitochondrial Quantification using MATLAB (MQM), a custom MATLAB script (Kerscher et al.

2015), from three images per well with areas of similar confluency (Supplementary Figure 5.1).

5.2.11 Contraction Analysis and Optical Mapping

Videos of spontaneously contracting tissues were acquired on days 11, 14, 17, and 42 using a phase contrast microscope with Andor Luca S camera. The videos were converted to tiff files and imported into an open-source motion tracking software for quantification of frequency (Hz), time interval (s), maximum contraction velocity (μm/s), and maximum relaxation velocity (μm/s) (Huebsch et al. 2015a).

Day 17 cardiac monolayers were incubated in the calcium sensitive dye Rhod-2 (Invitrogen) for 30 min followed by thorough rinsing with Tyrode's solution (1.8 mM $CaCl_2$, 5 mM glucose, 5 mM HEPES, 1.0 mM $MgCl_2$, 5.4 mM KCl, 135 mM NaCl, and 0.33 mM NaH_2PO_4, pH 7.4) before experimentation. To study calcium transient durations, 2D monolayers were optically mapped; duplicate recordings were taken in multiple tissue regions per sample using an Andor iXon+ 860 EMCCD camera and results were analyzed in a custom MATLAB code.

5.2.12 Gene expression

Two-step RT-qPCR was performed on control, 10 μM, and 70μM 3D-dECTs on days 0, 10, and 30 of differentiation. RNA was isolated from each tissue using a NucleoSpin RNA kit (Machery-Nagel). cDNA was synthesized using a SuperScript™ IV First-Strand Synthesis System (Thermo Fisher Scientific).

RT-qPCR was conducted on a QuantStudio™ using SYBR™ Green PCR Master Mix (Thermo Fisher Scientific) with KiCqStart® SYBR® Green Primers (Sigma

Aldrich) (Supplementary Table 1) or TaqMan™ Fast Advanced Master Mix with previously designed primers. SYBR Green reactions contained 5 ng of cDNA and 500 nM of forward and reverse primer. Taqman reactions were run in duplex with 5 ng cDNA, 200 nM forward and reverse primer (GAPDH and gene of interest), and 100 nM probe (HEX and FAM). Primers were annealed at 58 and 55 °C for SYBR green and Taqman, respectively. Gene expression values were normalized to GAPDH, and the fold change was quantified using the $2^{(-\Delta\Delta Ct)}$ method.

5.2.13 Enrichment for ECM proteins in microtissues

Three tissue samples from each treatment group were used for proteomics analysis. Half of each microtissue was used for proteomics analysis. Tissues were decellularized using 0.05% sodium dodecyl sulfate (SDS), 2 mL per tissue, on an inverter at room temperature for 30 minutes. Samples were then washed with deionized water with gentle agitation on an inverter at room temperature for 30 minutes, repeated once. Decellularized tissues were dried by lyophilization and frozen at -20°C until digestion.

Dried samples were precipitated using 2 mL cold acetone for 60 minutes at -20°C, centrifuged at 13,000 g for 10 min, and the supernatant removed. Acetone precipitation was repeated once to remove any remaining SDS and PEG.

5.2.14 Microtissue sample digestion into peptides

Microtissue samples were solubilized and disulfide bonds were reduced in 8M urea, 50 mM DTT, 50 mM TrisHCL (pH 8.5). Samples were minced with microscissors to aid in solubilization of the matrix and incubated at 37°C on an orbital shaker for 30 min. Fibrinogen solution (prior to PEGylation) was solubilized and reduced in 8M urea,

50mM DTT, 50 mM TrisHCL (pH 8.5) and incubated at 37°C on an orbital shaker for 45 min. Free cystines were alkylated by adding iodoacetamide at a final concentration of 100 mM for 15 min in the dark at room temperature. Samples were diluted to 2M urea with 50 mM TrisHCL with 1 mM calcium chloride (pH 8.5) and digested with trypsin (Sigma) at 1:50 protease:protein (wt:wt) for 13 hours at 37°C with agitation. Digestion was stopped by decreasing the pH to 2-3 using formic acid. Any particulates were removed with centrifugation at 10,000 rpm for 10 min, and the supernatant was removed and stored at -20°C until LC-MS/MS analysis.

5.2.15 Liquid Chromatography-Tandem Mass Spectrometry (LC-MS/MS)

Untargeted LC-MS/MS analysis was performed using a TripleTOF 5600 System (SCIEX, Framingham, MA) coupled to a 1260 Infinity liquid chromatography system (Agilent, Santa Clara, CA). 100 µL of peptide solution was injected with an aqueous solvent of LCMS grade water with 0.1% LCMS grade formic acid (Sigma-Aldrich) and separated on Ascentis Express Peptide ES-C18 column (Millipore Sigma, St. Louis, MO) of 15 cm length, 2.1 mm inner diameter, and 2.7 µm particle size. Peptides were eluted with a 65 min gradient from 2 - 45% acetonitrile with 0.1% formic acid. Information Dependent Acquisition was performed from 300 – 1250 Da with charge states from 2 – 5. Up to 50 candidate ions exceeding 100 cps were selected per cycle, with a 15 second exclusion after 1 count, for fragmentation with rolling collision energy.

5.2.16 Protein identification and data analysis for microtissue samples

Raw files were searched against a UniProt KB protein database for *homo sapiens* updated February 10, 2016 using ProteinPilot software's Paragon algorithm (AB SCIEX).

Search settings included trypsin specificity, urea denaturation, thorough ID search effort, and 0.05 (10.0%) detected protein threshold. Proteins matching the reversed database or contaminants were removed.

Relative quantification was obtained by spectral counts of peptides with at least 95% confidence normalized by total ECM spectral counts. Relative quantification across samples was obtained by spectral counts using a custom MATLAB script. Peptides identified with ≤ 95% confidence and proteins not associated with the extracellular matrix were removed. Peptides associated with each protein were counted and normalized to the total ECM spectral counts from the sample.

The results were analyzed with Prism (GraphPad, San Diego, CA) and the mean ± SD normalized to control tissues was reported. In order to perform statistical analysis, proteins which were not identified in at least 2 biological replicates of 2 conditions were removed. Within each protein, data was analyzed by one-way ANOVA with Tukey's multiple comparisons test. A value of $p < 0.05$ was considered statistically significant for all tests.

5.2.17 Protein identification and data analysis for fibrinogen precursor

Raw files were searched against a UniProt KB protein database for *bovine* updated August 2, 2017 using MaxQuant (Max Plank, Munich, DE) software. Proteins matching to the reversed database, contaminants, or not associated with the extracellular matrix were removed. Data visualization and statistical analysis after MaxQuant identification was carried out using Perseus (Max Plank, Munich, DE) and Prism.

Relative quantification was calculated based on intensity values derived from MaxQuant, normalized by total intensity of all proteins.

5.2.18 Statistics

Data are presented as mean ± SD, and statistical analysis was performed using Minitab 19 unless otherwise specified. The assumptions for normality and equal variances were confirmed, and one-way analysis of variance (ANOVA) was performed with Tukey's test for post-hoc analysis. A value of $p < 0.05$ was considered statistically significant.

5.3 Results

Thalidomide influenced the cardiac tissue formation process.

In this proof-of-concept study, we investigated if our 3D developing engineered cardiac tissues (3D-dECTs) directly differentiated from PEG-fibrinogen encapsulated hiPSCs could be used for identification and quantification of changes in tissue properties in response to drug exposure. Thalidomide, a known teratogen, whose mechanisms for defect formation are largely unknown (Ito, Ando, and Handa 2011), was used as a drug candidate to determine if 3D-dECTs uncover information about disease manifestation and progression, compared to standard 2D monolayer cardiac differentiation. Before evaluating the effect of thalidomide on cardiac differentiation from hiPSCs in a 3D microenvironment, short term effects of the drug-carrier, DMSO, and the highest thalidomide concentration (70 μM) were tested to verify that the drug and its carrier did

not cause abnormal changes in cell viability and proliferation at the selected concentrations (X. Gao, Sprando, and Yourick 2015). Monolayer hiPSCs were treated with the drug-carrier control (0 μM) and 70 μM thalidomide for 24 h; the hiPSCs maintained high viability and proliferation capacity after treatment. (Figure 5.1B,C and Supplementary Figure 5.1A,B). Furthermore, the mitochondria area and location, with respect to the nuclear membrane, of control and thalidomide-treated hiPSCs were evaluated using our custom developed MQM code (Kerscher et al. 2015). No significant differences in mitochondria distribution were detected between treatment groups (Supplementary Figure 5.1C).

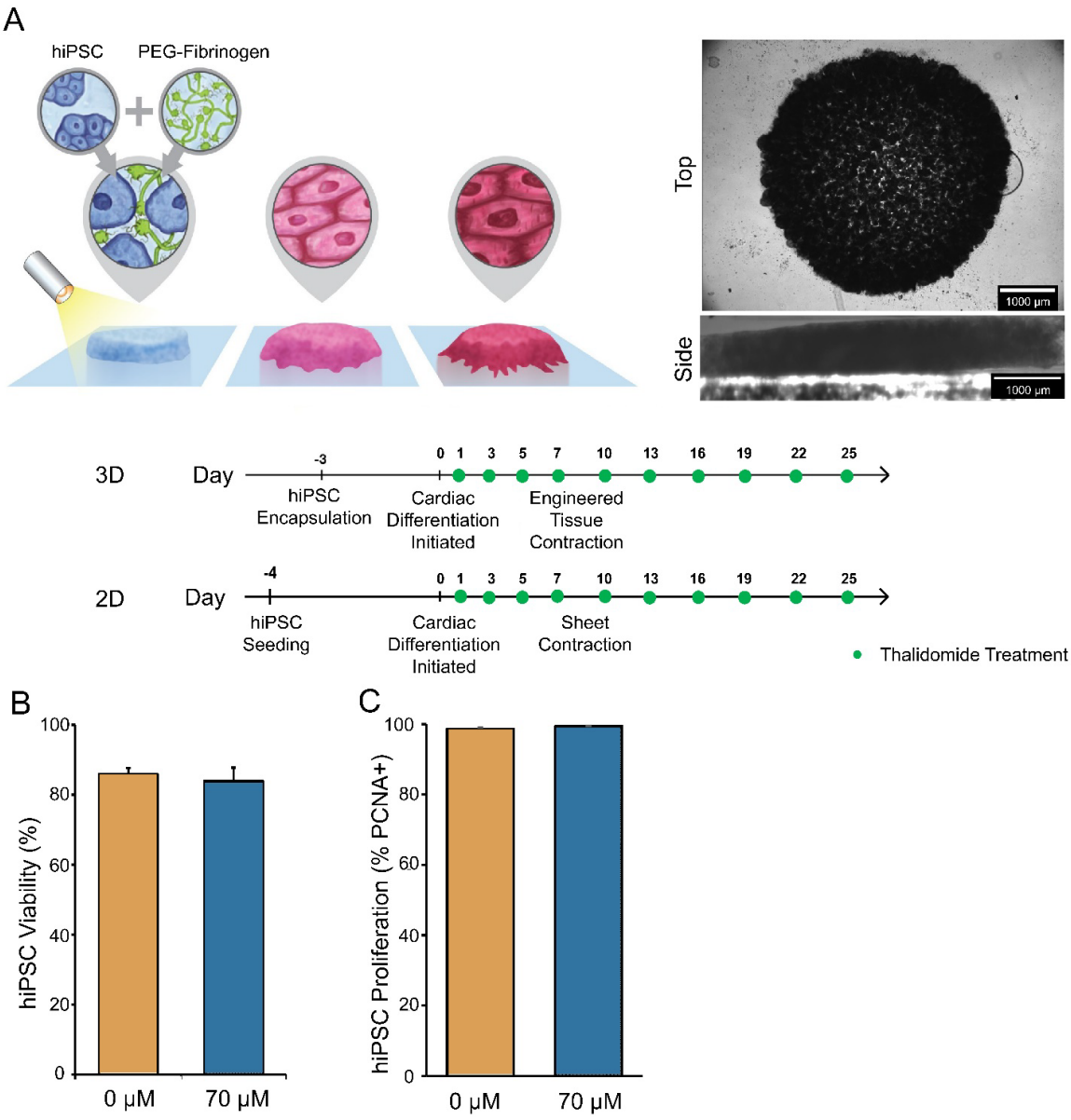

Figure 5.1 HiPSC differentiation timeline to form 3D developing human engineered cardiac tissues (3D-dECTs) and 2D monolayers for thalidomide drug-testing.

(A) HiPSCs were combined with aqueous PEG-fibrinogen precursor solution, photocrosslinked to form 3D-dECTs, and cultured for three days before initiation of cardiac differentiation. For 2D monolayer differentiation, hiPSCs were seeded onto a Matrigel coated 12-well plate and cultured for four days prior to initiation of cardiac differentiation on day 0. 3D and 2D differentiations

were assigned to thalidomide treatment groups, consisting of control (0 μM drug carrier), 10 μM, and 70 μM thalidomide, on days 1, 3, 5, 7, and every three days after that. Thalidomide treatment for 24 h did not influence hiPSC (B) viability or (C) proliferation, determined by percentage of PCNA+ cells (n = 3). Reprinted from Biomaterials Vol 83. Direct hydrogel encapsulation of pluripotent stem cells enables ontomimetic differentiation and growth of engineered human heart tissues, Petra Kerscher, Irene C. Turnbull, Alexander J. Hodge, Joonyul Kim, Dror Seliktar, Christopher J. Easley, Kevin D. Costa, Elizabeth A. Lipke, 383-395, Copyright 2016, with permission from Elsevier (Kerscher, Turnbull, et al. 2016)

To produce the 3D-dECTs, hiPSCs were encapsulated within a hybrid biomaterial, PEG-fibrinogen on day -3. For encapsulation, hiPSCs were collected in a cell pellet and combined with the polymer precursor solution, pipetted into PDMS molds on acrylated glass, and photocrosslinked using visible light. Cardiac differentiation was initiated three days later (day 0) through activation subsequent inhibition of Wnt signaling using previously established protocols (Kerscher, Turnbull, et al. 2016; Kerscher, Kaczmarek, et al. 2016b; Lian et al. 2013). For drug-treatment, thalidomide was administered at 0, 10, and 70 μM in the culture media on days 1, 3, 5, 7, and every 3 days thereafter with media changes (Figure 5.1A). These concentrations were chosen for this study because thalidomide doses of 10 and 70 μM previously showed significant changes during 2D hESC differentiation in transcriptomic and proteomic profiles (Meganathan et al. 2012). During cardiac differentiation changes in tissue formation progression were observed in thalidomide treated samples. In all treatment concentrations, an increase in lateral surface area was observed from day 1 to day 5 (Figure 5.2A). On day 5, control tissues displayed a significant increase in size compared

to treatment groups at 1.33 ± 0.03, 1.23 ± 0.04, and 1.17 ± 0.02 times the day 1 tissue size for 0, 10, and 70 µM thalidomide treated tissue, respectively; this change in tissue growth was accompanied by the presence of an increased amount of cell debris surrounding the 10 and 70 µM thalidomide-treated tissues (n = 9 tissues per group, $p < 0.05$). In comparison, control 3D-dECTs (0 µM) exhibited more defined edges throughout differentiation (Figure 5.2B). We attempted to use a 2D monolayer differentiation approach to study thalidomide-induced effects for comparison to the 3D microenvironment in the 3D-dECTs. However, 2D differentiation in the presence of 70 µM thalidomide did not result in contracting monolayers and had substantial cell loss and insufficient cardiac differentiation. This was expected due to the direct drug exposure in the 2D environment, and limited samples were able to be used for assessment of CM properties.

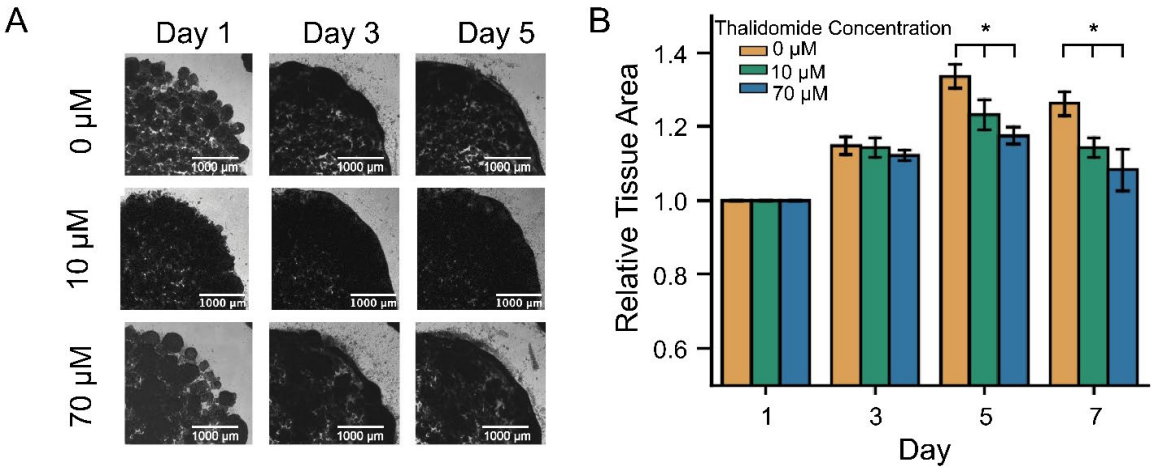

Figure 5.2 Thalidomide influenced the early tissue formation process and growth.

(A) After PEG-fibrinogen encapsulation, hiPSCs grew within the hydrogel. Edges of 0 µM (control), 10µM, and 70 µM thalidomide tissues started to differ on day 3 of differentiation, with

more cell debris and less dense tissue formation in 70 μM thalidomide treated tissues. (B) Relative tissue area increased from day 1 to day 5 for all groups. Control tissues showed a greater in increase in tissue area compared to thalidomide treated tissues on days 5 and 7 (n = 9 tissues per group, * $p < 0.05$).

Thalidomide influenced cardiac differentiation and resulting CM phenotype.

Following cardiac differentiation, the efficiency of cardiac differentiation was assessed by positive expression of cTnT and quantified with flow cytometry. Cardiac differentiation efficiency showed a dose dependent response with control 3D-dECTs having the highest percentage of CMs followed by 10 and 70 μM thalidomide-treated 3D-dECTs (Figure 5.3D); the percentage of cTnT+ cells on day 10 was 41.2 ± 2.57, 30.9 ± 1.91, and 25.1 ± 1.29 for 0, 10, and 70 μM, respectively, and 36.8 ± 2.57, 38.1 ± 11.2, and 33.0 ± 3.34 percentage on day 20 (n = 3 batches per treatment group, * $p < 0.05$). On day 17, the total cell number in control and thalidomide-treated 3D-dECTs was similar compared to control samples (0 μM: 1.00 ± 0.072, 70 μM: 0.896 ± 0.061 cells, Figure 5.5.3C).

To further investigate the CM population, cell size and sarcomere length were used as indicators of initial CM structural development and maturity. On day 38 of differentiation, 3D-dECTs from all three treatment groups were dissociated into single cells and replated to observe CM size and sarcomere length using positive expression of αSA. The area of CMs from 3D-dECTs treated with 10 μm thalidomide was 2150 ± 991 μm^2, which is significantly smaller in size compared to control CMs (3450 ± 898 μm^2) (n

≥ 11 tissues per treatment group, Figure 5.3A). Sarcomere length was 2.02 ± 0.16 and 1.88 ± 0.21 μm in control and 70 μM thalidomide-treated CMs, respectively (Figure 5.3B), which is within the range for native adult CM sarcomere length (2.0 – 2.2 μm) for the control CMs (Feric and Radisic 2016). Furthermore, the sarcomeres of control 3D-dECT CMs appeared to be more defined and organized compared to thalidomide treated CMs; sarcomere organization is an indicator of CM structural maturity (Figure 5.3E). In the 70 μM thalidomide treated samples, a high number of cells did not express αSA, a cardiomyocyte antibody, indicating a presence of non-CM cell types (Supplementary Figure 5.2).

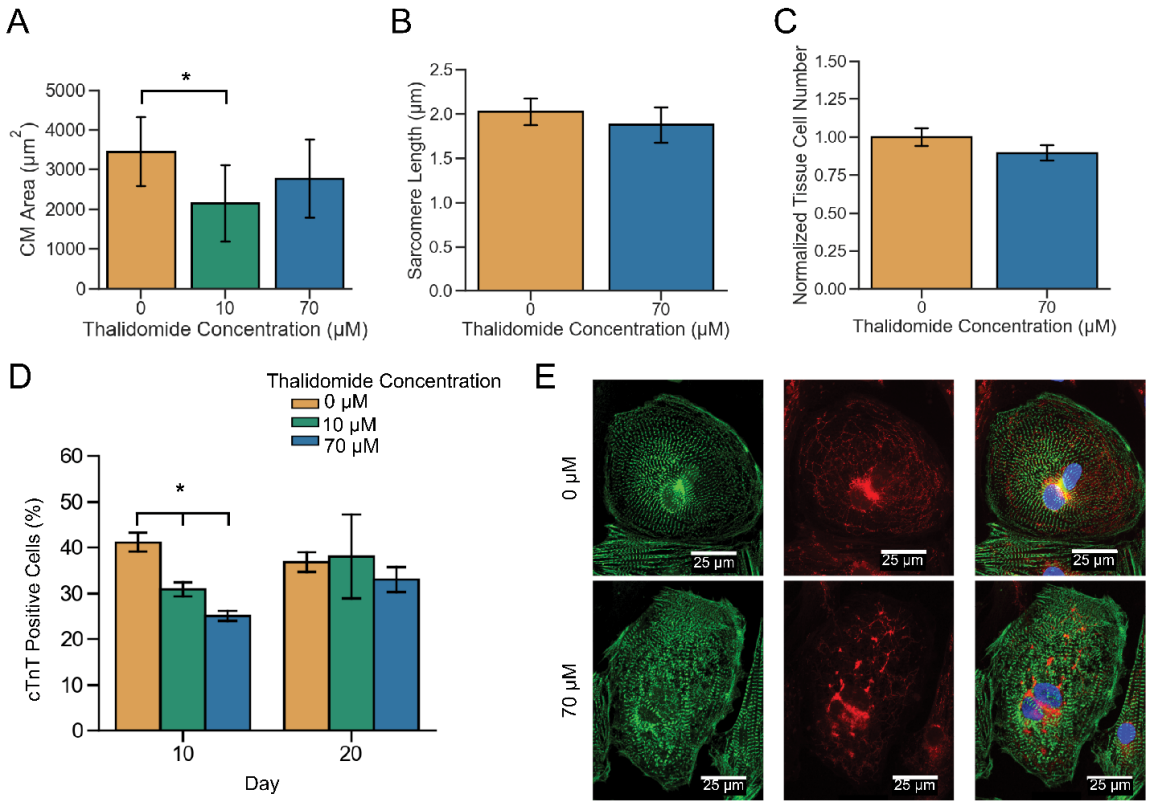

Figure 5.3 Thalidomide influenced cardiac differentiation and CM phenotype.

(A) On day 38, the 3D-dECTs were dissociated, and CMs treated with 10 μM thalidomide were significantly smaller compared to control CMs; 70 μM thalidomide-treated CMs also showed a trend in smaller cell size compared to control ($n \geq 11$ cells per condition, * $p < 0.05$) . (B) Sarcomere spacing was similar in 70 μM thalidomide treated tissues compared to age-matched controls ($n \geq 10$ cells per condition). (C) On day 17, quantification of total cell number per tissue showed a similar number of cells in thalidomide-treated tissues ($n = 3$ tissues per condition). (D) A lower percentage of CMs were detected in thalidomide-treated tissues compared to control, suggesting less efficient CM differentiation in the presence of thalidomide ($n = 3$ tissues per condition, * $p < 0.05$). (E) Sarcomeres (green) were more defined and organized in control CMs when compared to thalidomide-treated CMs; furthermore, the mitochondria (red) evenly

distributed throughout the cytoplasm of control CMs but were clustered in thalidomide-treated CMs.

Following thalidomide treatment during cardiac differentiation, there were differences in mitochondria structure and distribution in thalidomide treated CMs compared to controls. Mitochondria are the primary organelle responsible for energy production within the cell and are an important component influencing normal heart development and contractile function. During early stages of CM development, mitochondria are only a small portion within the cytoplasm of the cell and are structurally visible in a reticular arrangement, while in adult CMs, mitochondria occupy approximately 20-40% of the total CM volume because of the high energy requirements needed for contraction; at this stage, mitochondria exhibit a regular distribution with a "crystal-like lattice pattern" (Schaper, Meiser, and Stammler 1985). To visualize mitochondria distribution, control and 70 μM thalidomide treated CMs were stained with MitoRed. In control CMs (0 μM), mitochondria were evenly distributed throughout the entire cell, including overlapping with areas with well-defined sarcomeres (Figure 5.3E). The mitochondria structure, morphology, and location in the cytoplasm were visually different in thalidomide-treated cells, showing a clustered pattern (Figure 5.3E). In immature CMs, a large quantity of mitochondria is normally located close to the nucleus, which was seen in both treatment-group cells (0 and 70 μM).

Thalidomide-treated 3D-dECTs showed slower spontaneous contraction than age-matched controls.

Here, our control 3D-dECTs also showed first areas of spontaneous contraction on day 7, similar to our previously published results (Kerscher, Turnbull, et al. 2016); however, thalidomide-treated 3D-dECTs started to contract one or two days later (day 8 or day 9). Although contractions started later for thalidomide treated 3D-dECTs, there were no significant differences in the frequency of spontaneous contraction between control and thalidomide-treated 3D-dECTs. On day 11, the time interval between contraction and relaxation was significantly longer in 70 μM tissue compared to control *(*n = 3 tissues per condition. * $p < 0.05$). This trend continued on day 14 where both 10 and 70 μM tissues showed prolonged time intervals compared to control (Figure 5.4A). From day 17 to 42, control and 10 μM thalidomide-treated 3D-dECTs showed significant increases in contraction and relaxation velocity, whereas 70 μM thalidomide-treated tissues did not (Figure 5.4B, C, n = 3 tissues per condition. $p < 0.05$).

To evaluate the influence of thalidomide on calcium transient duration and conduction velocity, optical mapping of day 17 2D cardiac monolayers was performed. Both control and 70 μM thalidomide monolayers displayed spontaneous calcium propagation. Calcium transient durations in thalidomide-treated 2D monolayers were significantly longer for both 50 and 80% repolarization at 546 ± 176 ms and 874 ± 321 ms for control compared to 1212 ± 61 ms and 2162 ± 158 ms for 70 μM tissues (n = 3 tissues per condition. * $p < 0.05$). Additionally, the calcium conduction velocity was slower when compared to age-matched controls at 1.58 ± 0.07 and 1.05 ± 0.199 cm/s for control and 70 μM tissues, respectively (Figure 5.4D, E, F, G). Calcium transient

duration is important in the function and maturation of CMs. Our lab previously showed that nitric oxide-treated SC-CMs had a positive effect on CM differentiation; treated CMs also exhibited faster calcium transient durations compared to untreated controls (Hodge, Zhong, and Lipke 2016). Here, thalidomide, which negatively impacts CM function, had a detrimental impact on calcium transient duration.

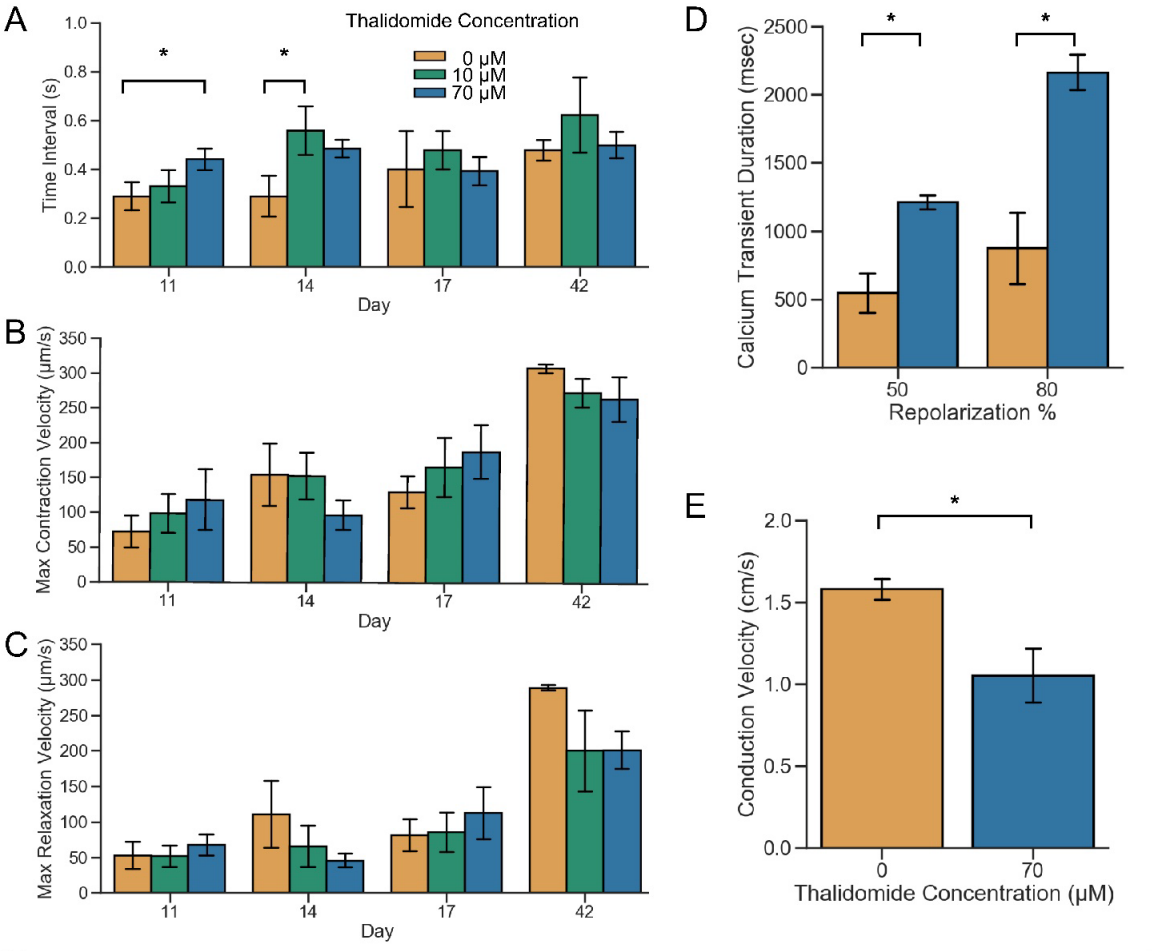
A
Thalidomide Concentration
0 µM
10 µM
70 µM
Time Interval (s)
Day
B
Max Contraction Velocity (µm/s)
Day
C
Max Relaxation Velocity (µm/s)
Day
D
Calcium Transient Duration (msec)
Repolarization %
E
Conduction Velocity (cm/s)
Thalidomide Concentration (µM)

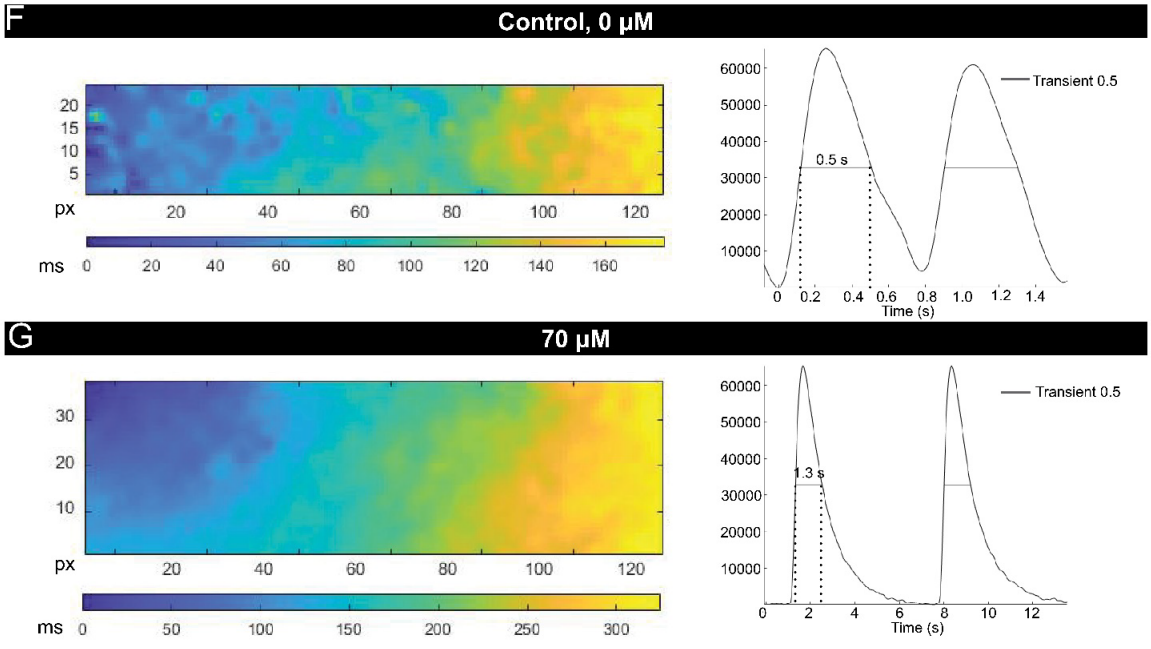
F
Control, 0 µM
px
ms
Transient 0.5
0.5 s
Time (s)
G
70 µM
px
ms
Transient 0.5
1.3 s
Time (s)

Figure 5.4 Thalidomide treatment induced differences in contractility and calcium handling.

(A) Significant differences in time interval between contraction and relaxation for control and 70 μM thalidomide-treated tissues were observed on days 11 and 14 ($n \geq 3$ tissues per condition). (B, C) Control and 10 μM tissues significantly increased contraction and relaxation velocity from day 17 to day 42 compared to 70 μM thalidomide treatment groups ($n \geq 3$ tissues per condition). Representative isochrone maps and traces of (F) Control and (G) 70 μM calcium wave propagation showed significantly longer (D) CTD at both 50 and 80% repolarization and (E) slower conduction velocity in thalidomide treated samples compared to control ($n = 3$ monolayers per condition, * $p < 0.05$).

Thalidomide treatment induces changes in gene expression and ECM production.

The direct mechanism by which thalidomide damages cardiac tissue is not fully and clearly established. Previous studies have indicated a potential target of thalidomide on genes that regulate ECM production (Choe et al. 2010). Several cardiac and ECM related genes were explored in this study using RT-qPCR to further elucidate differences in gene expression following treatment with the known teratogen. Expression of cardiac specific genes GJA5, MYH6, and MYH7 were similar in all treatment groups and changed appropriately over time (Figure 5.5A). MYH7 expression increased significantly between each timepoint in all groups, as expected. ECM related gene expression including FN1, COL1A1, and POSTN increased over time in all groups as the cells began to produce their own ECM proteins. On day 10, POSTN expression was significantly

higher in both thalidomide-treated samples compared to control (Figure 5.5D, $n = 3$ tissues per condition, * $p < 0.05$). The impact of thalidomide exposure on SALL4 and TBX20 expression has been explored in previous studies (Donovan et al. 2018; Khalil et al. 2017; Papaioannou 2014); here, SALL4 expression was downregulated over time and TBX20 expression was upregulated after differentiation with no significant differences between treatment groups (Figure 5.5A).

The ECM composition was characterized on day 20 by decellularization of the 3D-dECT, digestion of the protein into peptides, and quantification using untargeted LC-MS; protein identification occurred using a UniProt KB database. Relative quantification was obtained by spectral counts of peptides with at least 95% confidence normalized by total ECM spectral counts. To examine the deposited ECM proteins, the fibrinogens were removed from the analysis, as these were provided by the biomaterial, PEG-fibrinogen. Deposited ECM components included fibrillin, fibronectin, perlecan, collagen, vitronectin, EMILIN-2, laminin, and periostin (POSTN) (Figure 5.6A), with significant differences in collagen alpha-1(I) chain (COL1A1), collagen alpha-1(II) chain (COL2A1), and fibrillin-1 deposition (Figure 5.6B). COL2A1 was significantly higher in control samples compared to 10 and 70 μM thalidomide treated 3D-dECTs. The ECM characterization showed increased levels of COL1A1 in 70 μM thalidomide treated samples compared to control (Figure 5.6B), but there was not a significant increase in COL1A1 gene expression in 70 μM day 30 3D-dECTs (Figure 5.5C). The increase in COL1A1 can potentially be explained by changes in TGF-β expression over time. From day 10 to day 30, TGF-β expression remained upregulated in 70 μM samples compared to control tissues, where TGF-β expression was downregulated to pre-differentiation

levels. Previous studies have shown an increase in TGF-β stimulates ECM protein production (Hanna and Frangogiannis 2019) and inhibits collagenase secretions resulting in a buildup of ECM proteins over time (Bowers, Banerjee, and Baudino 2010). Through utilization of a 3D-dECT model, thalidomide induced changes to ECM composition and gene expression changes from the pluripotent state through cardiac tissue formation and differentiation could be quantified.

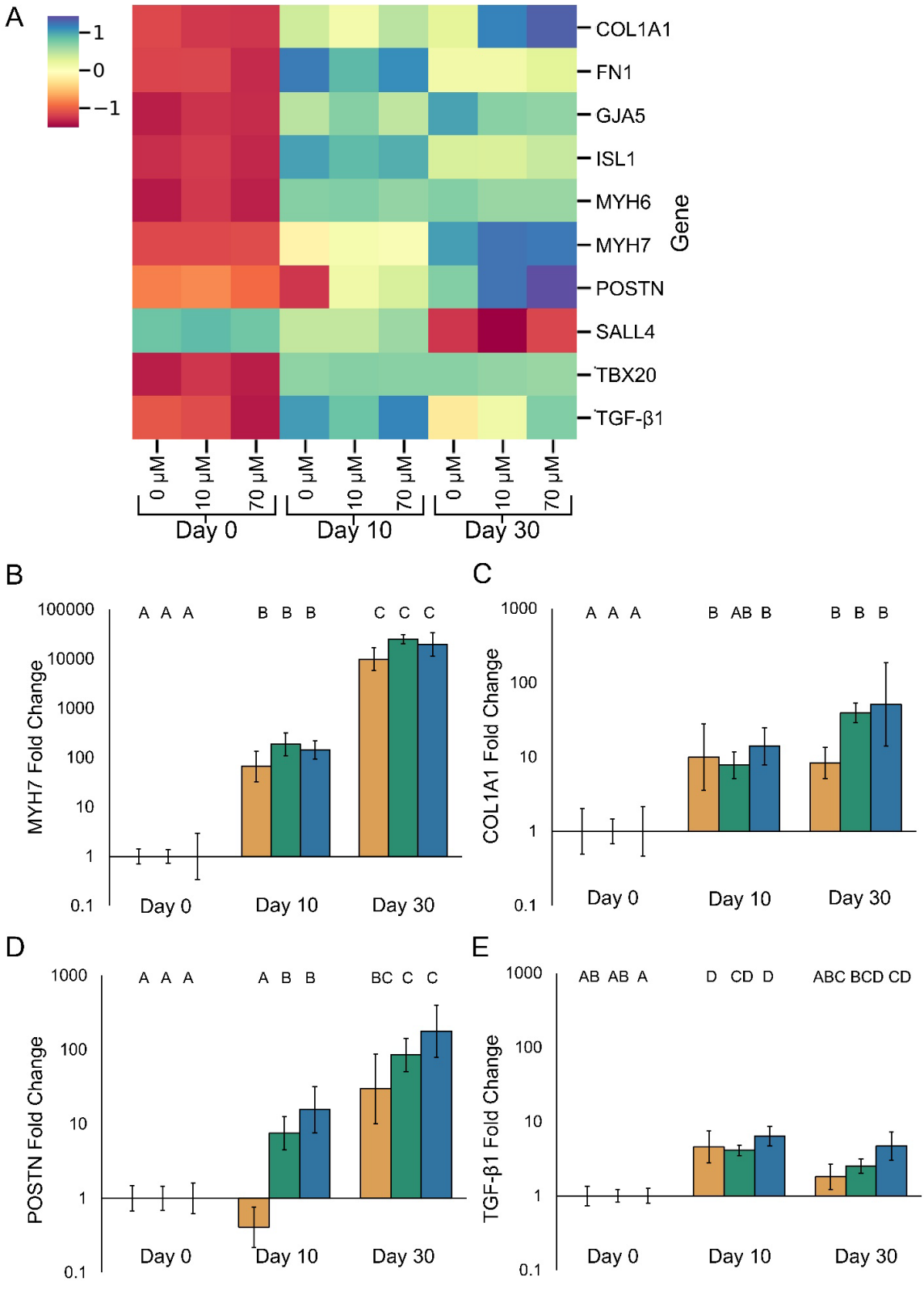
A
1
0
−1
COL1A1
FN1
GJA5
ISL1
MYH6
MYH7
POSTN
SALL4
TBX20
TGF-β1
Gene
0 μM
10 μM
70 μM
Day 0
Day 10
Day 30
B
MYH7 Fold Change
100000
10000
1000
100
10
1
0.1
A A A
B B B
C C C
C
COL1A1 Fold Change
A A A
B AB B
B B B
D
POSTN Fold Change
A A A
A B B
BC C C
E
TGF-β1 Fold Change
AB AB A
D CD D
ABC BCD CD

Figure 5.5 Thalidomide treatment impacts gene expression.

(A) A heat map comparing gene expression of various cardiac and ECM-related genes for each treatment group on days 0, 10, and 30 was produced. (B) Expression of cardiac gene MYH7 showed temporally appropriate upregulation in all groups over time. (C) Gene expression of COL1A1 increased in all groups from day 0 to day 10. (D) Periostin expression was higher in thalidomide treated samples on day 10. (E) From day 10 to day 30, TGF-β expression was maintained in 70 μM tissues compared and downregulated in control tissues (n = 3 samples per treatment group per timepoint, data is normalized to GAPDH and day 0 using $2^{(-\Delta\Delta Ct)}$ method, * $p < 0.05$).

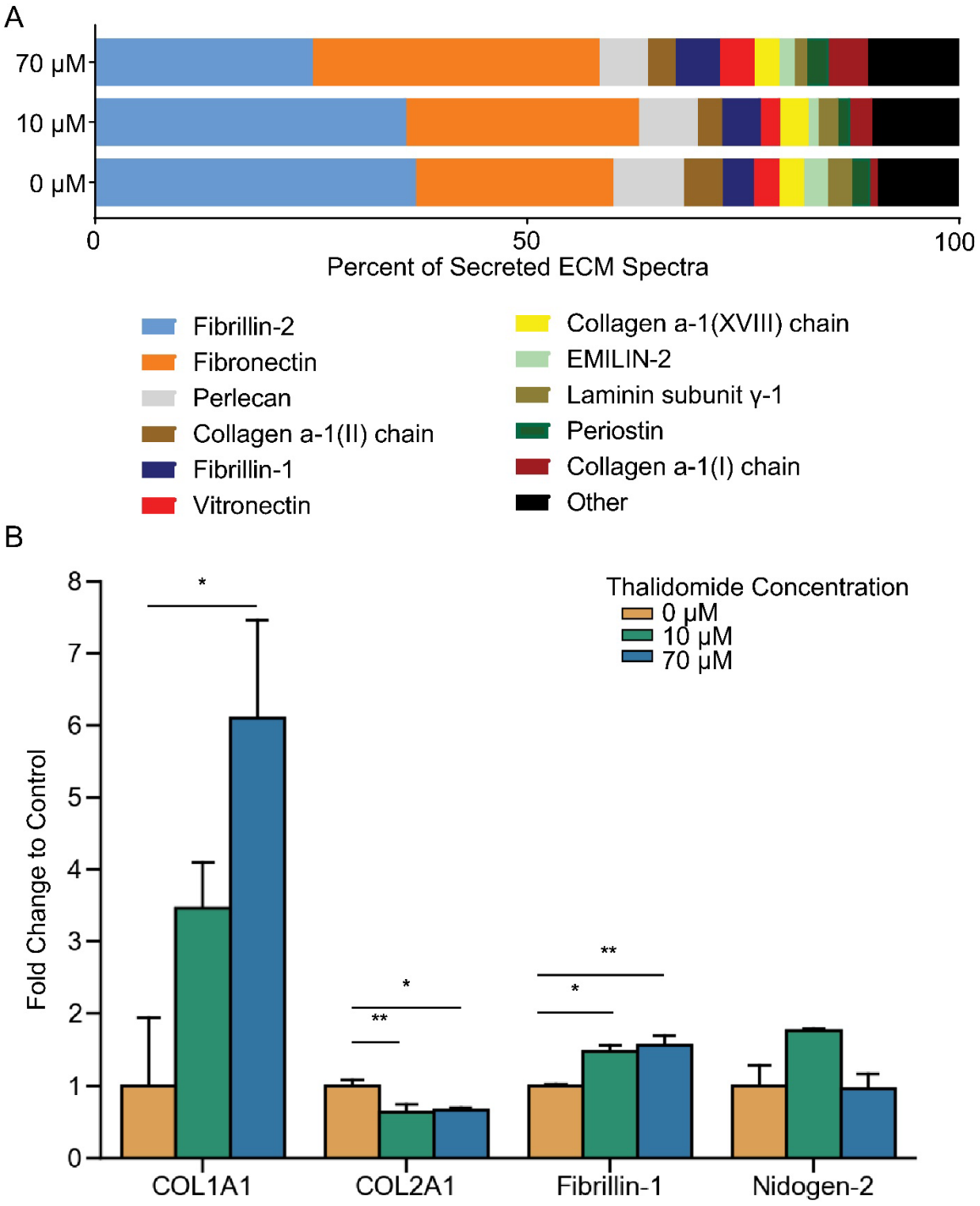

Figure 5.6 Thalidomide treatment impacts ECM composition.

(A) The ECM composition was characterized using LC-MS. The percent of secreted ECM spectra are shown for 0, 10, and 70 µM samples on day 20, with over 50% of the secreted ECM coming

from fibrillin-2 and fibronectin in all treatment groups. The total ECM composition includes fibrillin, fibronectin, perlecan, collagen, vitronectin, periostin and others. (B) 70 μM ECM had significantly higher presence of collagen alpha-1(I) chain. Additionally, control ECM had significantly higher collagen alpha-1(II) chain compared to thalidomide treated groups (n=3 tissues, fold change is percent compared to control, (A) one-way ANOVA, * $p < 0.05$, ** $p < 0.01$. (B) Tukey's multiple comparisons test within each protein, * $p < 0.05$, ** $p < 0.01$).

5.4 Discussion

In this proof-of-concept study, we show that our 3D developing engineered cardiac tissues (3D-dECTs) can be used to study drug-induced changes to cardiac tissue properties caused by thalidomide treatment during and after 3D cardiac differentiation. These developing cardiac tissues are directly differentiated from hiPSCs, allowing for examination of the cumulative effect of teratogen exposure on the cardiac tissue properties as well as during differentiation as the cells progress from pluripotent cells to cardiac tissue. Although thalidomide is a widely studied pharmaceutical, less is known about its interactions during development, particularly with differentiating hiPSCs. We first verified that thalidomide did not change short term hiPSC viability, proliferation, and mitochondria distribution compared to control groups. Thalidomide-treatment groups were administered to 3D-dECTs starting from day 1 of cardiac differentiation and showed effects after initial dosage administration. Tissue growth in thalidomide-treated 3D-dECTs was significantly less on days 5 and 7 when compared to control 3D-dECTs. In our 3D-dECT model we detected changes in tissue architecture and efficiency of cardiac differentiation on day 10 between the three treatment groups. Tissues began to

spontaneously contract in all treatment groups; however, in the 70 μM thalidomide treated 3D-dECTs, contractions initiated later than age-matched controls. Initial contraction time intervals of thalidomide-treated 3D-dECTs were significantly longer and tissue formation was not as apparent as controls. When dissociated, thalidomide treated CMs contained localized and clustered mitochondria while control CMs developed more evenly distributed mitochondria throughout the cytoplasm. Although most 2D monolayers did not result in contracting sheets when treated with thalidomide, some electrophysiological results could be obtained with this 2D approach. During optical mapping of control and thalidomide-treated 2D cardiac monolayers, calcium transient durations were longer and there was a slower conduction velocity in the thalidomide-treated samples compared to the control. By providing a 3D microenvironment throughout the timeline of stem cell differentiation, developmental changes and abnormalities that cannot be studied in 2D were identified in 3D-dECTs. Changes in ECM deposition were detected between the treatment groups; notably, thalidomide treated samples had a larger amount of collagen alpha-1(I) chain and fibrillin-1, and smaller amount of collagen alpha-1(II) chain; additionally, there were significant differences in nidogen-2 production. Appropriate changes in cardiac gene expression were detected in all three treatment groups, and there were significant differences in periostin and TGF-β1 expression between the treatment groups. Here we show that thalidomide negatively influences cardiac tissue formation, contractile function, mitochondria development, ECM composition, gene expression, and electrophysiology.

Historically for studying the formation of human CHDs, animal models (Ho et al. 1991), culture of explanted developing myocardium (Rivera-Feliciano and Tabin 2006),

and 2D cell culture models with control and diseased cell lines have been employed. Animal models provide the ability to study the systemic development *in vivo*; however, because of the high cost and recommendations to minimize animal testing, they are not conducive for use in high-throughput screening assays; furthermore, they do not always accurately detect human-specific developmental defects, such as with the drug thalidomide (Giacomotto and Segalat 2010). Explanted myocardium can provide relevant biological insights such as structural changes in tissue formation and changes in gene expression; however, there are a limited number of samples available and cannot be maintained long-term *in vitro.* Although *in vitro* models will always be an imperfect representation of the *in vivo* reality, reduction in the number of variables in the system can provide insights that would otherwise be clouded by systemic complexity. Previously, gene expression profiles of differentiating hiPSCs treated with thalidomide significantly downregulated a variety of genes, including genes important for cell differentiation and organ development (Mayshar, Yanuka, and Benvenisty 2011; Meganathan et al. 2012), indicating that an *in vitro* hiPSC derived model may successfully recapitulate key aspects of development and provide insight in thalidomide-induced cardiac defect formation.

Utilizing temporal addition of small molecules has resulted in recent improvements in cardiac differentiation efficiency in 2D monolayer differentiation systems, which provides better reproducibility between experiments and allows for more accurate drug-testing; however, to achieve high yields of CMs and reproducible results, a critical component for success is the initial cell seeding density and cell proliferation (Lian et al. 2012; Lian et al. 2013). Drug exposure impacts adherent cell concentration,

making 2D differentiation challenging for systematically assessing the effects of teratogens. Previous work has been done using hiPSCs as model systems to detect thalidomide induced changes, but these still rely on platforms that are only based on cells (Mayshar, Yanuka, and Benvenisty 2011; Xing et al. 2015; Z. Ma, Wang, et al. 2015). Alternatively, the approach of assembling of ECTs after CM differentiation does not allow for investigation of teratogen-induced changes that can occur during heart development**.** Particularly with thalidomide-induced genetic mutations, an *in vitro* 3D direct differentiation tissue model is advantageous to study the impact of the drug-treatment throughout the process of cardiac tissue differentiation and formation. Because cardiac development is a 3D process, creating a reproducible and straight-forward 3D developing engineered cardiac tissue (3D-dECT) platform for developmental pharmacology provides the opportunity to be able to detect changes that will influence the developing 3D tissue that cannot be detected in 2D.

Thalidomide, which was tested in high concentrations on mice and rats, did not show any teratogenicity; years later researchers discovered that the teratogenic effects of thalidomide are species specific. This species specificity emphasizes the importance of human based *in vitro* studies (Parman, Wiley, and Wells 1999). Previous research has suggested that thalidomide is anti-angiogenic (Therapontos et al. 2009), with effects on chondrogenesis, DNA intercalation, and cell survival and proliferation (Stephens, Bunde, and Fillmore 2000). Thalidomide is known to bind to CRBN, potentially explaining the limb deformities because of the resulting inhibition of E3 ubiquitin ligase function (Ito, Ando, and Handa 2011); more recently, it has been shown that thalidomide can bind to Tbx5 (Khalil et al. 2017) and promote degradation of SALL4 (Donovan et al. 2018),

potentially explaining the resulting cardiac phenotype. Additionally, thalidomide was previously shown to induce oxidative stress due to free radical production; in rabbits, thalidomide generates reactive oxygen species (ROS) that carry out DNA oxidation and inhibits fibroblast growth factor expression (Parman, Wiley, and Wells 1999; Hansen and Harris 2004). Knobloch *et al.* showed that thalidomide induced oxidative stress enhances Bmp signaling (i.e., up-regulation of Bmp) and inhibition of Wnt/β-catenin signaling pathways (Knobloch, Shaughnessy, and Ruther 2007). The upregulation of Bmp downregulates Akt signaling; the Akt1 gene is essential for angiogenesis in the heart (Shiojima and Walsh 2006). Both Bmp and Wnt signaling pathways are important in cardiac development, particularly in small molecule guided stem cell differentiation (Lian et al. 2013; Lian et al. 2012); furthermore, these pathways play a critical role in cell survival, proliferation, and death (Vargesson 2015). This perturbation in these developmental signaling pathways could therefore lead to thalidomide-induced CHDs and potentially explain the reason for lower efficiency of differentiation and resulting size of CMs in thalidomide treated samples in this study along with the noticeable differences in tissue growth and architecture.

The ECM composition of the resulting 3D-dECTs were quantified, and deposited ECM included fibrillin, fibronectin, perlecan, collagen, vitronectin, EMILIN-2, laminin, and periostin, with significant differences in COL1A1, COL2A1, fibrillin-1, and nidogen-2 deposition between thalidomide-treated 3D-dECTs and the control. Thalidomide has been previously investigated for improving the inflammatory response after heart failure; in these studies, thalidomide was found to decrease the collagen content (Yndestad et al. 2006). In addition, type I collagen production was significantly inhibited in cultured

human lung fibroblasts exposed to thalidomide (Tseng et al. 2013). Interestingly, the effects of thalidomide on (ECM) production during heart development in our 3D-dECT platform showed opposite effects of type 1 collagen, with significantly more COL1A1 ECM deposition in thalidomide treated samples, which can potentially be explained by increased TGF-β production. Furthermore, there was a significant decrease in COL2A1 ECM production in thalidomide treated samples.

Mitochondria are complex organelles that are important in ATP production and cell signaling (Dorn, Vega, and Kelly 2015), and differences in mitochondria distribution and structure could were observed following thalidomide administration. The thalidomide-treated 3D-dECTs contained CMs with clustered mitochondria that were not distributed evenly throughout the cytoplasm of cells. In comparison, control CMs contained mitochondria close to the cell nuclei, throughout the cytoplasm, and close to and between sarcomeres, which is common in healthy muscle cells (Hom and Sheu 2009). Differences in mitochondria morphology and volume are often associated with increased reactive oxygen species (ROS) production and apoptosis (Parra et al. 2008), a proposed mechanism of thalidomide treatment; however more experiments are needed to fully elucidate the mechanism for the clustering of mitochondria in thalidomide treated CMs.

Thalidomide forever changed the field of drug testing procedures and regulations, especially for those who are pregnant; however, thalidomide was eventually approved by the FDA in 1998 for treating multiple myeloma and leprosy, although major warnings and routine screenings are a requirement to ensure that patients do not become pregnant while taking this drug (Rehman, Arfons, and Lazarus 2011). Here, we used this known

teratogen as a proof-of-concept to demonstrate that the 3D-dECT model can be used to detect differences in tissue properties caused by drug administration during cardiac development. Because the successful production of contracting 3D-dECTs is not closely dependent on the initial seeding density and cell proliferation, all of our thalidomide-treated 3D-dECTs showed some degree of spontaneous contraction, which potentially would not have resulted in contracting CMs in other cell-based studies, particularly those carried out in 2D. Overall, this platform can be used to identify important differences between control and thalidomide treatment groups, including differences in tissue formation and architecture, cardiac differentiation, contractile function, mitochondrial distribution, ECM deposition, and gene expression profiles. This study revealed that the 3D-dECT platform can be used to study drug induced changes to tissue properties during cardiac development and has the potential to be used in high-throughput drug screening applications and disease modeling.

5.5 Supplementary Information

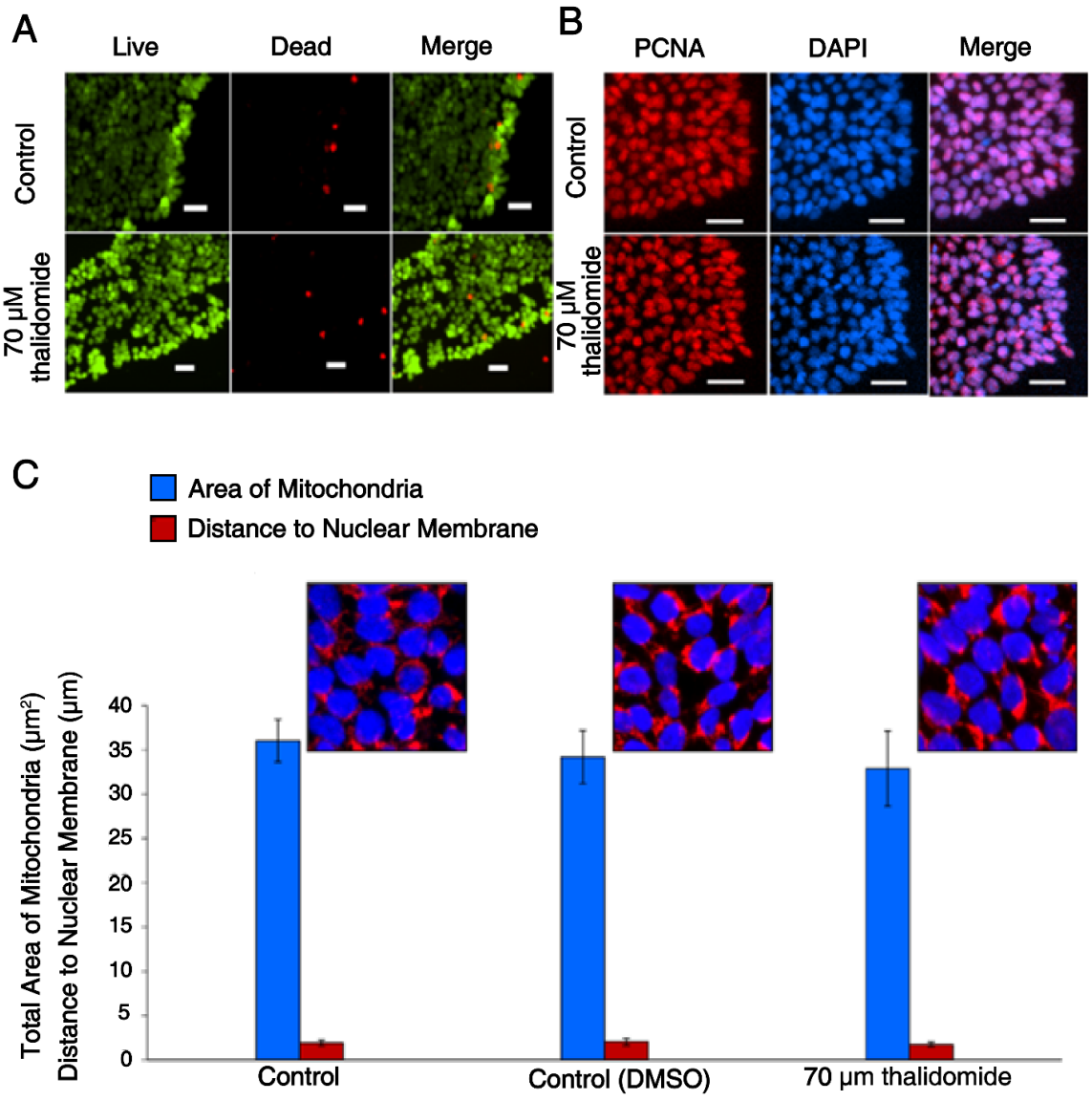

Supplementary Figure 5.1 Thalidomide exposure did not impact hiPSC viability, proliferation, and mitochondria distribution.

(A) Percentage of viable cells exceeded 90% for control and 70 µM thalidomide conditions. (B) Proliferating cell nuclear antigen (PCNA) staining confirmed greater than 98% cells for all tested conditions. All samples were counter stained with DAPI. Scale bar, 20 µm. (C) Total area of

mitochondria and distance to nuclear membrane did not change significantly between control and 70 µM thalidomide treatments.

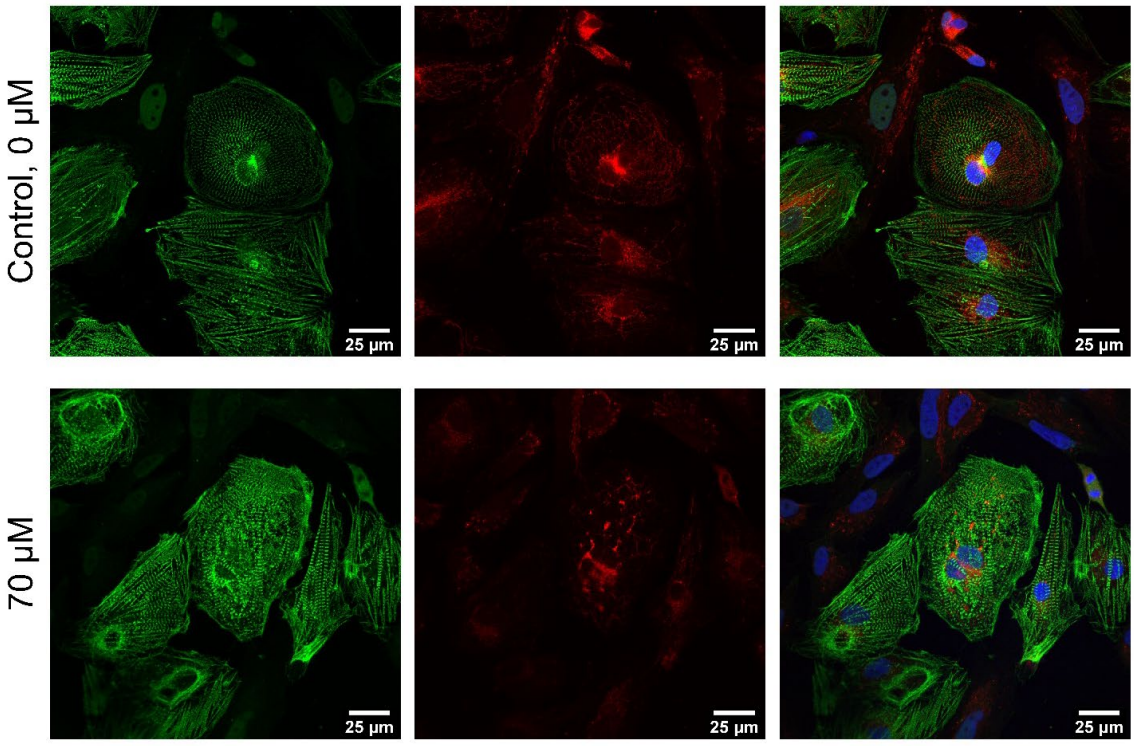

Supplemental Figure 5.2 A fewer number of αSA positive (green) cells were detected after cardiac tissue dissociation in thalidomide groups compared to control. Sarcomeres were more defined and organized in control CMs when compared to thalidomide-treated CMs.

A

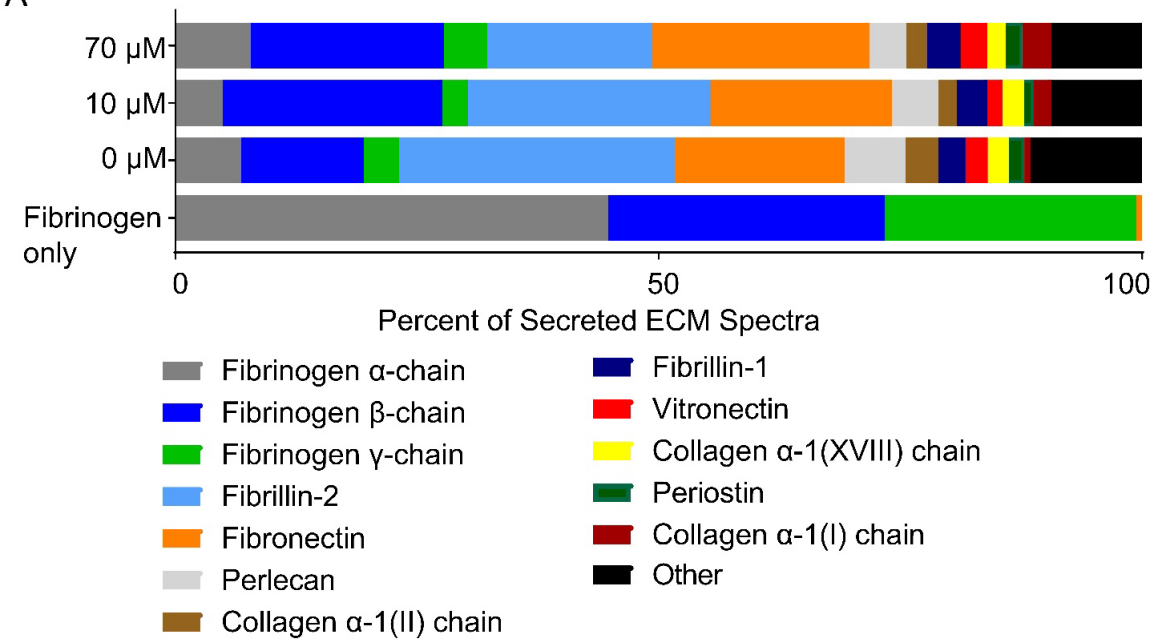
70 μM
10 μM
0 μM
Fibrinogen only
0
50
100
Percent of Secreted ECM Spectra
Fibrinogen α-chain
Fibrinogen β-chain
Fibrinogen γ-chain
Fibrillin-2
Fibronectin
Perlecan
Collagen α-1(II) chain
Fibrillin-1
Vitronectin
Collagen α-1(XVIII) chain
Periostin
Collagen α-1(I) chain
Other

B

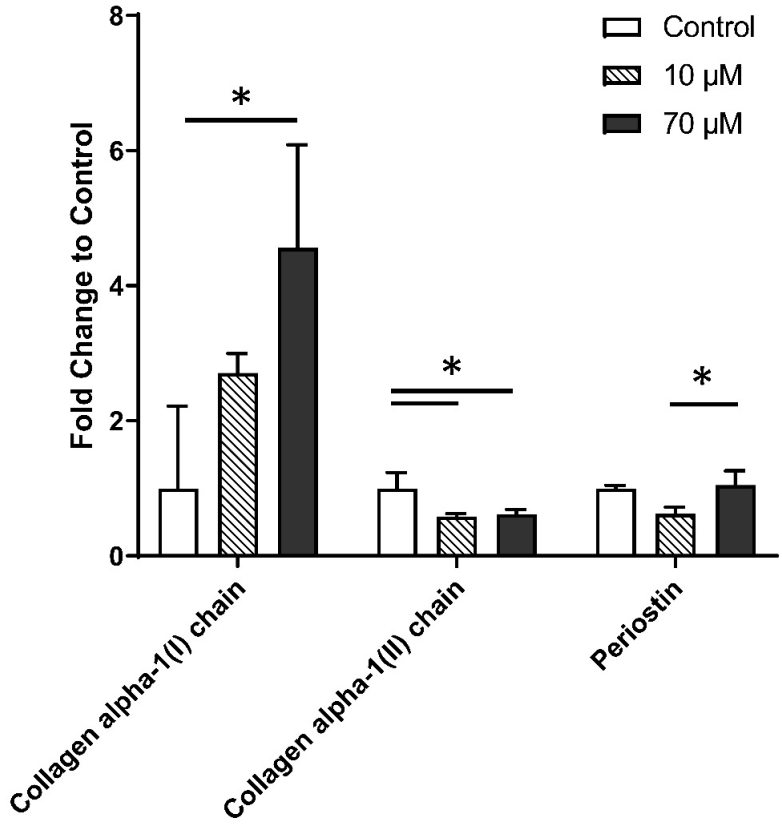
Control
10 μM
70 μM
Fold Change to Control
0
2
4
6
8
*
*
*
Collagen alpha-1(I) chain
Collagen alpha-1(II) chain
Periostin

Supplementary Figure 5.3 The ECM composition, including fibrinogen, was characterized using LC-MS.

(A) The percent of secreted ECM spectra are shown for 0, 10, and 70 μM samples on day 20. The total ECM composition includes fibrillin, fibronectin, perlecan, collagen, vitronectin, periostin and others. (C) 70 μM ECM had significantly higher presence of collagen alpha-1(I) chain. Additionally, control ECM had significantly higher collagen alpha-1(II) chain compared to thalidomide treated groups. 70 μM ECM had higher presence of periostin compared to 10 μM ECM (n=3 tissues, fold change is percent compared to control. Tukey's multiple comparisons test within each protein, * $p < 0.05$)

Supplementary Table 5.1 Primers for RT-qPCR

Gene (Product)	**Primers, F:Forward, R:Reverse, Pr:Probe (Taqman primers only)**
COL1A1 (Collagen Type I alpha 1 chain)	F: GCTATGATGAGAAATCAACCG R: TCATCTCCATTCTTTCCAGG
FN1 (Fibronectin)	F: CCATAGCTGAGAAGTGTTTTG R: CAAGTACAATCTACCATCATCC
GAPDH for SYBR Green	F: TCGGAGTCAACGGATTTG R: CAACAATATCCACTTTACCAGAG
GAPDH for Taqman	F: CCCCTTCATTGACCTCAACTACA R: TTGCTGATGATCTTGAGGCTGT P: /5Cy5/AAATCCCATCACCATCTTCCAGGAGC/3IAbRQSp/
GJA5 (Cx40)	F: CCTCTACCCAGTATACGAAG R: GCTGGTATGTAGAGAGAGAG
ISL1 (ISL1)	F: CTAATATCCAGGGGATGACAG R: CTGGTAACTTTGTACTTCCAC
MYH6 (αMHC)	F: ACCAACCTGTCCAAGTTCCG R: TTGCTTGGCACCAATGTCAC Pr: /56-FAM/AGCATGAGC /ZEN/TGGATGAGGCAGAG /3IABkFQ/
MYH7 (βMHC)	F: CACAGCCATGGGAGATTCGG R: CAGGCACGAAGACATCCTTCT Pr: /56-FAM/CCTACCTGC /ZEN/GCAAGTCAGAGAAGG

	/3IABkFQ/
POSTN (Periostin)	F: ATACTCTCCAGTGTTCTGAG R: TTGGCAGAATCAGGAATTAG
SALL4 (SALL4)	F: AAAGGTTCACTACATGACAC R: CCTTGGGAAAGATTTCTGAG
TBX20 (TBX20)	F: GAACTCAATGCATAAGTACCAG R: TATCAGTTGATTCTGGTAGGC
TGFβ1 (TGF-β-1)	F: CCCACAACGAAATCTATGAC R: TGTATTTCTGGTACAGCTCC

Chapter 6: Genetic Congenital Heart Disease model produced from LVNC patient-derived hiPSCs

6.1 Introduction

Congenital heart disease is the leading type of birth defect, causing the majority of infant deaths worldwide (Organization 2017). The causes of congenital heart disease are widespread but generally can be grouped into nongenetic and genetic causes. Nongenetic causes, including environmental teratogens, maternal exposures, and infectious agents have been widely studied in the field (Fahed et al. 2013). With advancements in genomic testing, significant efforts are being made worldwide to create comprehensive genomic analyses for CHD (van der Bom et al. 2011; Van der Velde et al. 2005). Genetic causes are more difficult to study due to the inherent complexities of cardiac development and the incomplete knowledge of how genes control developmental cardiac events (Bruneau 2008). Determining which of the many possible mutations is truly disease-causing is challenging when studying genetic causes because often there is not a direct correlation between gene mutation and presented defect (Gelb, Brueckner, Chung, Goldmuntz, Kaltman, Kaski, Kim, Kline, Mercer-Rosa, Porter, Roberts, Rosenberg, Seiden, Seidman, Sleeper, Tennstedt, Kaltman, Schramm, Burns, Pearson, Rosenberg, et al. 2013). This process is complicated by the fact that a single mutation can result in a variety of defects and, a single defect can be caused by a variety of mutations (Wessels and Willems 2010). Therefore, it is imperative that functional developing cardiac models be used to study the genetically heterogeneous, CHD.

Several disease modeling platforms have been investigated for CHD. Animal models, including canine, mouse, and rabbit modes, have been used to study electrophysiological and structural CHD *in vivo* (Basso et al. 2004; Kodo et al. 2016a; Georgakopoulos et al. 1999; Brunner et al. 2008). While these models provide a basic understanding of cardiac development and manifestation, they do not accurately recapitulate human development, physiology, and genetic information. Studies have shown that perinatal and postnatal cardiac development varies considerably between species and is dependent on gestation time, number of offspring per pregnancy, and transitions in proliferative capacity, growth, and nucleation (Velayutham, Agnew, and Yutzey 2019). For example, a mouse's gestation period is three weeks, resulting in rapid postnatal heart development; a mouse heart beats ten times faster than humans and uses different ion channels for repolarization making it difficult to compare electrophysiological and structural development between species (Davis et al. 2011).

With primary human cardiomyocytes (CMs) not being suitable for long term culture, the discovery of reprogrammed somatic cells to form induced pluripotent stem cells (hiPSCs) resulted in a paradigm shift in tissue engineering and disease modeling (Takahashi and Yamanaka 2006). Now, skin, blood or hair samples can be taken from patients with CHD disease and be reprogrammed into a virtually unlimited supply of hiPSCs. Reprogrammed cells maintain genetic information, can be differentiated into all three germ layers, and show characteristics of disease phenotype *in vitro* (Wu and Hochedlinger 2011). HiPSCs have been used for cardiac differentiation in a variety of CHD modeling platforms primarily in the form of pre-differentiated cells or embryoid bodies (EBs) (Moretti et al. 2010b; Itzhaki et al. 2011; Davis, Casini, van den Berg,

Hoekstra, Remme, Dambrot, Salvatori, Ward-van Oostwaard, et al. 2012; Jiang et al. 2014b; Jung et al. 2012; Novak et al. 2012; Sun et al. 2012b). These studies have provided invaluable knowledge on a cellular and molecular level but fail to demonstrate how CMs behave on a macrotissue level. Pre-differentiated hiPSC-CMs must be dissociated and rejoined to create contracting tissues, potentially damaging important cell-cell junctions required for CM functionality. Embryoid body differentiation often results in a low differentiation efficiency, with functional CM colonies being excised from EB constructs and cultured long term in 2D. To avoid these limitations, there is a necessity for a 3D engineered CHD model using patient derived hiPSCs to form functional developing cardiac tissues.

LVNC is the third most prevalent cause of cardiomyopathy in children behind dilated cardiomyopathy and hypertrophic cardiomyopathy (Nugent et al. 2003). LVNC results in deep hypertrabeculation of the left ventricular wall decreasing cardiac output and increasing the chances of arrhythmias, thromboembolism, and heart failure. LVNC has been attributed to interruption in compaction in the left ventricular wall as the heart develops *in utero* (Captur and Nihoyannopoulos 2010). In the developing heart, trabeculations emerge in the spongy endocardial tissue after the looping of the heart tube in week 4 of gestation. In weeks 5-8 of gestation, the epicardial layer of the ventricular wall undergoes compaction followed by the endocardial layer, resulting in a thickening of the compacted myocardium (Krishnan et al. 2014). However, in patients with LVNC, the trabeculations never compact leaving a spongy endocardium on a compacted epicardium. The onset of symptoms is highly variable and appear in patients as early as infancy or as late as adulthood (Sarma, Chana, and Elkayam 2010).

Like many genetic congenital heart diseases, the mechanisms and mutations associated with LVNC are not fully understood. LVNC can be a result of mutations in several genes including, cardiac troponin T, tafazinn, α-dystrobrevin, ZASP (Captur and Nihoyannopoulos 2010; Oechslin and Jenni 2011), and T-box genes (Kodo et al. 2016a). In addition, animal models often link LVNC to abnormal expression of growth factors, including NOTCH, NGR1/ERBB2 (Arbustini, Weidemann, and Hall 2014), and transforming growth factor beta (TGF-β) (Bartram et al. 2001; Shou et al. 1998), showing abnormal proliferation of developing CMs. In this study, we will explore cardiac development of LVNC caused by a mutation in the Tbx20 gene. The Tbx20 gene plays a large role in transcriptional activation and repression, and it interacts with other cardiac developmental genes including Nkx2.5, Gata4, Gata5, and Tbx5 (Kirk et al. 2007).

Current models of LVNC caused by Tbx20 mutations either use patient derived hiPSCs to create 2D cardiac monolayers or transgenic and knockout mouse models (Kodo et al. 2016a). These studies provided valuable insight about LVNC on a cellular level *in vitro* and a systemic level in mice but lack information about how this disease manifest in 3D human tissues. To overcome the limitations of this study, we used our established 3D hiPSC encapsulation platform (Seeto et al. 2019) with LVNC patient derived hiPSCs to create LVNC 3D engineered cardiac tissues. In this study, we demonstrate the ability to directly differentiate hiPSCs derived from a LVNC patient encapsulated in hydrogel microspheres to form LVNC cardiac microspheres.

6.2 Materials and Methods

All chemicals were purchased from Sigma-Aldrich unless otherwise specified.

6.2.1 HiPSC Culture

LVNC patient-derived hiPSCs were acquired from Joseph Wu at the Stanford Cardiovascular Institute. HiPSCs were cultured on Matrigel (BD Biosciences) at 37 ºC, 5% CO_2, and 85% relative humidity using E8 medium. HiPSCs were passaged every 3 days using Versene for 7 minutes at room temperature into E8 supplemented with 10 μM ROCK inhibitor (RI, Y-27632, Stem Cell Technologies) for 24 hours after passaging.

6.2.2 Monolayer Differentiation

Cardiac monolayers were produced using the previously described protocols (Burridge et al. 2014; Kodo et al. 2016b). Briefly, $1.25*10^4$ hiPSCs/cm^2 were added to a 12 well plate on day -4 of differentiation in E8 plus 10 μM ROCK inhibitor (RI, Y-27632, Stem Cell Technologies) for 24 hours. HiPSCs were culture for 3 additional days in E8 medium before initiation of differentiation on day 0 according to 4 established protocols (Figure 6.1b). All wells were cultured long term in RMPI B27 (Thermo Fisher Scientific).

6.2.3 Fabrication of Control and LVNC Cardiac Microspheres.

PEG-fibrinogen was synthesized, and the precursor solution was prepared as previously described (Kerscher, Turnbull, et al. 2016; DeLong, Moon, and West 2005; Plotkin et al. 2014). HiPSCs were combined with the polymer precursor solution at a cell density of 40 million hiPSCs per mL. Hydrogel microspheres were produced according to

previously established protocols (Seeto et al. 2019). Cardiac differentiation followed Protocol 4 (Figure 6.1b).

6.2.4 Early Microsphere Growth

Phase contrast images (2X) were captured throughout cardiac differentiation on days -2, 0, 2, 4, and 7. Diameter and aspect ratio of hydrogel microspheres on day-2 were quantified using standard ImageJ plugins.

6.2.5 Flow Cytometry

To quantify differentiation efficiency, flow cytometry was performed using cardiac markers MF20 and cardiac troponin T. Briefly, LVNC and control cardiac microspheres were dissociated in collagenase type B (Worthington) at 37°C for 10 minutes with gentle shaking. Dissociated cells were labeled with Zombie Green (Biolegends), blocked with 10% FBS with 1% BSA blocking buffer, and fixed with FoxP3 (Thermo Fisher Scientific) overnight at 4°C. The following day cells permeabilized, blocked, and then labeled with primary antibody MF 20 (Developmental Studies Hybridoma Bank) or cardiac troponin T (cTnT, Thermo Fisher Scientific). Lastly, cells were incubated with secondary antibody analyzed using a Cytoflex LX and FlowJo software. Data presented represents all live, single cells.

6.2.6 Optical Mapping of Cardiac Monolayers

To visualize the propagation of calcium through LVNC and control cardiac monolayers, optical mapping was performed using calcium dye Rhod-2 (5μM, Invitrogen) and myosin II inhibitor blebbistatin (10μM, Sigma Aldrich). Monolayers

were imaged in Tyrode's solution, pH 7.4. High frame rate recordings were captured using a high-speed camera and temperature was maintained at 37°C using a stage top incubator. Videos were processed and analyzed using a custom MATLAB code.

6.2.7 Contraction Analysis of Cardiac Microspheres

Videos of spontaneous contraction were recorded on days 15, 30, and 68 with a Nikon Ti Eclipse phase contrast microscope fitted with an Andor Luca S camera. The videos analyzed with optical flow MATLAB software (Huebsch et al. 2015a).

6.2.8 Statistics

All statistical analysis was performed using Minitab19. ANOVA using Tukey's test was performed for all comparisons with significance occurring at a $P < 0.05$.

6.3 Results

LVNC patient derived hiPSCs were differentiated using two platforms.

In this study we demonstrate the ability to differentiate LVNC patient derived hiPSCs using two differentiation platforms. LVNC patient and control hiPSCs lines were generated and graciously donated from the Stanford Cardiovascular Institute. Both lines were differentiated into cardiac monolayers according to one of four protocols (Figure 6.1b). These protocols were selected from two previously established cardiac differentiation protocols (Kodo et al. 2016b; Lian et al. 2013) with two different CHIR concentrations: 8μM, to mimic previous LVNC monolayer studies and 10μM, to recapitulate cardiac microsphere differentiation. Additionally, LVNC patient derived

hiPSCs were encapsulated in a hydrogel microsphere using a modified water and oil emulsion technique (Seeto et al. 2019) to produce hydrogel microspheres that were cultured for three days prior to initiation of cardiac differentiation (Figure 6.1c).

a.

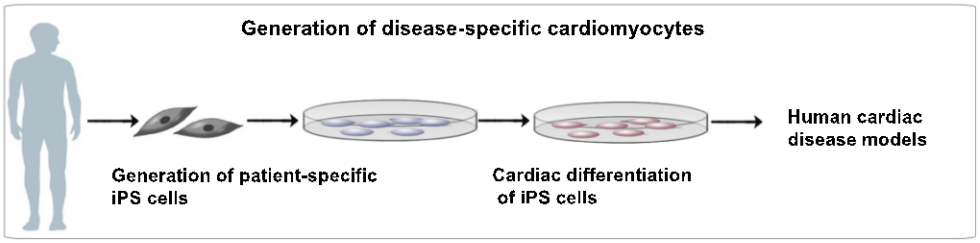

b.

Protocol	Day 0	Day 1	Day 2	Day 3	Day 4	Day 5	Day 6	Day 7
1	RPMI B27 - ins + 8 μM CHIR		RPMI B27 - ins	Fresh RPMIB27 - ins +5 μM IWP2		RPMIB27 - ins		RPMI B27
2	RPMI B27 - ins + 10 μM CHIR		RPMI B27 - ins	Fresh RPMIB27 - ins +5 μM IWP2		RPMIB27 - ins		RPMI B27
3	RPMI B27 - ins + 8 μM CHIR	RPMI B27 - ins		½ Fresh + ½ used RPMI B27 - ins +5 μM IWP2		RPMIB27 - ins		RPMI B27
4	RPMI B27 - ins + 10 μM CHIR	RPMI B27 - ins		½ Fresh + ½ used RPMIB27 - ins +5 μM IWP2		RPMIB27 - ins		RPMI B27

c.

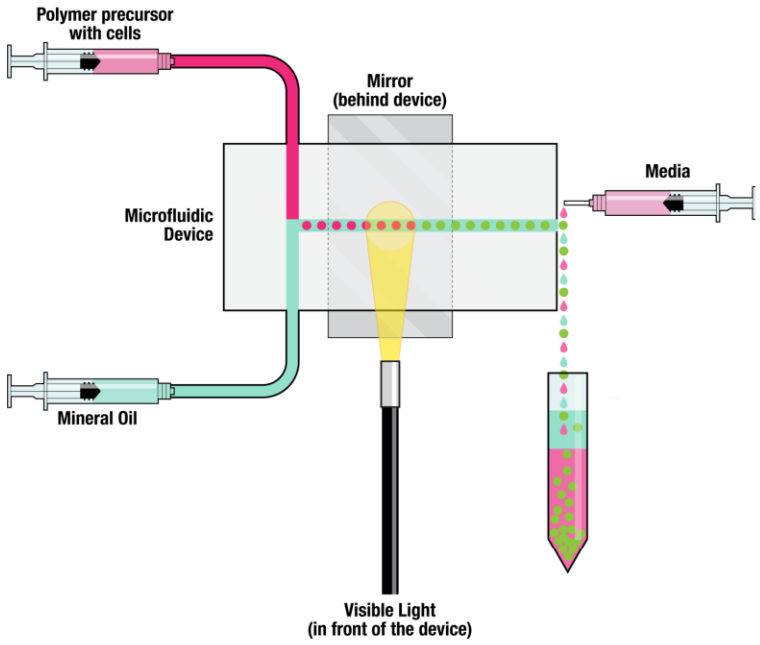

Figure 6.1 LVNC patient derived and control hiPSCs were differentiated using two platforms.

(a) Patient specific cell lines were acquired form the Stanford Cardiovascular Institute and (b) differentiated in cardiac monolayers using 4 different differentiation protocols. (c) LVNC patient and control hiPSCs were encapsulated in a hydrogel biomaterial using a novel microfluidic device and differentiated according to protocol 4. Reprinted from Small Vol 15, Issue 47. Rapid

Production of Cell-Laden Microspheres Using a Flexible Microfluidic Encapsulation Platform., Seeto, W. J., Tian, Y., Pradhan, S., Kerscher, P., Lipke, E. A., 383-395, Copyright 2019, with permission from John Wiley and Sons (Seeto et al. 2019)

Cardiac differentiation efficiency varied between LVNC patient derived and control hiPSCs monolayers.

Cardiac differentiation efficiency was assessed on day 10 in LVNC and control cardiac monolayers using cardiac marker MF20. The cell lines responded differently to each of the differentiation protocols. LVNC patient derived hiPSCs displayed the highest CM population using protocol 1 with 47% CMs. Control hiPSCs exhibited the highest CM population using protocol 4. Interestingly, previous studies have reported that protocol 1 results in 40% CM populations for LVNC patient derived hiPSCs and 80% CMs for control hiPSCs.

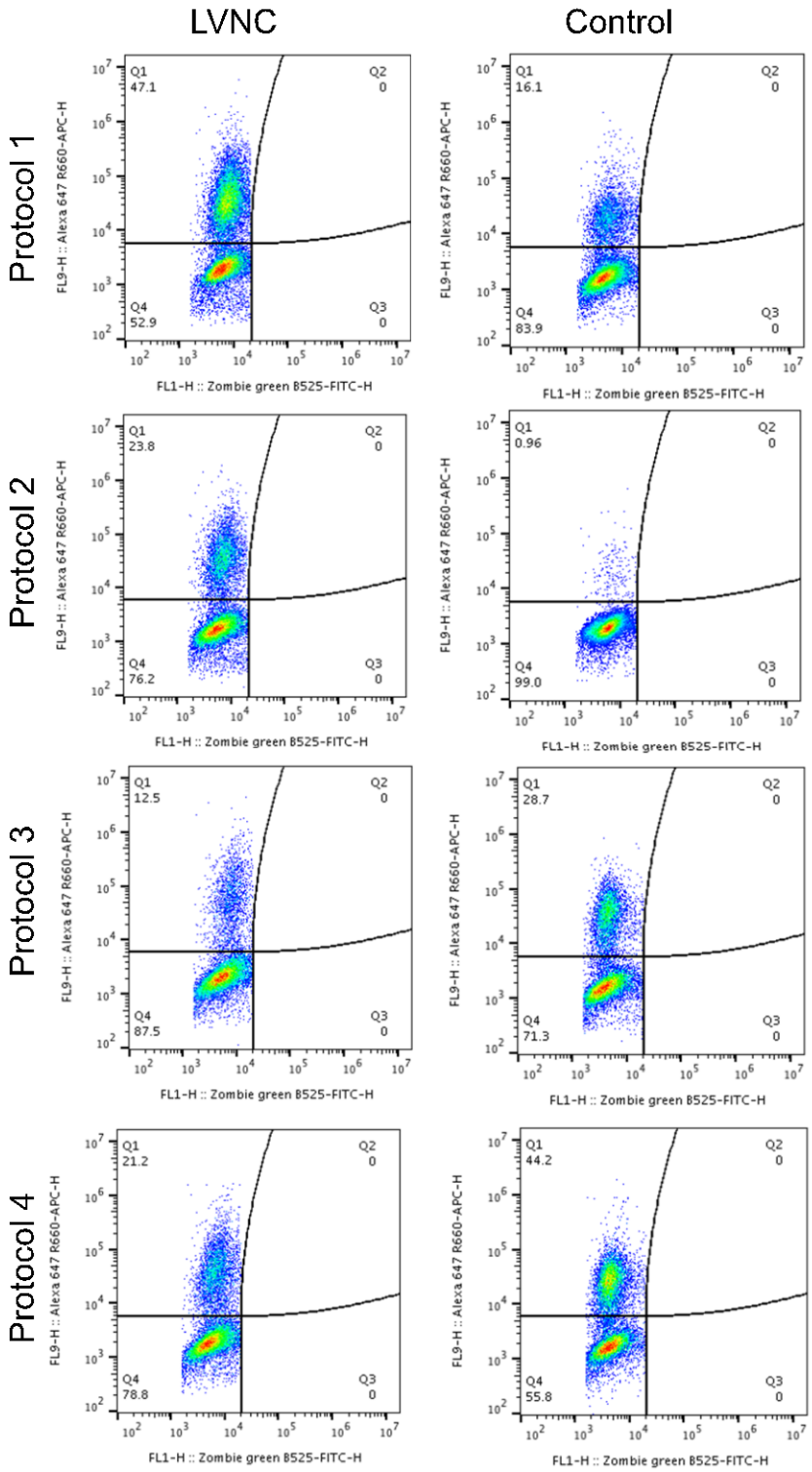

Figure 6.2 LVNC patient derived and control hiPSCs displayed different cardiac differentiation efficiencies.

LVNC cardiac monolayers contained 47.1, 23.8, 12.5 and 21.2 percent cardiomyocytes using the 4 differentiation protocols, respectively. Control cardiac monolayers contained 16.1, 0.96, 28.7 and 44.2 percent cardiomyocytes using the 4 differentiation protocols, respectively.

LVNC cardiac monolayers show prolonged calcium transients.

Calcium wave propagation was visualized and quantified using optical mapping and a custom MATLAB analysis code. Calcium transient duration (CTD) was quantified at 50 and 80% repolarization by calculating the time between the upstroke and downstroke of the trace at 50 and 80% of the down stroke height (Figure 6.3c, d) . LVNC cardiac monolayers showed significantly longer CTD50 and CTD80 at both compared to control cardiac monolayers. Additionally, LNVC displayed slower conduction velocity. Together, this could be indicative reduced electrophysiological function in LVNC monolayer compared to healthy controls.

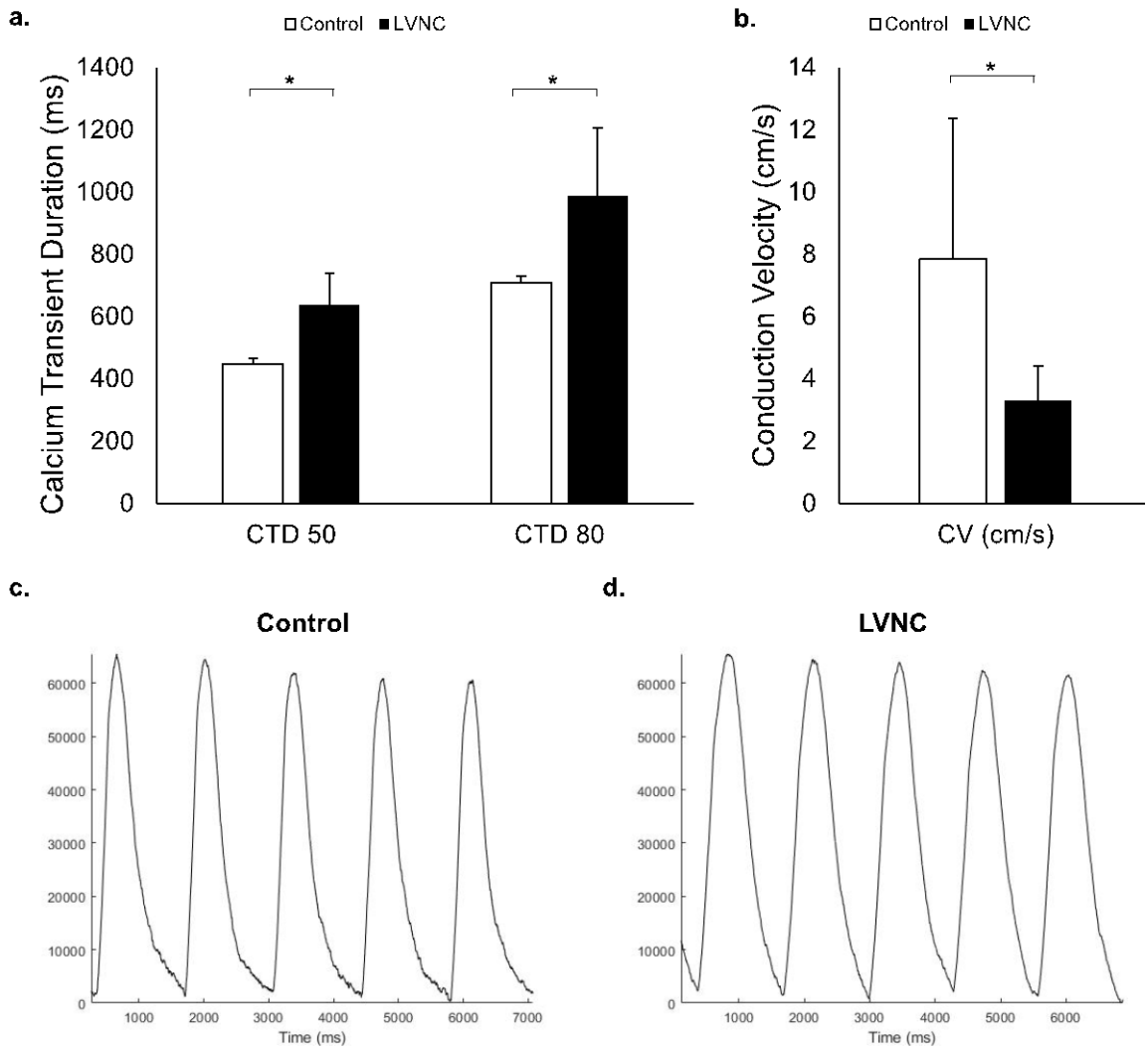

Figure 6.3 LVNC cardiac monolayers displayed slower calcium handling compared to control.

(a) The calcium transient duration at 50 and 80% repolarization was longer for LVNC cardiac monolayers compared to control at 638 and 449 ms for 50% repolarization and 999 and 708 ms at 80% repolarization. The conduction velocity of calcium waves was significantly faster in control cardiac monolayers compared to LVNC cardiac monolayers. Representative traces display differences in peak width for (c) control and (d) LVNC cardiac monolayer calcium wave propagations. ($n > 5$ locations per monolayer per group, Mean ± S.D. , ANOVA, * for $p < 0.05$)

LVNC patient derived hiPSCs successfully differentiated in hydrogel microspheres.

To study the development of LNVC in 3D, LVNC hiPSCs were encapsulated in a hydrogel biomaterials using a modified water and oil emulsion technique (Seeto et al. 2019). Resulting hydrogel microspheres displayed tight control over both size and shape (Figure 6.4b, c) on Day -2 both within and between batches. Similar size and shape on Day -2 are critical for comparing compaction in long term culture. LVNC hydrogel microspheres remodeled their microenvironment throughout differentiation becoming darker and denser over time (Figure 6.4a). Interestingly, LVNC hiPSCs differentiated much better in hydrogel microspheres (77%) using protocol 4 compared to LVNC cardiac monolayers (21%), indicating that hydrogel biomaterial may have served a protective role in the presence of increased CHIR concentration. Further studies need to be performed to directly compare the four differentiation protocols in 2D and 3D.

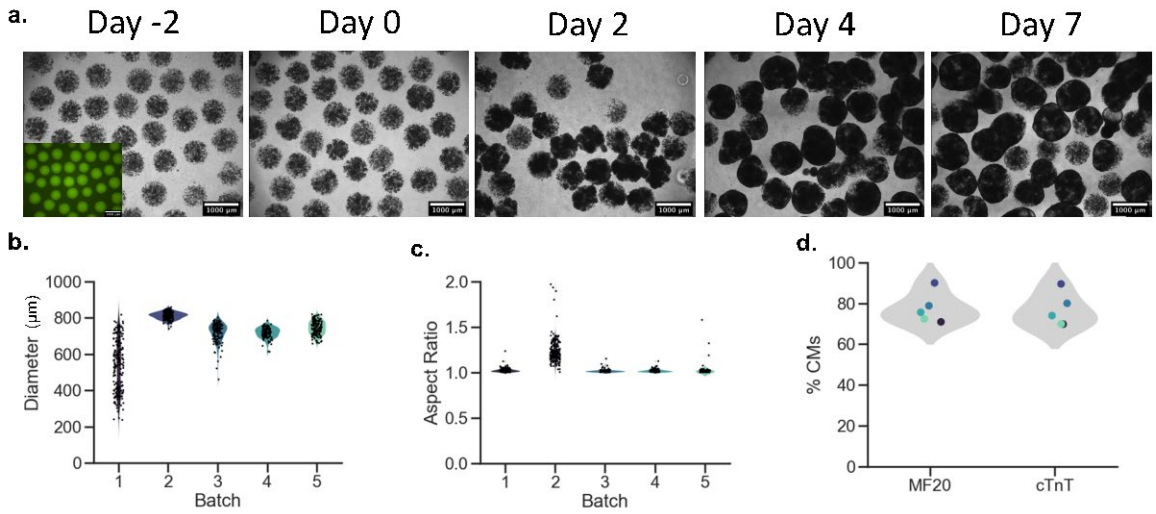

Figure 6.4 LVNC patient derived hiPSCs were encapsulated and differentiated to form LVNC cardiac microspheres.

(a) LVNC patient derived hiPSCs were encapsulated in a hydrogel biomaterial containing photoinitiator Eosin Y (green) via free radical polymerization. HiPSCs were monitored with phase contrast imaging throughout differentiation. (b, c) The microfluidic encapsulation platform produces LVNC patient derived hiPSC microspheres with uniform size and shape both within and between batches. Cardiac differentiation resulted in LVNC cardiac microspheres with 77.5% cardiomyocytes (77% for MF20 and 78% for cTnT).

LVNC cardiac microspheres show reduced contractile properties.

To compare cardiac contractility over time, videos were recorded throughout long term culture and analyzed using an opens source MATLAB code (Huebsch et al. 2015a). By day 68, LVNC cardiac microspheres contracted less frequently and at a slower velocity compared to control (Figure 6.5 a, c). Additionally, on days 15 and 30, LVNC cardiac microspheres showed a prolonged time interval between contraction and relaxation indicating a delay in repolarization (Figure 6.5b). Taken together, these assays

show decreased contractility in LVNC, which aligns with the decreased ejection fraction seen in LVNC patients.

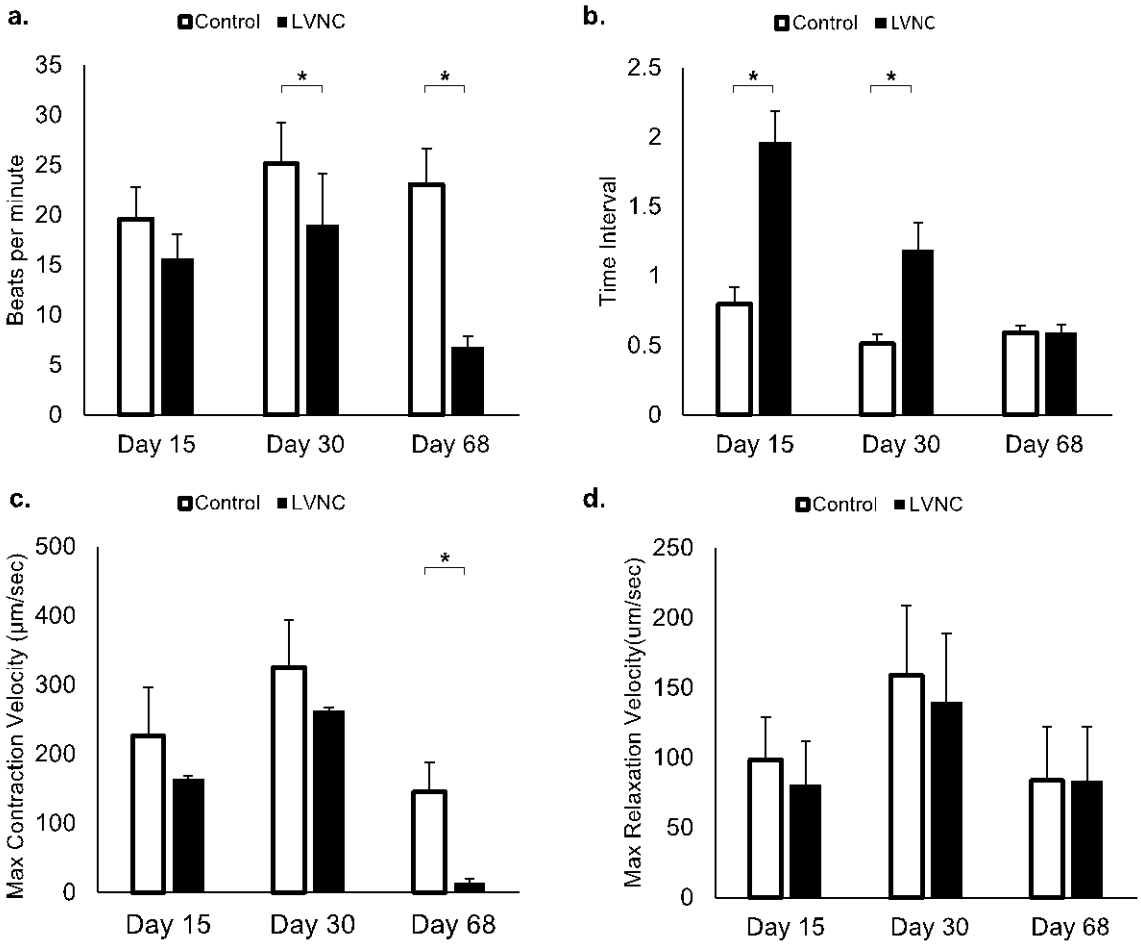

Figure 6.5 LVNC cardiac microspheres contract less frequently over time.

(a) Compared to control, LVNC cardiac microspheres decreased contraction frequency over time from 15 bpm on day 15 to 9.2 bpm on day 68. (b) On Day 15 and 30, LVNC cardiac microspheres showed an increased time interval between contraction and relaxation indicating a delay in repolarization. (c) LVNC cardiac microspheres contracted at a slower velocity compared to control which increased from day 15 to day 30 and then decreased by day 68. (d) Relaxation

velocity was similar in both groups at each time point. ($n > 8$ spheres per group per timepoint, Mean ± S.D. , ANOVA, * for $p < 0.05$)

6.4 Discussion and Future Work

Kodo *et al*. demonstrated the ability to differentiate LVNC patient derived hiPSCs in a 2D cardiac monolayer for single cell and gene expression assays (Kodo et al. 2016a). Previous studies of LVNC disease caused by Tbx20 mutations were performed using hiPSC derived cardiac monolayers and mouse models. LVNC monolayers show decreased differentiation efficiency and developmental cardiac transcription factors compared to control monolayers. Transgenic mouse models showed over expression of transforming growth factor –beta which resulted in decreased proliferation of CMs and noncompaction in the left ventricle (Kodo et al. 2016a).

It is challenging to study LVNC in a cardiac monolayer because LVNC affects several layers of cells that make up the 3D left ventricle. Compaction cannot be measured in a single layer of cells. Additionally, mouse cardiac development happens significantly faster than human cardiac development. The genes controlling development and cardiac electrophysiology are different between species (Krishnan et al. 2014). To further improve this study, our model seeks to eliminate the limitations of monolayer differentiation and animal model studies. Our microsphere differentiation platform produces LVNC hydrogel microspheres that can serve as a more representative portrayal of cardiac development and disease progression by providing a 3D microenvironment. In

our model, we aimed to recapitulate the 3D human disease environment and gained insight into how genetic mutations affect downstream development.

In this proof-of-concept study, we demonstrated the ability to differentiate LVNC hiPSCs in two different platforms, 2D cardiac monolayers and 3D cardiac microspheres. Differentiation of cardiac monolayers was performed using four differentiation protocols, in order to determine a single protocol that exhibits uniform differentiation efficiency in both cells lines and can be extended into 3D microsphere differentiations. Interestingly, the LVNC patient derived hiPSCs behave differently in 2D and 3D differentiations, where lower CHIR concentration for extended time (protocol 1) results in a higher percentage of cardiomyocytes in 2D compared to higher CHIR concentration for shorter time (protocol 4) in 3D. One caveat to this that cardiomyocyte populations were based on single live cells which does not take in to account the ratio of CMs to starting hiPSCs or cell that died throughout differentiation and were removed curing media changes.

Assays used to characterize CM functionality including optical mapping and contraction analysis were performed at late timepoints. Taking the 2D and 3D results together, we saw decreased cardiac functionality in LVNC cardiac monolayers and microspheres compared to control. These results were expected since LVNC patients often have decreased ejection fraction and electrical function as a result of noncompaction.

Future studies will be performed to further characterize LVNC cardiac microspheres and elucidate the genetic cascade that ultimately results in noncompaction including mechanical properties, gene expression, and extracellular matrix composition.

To analyze changes in mechanical properties in conjunction with gene expression and extracellular matrix composition throughout differentiation, parallel plate compression testing, RT-qPCR, and whole tissue proteomics will be performed at specific time points in culture to determine which genes play a role in compaction. Experiments will be performed on days 0, 2, 4, 7, 21, 35, and 70 based on the known genetic fluctuations that occur throughout differentiation to mimic *in utero* cardiac development. Tbx20 has been shown to interact directly with Nkx2.5, Gata4, Gata5, and Tbx5 (Kirk et al. 2007). Therefore, these genes will be used in RT-qPCR experiments to see how the Tbx20 mutation affects other developmental cardiac genes.

6.5 Conclusions

Overall, this proof-of-concept study demonstrated our ability to directly differentiate LVNC patient-derived hiPSCs in a 3D hydrogel microenvironment and detect difference in control and LVNC cardiomyocytes over time. Establishing this platform not only gave insights on LVNC but also provided knowledge about differences in 2D and 3D preclinical disease models. This platform shows potential to be implemented for studying human cardiac development and the role developmental cardiac genes play in developmental cardiac events, like ventricular compaction.

Chapter 7: Summary and Conclusions

This research focused on enhancing a previously established 3D direct differentiation platform and applying it to study CHD manifestation and progression from both environmental and genetic causes. The findings from these studies can be utilized to produce maturing engineered cardiac tissue for preclinical testing and can potentially be expanded to study other CHDs. The first part of this dissertation demonstrated the robust nature of our direct differentiation approach, as we are able to successfully encapsulate and differentiate hiPSCs in multiple biomaterials, including PEG-fibrinogen and gelatin methacryloyl, to produce functional 3D engineered cardiac tissue. Additionally, we are able to manipulate initial hiPSC encapsulation geometry to promote cardiomyocyte maturation without the use of external stimuli. The second part of this dissertation showed the ability of our 3D direct differentiation approach to be deployed to study thalidomide-induced defects and left ventricular noncompaction *in vitro*.

The first project established gelatin methacryloyl as a suitable biomaterial for hiPSC encapsulation and direct differentiation to produce GelMA human engineered cardiac tissues (GEhECTs). Conventional methods for producing ECTs require the assembly of pre-differentiated CMs, resulting in multiple cell-handling steps and disruption of important cell-cell junctions formed throughout differentiation. Producing ECTs directly from hiPSCs avoids multiple cell-handling steps and enables researchers to study cardiac development in 3D. Previously, our lab group demonstrated the ability to encapsulate hiPSCs in PEG-fibrinogen and directly differentiate them to form 3D human developing engineered cardiac tissues (Kerscher, Turnbull, et al. 2016). In this first study, we determined if this direct differentiation approach could be expanded to a different

hybrid biomaterial, gelatin methacryloyl (GelMA). GelMA is widely used in tissue engineering applications and fits many criteria required for use in cardiac tissue engineering. We demonstrated the ability to produce GelMA with a low degree of acrylation that could be crosslinked with visible light to form a soft hydrogel that was suitable for maintaining hiPSC viability and supporting cardiac differentiation. GEhECTs began spontaneously contracting on day 8 and increase contraction frequency and velocity over time. GEhECTs showed appropriate temporal changes in gene expression and responded appropriately to external pacing and drug treatment. Overall, the findings of this study demonstrated that GelMA is a suitable biomaterial for 3D direct cardiac differentiation and has the potential to be used in future bioprinting and drug testing applications.

In the second project, the primary objective was to investigate if initial encapsulation geometry impacted resulting cardiac tissue functionality. In previous studies, we utilized a microisland encapsulation geometry (Kerscher, Turnbull, et al. 2016). While this produced functional 3D engineered cardiac tissues with adult-like ultrastructural features, these tissues lacked homogeneity, as dense rings formed around the tissue edge. In this study, we utilized new PDMS molds with microisland, square, and rectangular openings to influence the initial encapsulation geometry. HiPSCs survived the encapsulation process and grew in their PEG-fibrinogen microenvironment. All geometries underwent successful cardiac differentiation and showed similar gene expression over culture time. Compared to microisland and square tissues, rectangular tissues showed more anisotropic contraction along the transverse axis. Additionally, square and rectangular tissues displayed a higher degree of myofibrillar organization and

sarcomere alignment compared to microislands, indicating a higher level of maturity. Overall, these findings suggested that initial encapsulation geometry impacts engineered cardiac tissue functionality, and that rectangular tissues more closely mimic the native adult myocardium.

Our 3D direct differentiation approach enables our group to study cardiac development and CHD mechanisms throughout differentiation, which is not possible with the use of pre-differentiated CMs. Using this platform, we can investigate the cumulative effects of both environmental exposures and genetic mutations throughout cardiac development.

In the third project, we investigated if our 3D direct differentiation model could detect thalidomide-induced defects and be used as a model for preclinical drug testing. The morning sickness drug, thalidomide, became notorious in the 1960s after it safely passed preclinical animal trials but was pulled off the market after it was determined to cause birth defects when prescribed to pregnant women. This is just one example of a drug that behaves differently in animals compared to humans. In this study, we encapsulated hiPSCs in PEG-fibrinogen and cultured these hydrogels for three days prior to cardiac differentiation. Thalidomide was administered on Day 1 of differentiation at 0, 10, and 70 μM and added with each subsequent media change throughout long term culture. Using this model, we identified thalidomide-induced changes in differentiation efficiency, ECM composition, mitochondria distribution, and cardiac electrophysiology. Overall, these findings demonstrated the ability of our 3D direct differentiation model to be used to detect drug-induced changes throughout cardiac development and the potential for it to be utilized in the future for preclinical testing.

The final project focused on producing a CHD model using patient-derived stem cells from a patient with a known mutation and disease phenotype. With the development of hiPSCs in 2006, researchers are now able to reprogram patient somatic cells to produce hiPSC lines that maintain their disease-causing genetic mutations (Takahashi and Yamanaka 2006). This discovery led to a paradigm shift in disease modeling, as researchers are now able to directly compare *in vitro* discoveries with known *in vivo* patient outcomes. This final study investigated if our 3D direct differentiation approach could be used with left ventricular noncompaction (LVNC) patient-derived hiPSCs to produce an *in vitro* 3D LVNC model. LVNC patient-derived hiPSCs were differentiated as 2D monolayers and as 3D PEG-fibrinogen microspheres, produced using a modified water and oil emulsion technique. HiPSCs were differentiated using a variety of differentiation protocols, CHIR concentrations, and small molecule time scales. 3D LVNC microspheres had consistent CM populations (70-80%), which was not seen in previous 2D experiments. Additionally, LVNC showed slower contraction frequency and velocity over time compared to control, which is indicative of the LVNC disease phenotype. Overall, this proof-of-concept study showed that the 3D direct differentiation approach is capable of capturing disease phenotype *in vitro* and has the potential to be used with other patient-derived hiPSC lines.

Taken together, these studies demonstrate the value of directly differentiating hiPSCs in 3D hydrogel biomaterials to study cardiac development *in vitro*. Using our robust single cell-handling step approach, we are able to 1) produce engineered cardiac tissues using multiple hydrogel biomaterials, 2) influence tissue maturity by changing encapsulation geometry, and apply this platform to study 3) drug-induced and 4) genetic

CHD *in vitro*. The findings of this dissertation lay the foundation for future drug testing and disease modeling to further our understanding of the complexities of cardiac development.

References

Adler, S., C. Pellizzer, L. Hareng, T. Hartung, and S. Bremer. 2008. "First steps in establishing a developmental toxicity test method based on human embryonic stem cells." *Toxicol In Vitro* 22 (1): 200-11. https://doi.org/10.1016/j.tiv.2007.07.013. http://www.ncbi.nlm.nih.gov/pubmed/17961973.

Ahadian, S., R. Civitarese, D. Bannerman, M. H. Mohammadi, R. Lu, E. Wang, L. Davenport-Huyer, B. Lai, B. Zhang, Y. Zhao, S. Mandla, A. Korolj, and M. Radisic. 2018. "Organ-On-A-Chip Platforms: A Convergence of Advanced Materials, Cells, and Microscale Technologies." *Adv Healthc Mater* 7 (2). https://doi.org/10.1002/adhm.201700506. https://www.ncbi.nlm.nih.gov/pubmed/29034591.

Alcantar, N. A., E. S. Aydil, and J. N. Israelachvili. 2000. "Polyethylene glycol-coated biocompatible surfaces." *J Biomed Mater Res* 51 (3): 343-51. https://www.ncbi.nlm.nih.gov/pubmed/10880075.

Almany, L., and D. Seliktar. 2005a. "Biosynthetic hydrogel scaffolds made from fibrinogen and polyethylene glycol for 3D cell cultures." *Biomaterials* 26 (15): 2467-2477. https://doi.org/10.1016/j.biomaterials.2004.06.047. <Go to ISI>://WOS:000226698400029.

---. 2005b. "Biosynthetic hydrogel scaffolds made from fibrinogen and polyethylene glycol for 3D cell cultures." *Biomaterials* 26 (15): 2467-77. https://doi.org/10.1016/j.biomaterials.2004.06.047. https://www.ncbi.nlm.nih.gov/pubmed/15585249.

Arbustini, E., F. Weidemann, and J. L. Hall. 2014. "Left Ventricular Noncompaction A Distinct Cardiomyopathy or a Trait Shared by Different Cardiac Diseases?" *Journal of the American College of Cardiology* 64 (17): 1840-1850. https://doi.org/10.1016/j.jacc.2014.08.030. <Go to ISI>://WOS:000344616600013.

Bao, Z. Z., B. G. Bruneau, J. G. Seidman, C. E. Seidman, and C. L. Cepko. 1999. "Regulation of chamber-specific gene expression in the developing heart by Irx4." *Science* 283 (5405): 1161-1164. https://doi.org/DOI 10.1126/science.283.5405.1161. <Go to ISI>://WOS:000078738400050.

Bartram, U., D. G. Molin, L. J. Wisse, A. Mohamad, L. P. Sanford, T. Doetschman, C. P. Speer, R. E. Poelmann, and A. C. Gittenberger-de Groot. 2001. "Double-outlet right ventricle and overriding tricuspid valve reflect disturbances of looping, myocardialization, endocardial cushion differentiation, and apoptosis in TGF-beta(2)-knockout mice." *Circulation* 103 (22): 2745-52. https://www.ncbi.nlm.nih.gov/pubmed/11390347.

Basso, C., P. R. Fox, K. M. Meurs, J. A. Towbin, A. W. Spier, F. Calabrese, B. J. Maron, and G. Thiene. 2004. "Arrhythmogenic right ventricular cardiomyopathy causing sudden cardiac death in boxer dogs: a new animal model of human disease." *Circulation* 109 (9): 1180-5. https://doi.org/10.1161/01.CIR.0000118494.07530.65. https://www.ncbi.nlm.nih.gov/pubmed/14993138.

Basson, C. T., D. R. Bachinsky, R. C. Lin, T. Levi, J. A. Elkins, J. Soults, D. Grayzel, E. Kroumpouzou, T. A. Traill, J. Leblanc-Straceski, B. Renault, R. Kucherlapati, J. G. Seidman, and C. E. Seidman. 1997. "Mutations in human TBX5 [corrected] cause limb and cardiac malformation in Holt-Oram syndrome." *Nat Genet* 15 (1): 30-5. https://doi.org/10.1038/ng0197-30. https://www.ncbi.nlm.nih.gov/pubmed/8988165.

Batalov, I., and A. W. Feinberg. 2015. "Differentiation of Cardiomyocytes from Human Pluripotent Stem Cells Using Monolayer Culture." *Biomark Insights* 10 (Suppl 1): 71-6. https://doi.org/10.4137/bmi.s20050.

Belair, D. G., G. Lu, L. E. Waller, J. A. Gustin, N. D. Collins, and K. L. Kolaja. 2020. "Thalidomide Inhibits Human iPSC Mesendoderm Differentiation by Modulating CRBN-dependent Degradation of SALL4." *Sci Rep* 10 (1): 2864. https://doi.org/10.1038/s41598-020-59542-x. https://www.ncbi.nlm.nih.gov/pubmed/32071327.

Benjamin, E. J., M. J. Blaha, S. E. Chiuve, M. Cushman, S. R. Das, R. Deo, S. D. de Ferranti, J. Floyd, M. Fornage, C. Gillespie, C. R. Isasi, M. C. Jimenez, L. C. Jordan, S. E. Judd, D. Lackland, J. H. Lichtman, L. Lisabeth, S. Liu, C. T. Longenecker, R. H. Mackey, K. Matsushita, D. Mozaffarian, M. E. Mussolino, K. Nasir, R. W. Neumar, L. Palaniappan, D. K. Pandey, R. R. Thiagarajan, M. J. Reeves, M. Ritchey, C. J. Rodriguez, G. A. Roth, W. D. Rosamond, C. Sasson, A. Towfighi, C. W. Tsao, M. B. Turner, S. S. Virani, J. H. Voeks, J. Z. Willey, J. T. Wilkins, J. H. Wu, H. M. Alger, S. S. Wong, P. Muntner, Committee American Heart Association Statistics, and Subcommittee Stroke Statistics. 2017. "Heart Disease and Stroke Statistics-2017 Update: A Report From the American Heart Association." *Circulation* 135 (10): e146-e603. https://doi.org/10.1161/CIR.0000000000000485. https://www.ncbi.nlm.nih.gov/pubmed/28122885.

Bergmann, O., R. D. Bhardwaj, S. Bernard, S. Zdunek, F. Barnabe-Heider, S. Walsh, J. Zupicich, K. Alkass, B. A. Buchholz, H. Druid, S. Jovinge, and J. Frisen. 2009. "Evidence for cardiomyocyte renewal in humans." *Science* 324 (5923): 98-102. https://doi.org/10.1126/science.1164680. https://www.ncbi.nlm.nih.gov/pubmed/19342590.

Bernstein, Harold S. 2011. *Tissue engineering in regenerative medicine*. In *Stem cell biology and regenerative medicine*. New York: Humana Press,.

Bers, D. M. 2001. *Excitation-contraction coupling and cardiac contractile force*. 2nd ed. Vol. 237*Developments in cardiovascular medicine*. Dordrecht ; Boston: Kluwer Academic Publishers.

Bertassoni, L. E., M. Cecconi, V. Manoharan, M. Nikkhah, J. Hjortnaes, A. L. Cristino, G. Barabaschi, D. Demarchi, M. R. Dokmeci, Y. Yang, and A. Khademhosseini. 2014. "Hydrogel bioprinted microchannel networks for vascularization of tissue engineering constructs." *Lab Chip* 14 (13): 2202-11. https://doi.org/10.1039/c4lc00030g. https://www.ncbi.nlm.nih.gov/pubmed/24860845.

Bian, W., N. Badie, H. D. th Himel, and N. Bursac. 2014. "Robust T-tubulation and maturation of cardiomyocytes using tissue-engineered epicardial mimetics."

Biomaterials 35 (12): 3819-28. https://doi.org/10.1016/j.biomaterials.2014.01.045. https://www.ncbi.nlm.nih.gov/pubmed/24508078.

Birket, M. J., M. C. Ribeiro, G. Kosmidis, D. Ward, A. R. Leitoguinho, V. van de Pol, C. Dambrot, H. D. Devalla, R. P. Davis, P. G. Mastroberardino, D. E. Atsma, R. Passier, and C. L. Mummery. 2015. "Contractile Defect Caused by Mutation in MYBPC3 Revealed under Conditions Optimized for Human PSC-Cardiomyocyte Function." *Cell Rep* 13 (4): 733-745. https://doi.org/10.1016/j.celrep.2015.09.025. https://www.ncbi.nlm.nih.gov/pubmed/26489474.

Black, L. D., J. D. Meyers, J. S. Weinbaum, Y. A. Shvelidze, and R. T. Tranquillo. 2009. "Cell-Induced Alignment Augments Twitch Force in Fibrin Gel-Based Engineered Myocardium via Gap Junction Modification." *Tissue Engineering Part A* 15 (10): 3099-3108. https://doi.org/10.1089/ten.tea.2008.0502. <Go to ISI>://WOS:000270553200030.

Bootle-Wilbraham, C. A., S. Tazzyman, W. D. Thompson, C. M. Stirk, and C. E. Lewis. 2001. "Fibrin fragment E stimulates the proliferation, migration and differentiation of human microvascular endothelial cells in vitro." *Angiogenesis* 4 (4): 269-75. https://www.ncbi.nlm.nih.gov/pubmed/12197472.

Bowers, S. L., I. Banerjee, and T. A. Baudino. 2010. "The extracellular matrix: at the center of it all." *J Mol Cell Cardiol* 48 (3): 474-82. https://doi.org/10.1016/j.yjmcc.2009.08.024. https://www.ncbi.nlm.nih.gov/pubmed/19729019.

Brown, R. D., S. K. Ambler, M. D. Mitchell, and C. S. Long. 2005. "The cardiac fibroblast: Therapeutic target in myocardial remodeling and failure." *Annual Review of Pharmacology and Toxicology* 45: 657-687. https://doi.org/10.1146/annurev.pharmtox.45.120403.095802. <Go to ISI>://WOS:000227504000027.

Bruneau, B. G. 2008. "The developmental genetics of congenital heart disease." *Nature* 451 (7181): 943-8. https://doi.org/10.1038/nature06801. https://www.ncbi.nlm.nih.gov/pubmed/18288184.

Brunner, M., X. W. Peng, G. X. Liu, X. Q. Ren, O. Ziv, B. R. Choi, R. Mathur, M. Hajjiri, K. E. Odening, E. Steinberg, E. J. Folco, E. Pringa, J. Centracchio, R. R. Macharzina, T. Donahay, L. Schofield, N. Rana, M. Kirk, G. F. Mitchell, A. Poppas, M. Zehender, and G. Koren. 2008. "Mechanisms of cardiac arrhythmias and sudden death in transgenic rabbits with long QT syndrome." *Journal of Clinical Investigation* 118 (6): 2246-2259. https://doi.org/10.1172/Jci33578. <Go to ISI>://WOS:000256445100028.

Buckingham, M., S. Meilhac, and S. Zaffran. 2005. "Building the mammalian heart from two sources of myocardial cells." *Nat Rev Genet* 6 (11): 826-35. https://doi.org/10.1038/nrg1710. https://www.ncbi.nlm.nih.gov/pubmed/16304598.

Burridge, P. W., E. Matsa, P. Shukla, Z. C. Lin, J. M. Churko, A. D. Ebert, F. Lan, S. Diecke, B. Huber, N. M. Mordwinkin, J. R. Plews, O. J. Abilez, B. Cui, J. D. Gold, and J. C. Wu. 2014. "Chemically defined generation of human cardiomyocytes." *Nat Methods* 11 (8): 855-60.

https://doi.org/10.1038/nmeth.2999.
https://www.ncbi.nlm.nih.gov/pubmed/24930130.

Burridge, P. W., S. Thompson, M. A. Millrod, S. Weinberg, X. Yuan, A. Peters, V. Mahairaki, V. E. Koliatsos, L. Tung, and E. T. Zambidis. 2011. "A universal system for highly efficient cardiac differentiation of human induced pluripotent stem cells that eliminates interline variability." *PLoS One* 6 (4): e18293. https://doi.org/10.1371/journal.pone.0018293.
https://www.ncbi.nlm.nih.gov/pubmed/21494607.

Captur, G., and P. Nihoyannopoulos. 2010. "Left ventricular non-compaction: genetic heterogeneity, diagnosis and clinical course." *Int J Cardiol* 140 (2): 145-53. https://doi.org/10.1016/j.ijcard.2009.07.003.
https://www.ncbi.nlm.nih.gov/pubmed/19664830.

Carvajal-Vergara, X., A. Sevilla, S. L. D'Souza, Y. S. Ang, C. Schaniel, D. F. Lee, L. Yang, A. D. Kaplan, E. D. Adler, R. Rozov, Y. Ge, N. Cohen, L. J. Edelmann, B. Chang, A. Waghray, J. Su, S. Pardo, K. D. Lichtenbelt, M. Tartaglia, B. D. Gelb, and I. R. Lemischka. 2010. "Patient-specific induced pluripotent stem-cell-derived models of LEOPARD syndrome." *Nature* 465 (7299): 808-12. https://doi.org/10.1038/nature09005.
https://www.ncbi.nlm.nih.gov/pubmed/20535210.

Caspi, O., I. Itzhaki, I. Kehat, A. Gepstein, G. Arbel, I. Huber, J. Satin, and L. Gepstein. 2009. "In vitro electrophysiological drug testing using human embryonic stem cell derived cardiomyocytes." *Stem Cells Dev* 18 (1): 161-72. https://doi.org/10.1089/scd.2007.0280.
http://www.ncbi.nlm.nih.gov/pubmed/18510453.

Chen, H. S., C. Kim, and M. Mercola. 2009. "Electrophysiological challenges of cell-based myocardial repair." *Circulation* 120 (24): 2496-508. https://doi.org/10.1161/CIRCULATIONAHA.107.751412.
https://www.ncbi.nlm.nih.gov/pubmed/20008740.

Chen, Ming, Yong-Qing Lin, Shuang-Lun Xie, Hong-Fu Wu, and Jing-Feng Wang. 2011. "Enrichment of cardiac differentiation of mouse embryonic stem cells by optimizing the hanging drop method." *Biotechnology Letters* 33 (4): 853-858. https://doi.org/10.1007/s10529-010-0494-3. https://doi.org/10.1007/s10529-010-0494-3.

Chen, Q. Z., S. E. Harding, N. N. Ali, A. R. Lyon, and A. R. Boccaccini. 2008. "Biomaterials in cardiac tissue engineering: Ten years of research survey." *Materials Science & Engineering R-Reports* 59 (1-6): 1-37. https://doi.org/10.1016/j.mser.2007.08.001. <Go to ISI>://WOS:000254692100001.

Chen, Y. C., R. Z. Lin, H. Qi, Y. Yang, H. Bae, J. M. Melero-Martin, and A. Khademhosseini. 2012. "Functional Human Vascular Network Generated in Photocrosslinkable Gelatin Methacrylate Hydrogels." *Adv Funct Mater* 22 (10): 2027-2039. https://doi.org/10.1002/adfm.201101662.
https://www.ncbi.nlm.nih.gov/pubmed/22907987.

Ching, Y. H., T. K. Ghosh, S. J. Cross, E. A. Packham, L. Honeyman, S. Loughna, T. E. Robinson, A. M. Dearlove, G. Ribas, A. J. Bonser, N. R. Thomas, A. J. Scotter, L.

S. Caves, G. P. Tyrrell, R. A. Newbury-Ecob, A. Munnich, D. Bonnet, and J. D. Brook. 2005. "Mutation in myosin heavy chain 6 causes atrial septal defect." *Nat Genet* 37 (4): 423-8. https://doi.org/10.1038/ng1526. https://www.ncbi.nlm.nih.gov/pubmed/15735645.

Choe, J. Y., H. J. Jung, K. Y. Park, Y. S. Kum, G. G. Song, D. S. Hyun, S. H. Park, and S. K. Kim. 2010. "Anti-fibrotic effect of thalidomide through inhibiting TGF-beta-induced ERK1/2 pathways in bleomycin-induced lung fibrosis in mice." *Inflamm Res* 59 (3): 177-88. https://doi.org/10.1007/s00011-009-0084-9. https://www.ncbi.nlm.nih.gov/pubmed/19757088.

Chung, C. Y., H. Bien, and E. Entcheva. 2007. "The role of cardiac tissue alignment in modulating electrical function." *J Cardiovasc Electrophysiol* 18 (12): 1323-9. https://doi.org/10.1111/j.1540-8167.2007.00959.x. https://www.ncbi.nlm.nih.gov/pubmed/17916158.

Dahlmann, J., G. Awad, C. Dolny, S. Weinert, K. Richter, K. D. Fischer, T. Munsch, V. Leßmann, M. Volleth, M. Zenker, Y. Chen, C. Merkl, A. Schnieke, H. Baraki, I. Kutschka, and G. Auid-Orcid Kensah. "Generation of functional cardiomyocytes from rat embryonic and induced pluripotent stem cells using feeder-free expansion and differentiation in suspension culture." (1932-6203 (Electronic)).

Dambrot, C., R. Passier, D. Atsma, and C. L. Mummery. 2011a. "Cardiomyocyte differentiation of pluripotent stem cells and their use as cardiac disease models." *Biochemical Journal* 434: 25-35. https://doi.org/10.1042/Bj20101707. <Go to ISI>://WOS:000287461000003.

---. 2011b. "Cardiomyocyte differentiation of pluripotent stem cells and their use as cardiac disease models." *Biochem J* 434 (1): 25-35. https://doi.org/10.1042/BJ20101707. https://www.ncbi.nlm.nih.gov/pubmed/21269276.

Davis, R. P., S. Casini, C. W. van den Berg, M. Hoekstra, C. A. Remme, C. Dambrot, D. Salvatori, D. W. Oostwaard, A. A. Wilde, C. R. Bezzina, A. O. Verkerk, C. Freund, and C. L. Mummery. 2012. "Cardiomyocytes derived from pluripotent stem cells recapitulate electrophysiological characteristics of an overlap syndrome of cardiac sodium channel disease." *Circulation* 125 (25): 3079-91. https://doi.org/10.1161/CIRCULATIONAHA.111.066092. https://www.ncbi.nlm.nih.gov/pubmed/22647976.

Davis, R. P., S. Casini, C. W. van den Berg, M. Hoekstra, C. A. Remme, C. Dambrot, D. Salvatori, D. Ward-van Oostwaard, A. A. M. Wilde, C. R. Bezzina, A. O. Verkerk, C. Freund, and C. L. Mummery. 2012. "Cardiomyocytes Derived From Pluripotent Stem Cells Recapitulate Electrophysiological Characteristics of an Overlap Syndrome of Cardiac Sodium Channel Disease." *Circulation* 125 (25): 3079-+. https://doi.org/10.1161/Circulationaha.111.066092. <Go to ISI>://WOS:000306977000015.

Davis, R. P., C. W. van den Berg, S. Casini, S. R. Braam, and C. L. Mummery. 2011. "Pluripotent stem cell models of cardiac disease and their implication for drug discovery and development." *Trends in Molecular Medicine* 17 (9): 475-484. https://doi.org/10.1016/j.molmed.2011.05.001. <Go to ISI>://WOS:000294941000002.

Dean, E. W., B. Udelsman, and C. K. Breuer. 2012. "Current advances in the translation of vascular tissue engineering to the treatment of pediatric congenital heart disease." *Yale J Biol Med* 85 (2): 229-38. http://www.ncbi.nlm.nih.gov/pubmed/22737051.

DeLong, S. A., J. J. Moon, and J. L. West. 2005. "Covalently immobilized gradients of bFGF on hydrogel scaffolds for directed cell migration." *Biomaterials* 26 (16): 3227-34. https://doi.org/10.1016/j.biomaterials.2004.09.021. https://www.ncbi.nlm.nih.gov/pubmed/15603817.

Denning, C., Helen Allegrucci C Fau - Priddle, Maria D. Priddle H Fau - Barbadillo-Muñoz, David Barbadillo-Muñoz Md Fau - Anderson, Tim Anderson D Fau - Self, Nigel M. Self T Fau - Smith, C. Tony Smith Nm Fau - Parkin, Lorraine E. Parkin Ct Fau - Young, and L. E. Young. "Common culture conditions for maintenance and cardiomyocyte differentiation of the human embryonic stem cell lines, BG01 and HUES-7." (0214-6282 (Print)).

Dikovsky, D., H. Bianco-Peled, and D. Seliktar. 2006. "The effect of structural alterations of PEG-fibrinogen hydrogel scaffolds on 3-D cellular morphology and cellular migration." *Biomaterials* 27 (8): 1496-506. https://doi.org/10.1016/j.biomaterials.2005.09.038. http://www.ncbi.nlm.nih.gov/pubmed/16243393.

Dolk, H., M. Loane, E. Garne, and Group European Surveillance of Congenital Anomalies Working. 2011. "Congenital heart defects in Europe: prevalence and perinatal mortality, 2000 to 2005." *Circulation* 123 (8): 841-9. https://doi.org/10.1161/CIRCULATIONAHA.110.958405. https://www.ncbi.nlm.nih.gov/pubmed/21321151.

Donovan, K. A., J. An, R. P. Nowak, J. C. Yuan, E. C. Fink, B. C. Berry, B. L. Ebert, and E. S. Fischer. 2018. "Thalidomide promotes degradation of SALL4, a transcription factor implicated in Duane Radial Ray syndrome." *Elife* 7. https://doi.org/10.7554/eLife.38430. https://www.ncbi.nlm.nih.gov/pubmed/30067223.

Dorn, G. W., 2nd, R. B. Vega, and D. P. Kelly. 2015. "Mitochondrial biogenesis and dynamics in the developing and diseased heart." *Genes Dev* 29 (19): 1981-91. https://doi.org/10.1101/gad.269894.115. http://www.ncbi.nlm.nih.gov/pubmed/26443844.

Duan, B., E. Kapetanovic, L. A. Hockaday, and J. T. Butcher. 2014. "Three-dimensional printed trileaflet valve conduits using biological hydrogels and human valve interstitial cells." *Acta Biomater* 10 (5): 1836-46. https://doi.org/10.1016/j.actbio.2013.12.005. https://www.ncbi.nlm.nih.gov/pubmed/24334142.

Dunn, D. A., A. J. Hodge, and E. A. Lipke. 2014. "Biomimetic materials design for cardiac tissue regeneration." *Wiley Interdiscip Rev Nanomed Nanobiotechnol* 6 (1): 15-39. https://doi.org/10.1002/wnan.1241. http://www.ncbi.nlm.nih.gov/pubmed/24123919.

Durocher, D., F. Charron, R. J. Schwartz, R. Warren, and M. Nemer. 1997. "The cardiac transcription factors Nkx2-5 and GATA-4 are mutual cofactors." *Embo Journal*

16 (18): 5687-5696. https://doi.org/DOI 10.1093/emboj/16.18.5687. <Go to ISI>://WOS:A1997XY11200021.

Eisenbarth, E. 2007. "Biomaterials for tissue engineering." *Advanced Engineering Materials* 9 (12): 1051-1060. https://doi.org/10.1002/adem.200700287. <Go to ISI>://WOS:000252479300007.

Eschenhagen, T., A. Eder, I. Vollert, and A. Hansen. 2012. "Physiological aspects of cardiac tissue engineering." *Am J Physiol Heart Circ Physiol* 303 (2): H133-43. https://doi.org/10.1152/ajpheart.00007.2012. https://www.ncbi.nlm.nih.gov/pubmed/22582087.

Eschenhagen, T., C. Fink, U. Remmers, H. Scholz, J. Wattchow, J. Weil, W. Zimmermann, H. H. Dohmen, H. Schafer, N. Bishopric, T. Wakatsuki, and E. L. Elson. 1997. "Three-dimensional reconstitution of embryonic cardiomyocytes in a collagen matrix: a new heart muscle model system." *FASEB J* 11 (8): 683-94. https://www.ncbi.nlm.nih.gov/pubmed/9240969.

Eschenhagen, T., and W. H. Zimmermann. 2005. "Engineering myocardial tissue." *Circ Res* 97 (12): 1220-31. https://doi.org/10.1161/01.RES.0000196562.73231.7d. https://www.ncbi.nlm.nih.gov/pubmed/16339494.

Fahed, A. C., B. D. Gelb, J. G. Seidman, and C. E. Seidman. 2013. "Genetics of congenital heart disease: the glass half empty." *Circ Res* 112 (4): 707-20. https://doi.org/10.1161/CIRCRESAHA.112.300853. https://www.ncbi.nlm.nih.gov/pubmed/23410880.

Fan, D., A. Takawale, J. Lee, and Z. Kassiri. 2012. "Cardiac fibroblasts, fibrosis and extracellular matrix remodeling in heart disease." *Fibrogenesis Tissue Repair* 5 (1): 15. https://doi.org/10.1186/1755-1536-5-15. https://www.ncbi.nlm.nih.gov/pubmed/22943504.

Faulkner-Jones, A., C. Fyfe, D. J. Cornelissen, J. Gardner, J. King, A. Courtney, and W. M. Shu. 2015. "Bioprinting of human pluripotent stem cells and their directed differentiation into hepatocyte-like cells for the generation of mini-livers in 3D." *Biofabrication* 7 (4). https://doi.org/Artn 044102
10.1088/1758-5090/7/4/044102. <Go to ISI>://WOS:000366896900002.

Feric, N. T., and M. Radisic. 2016. "Maturing human pluripotent stem cell-derived cardiomyocytes in human engineered cardiac tissues." *Adv Drug Deliv Rev* 96: 110-34. https://doi.org/10.1016/j.addr.2015.04.019. https://www.ncbi.nlm.nih.gov/pubmed/25956564.

Finsterer, J., C. Stollberger, and J. A. Towbin. 2017. "Left ventricular noncompaction cardiomyopathy: cardiac, neuromuscular, and genetic factors." *Nat Rev Cardiol* 14 (4): 224-237. https://doi.org/10.1038/nrcardio.2016.207. https://www.ncbi.nlm.nih.gov/pubmed/28079110.

Franco, C. L., J. Price, and J. L. West. 2011. "Development and optimization of a dual-photoinitiator, emulsion-based technique for rapid generation of cell-laden hydrogel microspheres." *Acta Biomater* 7 (9): 3267-76. https://doi.org/10.1016/j.actbio.2011.06.011. https://www.ncbi.nlm.nih.gov/pubmed/21704198.

Frisman, I., D. Seliktar, and H. Bianco-Peled. 2011. "Nanostructuring PEG-fibrinogen hydrogels to control cellular morphogenesis." *Biomaterials* 32 (31): 7839-7846.

https://doi.org/10.1016/j.biomaterials.2011.06.078. <Go to ISI>://WOS:000295072600010.

Fuoco, C., M. L. Salvatori, A. Biondo, K. Shapira-Schweitzer, S. Santoleri, S. Antonini, S. Bernardini, F. S. Tedesco, S. Cannata, D. Seliktar, G. Cossu, and C. Gargioli. 2012. "Injectable polyethylene glycol-fibrinogen hydrogel adjuvant improves survival and differentiation of transplanted mesoangioblasts in acute and chronic skeletal-muscle degeneration." *Skelet Muscle* 2 (1): 24. https://doi.org/10.1186/2044-5040-2-24. https://www.ncbi.nlm.nih.gov/pubmed/23181356.

Gajewski, K., Y. Kim, Y. M. Lee, E. N. Olson, and R. A. Schulz. 1997. "D-mef2 is a target for Tinman activation during Drosophila heart development." *Embo Journal* 16 (3): 515-522. https://doi.org/DOI 10.1093/emboj/16.3.515. <Go to ISI>://WOS:A1997WH23600008.

Galvin, K. M., M. J. Donovan, C. A. Lynch, R. I. Meyer, R. J. Paul, J. N. Lorenz, V. Fairchild-Huntress, K. L. Dixon, J. H. Dunmore, M. A. Gimbrone, D. Falb, and D. Huszar. 2000. "A role for Smad6 in development and homeostasis of the cardiovascular system." *Nature Genetics* 24 (2): 171-174. https://doi.org/Doi 10.1038/72835. <Go to ISI>://WOS:000085104600019.

Gao, C., and Y. Wang. 2014. "Transcriptome complexity in cardiac development and diseases--an expanding universe between genome and phenome." *Circ J* 78 (5): 1038-47. https://doi.org/10.1253/circj.cj-14-0412. https://www.ncbi.nlm.nih.gov/pubmed/24759793.

Gao, X., R. L. Sprando, and J. J. Yourick. 2015. "Thalidomide induced early gene expression perturbations indicative of human embryopathy in mouse embryonic stem cells." *Toxicol Appl Pharmacol* 287 (1): 43-51. https://doi.org/10.1016/j.taap.2015.05.009. http://www.ncbi.nlm.nih.gov/pubmed/26006729.

Garg, V., I. S. Kathiriya, R. Barnes, M. K. Schluterman, I. N. King, C. A. Butler, C. R. Rothrock, R. S. Eapen, K. Hirayama-Yamada, K. Joo, R. Matsuoka, and J. C. Cohen. 2003. "GATA4 mutations cause human congenital heart defects and reveal an interaction with TBX5." *Circulation* 108 (17): 141-142. <Go to ISI>://WOS:000186360600729.

Gati, S., R. Rajani, G. S. Carr-White, and J. B. Chambers. 2014. "Adult left ventricular noncompaction: reappraisal of current diagnostic imaging modalities." *JACC Cardiovasc Imaging* 7 (12): 1266-75. https://doi.org/10.1016/j.jcmg.2014.09.005. https://www.ncbi.nlm.nih.gov/pubmed/25496545.

Ge, D., X. Liu, L. Li, J. Wu, Q. Tu, Y. Shi, and H. Chen. 2009. "Chemical and physical stimuli induce cardiomyocyte differentiation from stem cells." *Biochem Biophys Res Commun* 381 (3): 317-21. https://doi.org/10.1016/j.bbrc.2009.01.173. https://www.ncbi.nlm.nih.gov/pubmed/19309791.

Gelb, B., M. Brueckner, W. Chung, E. Goldmuntz, J. Kaltman, J. P. Kaski, R. Kim, J. Kline, L. Mercer-Rosa, G. Porter, A. Roberts, E. Rosenberg, H. Seiden, C. Seidman, L. Sleeper, S. Tennstedt, J. Kaltman, C. Schramm, K. Burns, G. Pearson, and E. Rosenberg. 2013. "The Congenital Heart Disease Genetic Network Study: rationale, design, and early results." *Circ Res* 112 (4): 698-706.

https://doi.org/10.1161/CIRCRESAHA.111.300297. http://www.ncbi.nlm.nih.gov/pubmed/23410879.

Gelb, B., M. Brueckner, W. Chung, E. Goldmuntz, J. Kaltman, J. P. Kaski, R. Kim, J. Kline, L. Mercer-Rosa, G. Porter, A. Roberts, E. Rosenberg, H. Seiden, C. Seidman, L. Sleeper, S. Tennstedt, J. Kaltman, C. Schramm, K. Burns, G. Pearson, E. Rosenberg, J. Newburger, R. Breitbart, S. Colan, J. Geva, A. Monafo, A. Roberts, J. Stryker, C. Seidman, B. McDonough, J. Seidman, E. Goldmuntz, S. Edman, J. Garbarini, H. Hakonarson, L. Mercer-Rosa, L. Mitchell, J. Tusi, P. White, S. Woyciechowski, W. Chung, D. Warburton, D. Awad, K. Celia, D. Etwaru, J. K. Sond, J. Kline, R. Korsin, A. Lanz, E. Marquez, I. Williams, A. Wilpers, R. Yee, D. Guevara, A. Julian, M. Mac Neal, C. Mintz, I. Peter, R. Sachidanandam, H. Seiden, A. Romano-Adesman, D. Gruber, N. Stellato, M. Brueckner, R. Lifton, N. Cross, J. Deanfield, A. Giardini, K. Flack, G. Porter, E. Taillie, R. Kim, N. Tran, S. Tennstedt, R. Breitbart, K. Dandreo, D. Gallagher, M. M. Lu, L. Sleeper, D. Berlin, C. Beiswanger, R. Lifton, J. Seidman, H. Hakonarson, P. White, M. Italia, W. Chung, C. Seidman, M. Brooks, M. Olive, J. Botkin, J. Dupuis, V. Garg, M. Watson, J. Bristow, T. Evans, C. Kendziorski, E. Mardis, J. Murray, J. Saltz, H. Wong, and Pediatric Cardiac Genomics Consort. 2013. "The Congenital Heart Disease Genetic Network Study Rationale, Design, and Early Results." *Circulation Research* 112 (4): 698-706. https://doi.org/10.1161/Circresaha.111.300297. <Go to ISI>://WOS:000314939400017.

Gelmi, A., A. Cieslar-Pobuda, E. de Muinck, M. Los, M. Rafat, and E. W. Jager. 2016. "Direct Mechanical Stimulation of Stem Cells: A Beating Electromechanically Active Scaffold for Cardiac Tissue Engineering." *Adv Healthc Mater* 5 (12): 1471-80. https://doi.org/10.1002/adhm.201600307. https://www.ncbi.nlm.nih.gov/pubmed/27126086.

Georgakopoulos, D., M. E. Christe, M. Giewat, C. M. Seidman, J. G. Seidman, and D. A. Kass. 1999. "The pathogenesis of familial hypertrophic cardiomyopathy: early and evolving effects from an alpha-cardiac myosin heavy chain missense mutation." *Nat Med* 5 (3): 327-30. https://doi.org/10.1038/6549. https://www.ncbi.nlm.nih.gov/pubmed/10086390.

Gerbin, K. A., and C. E. Murry. 2015. "The winding road to regenerating the human heart." *Cardiovasc Pathol* 24 (3): 133-40. https://doi.org/10.1016/j.carpath.2015.02.004. https://www.ncbi.nlm.nih.gov/pubmed/25795463.

Giacomotto, J., and L. Segalat. 2010. "High-throughput screening and small animal models, where are we?" *Br J Pharmacol* 160 (2): 204-16. https://doi.org/10.1111/j.1476-5381.2010.00725.x. http://www.ncbi.nlm.nih.gov/pubmed/20423335.

Gilboa, S. M., J. L. Salemi, W. N. Nembhard, D. E. Fixler, and A. Correa. 2010. "Mortality Resulting From Congenital Heart Disease Among Children and Adults in the United States, 1999 to 2006." *Circulation* 122 (22): 2254-2263. https://doi.org/10.1161/Circulationaha.110.947002. <Go to ISI>://WOS:000284691700013.

Gomez-Guillen, M. C., B. Gimenez, M. E. Lopez-Caballero, and M. P. Montero. 2011. "Functional and bioactive properties of collagen and gelatin from alternative sources: A review." *Food Hydrocolloids* 25 (8): 1813-1827. https://doi.org/10.1016/j.foodhyd.2011.02.007. <Go to ISI>://WOS:000293580300004.

Goud, A., and S. Padmanabhan. 2016. "A rare form of cardiomyopathy: left ventricular non-compaction cardiomyopathy." *J Community Hosp Intern Med Perspect* 6 (1): 29888. https://doi.org/10.3402/jchimp.v6.29888. https://www.ncbi.nlm.nih.gov/pubmed/26908378.

Gourdie, R. G., B. S. Harris, J. Bond, C. Justus, K. W. Hewett, T. X. O'Brien, R. P. Thompson, and D. Sedmera. 2003. "Development of the cardiac pacemaking and conduction system." *Birth Defects Res C Embryo Today* 69 (1): 46-57. https://doi.org/10.1002/bdrc.10008. https://www.ncbi.nlm.nih.gov/pubmed/12768657.

Grant, A. O. 2009. "Cardiac ion channels." *Circ Arrhythm Electrophysiol* 2 (2): 185-94. https://doi.org/10.1161/CIRCEP.108.789081. https://www.ncbi.nlm.nih.gov/pubmed/19808464.

Gray, Henry, and Warren H. Lewis. 1918. *Anatomy of the human body*. 20th ed. Philadelphia and New York,: Lea & Febiger.

Grimm, F. A., A. Blanchette, J. S. House, K. Ferguson, N. H. Hsieh, C. Dalaijamts, A. A. Wright, B. Anson, F. A. Wright, W. A. Chiu, and I. Rusyn. 2018. "A Human Population-Based Organotypic In Vitro Model for Cardiotoxicity Screening." *Altex-Alternatives to Animal Experimentation* 35 (4): 441-452. https://doi.org/10.14573/altex.1805301. <Go to ISI>://WOS:000450970600003.

Gruber, P. J., S. W. Kubalak, T. Pexieder, H. M. Sucov, R. M. Evans, and K. R. Chien. 1996. "RXR alpha deficiency confers genetic susceptibility for aortic sac, conotruncal, atrioventricular cushion, and ventricular muscle defects in mice." *J Clin Invest* 98 (6): 1332-43. https://doi.org/10.1172/JCI118920. https://www.ncbi.nlm.nih.gov/pubmed/8823298.

Hanna, A., and N. G. Frangogiannis. 2019. "The Role of the TGF-beta Superfamily in Myocardial Infarction." *Front Cardiovasc Med* 6: 140. https://doi.org/10.3389/fcvm.2019.00140. https://www.ncbi.nlm.nih.gov/pubmed/31620450.

Hansen, J. M., and C. Harris. 2004. "A novel hypothesis for thalidomide-induced limb teratogenesis: redox misregulation of the NF-kappaB pathway." *Antioxid Redox Signal* 6 (1): 1-14. https://doi.org/10.1089/152308604771978291. https://www.ncbi.nlm.nih.gov/pubmed/14713331.

Harvey, R. P. 1996. "NK-2 homeobox genes and heart development." *Dev Biol* 178 (2): 203-16. https://doi.org/10.1006/dbio.1996.0212. https://www.ncbi.nlm.nih.gov/pubmed/8812123.

He, W., Shichong Ye L Fau - Li, Hong Li S Fau - Liu, Qiwei Liu H Fau - Wang, Xiaobing Wang Q Fau - Fu, Weidong Fu X Fau - Han, Zhaolie Han W Fau - Chen, and Z. Chen. "Stirred suspension culture improves embryoid body formation and cardiogenic differentiation of genetically modified embryonic stem cells." (1347-5215 (Electronic)).

Henderson, D. J., and A. J. Copp. 1998. "Versican expression is associated with chamber specification, septation, and valvulogenesis in the developing mouse heart." *Circulation Research* 83 (5): 523-532. <Go to ISI>://WOS:000075690900007.

Herrick, S., O. Blanc-Brude, A. Gray, and G. Laurent. 1999. "Fibrinogen." *Int J Biochem Cell Biol* 31 (7): 741-6. https://www.ncbi.nlm.nih.gov/pubmed/10467729.

Herron, T. J., A. M. Rocha, K. F. Campbell, D. Ponce-Balbuena, B. C. Willis, G. Guerrero-Serna, Q. Liu, M. Klos, H. Musa, M. Zarzoso, A. Bizy, J. Furness, J. Anumonwo, S. Mironov, and J. Jalife. 2016. "Extracellular Matrix-Mediated Maturation of Human Pluripotent Stem Cell-Derived Cardiac Monolayer Structure and Electrophysiological Function." *Circ Arrhythm Electrophysiol* 9 (4): e003638. https://doi.org/10.1161/circep.113.003638.

Hirt, M. N., A. Hansen, and T. Eschenhagen. 2014. "Cardiac tissue engineering: state of the art." *Circ Res* 114 (2): 354-67. https://doi.org/10.1161/CIRCRESAHA.114.300522. https://www.ncbi.nlm.nih.gov/pubmed/24436431.

Ho, S. Y., R. P. Thompson, S. R. Gibbs, M. M. Swindle, and R. H. Anderson. 1991. "Ventricular septal defects in a family of Yucatan miniature pigs." *Int J Cardiol* 33 (3): 419-25. http://www.ncbi.nlm.nih.gov/pubmed/1761337.

Hodge, A. J., J. Zhong, and E. A. Lipke. 2016. "Enhanced stem cell-derived cardiomyocyte differentiation in suspension culture by delivery of nitric oxide using S-nitrosocysteine." *Biotechnol Bioeng* 113 (4): 882-94. https://doi.org/10.1002/bit.25849. https://www.ncbi.nlm.nih.gov/pubmed/26444682.

Hoes, M. F., N. Bomer, and P. van der Meer. 2019. "Concise Review: The Current State of Human In Vitro Cardiac Disease Modeling: A Focus on Gene Editing and Tissue Engineering." *Stem Cells Transl Med* 8 (1): 66-74. https://doi.org/10.1002/sctm.18-0052. https://www.ncbi.nlm.nih.gov/pubmed/30302938.

Hom, J., and S. S. Sheu. 2009. "Morphological dynamics of mitochondria--a special emphasis on cardiac muscle cells." *J Mol Cell Cardiol* 46 (6): 811-20. https://doi.org/10.1016/j.yjmcc.2009.02.023. http://www.ncbi.nlm.nih.gov/pubmed/19281816.

Hong, S. H., Veronica Werbowetski-Ogilvie T Fau - Ramos-Mejia, Jung Bok Ramos-Mejia V Fau - Lee, Mickie Lee Jb Fau - Bhatia, and M. Bhatia. "Multiparameter comparisons of embryoid body differentiation toward human stem cell applications." (1876-7753 (Electronic)).

Hubbell, J. A. 1995. "Biomaterials in Tissue Engineering." *Bio-Technology* 13 (6): 565-576. https://doi.org/DOI 10.1038/nbt0695-565. <Go to ISI>://WOS:A1995RA25500018.

Huebsch, N., P. Loskill, M. A. Mandegar, N. C. Marks, A. S. Sheehan, Z. Ma, A. Mathur, T. N. Nguyen, J. C. Yoo, L. M. Judge, C. I. Spencer, A. C. Chukka, C. R. Russell, P. L. So, B. R. Conklin, and K. E. Healy. 2015a. "Automated Video-Based Analysis of Contractility and Calcium Flux in Human-Induced Pluripotent Stem Cell-Derived Cardiomyocytes Cultured over Different Spatial Scales." *Tissue Eng*

Part C Methods 21 (5): 467-79. https://doi.org/10.1089/ten.TEC.2014.0283. https://www.ncbi.nlm.nih.gov/pubmed/25333967.

---. 2015b. "Automated Video-Based Analysis of Contractility and Calcium Flux in Human-Induced Pluripotent Stem Cell-Derived Cardiomyocytes Cultured over Different Spatial Scales." *Tissue Engineering Part C-Methods* 21 (5): 467-479. https://doi.org/10.1089/ten.tec.2014.0283. <Go to ISI>://WOS:000353504800005.

Iaizzo, Paul A. 2005. *Handbook of cardiac anatomy, physiology, and devices*.*Current clinical oncology*. Totowa, N.J.: Humana Press.

Ito, T., H. Ando, and H. Handa. 2011. "Teratogenic effects of thalidomide: molecular mechanisms." *Cell Mol Life Sci* 68 (9): 1569-79. https://doi.org/10.1007/s00018-010-0619-9. http://www.ncbi.nlm.nih.gov/pubmed/21207098.

Itzhaki, I., L. Maizels, I. Huber, L. Zwi-Dantsis, O. Caspi, A. Winterstern, O. Feldman, A. Gepstein, G. Arbel, H. Hammerman, M. Boulos, and L. Gepstein. 2011. "Modelling the long QT syndrome with induced pluripotent stem cells." *Nature* 471 (7337): 225-9. https://doi.org/10.1038/nature09747. https://www.ncbi.nlm.nih.gov/pubmed/21240260.

Jacot, J. G., A. D. McCulloch, and J. H. Omens. 2008. "Substrate stiffness affects the functional maturation of neonatal rat ventricular myocytes." *Biophys J* 95 (7): 3479-87. https://doi.org/10.1529/biophysj.107.124545. https://www.ncbi.nlm.nih.gov/pubmed/18586852.

Jeziorowska, D., V. Fontaine, C. Jouve, E. Villard, S. Dussaud, D. Akbar, V. Letang, P. Cervello, J. M. Itier, M. P. Pruniaux, and J. S. Hulot. 2017. "Differential Sarcomere and Electrophysiological Maturation of Human iPSC-Derived Cardiac Myocytes in Monolayer vs. Aggregation-Based Differentiation Protocols." *Int J Mol Sci* 18 (6). https://doi.org/10.3390/ijms18061173.

Jiang, Y., S. Habibollah, K. Tilgner, J. Collin, T. Barta, J. Y. Al-Aama, L. Tesarov, R. Hussain, A. W. Trafford, G. Kirkwood, E. Sernagor, C. G. Eleftheriou, S. Przyborski, M. Stojkovic, M. Lako, B. Keavney, and L. Armstrong. 2014a. "An induced pluripotent stem cell model of hypoplastic left heart syndrome (HLHS) reveals multiple expression and functional differences in HLHS-derived cardiac myocytes." *Stem Cells Transl Med* 3 (4): 416-23. https://doi.org/10.5966/sctm.2013-0105. https://www.ncbi.nlm.nih.gov/pubmed/24591732.

---. 2014b. "An Induced Pluripotent Stem Cell Model of Hypoplastic Left Heart Syndrome (HLHS) Reveals Multiple Expression and Functional Differences in HLHS-Derived Cardiac Myocytes." *Stem Cells Translational Medicine* 3 (4): 416-423. https://doi.org/10.5966/sctm.2013-0105. <Go to ISI>://WOS:000333938200007.

Johnson, M. T., S. Zhang, R. Gilkeson, R. Ameduri, E. Siwik, C. R. Patel, O. Chebotarev, A. B. Kenton, K. R. Bowles, J. A. Towbin, N. H. Robin, F. Brozovich, and B. D. Hoit. 2006. "Intrafamilial variability of noncompaction of the ventricular myocardium." *Am Heart J* 151 (5): 1012 e7-14. https://doi.org/10.1016/j.ahj.2006.01.021. https://www.ncbi.nlm.nih.gov/pubmed/16644324.

Jung, C. B., A. Moretti, M. Mederos y Schnitzler, L. Iop, U. Storch, M. Bellin, T. Dorn, S. Ruppenthal, S. Pfeiffer, A. Goedel, R. J. Dirschinger, M. Seyfarth, J. T. Lam, D. Sinnecker, T. Gudermann, P. Lipp, and K. L. Laugwitz. 2012. "Dantrolene rescues arrhythmogenic RYR2 defect in a patient-specific stem cell model of catecholaminergic polymorphic ventricular tachycardia." *EMBO Mol Med* 4 (3): 180-91. https://doi.org/10.1002/emmm.201100194. https://www.ncbi.nlm.nih.gov/pubmed/22174035.

Kattman, S. J., A. D. Witty, M. Gagliardi, N. C. Dubois, M. Niapour, A. Hotta, J. Ellis, and G. Keller. 2011. "Stage-specific optimization of activin/nodal and BMP signaling promotes cardiac differentiation of mouse and human pluripotent stem cell lines." *Cell Stem Cell* 8 (2): 228-40. https://doi.org/10.1016/j.stem.2010.12.008. https://www.ncbi.nlm.nih.gov/pubmed/21295278.

Kehat, I., D. Kenyagin-Karsenti, M. Snir, H. Segev, M. Amit, A. Gepstein, E. Livne, O. Binah, J. Itskovitz-Eldor, and L. Gepstein. 2001. "Human embryonic stem cells can differentiate into myocytes with structural and functional properties of cardiomyocytes." *J Clin Invest* 108 (3): 407-14. https://doi.org/10.1172/jci12131.

Kerscher, P., B. S. Bussie, K. M. DeSimone, D. A. Dunn, and E. A. Lipke. 2015. "Characterization of mitochondrial populations during stem cell differentiation." *Methods Mol Biol* 1264: 453-63. https://doi.org/10.1007/978-1-4939-2257-4_37. http://www.ncbi.nlm.nih.gov/pubmed/25631034.

Kerscher, P., I. C. Turnbull, A. J. Hodge, J. Kim, D. Seliktar, C. J. Easley, K. D. Costa, and E. A. Lipke. 2016. "Direct hydrogel encapsulation of pluripotent stem cells enables ontomimetic differentiation and growth of engineered human heart tissues." *Biomaterials* 83: 383-95. https://doi.org/10.1016/j.biomaterials.2015.12.011. https://www.ncbi.nlm.nih.gov/pubmed/26826618.

Kerscher, Petra, Jennifer A. Kaczmarek, Sara E. Head, Morgan E. Ellis, Wen J. Seeto, Joonyul Kim, Subhrajit Bhattacharya, Vishnu Suppiramaniam, and Elizabeth A. Lipke. 2016a. "Direct Production of Human Cardiac Tissues by Pluripotent Stem Cell Encapsulation in Gelatin Methacryloyl." *ACS Biomaterials Science & Engineering*. https://doi.org/10.1021/acsbiomaterials.6b00226.

---. 2016b. "Direct Production of Human Cardiac Tissues by Pluripotent Stem Cell Encapsulation in Gelatin Methacryloyl." *ACS Biomaterials Science & Engineering* 3 (8): 1499-1509. https://doi.org/10.1021/acsbiomaterials.6b00226.

Khalil, A., R. Tanos, N. El-Hachem, M. Kurban, P. Bouvagnet, F. Bitar, and G. Nemer. 2017. "A HAND to TBX5 Explains the Link Between Thalidomide and Cardiac Diseases." *Sci Rep* 7 (1): 1416. https://doi.org/10.1038/s41598-017-01641-3. https://www.ncbi.nlm.nih.gov/pubmed/28469241.

Khan, M. I. Gabriel. 1997. *Rapid ECG interpretation*. Philadelphia: Saunders.

Kim, D. H., E. A. Lipke, P. Kim, R. Cheong, S. Thompson, M. Delannoy, K. Y. Suh, L. Tung, and A. Levchenko. 2010. "Nanoscale cues regulate the structure and function of macroscopic cardiac tissue constructs." *Proceedings of the National Academy of Sciences of the United States of America* 107 (2): 565-570. https://doi.org/10.1073/pnas.0906504107. <Go to ISI>://WOS:000273559300011.

Kim, T. W., J. H. Che, and J. W. Yun. 2019. "Use of stem cells as alternative methods to animal experimentation in predictive toxicology." *Regulatory Toxicology and Pharmacology* 105: 15-29. https://doi.org/10.1016/j.yrtph.2019.03.016. <Go to ISI>://WOS:000476683800002.

Kioussi, C., P. Briata, S. H. Baek, D. W. Rose, N. S. Hamblet, T. Herman, K. A. Ohgi, C. Lin, A. Gleiberman, J. Wang, V. Brault, P. Ruiz-Lozano, H. D. Nguyen, R. Kemler, C. K. Glass, A. Wynshaw-Boris, and M. G. Rosenfeld. 2002. "Identification of a Wnt/Dvl/beta-Catenin --> Pitx2 pathway mediating cell-type-specific proliferation during development." *Cell* 111 (5): 673-85. https://www.ncbi.nlm.nih.gov/pubmed/12464179.

Kirk, E. P., M. Sunde, M. W. Costa, S. A. Rankin, O. Wolstein, M. L. Castro, T. L. Butler, C. Hyun, G. Guo, R. Otway, J. P. Mackay, L. B. Waddell, A. D. Cole, C. Hayward, A. Keogh, P. Macdonald, L. Griffiths, D. Fatkin, G. F. Sholler, A. M. Zorn, M. P. Feneley, D. S. Winlaw, and R. P. Harvey. 2007. "Mutations in cardiac T-box factor gene TBX20 are associated with diverse cardiac pathologies, including defects of septation and valvulogenesis and cardiomyopathy." *Am J Hum Genet* 81 (2): 280-91. https://doi.org/10.1086/519530. https://www.ncbi.nlm.nih.gov/pubmed/17668378.

Klabunde, R. E. 2017. "Cardiac electrophysiology: normal and ischemic ionic currents and the ECG." *Advances in Physiology Education* 41 (1): 29-37. https://doi.org/10.1152/advan.00105.2016. <Go to ISI>://WOS:000397104700005.

Kleber, A. G., and Y. Rudy. 2004. "Basic mechanisms of cardiac impulse propagation and associated arrhythmias." *Physiological Reviews* 84 (2): 431-488. https://doi.org/10.1152/physrev.00025.2003. <Go to ISI>://WOS:000220518500004.

Knobloch, J., J. D. Shaughnessy, Jr., and U. Ruther. 2007. "Thalidomide induces limb deformities by perturbing the Bmp/Dkk1/Wnt signaling pathway." *FASEB J* 21 (7): 1410-21. https://doi.org/10.1096/fj.06-7603com. http://www.ncbi.nlm.nih.gov/pubmed/17283219.

Kodo, K., S. G. Ong, F. Jahanbani, V. Termglinchan, K. Hirono, K. InanlooRahatloo, A. D. Ebert, P. Shukla, O. J. Abilez, J. M. Churko, I. Karakikes, G. Jung, F. Ichida, S. M. Wu, M. P. Snyder, D. Bernstein, and J. C. Wu. 2016a. "iPSC-derived cardiomyocytes reveal abnormal TGF-beta signalling in left ventricular non-compaction cardiomyopathy." *Nature Cell Biology* 18 (10): 1031-1042. https://doi.org/10.1038/ncb3411. <Go to ISI>://WOS:000384961700003.

---. 2016b. "iPSC-derived cardiomyocytes reveal abnormal TGF-beta signalling in left ventricular non-compaction cardiomyopathy." *Nat Cell Biol* 18 (10): 1031-42. https://doi.org/10.1038/ncb3411. https://www.ncbi.nlm.nih.gov/pubmed/27642787.

Kolesky, D. B., R. L. Truby, A. S. Gladman, T. A. Busbee, K. A. Homan, and J. A. Lewis. 2014. "3D Bioprinting of Vascularized, Heterogeneous Cell-Laden Tissue Constructs." *Advanced Materials* 26 (19): 3124-3130. https://doi.org/10.1002/adma.201305506. <Go to ISI>://WOS:000335869100025.

Krishnan, A., R. Samtani, P. Dhanantwari, E. Lee, S. Yamada, K. Shiota, M. T. Donofrio, L. Leatherbury, and C. W. Lo. 2014. "A detailed comparison of mouse and human cardiac development." *Pediatr Res* 76 (6): 500-7. https://doi.org/10.1038/pr.2014.128. https://www.ncbi.nlm.nih.gov/pubmed/25167202.

Kumar, N., U. Sharma, C. Singh, and B. Singh. 2012. "Thalidomide: chemistry, therapeutic potential and oxidative stress induced teratogenicity." *Curr Top Med Chem* 12 (13): 1436-55. http://www.ncbi.nlm.nih.gov/pubmed/22650376.

Kumar, V. A., N. L. Taylor, A. A. Jalan, L. K. Hwang, B. K. Wang, and J. D. Hartgerink. 2014. "A Nanostructured Synthetic Collagen Mimic for Hemostasis." *Biomacromolecules* 15 (4): 1484-1490. https://doi.org/10.1021/bm500091e. <Go to ISI>://WOS:000334571600042.

Kuo, H. H., X. Gao, J. M. DeKeyser, K. A. Fetterman, E. A. Pinheiro, C. J. Weddle, H. Fonoudi, M. V. Orman, M. Romero-Tejeda, M. Jouni, M. Blancard, T. Magdy, C. L. Epting, A. L. George, Jr., and P. W. Burridge. 2020. "Negligible-Cost and Weekend-Free Chemically Defined Human iPSC Culture." *Stem Cell Reports*. https://doi.org/10.1016/j.stemcr.2019.12.007. https://www.ncbi.nlm.nih.gov/pubmed/31928950.

Kupfer, M. E., W. H. Lin, V. Ravikumar, K. Qiu, L. Wang, L. Gao, D. Bhuiyan, M. Lenz, J. Ai, R. R. Mahutga, D. Townsend, J. Zhang, M. C. McAlpine, E. G. Tolkacheva, and B. M. Ogle. 2020. "In Situ Expansion, Differentiation and Electromechanical Coupling of Human Cardiac Muscle in a 3D Bioprinted, Chambered Organoid." *Circ Res*. https://doi.org/10.1161/CIRCRESAHA.119.316155. https://www.ncbi.nlm.nih.gov/pubmed/32228120.

Kurosawa, H. 2007a. "Methods for inducing embryoid body formation: In vitro differentiation system of embryonic stem cells." *Journal of Bioscience and Bioengineering* 103 (5): 389-398. https://doi.org/10.1263/jbb.103.389. <Go to ISI>://WOS:000247838900001.

---. 2007b. "Methods for inducing embryoid body formation: in vitro differentiation system of embryonic stem cells." *J Biosci Bioeng* 103 (5): 389-98. https://doi.org/10.1263/jbb.103.389. https://www.ncbi.nlm.nih.gov/pubmed/17609152.

Lan, F., A. S. Lee, P. Liang, V. Sanchez-Freire, P. K. Nguyen, L. Wang, L. Han, M. Yen, Y. M. Wang, N. Sun, O. J. Abilez, S. J. Hu, A. D. Ebert, E. G. Navarrete, C. S. Simmons, M. Wheeler, B. Pruitt, R. Lewis, Y. Yamaguchi, E. A. Ashley, D. M. Bers, R. C. Robbins, M. T. Longaker, and J. C. Wu. 2013. "Abnormal Calcium Handling Properties Underlie Familial Hypertrophic Cardiomyopathy Pathology in Patient-Specific Induced Pluripotent Stem Cells." *Cell Stem Cell* 12 (1): 101-113. https://doi.org/10.1016/j.stem.2012.10.010. <Go to ISI>://WOS:000313839500014.

Lee, E. J., F. K. Kasper, and A. G. Mikos. 2014a. "Biomaterials for Tissue Engineering." *Annals of Biomedical Engineering* 42 (2): 323-337. https://doi.org/10.1007/s10439-013-0859-6. <Go to ISI>://WOS:000331976300008.

---. 2014b. "Biomaterials for tissue engineering." *Ann Biomed Eng* 42 (2): 323-37. https://doi.org/10.1007/s10439-013-0859-6. https://www.ncbi.nlm.nih.gov/pubmed/23820768.

Lee, Y. K., Y. M. Lau, Z. J. Cai, W. H. Lai, L. Y. Wong, H. F. Tse, K. M. Ng, and C. W. Siu. 2017. "Modeling Treatment Response for Lamin A/C Related Dilated Cardiomyopathy in Human Induced Pluripotent Stem Cells." *J Am Heart Assoc* 6 (8). https://doi.org/10.1161/JAHA.117.005677. https://www.ncbi.nlm.nih.gov/pubmed/28754655.

Leoni, G., and O. Soehnlein. 2018. "(Re) Solving Repair After Myocardial Infarction." *Front Pharmacol* 9: 1342. https://doi.org/10.3389/fphar.2018.01342. https://www.ncbi.nlm.nih.gov/pubmed/30534069.

Lesman, A., M. Habib, O. Caspi, A. Gepstein, G. Arbel, S. Levenberg, and L. Gepstein. 2010. "Transplantation of a tissue-engineered human vascularized cardiac muscle." *Tissue Eng Part A* 16 (1): 115-25. https://doi.org/10.1089/ten.TEA.2009.0130. https://www.ncbi.nlm.nih.gov/pubmed/19642856.

Lian, X., C. Hsiao, G. Wilson, K. Zhu, L. B. Hazeltine, S. M. Azarin, K. K. Raval, J. Zhang, T. J. Kamp, and S. P. Palecek. 2012. "Robust cardiomyocyte differentiation from human pluripotent stem cells via temporal modulation of canonical Wnt signaling." *Proc Natl Acad Sci U S A* 109 (27): E1848-57. https://doi.org/10.1073/pnas.1200250109. http://www.ncbi.nlm.nih.gov/pubmed/22645348.

Lian, X., J. Zhang, S. M. Azarin, K. Zhu, L. B. Hazeltine, X. Bao, C. Hsiao, T. J. Kamp, and S. P. Palecek. 2013. "Directed cardiomyocyte differentiation from human pluripotent stem cells by modulating Wnt/beta-catenin signaling under fully defined conditions." *Nat Protoc* 8 (1): 162-75. https://doi.org/10.1038/nprot.2012.150. https://www.ncbi.nlm.nih.gov/pubmed/23257984.

Limperopoulos, C., A. Majnemer, M. I. Shevell, B. Rosenblatt, C. Rohlicek, and C. Tchervenkov. 1999. "Neurologic status of newborns with congenital heart defects before open heart surgery." *Pediatrics* 103 (2): 402-8. http://www.ncbi.nlm.nih.gov/pubmed/9925832.

Lin, Q., J. Schwarz, C. Bucana, and E. N. Olson. 1997. "Control of mouse cardiac morphogenesis and myogenesis by transcription factor MEF2C." *Science* 276 (5317): 1404-7. https://www.ncbi.nlm.nih.gov/pubmed/9162005.

Loessner, D., C. Meinert, E. Kaemmerer, L. C. Martine, K. Yue, P. A. Levett, T. J. Klein, F. P. W. Melchels, A. Khademhosseini, and D. W. Hutmacher. 2016. "Functionalization, preparation and use of cell-laden gelatin methacryloyl-based hydrogels as modular tissue culture platforms." *Nature Protocols* 11 (4): 727-746. https://doi.org/10.1038/nprot.2016.037. <Go to ISI>://WOS:000373060200007.

Loessner, D., K. S. Stok, M. P. Lutolf, D. W. Hutmacher, J. A. Clements, and S. C. Rizzi. 2010. "Bioengineered 3D platform to explore cell-ECM interactions and drug resistance of epithelial ovarian cancer cells." *Biomaterials* 31 (32): 8494-8506. https://doi.org/10.1016/j.biomaterials.2010.07.064. <Go to ISI>://WOS:000283112700041.

Ltd., Regentis Biomaterials, 2016, "Regentis Receives IDE Approval for Pivotal GelrinC Clinical Trial," http://www.prnewswire.com/news-releases/regentis-receives-ide-approval-for-pivotal-gelrinc-clinical-trial-594800251.html.

Lutolf, M. P., and J. A. Hubbell. 2003. "Synthesis and physicochemical characterization of end-linked poly(ethylene glycol)-co-peptide hydrogels formed by Michael-type addition." *Biomacromolecules* 4 (3): 713-22. https://doi.org/10.1021/bm025744e. https://www.ncbi.nlm.nih.gov/pubmed/12741789.

Ma, D., H. Wei, J. Lu, S. Ho, G. Zhang, X. Sun, Y. Oh, S. H. Tan, M. L. Ng, W. Shim, P. Wong, and R. Liew. 2013. "Generation of patient-specific induced pluripotent stem cell-derived cardiomyocytes as a cellular model of arrhythmogenic right ventricular cardiomyopathy." *Eur Heart J* 34 (15): 1122-33. https://doi.org/10.1093/eurheartj/ehs226. https://www.ncbi.nlm.nih.gov/pubmed/22798562.

Ma, Y. F., Y. Ji, G. Y. Huang, K. Ling, X. H. Zhang, and F. Xu. 2015. "Bioprinting 3D cell-laden hydrogel microarray for screening human periodontal ligament stem cell response to extracellular matrix." *Biofabrication* 7 (4). https://doi.org/Artn 044105

10.1088/1758-5090/7/4/044105. <Go to ISI>://WOS:000366896900005.

Ma, Z., J. Wang, P. Loskill, N. Huebsch, S. Koo, F. L. Svedlund, N. C. Marks, E. W. Hua, C. P. Grigoropoulos, B. R. Conklin, and K. E. Healy. 2015. "Self-organizing human cardiac microchambers mediated by geometric confinement." *Nat Commun* 6: 7413. https://doi.org/10.1038/ncomms8413. http://www.ncbi.nlm.nih.gov/pubmed/26172574.

Mandalenakis, Z., C. Karazisi, K. Skoglund, A. Rosengren, G. Lappas, P. Eriksson, and M. Dellborg. 2019. "Risk of Cancer Among Children and Young Adults With Congenital Heart Disease Compared With Healthy Controls." *Jama Network Open* 2 (7). https://doi.org/ARTN e196762

10.1001/jamanetworkopen.2019.6762. <Go to ISI>://WOS:000477895900019.

Marsano, A., R. Maidhof, L. Q. Wan, Y. Wang, J. Gao, N. Tandon, and G. Vunjak-Novakovic. 2010. "Scaffold stiffness affects the contractile function of three-dimensional engineered cardiac constructs." *Biotechnol Prog* 26 (5): 1382-90. https://doi.org/10.1002/btpr.435. https://www.ncbi.nlm.nih.gov/pubmed/20945492.

Mayshar, Y., O. Yanuka, and N. Benvenisty. 2011. "Teratogen screening using transcriptome profiling of differentiating human embryonic stem cells." *J Cell Mol Med* 15 (6): 1393-401. https://doi.org/10.1111/j.1582-4934.2010.01105.x. http://www.ncbi.nlm.nih.gov/pubmed/20561110.

McCredie, J. 2009. "History, heresy and radiology in scientific discovery." *J Med Imaging Radiat Oncol* 53 (5): 433-41. https://doi.org/10.1111/j.1754-9485.2009.02101.x. https://www.ncbi.nlm.nih.gov/pubmed/19788478.

McDevitt, T. C., J. C. Angello, M. L. Whitney, H. Reinecke, S. D. Hauschka, C. E. Murry, and P. S. Stayton. 2002a. "In vitro generation of differentiated cardiac myofibers on micropatterned laminin surfaces." *J Biomed Mater Res* 60 (3): 472-9. https://doi.org/DOI 10.1002/jbm.1292. https://www.ncbi.nlm.nih.gov/pubmed/11920672.

---. 2002b. "In vitro generation of differentiated cardiac myofibers on micropatterned laminin surfaces." *Journal of Biomedical Materials Research* 60 (3): 472-479. https://doi.org/DOI 10.1002/jbm.1292. <Go to ISI>://WOS:000174717200017.

Meganathan, K., S. Jagtap, V. Wagh, J. Winkler, J. A. Gaspar, D. Hildebrand, M. Trusch, K. Lehmann, J. Hescheler, H. Schluter, and A. Sachinidis. 2012. "Identification of thalidomide-specific transcriptomics and proteomics signatures during differentiation of human embryonic stem cells." *PLoS One* 7 (8): e44228. https://doi.org/10.1371/journal.pone.0044228. http://www.ncbi.nlm.nih.gov/pubmed/22952932.

Menasche, P., V. Vanneaux, A. Hagege, A. Bel, B. Cholley, I. Cacciapuoti, A. Parouchev, N. Benhamouda, G. Tachdjian, L. Tosca, J. H. Trouvin, J. R. Fabreguettes, V. Bellamy, R. Guillemain, C. Suberbielle Boissel, E. Tartour, M. Desnos, and J. Larghero. 2015. "Human embryonic stem cell-derived cardiac progenitors for severe heart failure treatment: first clinical case report." *Eur Heart J* 36 (30): 2011-7. https://doi.org/10.1093/eurheartj/ehv189. https://www.ncbi.nlm.nih.gov/pubmed/25990469.

Meno, C., Y. Saijoh, H. Fujii, M. Ikeda, T. Yokoyama, M. Yokoyama, Y. Toyoda, and H. Hamada. 1996. "Left-right asymmetric expression of the TGF beta-family member lefty in mouse embryos." *Nature* 381 (6578): 151-5. https://doi.org/10.1038/381151a0. https://www.ncbi.nlm.nih.gov/pubmed/8610011.

Meseguer-Ripolles, J., S. R. Khetani, J. G. Blanco, M. Iredale, and D. C. Hay. 2018. "Pluripotent Stem Cell-Derived Human Tissue: Platforms to Evaluate Drug Metabolism and Safety (vol 20, 2017)." *Aaps Journal* 20 (2). https://doi.org/UNSP 30
10.1208/s12248-018-0191-z. <Go to ISI>://WOS:000427539900011.

Molkentin, J. D., Q. Lin, S. A. Duncan, and E. N. Olson. 1997. "Requirement of the transcription factor GATA4 for heart tube formation and ventral morphogenesis." *Genes & Development* 11 (8): 1061-1072. https://doi.org/DOI 10.1101/gad.11.8.1061. <Go to ISI>://WOS:A1997WY94000009.

Moore, Keith L., and T. V. N. Persaud. 1998. *The developing human : clinically oriented embryology*. 6th ed. Philadelphia: Saunders.

Moretti, A., M. Bellin, A. Welling, C. B. Jung, J. T. Lam, L. Bott-Flugel, T. Dorn, A. Goedel, C. Hohnke, F. Hofmann, M. Seyfarth, D. Sinnecker, A. Schomig, and K. L. Laugwitz. 2010a. "Patient-specific induced pluripotent stem-cell models for long-QT syndrome." *N Engl J Med* 363 (15): 1397-409. https://doi.org/10.1056/NEJMoa0908679. https://www.ncbi.nlm.nih.gov/pubmed/20660394.

---. 2010b. "Patient-Specific Induced Pluripotent Stem-Cell Models for Long-QT Syndrome." *New England Journal of Medicine* 363 (15): 1397-1409. https://doi.org/10.1056/NEJMoa0908679. <Go to ISI>://WOS:000282575100005.

Moscona, A. A. 1959. "Tissues from dissociated cells." *Sci Am* 200 (5): 132-4 passim. https://www.ncbi.nlm.nih.gov/pubmed/13646649.

Mussatto, K. A., R. Hoffmann, G. Hoffman, J. S. Tweddell, L. Bear, Y. M. Cao, J. Tanem, and C. Brosig. 2015. "Risk Factors for Abnormal Developmental

Trajectories in Young Children With Congenital Heart Disease." *Circulation* 132 (8): 755-761. https://doi.org/10.1161/Circulationaha.114.014521. <Go to ISI>://WOS:000360204800013.

Nakagawa, O., M. Nakagawa, J. A. Richardson, E. N. Olson, and D. Srivastava. 1999. "HRT1, HRT2, and HRT3: A new subclass of bHLH transcription factors marking specific cardiac, somitic, and pharyngeal arch segments." *Developmental Biology* 216 (1): 72-84. https://doi.org/DOI 10.1006/dbio.1999.9454. <Go to ISI>://WOS:000084171500006.

Nattel, S., and L. Carlsson. 2006. "Innovative approaches to anti-arrhythmic drug therapy." *Nat Rev Drug Discov* 5 (12): 1034-49. https://doi.org/10.1038/nrd2112. https://www.ncbi.nlm.nih.gov/pubmed/17139288.

Nerbonne, J. M. 2004. "Studying cardiac arrhythmias in the mouse--a reasonable model for probing mechanisms?" *Trends Cardiovasc Med* 14 (3): 83-93. https://doi.org/10.1016/j.tcm.2003.12.006. https://www.ncbi.nlm.nih.gov/pubmed/15121155.

Nguyen, D. C., T. A. Hookway, Q. Wu, R. Jha, M. K. Preininger, X. Chen, C. A. Easley, P. Spearman, S. R. Deshpande, K. Maher, M. B. Wagner, T. C. McDevitt, and C. Xu. 2014. "Microscale generation of cardiospheres promotes robust enrichment of cardiomyocytes derived from human pluripotent stem cells." *Stem Cell Reports* 3 (2): 260-8. https://doi.org/10.1016/j.stemcr.2014.06.002. https://www.ncbi.nlm.nih.gov/pubmed/25254340.

Nguyen, K. T., and J. L. West. 2002. "Photopolymerizable hydrogels for tissue engineering applications." *Biomaterials* 23 (22): 4307-4314. https://doi.org/Pii S0142-9612(02)00175-8

Doi 10.1016/S0142-9612(02)00175-8. <Go to ISI>://WOS:000177667400002.

Nichol, J. W., S. T. Koshy, H. Bae, C. M. Hwang, S. Yamanlar, and A. Khademhosseini. 2010. "Cell-laden microengineered gelatin methacrylate hydrogels." *Biomaterials* 31 (21): 5536-44. https://doi.org/10.1016/j.biomaterials.2010.03.064. https://www.ncbi.nlm.nih.gov/pubmed/20417964.

Nielsen, S. H., A. J. Mouton, K. Y. DeLeon-Pennell, F. Genovese, M. Karsdal, and M. L. Lindsey. 2017. "Understanding cardiac extracellular matrix remodeling to develop biomarkers of myocardial infarction outcomes." *Matrix Biol*. https://doi.org/10.1016/j.matbio.2017.12.001. https://www.ncbi.nlm.nih.gov/pubmed/29247693.

Nomura, M., and E. Li. 1998. "Smad2 role in mesoderm formation, left-right patterning and craniofacial development." *Nature* 393 (6687): 786-790. <Go to ISI>://WOS:000074433100049.

Novak, A., L. Barad, N. Zeevi-Levin, R. Shick, R. Shtrichman, A. Lorber, J. Itskovitz-Eldor, and O. Binah. 2012. "Cardiomyocytes generated from CPVTD307H patients are arrhythmogenic in response to beta-adrenergic stimulation." *J Cell Mol Med* 16 (3): 468-82. https://doi.org/10.1111/j.1582-4934.2011.01476.x. https://www.ncbi.nlm.nih.gov/pubmed/22050625.

Nugent, A. W., P. E. Daubeney, P. Chondros, J. B. Carlin, M. Cheung, L. C. Wilkinson, A. M. Davis, S. G. Kahler, C. W. Chow, J. L. Wilkinson, R. G. Weintraub, and Study National Australian Childhood Cardiomyopathy. 2003. "The epidemiology

of childhood cardiomyopathy in Australia." *N Engl J Med* 348 (17): 1639-46. https://doi.org/10.1056/NEJMoa021737. https://www.ncbi.nlm.nih.gov/pubmed/12711738.

Nunes, S. S., J. W. Miklas, J. Liu, R. Aschar-Sobbi, Y. Xiao, B. Zhang, J. Jiang, S. Masse, M. Gagliardi, A. Hsieh, N. Thavandiran, M. A. Laflamme, K. Nanthakumar, G. J. Gross, P. H. Backx, G. Keller, and M. Radisic. 2013. "Biowire: a platform for maturation of human pluripotent stem cell-derived cardiomyocytes." *Nat Methods* 10 (8): 781-7. https://doi.org/10.1038/nmeth.2524. https://www.ncbi.nlm.nih.gov/pubmed/23793239.

Oechslin, E., and R. Jenni. 2011. "Left ventricular non-compaction revisited: a distinct phenotype with genetic heterogeneity?" *Eur Heart J* 32 (12): 1446-56. https://doi.org/10.1093/eurheartj/ehq508. https://www.ncbi.nlm.nih.gov/pubmed/21285074.

Organization, Geneva: World Health. 2017. "World health statistics 2017: monitoring health for the SDGs, Sustainable Development Goals.".

Ott, H. C., T. S. Matthiesen, S. K. Goh, L. D. Black, S. M. Kren, T. I. Netoff, and D. A. Taylor. 2008. "Perfusion-decellularized matrix: using nature's platform to engineer a bioartificial heart." *Nat Med* 14 (2): 213-21. https://doi.org/10.1038/nm1684. https://www.ncbi.nlm.nih.gov/pubmed/18193059.

Papaioannou, V. E. 2014. "The T-box gene family: emerging roles in development, stem cells and cancer." *Development* 141 (20): 3819-33. https://doi.org/10.1242/dev.104471. https://www.ncbi.nlm.nih.gov/pubmed/25294936.

Parman, T., M. J. Wiley, and P. G. Wells. 1999. "Free radical-mediated oxidative DNA damage in the mechanism of thalidomide teratogenicity." *Nat Med* 5 (5): 582-5. https://doi.org/10.1038/8466. http://www.ncbi.nlm.nih.gov/pubmed/10229238.

Parra, V., V. Eisner, M. Chiong, A. Criollo, F. Moraga, A. Garcia, S. Hartel, E. Jaimovich, A. Zorzano, C. Hidalgo, and S. Lavandero. 2008. "Changes in mitochondrial dynamics during ceramide-induced cardiomyocyte early apoptosis." *Cardiovasc Res* 77 (2): 387-97. https://doi.org/10.1093/cvr/cvm029. http://www.ncbi.nlm.nih.gov/pubmed/18006463.

Peled, E., J. Boss, J. Bejar, C. Zinman, and D. Seliktar. 2007. "A novel poly(ethylene glycol)-fibrinogen hydrogel for tibial segmental defect repair in a rat model." *Journal of Biomedical Materials Research Part A* 80a (4): 874-884. https://doi.org/10.1002/jbm.a.30928. <Go to ISI>://WOS:000244429600011.

Pereira, F. A., Y. H. Qiu, G. Zhou, M. J. Tsai, and S. Y. Tsai. 1999. "The orphan nuclear receptor COUP-TFII is required for angiogenesis and heart development." *Genes & Development* 13 (8): 1037-1049. https://doi.org/DOI 10.1101/gad.13.8.1037. <Go to ISI>://WOS:000079983400012.

Pesl, Martin, Ivana Acimovic, Jan Pribyl, Renata Hezova, Aleksandra Vilotic, Jeremy Fauconnier, Jan Vrbsky, Peter Kruzliak, Petr Skladal, Tomas Kara, Vladimir Rotrekl, Alain Lacampagne, Petr Dvorak, and Albano C. Meli. 2014. "Forced aggregation and defined factors allow highly uniform-sized embryoid bodies and functional cardiomyocytes from human embryonic and induced pluripotent stem

cells." *Heart and Vessels* 29 (6): 834-846. https://doi.org/10.1007/s00380-013-0436-9. https://doi.org/10.1007/s00380-013-0436-9.

Peter, A. K., M. A. Bjerke, and L. A. Leinwand. 2016. "Biology of the cardiac myocyte in heart disease." *Mol Biol Cell* 27 (14): 2149-60. https://doi.org/10.1091/mbc.E16-01-0038. https://www.ncbi.nlm.nih.gov/pubmed/27418636.

Pfeffer, M. A., and E. Braunwald. 1990. "Ventricular remodeling after myocardial infarction. Experimental observations and clinical implications." *Circulation* 81 (4): 1161-72. https://www.ncbi.nlm.nih.gov/pubmed/2138525.

Plotkin, M., S. R. Vaibavi, A. J. Rufaihah, V. Nithya, J. Wang, Y. Shachaf, T. Kofidis, and D. Seliktar. 2014. "The effect of matrix stiffness of injectable hydrogels on the preservation of cardiac function after a heart attack." *Biomaterials* 35 (5): 1429-38. https://doi.org/10.1016/j.biomaterials.2013.10.058. https://www.ncbi.nlm.nih.gov/pubmed/24268664.

Pradhan, S., I. Hassani, W. J. Seeto, and E. A. Lipke. 2017. "PEG-fibrinogen hydrogels for three-dimensional breast cancer cell culture." *J Biomed Mater Res A* 105 (1): 236-252. https://doi.org/10.1002/jbm.a.35899. https://www.ncbi.nlm.nih.gov/pubmed/27615742.

Radisic, M. 2015. "Biomaterials for cardiac tissue engineering." *Biomed Mater* 10 (3): 030301. https://doi.org/10.1088/1748-6041/10/3/030301. https://www.ncbi.nlm.nih.gov/pubmed/26065444.

Radisic, M., J. Malda, E. Epping, W. Geng, R. Langer, and G. Vunjak-Novakovic. 2006. "Oxygen gradients correlate with cell density and cell viability in engineered cardiac tissue." *Biotechnol Bioeng* 93 (2): 332-43. https://doi.org/10.1002/bit.20722. https://www.ncbi.nlm.nih.gov/pubmed/16270298.

Radisic, M., L. Yang, J. Boublik, R. J. Cohen, R. Langer, L. E. Freed, and G. Vunjak-Novakovic. 2004a. "Medium perfusion enables engineering of compact and contractile cardiac tissue." *Am J Physiol Heart Circ Physiol* 286 (2): H507-16. https://doi.org/10.1152/ajpheart.00171.2003. https://www.ncbi.nlm.nih.gov/pubmed/14551059.

Radisic, M., L. M. Yang, J. Boublik, R. J. Cohen, R. Langer, L. E. Freed, and G. Vunjak-Novakovic. 2004b. "Medium perfusion enables engineering of compact and contractile cardiac tissue." *American Journal of Physiology-Heart and Circulatory Physiology* 286 (2): H507-H516. https://doi.org/10.1152/ajpheart.00171.2003. <Go to ISI>://WOS:000187911900005.

Ranger, A. M., M. J. Grusby, M. R. Hodge, E. M. Gravallese, F. C. de la Brousse, T. Hoey, C. Mickanin, H. S. Baldwin, and L. H. Glimcher. 1998. "The transcription factor NF-ATc is essential for cardiac valve formation." *Nature* 392 (6672): 186-190. https://doi.org/Doi 10.1038/32426. <Go to ISI>://WOS:000072462700064.

Rehman, W., L. M. Arfons, and H. M. Lazarus. 2011. "The rise, fall and subsequent triumph of thalidomide: lessons learned in drug development." *Ther Adv Hematol* 2 (5): 291-308. https://doi.org/10.1177/2040620711413165. https://www.ncbi.nlm.nih.gov/pubmed/23556097.

Reiter, J. F., J. Alexander, A. Rodaway, D. Yelon, R. Patient, N. Holder, and D. Y. R. Stainier. 1999. "Gata5 is required for the development of the heart and endoderm in zebrafish." *Genes & Development* 13 (22): 2983-2995. https://doi.org/DOI 10.1101/gad.13.22.2983. <Go to ISI>://WOS:000084048600008.

Reller, M. D., M. J. Strickland, T. Riehle-Colarusso, W. T. Mahle, and A. Correa. 2008. "Prevalence of congenital heart defects in metropolitan Atlanta, 1998-2005." *J Pediatr* 153 (6): 807-13. https://doi.org/10.1016/j.jpeds.2008.05.059. https://www.ncbi.nlm.nih.gov/pubmed/18657826.

Riley, P., L. Anson-Cartwright, and J. C. Cross. 1998. "The Hand1 bHLH transcription factor is essential for placentation and cardiac morphogenesis." *Nature Genetics* 18 (3): 271-275. https://doi.org/DOI 10.1038/ng0398-271. <Go to ISI>://WOS:000072325000027.

Riley, P. R. 2008. "The adult epicardium: realizing the potential for neovascular therapy." *Arterioscler Thromb Vasc Biol* 28 (5): 803-4. https://doi.org/10.1161/ATVBAHA.108.165191. https://www.ncbi.nlm.nih.gov/pubmed/18421004.

Rivera-Feliciano, J., and C. J. Tabin. 2006. "Bmp2 instructs cardiac progenitors to form the heart-valve-inducing field." *Dev Biol* 295 (2): 580-8. https://doi.org/10.1016/j.ydbio.2006.03.043. http://www.ncbi.nlm.nih.gov/pubmed/16730346.

Robert M. Berne, Matthew N. Levy. 1997. *Cardiovascular Physiology*. 7th ed., edited by Emma D. Underdown: Mosby-Yea Book Inc.

Robertson, C., D. D. Tran, and S. C. George. 2013. "Concise review: maturation phases of human pluripotent stem cell-derived cardiomyocytes." *Stem Cells* 31 (5): 829-37. https://doi.org/10.1002/stem.1331.

Rungarunlert, S., Theerawat Klincumhom N Fau - Tharasanit, Mongkol Tharasanit T Fau - Techakumphu, Melinda K. Techakumphu M Fau - Pirity, Andras Pirity Mk Fau - Dinnyes, and A. Dinnyes. "Slow turning lateral vessel bioreactor improves embryoid body formation and cardiogenic differentiation of mouse embryonic stem cells." (2152-4998 (Electronic)).

Sarma, R. J., A. Chana, and U. Elkayam. 2010. "Left ventricular noncompaction." *Prog Cardiovasc Dis* 52 (4): 264-73. https://doi.org/10.1016/j.pcad.2009.11.001. https://www.ncbi.nlm.nih.gov/pubmed/20109597.

Sawai, S., A. Shimono, Y. Wakamatsu, C. Palmes, K. Hanaoka, and H. Kondoh. 1993. "Defects of Embryonic Organogenesis Resulting from Targeted Disruption of the N-Myc Gene in the Mouse." *Development* 117 (4): 1445-1455. <Go to ISI>://WOS:A1993LD08900023.

Schaaf, Sebastian, Aya Shibamiya, Marco Mewe, Alexandra Eder, Andrea Stöhr, Marc N. Hirt, Thomas Rau, Wolfram-Hubertus Zimmermann, Lenard Conradi, Thomas Eschenhagen, and Arne Hansen. 2011. "Human engineered heart tissue as a versatile tool in basic research and preclinical toxicology." *PloS one* 6 (10): e26397-e26397. https://doi.org/10.1371/journal.pone.0026397. https://pubmed.ncbi.nlm.nih.gov/22028871
https://www.ncbi.nlm.nih.gov/pmc/articles/PMC3197640/.

Schaper, J., E. Meiser, and G. Stammler. 1985. "Ultrastructural morphometric analysis of myocardium from dogs, rats, hamsters, mice, and from human hearts." *Circ Res* 56 (3): 377-91. http://www.ncbi.nlm.nih.gov/pubmed/3882260.

Schott, J. J., D. W. Benson, C. T. Basson, W. Pease, G. M. Silberbach, J. P. Moak, B. J. Maron, C. E. Seidman, and J. G. Seidman. 1998. "Congenital heart disease caused by mutations in the transcription factor NKX2-5." *Science* 281 (5373): 108-111. https://doi.org/DOI 10.1126/science.281.5373.108. <Go to ISI>://WOS:000074685800049.

Schultheiss, T. M., J. B. E. Burch, and A. B. Lassar. 1997. "A role for bone morphogenetic proteins in the induction of cardiac myogenesis." *Genes & Development* 11 (4): 451-462. https://doi.org/DOI 10.1101/gad.11.4.451. <Go to ISI>://WOS:A1997WK69000004.

Schultheiss, T. M., S. Xydas, and A. B. Lassar. 1995. "Induction of avian cardiac myogenesis by anterior endoderm." *Development* 121 (12): 4203-14. https://www.ncbi.nlm.nih.gov/pubmed/8575320.

Schuurman, W., P. A. Levett, M. W. Pot, P. R. van Weeren, W. J. Dhert, D. W. Hutmacher, F. P. Melchels, T. J. Klein, and J. Malda. 2013. "Gelatin-methacrylamide hydrogels as potential biomaterials for fabrication of tissue-engineered cartilage constructs." *Macromol Biosci* 13 (5): 551-61. https://doi.org/10.1002/mabi.201200471. https://www.ncbi.nlm.nih.gov/pubmed/23420700.

Seeto, W. J., Y. Tian, S. Pradhan, P. Kerscher, and E. A. Lipke. 2019. "Rapid Production of Cell-Laden Microspheres Using a Flexible Microfluidic Encapsulation Platform." *Small* 15 (47): e1902058. https://doi.org/10.1002/smll.201902058. https://www.ncbi.nlm.nih.gov/pubmed/31468632.

Severs, N. J. 2000. "The cardiac muscle cell." *Bioessays* 22 (2): 188-99. https://doi.org/10.1002/(SICI)1521-1878(200002)22:2<188::AID-BIES10>3.0.CO;2-T. https://www.ncbi.nlm.nih.gov/pubmed/10655038.

Shadrin, I. Y., B. W. Allen, Y. Qian, C. P. Jackman, A. L. Carlson, M. E. Juhas, and N. Bursac. 2017. "Cardiopatch platform enables maturation and scale-up of human pluripotent stem cell-derived engineered heart tissues." *Nat Commun* 8 (1): 1825. https://doi.org/10.1038/s41467-017-01946-x. https://www.ncbi.nlm.nih.gov/pubmed/29184059.

Shapira-Schweitzer, K., and D. Seliktar. 2007. "Matrix stiffness affects spontaneous contraction of cardiomyocytes cultured within a PEGylated fibrinogen biomaterial." *Acta Biomater* 3 (1): 33-41. https://doi.org/10.1016/j.actbio.2006.09.003. https://www.ncbi.nlm.nih.gov/pubmed/17098488.

Shin, S. R., S. M. Jung, M. Zalabany, K. Kim, P. Zorlutuna, S. B. Kim, M. Nikkhah, M. Khabiry, M. Azize, J. Kong, K. T. Wan, T. Palacios, M. R. Dokmeci, H. Bae, X. W. Tang, and A. Khademhosseini. 2013. "Carbon-Nanotube-Embedded Hydrogel Sheets for Engineering Cardiac Constructs and Bioactuators." *Acs Nano* 7 (3): 2369-2380. https://doi.org/10.1021/nn305559j. <Go to ISI>://WOS:000316846700054.

Shiojima, I., and K. Walsh. 2006. "Regulation of cardiac growth and coronary angiogenesis by the Akt/PKB signaling pathway." *Genes Dev* 20 (24): 3347-65. https://doi.org/10.1101/gad.1492806. http://www.ncbi.nlm.nih.gov/pubmed/17182864.

Shou, W., B. Aghdasi, D. L. Armstrong, Q. Guo, S. Bao, M. J. Charng, L. M. Mathews, M. D. Schneider, S. L. Hamilton, and M. M. Matzuk. 1998. "Cardiac defects and altered ryanodine receptor function in mice lacking FKBP12." *Nature* 391 (6666): 489-92. https://doi.org/10.1038/35146. https://www.ncbi.nlm.nih.gov/pubmed/9461216.

Smithells, R. W., and C. G. Newman. 1992. "Recognition of thalidomide defects." *J Med Genet* 29 (10): 716-23. http://www.ncbi.nlm.nih.gov/pubmed/1433232.

Spearman, B. S., A. J. Hodge, J. L. Porter, J. G. Hardy, Z. D. Davis, T. Xu, X. Zhang, C. E. Schmidt, M. C. Hamilton, and E. A. Lipke. 2015. "Conductive interpenetrating networks of polypyrrole and polycaprolactone encourage electrophysiological development of cardiac cells." *Acta Biomater* 28: 109-20. https://doi.org/10.1016/j.actbio.2015.09.025. https://www.ncbi.nlm.nih.gov/pubmed/26407651.

Srivastava, D., and E. N. Olson. 2000. "A genetic blueprint for cardiac development." *Nature* 407 (6801): 221-6. https://doi.org/10.1038/35025190. https://www.ncbi.nlm.nih.gov/pubmed/11001064.

Stephens, T. D. 1988. "Proposed mechanisms of action in thalidomide embryopathy." *Teratology* 38 (3): 229-39. https://doi.org/10.1002/tera.1420380307. https://www.ncbi.nlm.nih.gov/pubmed/3067416.

Stephens, T. D., C. J. Bunde, and B. J. Fillmore. 2000. "Mechanism of action in thalidomide teratogenesis." *Biochem Pharmacol* 59 (12): 1489-99. http://www.ncbi.nlm.nih.gov/pubmed/10799645.

Stollberger, C., B. Gerecke, J. Finsterer, and R. Engberding. 2013. "Refinement of echocardiographic criteria for left ventricular noncompaction." *Int J Cardiol* 165 (3): 463-7. https://doi.org/10.1016/j.ijcard.2011.08.845. https://www.ncbi.nlm.nih.gov/pubmed/21944384.

Sun, N., M. Yazawa, J. Liu, L. Han, V. Sanchez-Freire, O. J. Abilez, E. G. Navarrete, S. Hu, L. Wang, A. Lee, A. Pavlovic, S. Lin, R. Chen, R. J. Hajjar, M. P. Snyder, R. E. Dolmetsch, M. J. Butte, E. A. Ashley, M. T. Longaker, R. C. Robbins, and J. C. Wu. 2012a. "Patient-specific induced pluripotent stem cells as a model for familial dilated cardiomyopathy." *Sci Transl Med* 4 (130): 130ra47. https://doi.org/10.1126/scitranslmed.3003552. https://www.ncbi.nlm.nih.gov/pubmed/22517884.

Sun, N., M. Yazawa, J. W. Liu, L. Han, V. Sanchez-Freire, O. J. Abilez, E. G. Navarrete, S. J. Hu, L. Wang, A. Lee, A. Pavlovic, S. Lin, R. Chen, R. J. Hajjar, M. P. Snyder, R. E. Dolmetsch, M. J. Butte, E. A. Ashley, M. T. Longaker, R. C. Robbins, and J. C. Wu. 2012b. "Patient-Specific Induced Pluripotent Stem Cells as a Model for Familial Dilated Cardiomyopathy." *Science Translational Medicine* 4 (130). https://doi.org/ARTN 130ra47
10.1126/scitranslmed.3003552. <Go to ISI>://WOS:000303045900004.

Takahashi, K., K. Tanabe, M. Ohnuki, M. Narita, T. Ichisaka, K. Tomoda, and S. Yamanaka. 2007. "Induction of pluripotent stem cells from adult human fibroblasts by defined factors." *Cell* 131 (5): 861-72. https://doi.org/10.1016/j.cell.2007.11.019. https://www.ncbi.nlm.nih.gov/pubmed/18035408.

Takahashi, K., and S. Yamanaka. 2006. "Induction of pluripotent stem cells from mouse embryonic and adult fibroblast cultures by defined factors." *Cell* 126 (4): 663-76. https://doi.org/10.1016/j.cell.2006.07.024. https://www.ncbi.nlm.nih.gov/pubmed/16904174.

Tandon, N., C. Cannizzaro, P. H. Chao, R. Maidhof, A. Marsano, H. T. Au, M. Radisic, and G. Vunjak-Novakovic. 2009. "Electrical stimulation systems for cardiac tissue engineering." *Nat Protoc* 4 (2): 155-73. https://doi.org/10.1038/nprot.2008.183. https://www.ncbi.nlm.nih.gov/pubmed/19180087.

Therapontos, C., L. Erskine, E. R. Gardner, W. D. Figg, and N. Vargesson. 2009. "Thalidomide induces limb defects by preventing angiogenic outgrowth during early limb formation." *Proc Natl Acad Sci U S A* 106 (21): 8573-8. https://doi.org/10.1073/pnas.0901505106. http://www.ncbi.nlm.nih.gov/pubmed/19433787.

Timmerman, L. A., J. Grego-Bessa, A. Raya, E. Bertran, J. M. Perez-Pomares, J. Diez, S. Aranda, S. Palomo, F. McCormick, J. C. Izpisua-Belmonte, and J. L. de la Pompa. 2004. "Notch promotes epithelial-mesenchymal transition during cardiac development and oncogenic transformation." *Genes Dev* 18 (1): 99-115. https://doi.org/10.1101/gad.276304. https://www.ncbi.nlm.nih.gov/pubmed/14701881.

Trantidou, T., C. M. Terracciano, D. Kontziampasis, E. J. Humphrey, and T. Prodromakis. 2015. "Biorealistic cardiac cell culture platforms with integrated monitoring of extracellular action potentials." *Scientific Reports* 5. https://doi.org/ARTN 11067

10.1038/srep11067. <Go to ISI>://WOS:000356069400001.

Tsang, K. M. C., N. Annabi, F. Ercole, K. Zhou, D. J. Karst, F. Y. Li, J. M. Haynes, R. A. Evans, H. Thissen, A. Khademhosseini, and J. S. Forsythe. 2015. "Facile One-Step Micropatterning Using Photodegradable Gelatin Hydrogels for Improved Cardiomyocyte Organization and Alignment." *Advanced Functional Materials* 25 (6): 977-986. https://doi.org/10.1002/adfm.201403124. <Go to ISI>://WOS:000349629600018.

Tseng, C. M., Y. H. Hsiao, V. Y. Su, K. C. Su, Y. C. Wu, K. T. Chang, and D. W. Perng. 2013. "The suppression effects of thalidomide on human lung fibroblasts: cell proliferation, vascular endothelial growth factor release, and collagen production." *Lung* 191 (4): 361-8. https://doi.org/10.1007/s00408-013-9477-1. http://www.ncbi.nlm.nih.gov/pubmed/23722461.

Tulloch, N. L., V. Muskheli, M. V. Razumova, F. S. Korte, M. Regnier, K. D. Hauch, L. Pabon, H. Reinecke, and C. E. Murry. 2011. "Growth of engineered human myocardium with mechanical loading and vascular coculture." *Circ Res* 109 (1):

47-59. https://doi.org/10.1161/CIRCRESAHA.110.237206. https://www.ncbi.nlm.nih.gov/pubmed/21597009.

Turnbull, I. C., I. Karakikes, G. W. Serrao, P. Backeris, J. J. Lee, C. Xie, G. Senyei, R. E. Gordon, R. A. Li, F. G. Akar, R. J. Hajjar, J. S. Hulot, and K. D. Costa. 2014. "Advancing functional engineered cardiac tissues toward a preclinical model of human myocardium." *FASEB J* 28 (2): 644-54. https://doi.org/10.1096/fj.13-228007. https://www.ncbi.nlm.nih.gov/pubmed/24174427.

Ungrin, Mark D., Chirag Joshi, Andra Nica, Céline Bauwens, and Peter W. Zandstra. 2008. "Reproducible, ultra high-throughput formation of multicellular organization from single cell suspension-derived human embryonic stem cell aggregates." *PloS one* 3 (2): e1565-e1565. https://doi.org/10.1371/journal.pone.0001565. https://pubmed.ncbi.nlm.nih.gov/18270562 https://www.ncbi.nlm.nih.gov/pmc/articles/PMC2215775/.

Van Den Bulcke, A. I., B. Bogdanov, N. De Rooze, E. H. Schacht, M. Cornelissen, and H. Berghmans. 2000. "Structural and rheological properties of methacrylamide modified gelatin hydrogels." *Biomacromolecules* 1 (1): 31-8. https://www.ncbi.nlm.nih.gov/pubmed/11709840.

van den Heuvel, N. H., T. A. van Veen, B. Lim, and M. K. Jonsson. 2014. "Lessons from the heart: mirroring electrophysiological characteristics during cardiac development to in vitro differentiation of stem cell derived cardiomyocytes." *J Mol Cell Cardiol* 67: 12-25. https://doi.org/10.1016/j.yjmcc.2013.12.011. http://www.ncbi.nlm.nih.gov/pubmed/24370890.

van der Bom, T., A. C. Zomer, A. H. Zwinderman, F. J. Meijboom, B. J. Bouma, and B. J. Mulder. 2011. "The changing epidemiology of congenital heart disease." *Nat Rev Cardiol* 8 (1): 50-60. https://doi.org/10.1038/nrcardio.2010.166. https://www.ncbi.nlm.nih.gov/pubmed/21045784.

van der Linde, D., E. E. Konings, M. A. Slager, M. Witsenburg, W. A. Helbing, J. J. Takkenberg, and J. W. Roos-Hesselink. 2011. "Birth prevalence of congenital heart disease worldwide: a systematic review and meta-analysis." *J Am Coll Cardiol* 58 (21): 2241-7. https://doi.org/10.1016/j.jacc.2011.08.025. https://www.ncbi.nlm.nih.gov/pubmed/22078432.

Van der Velde, E. T., J. W. J. Vriend, M. M. A. M. Mannens, C. S. P. M. Uiterwaal, R. Brand, and B. J. M. Mulder. 2005. "CONCOR, an initiative towards a national registry and DNA-bank of patients with congenital heart disease in the Netherlands: Rationale, design, and first results." *European Journal of Epidemiology* 20 (6): 549-557. https://doi.org/10.1007/s10654-005-4264-9. <Go to ISI>://WOS:000231222900010.

Vargesson, N. 2015. "Thalidomide-induced teratogenesis: history and mechanisms." *Birth Defects Res C Embryo Today* 105 (2): 140-56. https://doi.org/10.1002/bdrc.21096. https://www.ncbi.nlm.nih.gov/pubmed/26043938.

Velayutham, N., E. J. Agnew, and K. E. Yutzey. 2019. "Postnatal Cardiac Development and Regenerative Potential in Large Mammals." *Pediatr Cardiol* 40 (7): 1345-

1358. https://doi.org/10.1007/s00246-019-02163-7. https://www.ncbi.nlm.nih.gov/pubmed/31346664.

Virani, S. S., A. Alonso, E. J. Benjamin, M. S. Bittencourt, C. W. Callaway, A. P. Carson, A. M. Chamberlain, A. R. Chang, S. Cheng, F. N. Delling, L. Djousse, M. S. V. Elkind, J. F. Ferguson, M. Fornage, S. S. Khan, B. M. Kissela, K. L. Knutson, T. W. Kwan, D. T. Lackland, T. T. Lewis, J. H. Lichtman, C. T. Longenecker, M. S. Loop, P. L. Lutsey, S. S. Martin, K. Matsushita, A. E. Moran, M. E. Mussolino, A. M. Perak, W. D. Rosamond, G. A. Roth, U. K. A. Sampson, G. M. Satou, E. B. Schroeder, S. H. Shah, C. M. Shay, N. L. Spartano, A. Stokes, D. L. Tirschwell, L. B. VanWagner, C. W. Tsao, Epidemiology American Heart Association Council on, Committee Prevention Statistics, and Subcommittee Stroke Statistics. 2020. "Heart Disease and Stroke Statistics-2020 Update: A Report From the American Heart Association." *Circulation* 141 (9): e139-e596. https://doi.org/10.1161/CIR.0000000000000757. https://www.ncbi.nlm.nih.gov/pubmed/31992061.

Weiford, B. C., V. D. Subbarao, and K. M. Mulhern. 2004. "Noncompaction of the ventricular myocardium." *Circulation* 109 (24): 2965-71. https://doi.org/10.1161/01.CIR.0000132478.60674.D0. https://www.ncbi.nlm.nih.gov/pubmed/15210614.

Wessels, M. W., and P. J. Willems. 2010. "Genetic factors in non-syndromic congenital heart malformations." *Clin Genet* 78 (2): 103-23. https://doi.org/10.1111/j.1399-0004.2010.01435.x. https://www.ncbi.nlm.nih.gov/pubmed/20497191.

Writing Group, Members, D. Mozaffarian, E. J. Benjamin, A. S. Go, D. K. Arnett, M. J. Blaha, M. Cushman, S. R. Das, S. de Ferranti, J. P. Despres, H. J. Fullerton, V. J. Howard, M. D. Huffman, C. R. Isasi, M. C. Jimenez, S. E. Judd, B. M. Kissela, J. H. Lichtman, L. D. Lisabeth, S. Liu, R. H. Mackey, D. J. Magid, D. K. McGuire, E. R. Mohler, 3rd, C. S. Moy, P. Muntner, M. E. Mussolino, K. Nasir, R. W. Neumar, G. Nichol, L. Palaniappan, D. K. Pandey, M. J. Reeves, C. J. Rodriguez, W. Rosamond, P. D. Sorlie, J. Stein, A. Towfighi, T. N. Turan, S. S. Virani, D. Woo, R. W. Yeh, M. B. Turner, Committee American Heart Association Statistics, and Subcommittee Stroke Statistics. 2016. "Heart Disease and Stroke Statistics-2016 Update: A Report From the American Heart Association." *Circulation* 133 (4): e38-360. https://doi.org/10.1161/CIR.0000000000000350. https://www.ncbi.nlm.nih.gov/pubmed/26673558.

Wu, S. M., and K. Hochedlinger. 2011. "Harnessing the potential of induced pluripotent stem cells for regenerative medicine." *Nat Cell Biol* 13 (5): 497-505. https://doi.org/10.1038/ncb0511-497. https://www.ncbi.nlm.nih.gov/pubmed/21540845.

Xin, M., E. N. Olson, and R. Bassel-Duby. 2013a. "Mending broken hearts: cardiac development as a basis for adult heart regeneration and repair." *Nat Rev Mol Cell Biol* 14 (8): 529-41. https://doi.org/10.1038/nrm3619. https://www.ncbi.nlm.nih.gov/pubmed/23839576.

---. 2013b. "Mending broken hearts: cardiac development as a basis for adult heart regeneration and repair." *Nature Reviews Molecular Cell Biology* 14 (8): 529-541. https://doi.org/10.1038/nrm3619. <Go to ISI>://WOS:000322118200014.

Xin, M., E. M. Small, E. van Rooij, X. Qi, J. A. Richardson, D. Srivastava, O. Nakagawa, and E. N. Olson. 2007. "Essential roles of the bHLH transcription factor Hrt2 in repression of atrial gene expression and maintenance of postnatal cardiac function." *Proceedings of the National Academy of Sciences of the United States of America* 104 (19): 7975-7980. https://doi.org/10.1073/pnas.0702447104. <Go to ISI>://WOS:000246461500045.

Xing, J., Y. C. Toh, S. Xu, and H. Yu. 2015. "A method for human teratogen detection by geometrically confined cell differentiation and migration." *Sci Rep* 5: 10038. https://doi.org/10.1038/srep10038. http://www.ncbi.nlm.nih.gov/pubmed/25966467.

Xu, H. S., M. Morishima, J. N. Wylie, R. J. Schwartz, B. G. Bruneau, E. A. Lindsay, and A. Baldini. 2004. "Tbx1 has a dual role in the morphogenesis of the cardiac outflow tract." *Development* 131 (13): 3217-3227. https://doi.org/10.1242/dev.01174. <Go to ISI>://WOS:000222871400017.

Yang, L., M. H. Soonpaa, E. D. Adler, T. K. Roepke, S. J. Kattman, M. Kennedy, E. Henckaerts, K. Bonham, G. W. Abbott, R. M. Linden, L. J. Field, and G. M. Keller. 2008. "Human cardiovascular progenitor cells develop from a KDR+ embryonic-stem-cell-derived population." *Nature* 453 (7194): 524-8. https://doi.org/10.1038/nature06894. https://www.ncbi.nlm.nih.gov/pubmed/18432194.

Yang, X., L. Pabon, and C. E. Murry. 2014. "Engineering adolescence: maturation of human pluripotent stem cell-derived cardiomyocytes." *Circ Res* 114 (3): 511-23. https://doi.org/10.1161/CIRCRESAHA.114.300558. https://www.ncbi.nlm.nih.gov/pubmed/24481842.

Yazawa, M., B. Hsueh, X. Jia, A. M. Pasca, J. A. Bernstein, J. Hallmayer, and R. E. Dolmetsch. 2011. "Using induced pluripotent stem cells to investigate cardiac phenotypes in Timothy syndrome." *Nature* 471 (7337): 230-4. https://doi.org/10.1038/nature09855. http://www.ncbi.nlm.nih.gov/pubmed/21307850.

Ye, K. Y., K. E. Sullivan, and L. D. Black. 2011. "Encapsulation of Cardiomyocytes in a Fibrin Hydrogel for Cardiac Tissue Engineering." *Jove-Journal of Visualized Experiments* (55). https://doi.org/UNSP e3251
10.3791/3251. <Go to ISI>://WOS:000209222100040.

Yin, J., M. Yan, Y. Wang, J. Fu, and H. Suo. 2018. "3D Bioprinting of Low-Concentration Cell-Laden Gelatin Methacrylate (GelMA) Bioinks with a Two-Step Cross-linking Strategy." *ACS Appl Mater Interfaces* 10 (8): 6849-6857. https://doi.org/10.1021/acsami.7b16059. https://www.ncbi.nlm.nih.gov/pubmed/29405059.

Yndestad, A., L. E. Vinge, R. Bjornerheim, T. Ueland, J. E. Wang, S. S. Froland, H. Attramadal, P. Aukrust, and E. Oie. 2006. "Thalidomide attenuates the development of fibrosis during post-infarction myocardial remodelling in rats." *Eur J Heart Fail* 8 (8): 790-6. https://doi.org/10.1016/j.ejheart.2006.02.007. http://www.ncbi.nlm.nih.gov/pubmed/16549389.

Yoon, B. S., S. J. Yoo, J. E. Lee, S. You, H. T. Lee, and H. S. Yoon. 2006. "Enhanced differentiation of human embryonic stem cells into cardiomyocytes by combining

hanging drop culture and 5-azacytidine treatment." *Differentiation* 74 (4): 149-59. https://doi.org/10.1111/j.1432-0436.2006.00063.x.

Yue, K., G. Trujillo-de Santiago, M. M. Alvarez, A. Tamayol, N. Annabi, and A. Khademhosseini. 2015. "Synthesis, properties, and biomedical applications of gelatin methacryloyl (GelMA) hydrogels." *Biomaterials* 73: 254-71. https://doi.org/10.1016/j.biomaterials.2015.08.045. https://www.ncbi.nlm.nih.gov/pubmed/26414409.

Zhao, X., Q. Lang, L. Yildirimer, Z. Y. Lin, W. Cui, N. Annabi, K. W. Ng, M. R. Dokmeci, A. M. Ghaemmaghami, and A. Khademhosseini. 2016. "Photocrosslinkable Gelatin Hydrogel for Epidermal Tissue Engineering." *Adv Healthc Mater* 5 (1): 108-18. https://doi.org/10.1002/adhm.201500005. https://www.ncbi.nlm.nih.gov/pubmed/25880725.

Zheng, J. W., J. M. Zhang, S. Danioko, H. Yao, H. Y. Guo, and C. Rakovski. 2020. "A 12-lead electrocardiogram database for arrhythmia research covering more than 10,000 patients." *Scientific Data* 7 (1). https://doi.org/ARTN 48
10.1038/s41597-020-0386-x. <Go to ISI>://WOS:000514649300001.

Zhou, S., F. Wang, T. C. Hsieh, J. M. Wu, and E. Wu. 2013. "Thalidomide-a notorious sedative to a wonder anticancer drug." *Curr Med Chem* 20 (33): 4102-8. https://doi.org/10.2174/09298673113209990198. https://www.ncbi.nlm.nih.gov/pubmed/23931282.

Zhu, J. M. 2010. "Bioactive modification of poly(ethylene glycol) hydrogels for tissue engineering." *Biomaterials* 31 (17): 4639-4656. https://doi.org/10.1016/j.biomaterials.2010.02.044. <Go to ISI>://WOS:000277899500004.

Zhu, W. Z., Y. Xie, K. W. Moyes, J. D. Gold, B. Askari, and M. A. Laflamme. 2010. "Neuregulin/ErbB signaling regulates cardiac subtype specification in differentiating human embryonic stem cells." *Circ Res* 107 (6): 776-86. https://doi.org/10.1161/CIRCRESAHA.110.223917. https://www.ncbi.nlm.nih.gov/pubmed/20671236.

Appendix A: Direct Production of Engineered Cardiac Tissues using Hybrid Biomaterials

Cardiovascular Tissue Engineering

Cardiovascular disease is the leading cause of death worldwide, mainly due to the heart's inability to regenerate itself after injury. The contracting cells in the heart, called cardiomyocytes, are responsible for the generation of force that propels blood throughout the body. Cardiomyocytes are a highly specialized cell type with the continual requirement to meet stringent functional demands. This provides limited potential to expend resources on cell division. It has been shown that only 1% of cardiomyocytes turnover each year up until age 25; this further reduces to 0.45% by the age of 75 (Bergmann et al. 2009). Damage to the heart can occur as a result of disease, in response to cardiotoxic compounds, or following cardiac trauma, such as myocardial infarction, or heart attack. Cardiomyocytes that experience trauma undergo apoptosis, or cell death, causing breaches in the tightly aligned muscular wall. Given the low potential of cardiomyocytes to replicate, these breaches in contractile tissue persist long-term.

The heart's lack of regenerative capacity has serious consequences for patients' health and quality of life. Following a heart attack, more than 1 billion cells can die (Gerbin and Murry 2015). The heart recruits fibroblasts and growth factors to the injury site for repair (Fan et al. 2012). This process is unable to fully reverse damage, resulting in changes to the muscular architecture (Pfeffer and Braunwald 1990) and increased tissue stiffness (Nielsen et al. 2017), leading to chronic heart failure. In addition to

trauma caused by ischemia during a heart attack, many prescribed medications are cardiotoxic, especially those used in chemotherapy. While sometimes the only effective option for treating other very serious diseases, these medications can also have long-term effects on the heart, resulting in chronic heart failure.

Tissue engineering provides promise for overcoming the challenges associated with regenerating diseased and damaged heart tissue. Cardiac tissue engineering seeks to create functional human heart tissues with electrophysiological and structural properties as similar as possible to native human heart tissue. Engineered heart tissue has the potential to improve cardiovascular outcomes both through direct use in regenerating the heart, as well as through supporting the discovery and development of new therapeutics (Dunn, Hodge, and Lipke 2014). In order to form engineered cardiac tissues, researchers largely rely on biomimetic materials, biomolecules, and stem cells, due to the inability to culture native human cardiomyocytes *in vitro,* or outside the body *(Q.Z. Chen et al. 2008)*. Biomimetic materials, or materials that mimic the biological environment, strive to provide the appropriate mechanical, electrical, and structural cues required for creating functional cardiac tissues.

Cardiac tissue engineering has made significant strides since the first man-made 3D heart tissues were formed in the mid-1900s (Eschenhagen and Zimmermann 2005). The first successes in the field involved gyrating dissociated embryonic chicken cardiomyocytes to form spontaneously beating cell aggregates that showed improved functionality over 2D cultured counterparts (Moscona 1959). Since then, a variety of cardiac tissue engineering platforms have developed including cell sheets (Shadrin et al. 2017), engineered matrices (Lesman et al. 2010; Marsano et al. 2010), decellularized

heart tissue (Ott et al. 2008), and hydrogels (Eschenhagen et al. 1997). Even with significant advancement in the field, some overarching challenges remain including vascularization, mechanical and electrical stimulation, cell population, and maturation (Hirt, Hansen, and Eschenhagen 2014; Eschenhagen et al. 2012).

Currently, cardiac tissue engineering research primarily employs two-dimensional (2D) sheets for production of cardiomyocytes. These cardiac cell sheets are either studied directly or the cardiomyocytes are dissociated and combined with a biomaterial and other cell types to create a 3D structure. These models have provided significant advances in the development of potential regenerative therapies and drug testing platforms and a mechanistic understanding of heart disease. Cardiac cell sheets have provided substantial information about the responses of interconnected cardiomyocytes to a range of mechanical, electrical, and structural stimuli, including the impact on electrophysiological function, which is substantially more challenging to study in 3D models. Since these 2D models do not accurately recapitulate the cell-cell and cell-matrix interactions found in the native human heart, dissociated and reassembled 3D cardiac tissue constructs are employed to better recapitulate these important aspects of 3D heart structure and make functional tissues. Nonetheless, this approach of dissociating cardiomyocytes to produce subsequent cardiac tissue has inherent drawbacks. In addition to the technical complexity of this multi-step approach, dissociation and reassembly of 3D cardiac tissues disrupts microenvironmental cues that are critical in human cardiac development, destroys critical cell-cell junctions required for action potential propagation and results in substantial cell loss.

For commercial production of engineered heart tissues, minimizing the complexity of production is critical. Particularly important to creating a robust production platform is minimizing cell handling steps to the greatest degree possible. Additionally, significant work is still required to overcome other barriers to commercialization including scaled-up of production, automation, utilization of fully defined materials and cell culture media, and reproducibility of 3D cardiac constructs. Important design considerations in the process of engineered heart tissue production include the choice of cardiomyocyte cell source, biomimetic materials for recapitulating 3D structure, and methodology for creating 3D cardiac tissues.

hiPSCs: A cell source for generation of cardiomyocytes

Human cardiomyocytes are a highly specialized cell type with limited regenerative capacity. Due to the inability to culture these cells *in vitro*, alternative cell sources must be used for studying cardiac regeneration and disease modeling. Current cell sources include both animal and human cells. Animal cells are often used in cardiac models due to their ease of extraction and ability to be cultured longer term (Peter, Bjerke, and Leinwand 2016). However, while animal models have provided significant insights into disease processes, they do not accurately recapitulate human disease development and are irrelevant for use in clinical cardiac regeneration. Pluripotent stem cells, i.e. cells having the potential to be differentiated into any cell type in the body, can be used for the generation of cardiomyocytes. Human pluripotent stem cell sources include embryonic stem cells and human induced pluripotent stem cells (hiPSCs), both of which can be differentiated into cardiomyocytes.

The ability to reprogram differentiated somatic cells back to a pluripotent state brought about a major transition in biomedical research, including tissue engineering. In 2006, after testing a combination of 24 transcription factors, Takahashi and Yamanaka discovered four factors capable of reprogramming somatic cells via retrovirus-mediated transfection: Oct3/4, Sox2, c-Myc, and Klf4. The newly reprogrammed cells were designated "human induced pluripotent stem cells" (hiPSCs). When compared to embryonic stem cells, they displayed similar morphology, growth patterns, and gene expression profiles. When implanted, the hiPSCs differentiated into all three germ layers, like their embryonic stem cell counterparts (Takahashi and Yamanaka 2006). Since this discovery, significant progress has been made in reprogramming technology. Increased efficiency in reprogramming, as well as more easily accessible somatic cell sources, has enabled generation of hiPSCs from thousands of patients and facilitated the incorporation of hiPSCs into disease modeling and drug screening platforms. Additionally, the first clinical trials are current in place using pluripotent stem cells for cardiac patch differentiation and implantation into patients with advanced heart failure (Menasche et al. 2015).

With the establishment of hiPSCs, personalized therapeutic and regenerative medicine are much closer to becoming a reality (Wu and Hochedlinger 2011). Using this novel stem cell technology, diseases can be modeled and studied in a more robust and accurate way than before. Now, hiPSCs can be derived from patients afflicted with genetic diseases and then differentiated, or transformed into specialized cell types, in order to study disease manifestation in the affected tissues. When somatic cells are reprogrammed to their pluripotent state, their genetic information is maintained.

Therefore, the disease-causing genetic mutation will still be present after differentiation into the affected tissue type. Several studies have shown that differentiation of patient-derived hiPSCs provides cells that demonstrate characteristics of the patient disease *in vitro* (Yazawa et al. 2011; Moretti et al. 2010a; Itzhaki et al. 2011; Davis, Casini, van den Berg, Hoekstra, Remme, Dambrot, Salvatori, Oostwaard, et al. 2012; Jiang et al. 2014a; Jung et al. 2012; Novak et al. 2012; Sun et al. 2012a). Long-term hiPSC technology has the capacity to enable personalized medicine.

By employing hiPSCs, scientists have gained the ability to generate and study human cardiomyocytes *in vitro.* This was not possible with postnatal human cardiomyocytes due to their low regenerative capacity and limited viability outside the body. Researchers in the cardiac tissue engineering field have developed a variety of differentiation protocols for directing hiPSCs to the cardiac linage, including embryoid body differentiation (Kurosawa 2007b) and 2D monolayer differentiation (Lian et al. 2013). These protocols often consist of media changes with the addition of growth factors and small molecules at various time points to drive hiPSCs toward becoming cardiomyocytes, followed by cardiac maintenance media for long term cardiomyocyte culture and maturation (Lian et al. 2013). Figure 1 shows the series of events that occur in transforming hiPSCs into hiPSC-derived cardiomyocytes (Dambrot et al. 2011b). Whereas efficiency and reproducibility of cardiac differentiation has been vastly improved in recent years, resulting cardiomyocytes are often suspended in a fetal or immature state and methodologies for hiPSC differentiation and engineered heart tissue production are frequently labor intensive, involving multiple cell handling steps. Overcoming these challenges will become instrumental in studying developmental

cardiac biology, heart disease, and regenerative medicine, as well as for use in clinical and commercial applications.

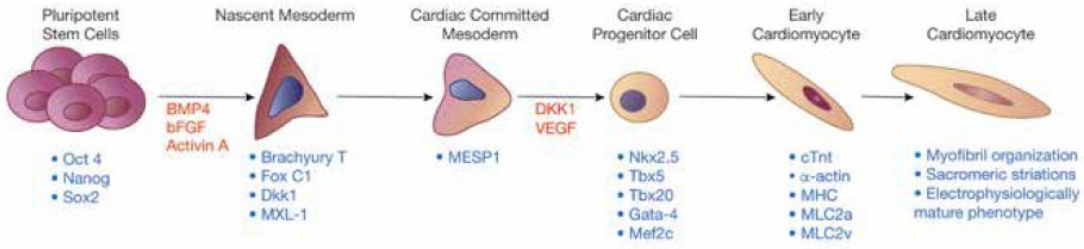

Figure A.1 Adding growth factors and small molecules (red text) causes human induced pluripotent stem cells (hiPSCs) to undergo cardiac differentiation and transition through a series of cell types before becoming adult cardiomyocytes.

Each step in the process is distinguished by a certain cell characteristic or the expression of various transcription factors (blue text) Source: Dambrot et al. Biochemical Journal. 2011; 434: 25-35

Advantages of Hybrid Biomaterials for Cardiac Tissue Engineering

With the discovery of human induced pluripotent stem cells (hiPSCs) (Takahashi and Yamanaka 2006) and advancements in highly efficient differentiation protocols (Lian et al. 2013), the potential to achieve cardiac tissue regeneration has been advanced considerably. To employ these cells to produce a physiologically relevant developing cardiac tissue, it is important to mimic the extracellular matrix (ECM) and cell-cell interactions of the native heart environment. Using biomimetic materials to encapsulate hiPSCs provides an appropriate microenvironment for maintaining cell viability and proliferation, driving differentiation, and encouraging proper cellular function (E.J. Lee, Kasper, and Mikos 2014b). Biomaterials used in cardiac tissue engineering require a

specific set of constraints for creating tissues that can appropriately integrate into the native tissue without causing arrhythmias or further tissue damage. These materials are required to withstand contractile motion and electrical signaling between cells while also allowing for vascularization to prevent tissue ischemia (Radisic 2015). Cardiac biomaterials must support cell differentiation, encourage cardiomyocyte maturation, and promote wound healing at injury sites (Q.Z. Chen et al. 2008).

Historically, naturally occurring ECM proteins have been an attractive biomaterial option for cardiac tissue engineering since they are abundant in the native heart tissue. These materials provide tissues with cell adhesion sites, support proliferation, and allow for differentiation. Several natural ECM components have been used in cardiac tissue engineering including alginate, fibrin, gelatin, and collagen (Ahadian et al. 2018). Collagen is a naturally abundant protein in the ECM of the developing heart (Gomez-Guillen et al. 2011), making it a well-suited biomaterial for supporting direct differentiation of hiPSCs to generate cardiomyocytes. However, commercially available collagen, like other natural biomaterials, presents many challenges due to immunogenicity, batch-to-batch variability, and the inability to form mechanically tunable constructs.

Although they are advantageous in terms of cellular interactions, natural biomaterials lack tunable biomechanical properties and have batch-to-batch variability. To reconcile these issues, hybrid biomaterials are often synthesized by combining a naturally occurring component with a tunable synthetic component. This enables hybrid biomaterials to support biological function while simultaneously providing a level of consistency and control of mechanical properties not possible with purely natural ECM

materials (Dunn, Hodge, and Lipke 2014). Some commonly used hybrid biomaterials used in cardiac tissue engineering include PEG-fibrinogen, poly (ε-caprolactone) gelatin, and gelatin methacryloyl.

Gelatin methacryloyl (GelMA) is a hybrid biomaterial composed of a modified natural component, gelatin, functionalized with methacryloyl groups to form a polymer precursor suitable for 3D hydrogel formation (Nichol et al. 2010). When combined, these materials create a highly tunable polymeric solution containing cell adhesion sites and structural support for tissue formation (Y.C. Chen et al. 2012).

Gelatin is derived from naturally abundant collagen found in cartilage, bones, and skin, and is formed when the collagen triple helix is destabilized and broken to form soluble gelatin coils. Two different types of gelatin, Type A and Type B, can be formed based on the acidic or basic pre-treatment methods (Gomez-Guillen et al. 2011). Derived from collagen, gelatin maintains several arginine-glycine-aspartic acid (RGD) sequences that support cell attachment. When compared to collagen, gelatin has a better solubility and a lesser chance of eliciting an immune response (Yue et al. 2015).

Methacryloyl groups are used to functionalize pure gelatin, altering the mechanical properties of the tissue engineered product. These groups allow photocrosslinking to the occur in the presence of a photoinitiator, which can be utilized for form a 3D hydrogel (Lutolf and Hubbell 2003). The degree of gelatin functionalization directly correlates with the crosslinking density. A larger degree of functionalization (DoF) increases the mechanical stiffness and decreases the porosity of the hydrogel (Van Den Bulcke et al. 2000). The methacryloyl groups are added to the gelatin via substitution of free amine groups of the gelatin backbone, as seen in Figure 2

(Nichol et al. 2010). The degree of functionalization can be controlled by reaction time, temperature, and mass ratio of gelatin to methacrylic anhydride (Loessner et al. 2016).

GelMA has a wide variety of applications in tissue engineering due to its highly tunable nature. It has been used for cardiovascular (Kerscher, Kaczmarek, et al. 2016b), skin (Zhao et al. 2016), and cartilage (Schuurman et al. 2013) formation, as well as for others. Bioprinting platforms that employ GelMA as a bioink have also been established. Based on GelMA's biological composition and tunable mechanical properties, we found that it had strong potential to support direct formation of engineered cardiac tissue through our "single cell-handling step approach" of encapsulation and 3D differentiation of hiPSCs.

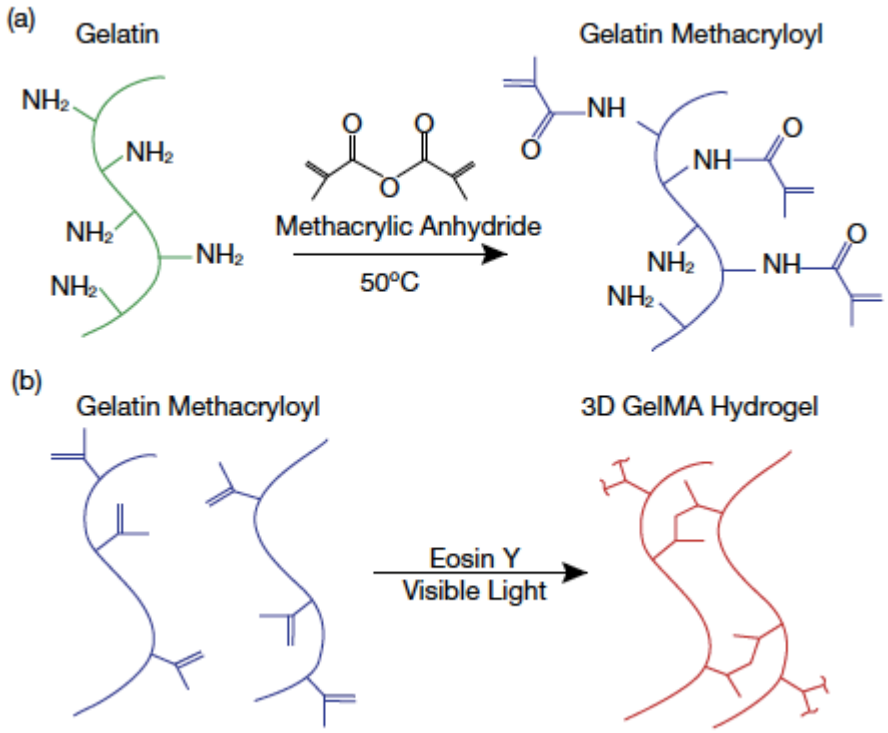

Figure A.2 Gelatin Methacryloyl is a hybrid biomaterial synthesized by functionalizing the natural component, gelatin, with synthetic component, methacrylate anhydride.

The degree of functionalization is controlled by altering the reaction parameters. In the presence of a photoinitiator, GelMA can be crosslinked with visible light to form a 3D hydrogel. Adapted from: Nichol et al., Biomaterials, 31, pp. 5536-5544 (2010)

Single Cell-Handling Step Approach to Forming Engineered Cardiac Tissue

Most protocols for creating three-dimensional cardiac tissues involve encapsulation of pre-differentiated stem cells (D.C. Nguyen et al. 2014; Turnbull et al. 2014), or tissue samples taken directly from human hearts(Shapira-Schweitzer and Seliktar 2007; Bian et al. 2014). Forming engineered cardiac tissues from pre-

differentiated stem cell requires contracting cardiomyocyte aggregates to be dissociated and then encapsulated in a 3D hydrogel biomaterial (Figure 3). The dissociation of contracting aggregates has a negative impact on cell viability and disrupts cell-cell junctions that are required for cardiac tissue development and functionality.

A newly established approach for the formation of engineered cardiac tissues is the direct encapsulation of hiPSCs, rather than pre-differentiated cardiomyocytes, within a biomimetic material, followed by subsequent differentiation into engineered cardiac tissues (Kerscher, Turnbull, et al. 2016; Kerscher, Kaczmarek, et al. 2016b). As compared to the typical approach, this method only requires a single cell-handling step. We have first shown this encapsulation technique for producing 3D cardiac tissue using hiPSCs to be successful using the hybrid biomaterial poly (ethylene glycol)-fibrinogen (PEG-fibrinogen). This encapsulation method eliminates multiple cell handling steps, most importantly the dissociation of the cardiac cell monolayer, which disrupts the critical cell-cell interactions responsible for propagating contractions. Additionally, this method enables us to study cardiac tissue development from the pluripotent state to cardiac lineage, as seen *in utero*. Using this method, we encapsulated and differentiated hiPSCs, to create 3D developing human engineered cardiac tissues (3D-dhECTs) (Kerscher, Turnbull, et al. 2016).

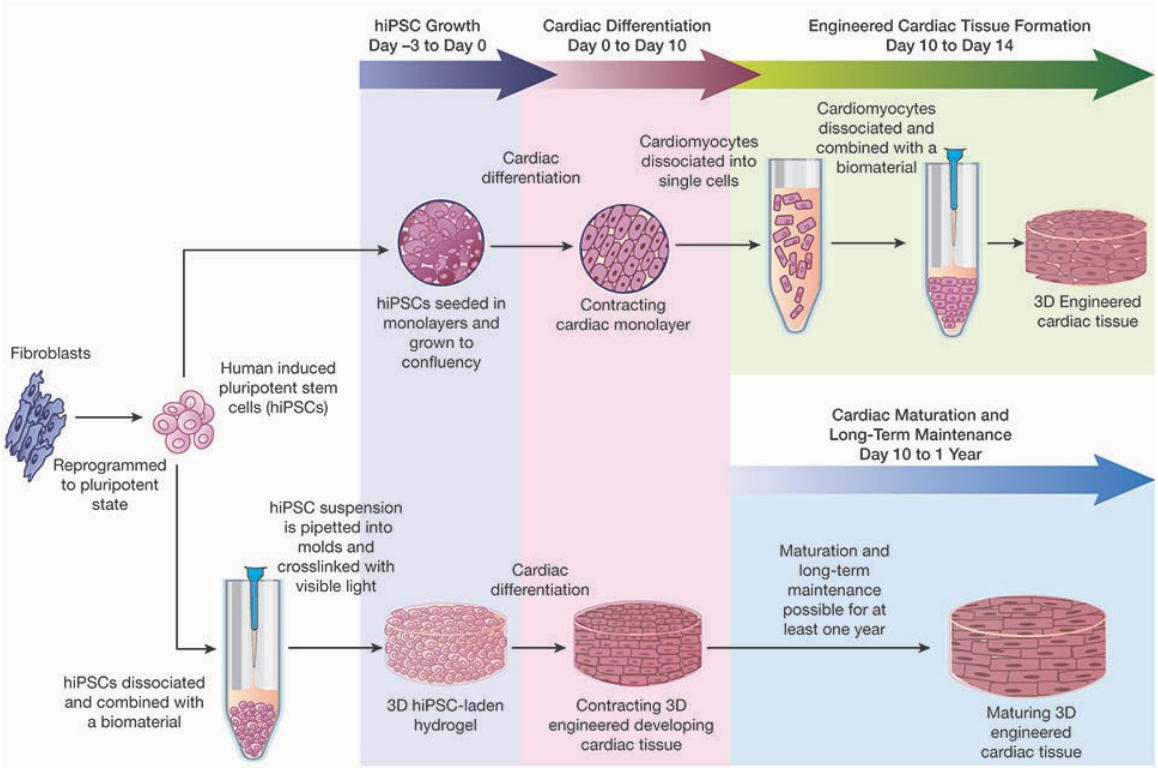

Figure A.3 Schematic representation of the cell handling steps required for classic cardiac tissue engineering compared to the single cell-handling approach developed by our research group.

(Top) Classic cardiac tissue engineering involves differentiating a confluent hiPSC monolayer into a contracting cardiac monolayer that is then dissociated and combined with a biomaterial to form a 3D engineered cardiac tissue. (Bottom) Our method combines hiPSCs with a biomaterial to form a hiPSC-laden hydrogel that undergoes direct differentiation to form 3D developing engineered cardiac tissue. This method eliminates the need for dissociating cardiomyocytes that have already formed important cell-cell interaction, while simultaneously reducing production time.

Building on this prior work with PEG-fibrinogen, we have recently produced GelMA human engineered cardiac tissues (GEhECTs) using our single cell-handling step approach. GEhECTs were formed through hiPSC encapsulation and direct differentiation in soft GelMA hydrogels (Figure 4). We began by synthesizing GelMA with 22% substitution of methacryloyl groups and test acellular hydrogels for biodegradability. Next, we formed cell-laden GelMA hydrogels by mixing hiPSCs with a GelMA precursor solution and photo-crosslinked with visible light for less than one minute. HiPSC viability was confirmed using a live/dead assay and cardiac differentiation efficiency was verified using flow cytometry. Onset of spontaneous contraction was observed in isolated areas by day 8 of differentiation with synchronous whole tissue contractions occurring by day 14. Cells in the hydrogel constructs remodeled their environment and transitioned from the round stem cell morphology to elongated cardiac muscle morphology. Temporal differentiation of cells formed a contracting tissue that increased in frequency and velocity and showed appropriate gene expression changes over time. GEhECTs-cardiomyocytes were immunostained with a marker, α-sarcomeric actinin, to visualize aligned sarcomeres, or contractile units of the cells. Lastly, cardiomyocyte functionality was validated with appropriate response to pacing and drug treatment.

Overall, our results show that GelMA is a suitable biomaterial for differentiating hiPSCs to form GEhECTs. HiPSCs survived the encapsulation process and were successfully differentiated into contracting GEhECTs, with over 70% of cells being cardiomyocytes. With a high differentiation efficiency, this process eliminated the need

to re-dissociate the cardiomyocytes post-differentiation, leaving important cell-cell interactions intact.

We now must consider the scalability of our process to make relevant numbers of engineered cardiac tissues for applications in drug testing and cardiac regeneration. Several researchers have shown the ability of GelMA to be used in bioprinting applications including tri-leaflet valve formation using human aortic valve interstitial cells (Duan et al. 2014), printed vascularization using endothelial cells (Bertassoni et al. 2014), and high viability stem cell-laden bioinks (Yin et al. 2018). These studies suggest the potential for translating our single cell handling step approach to a bioprinting platform for creating engineered cardiac tissues directly from encapsulated human induced pluripotent stem cells.

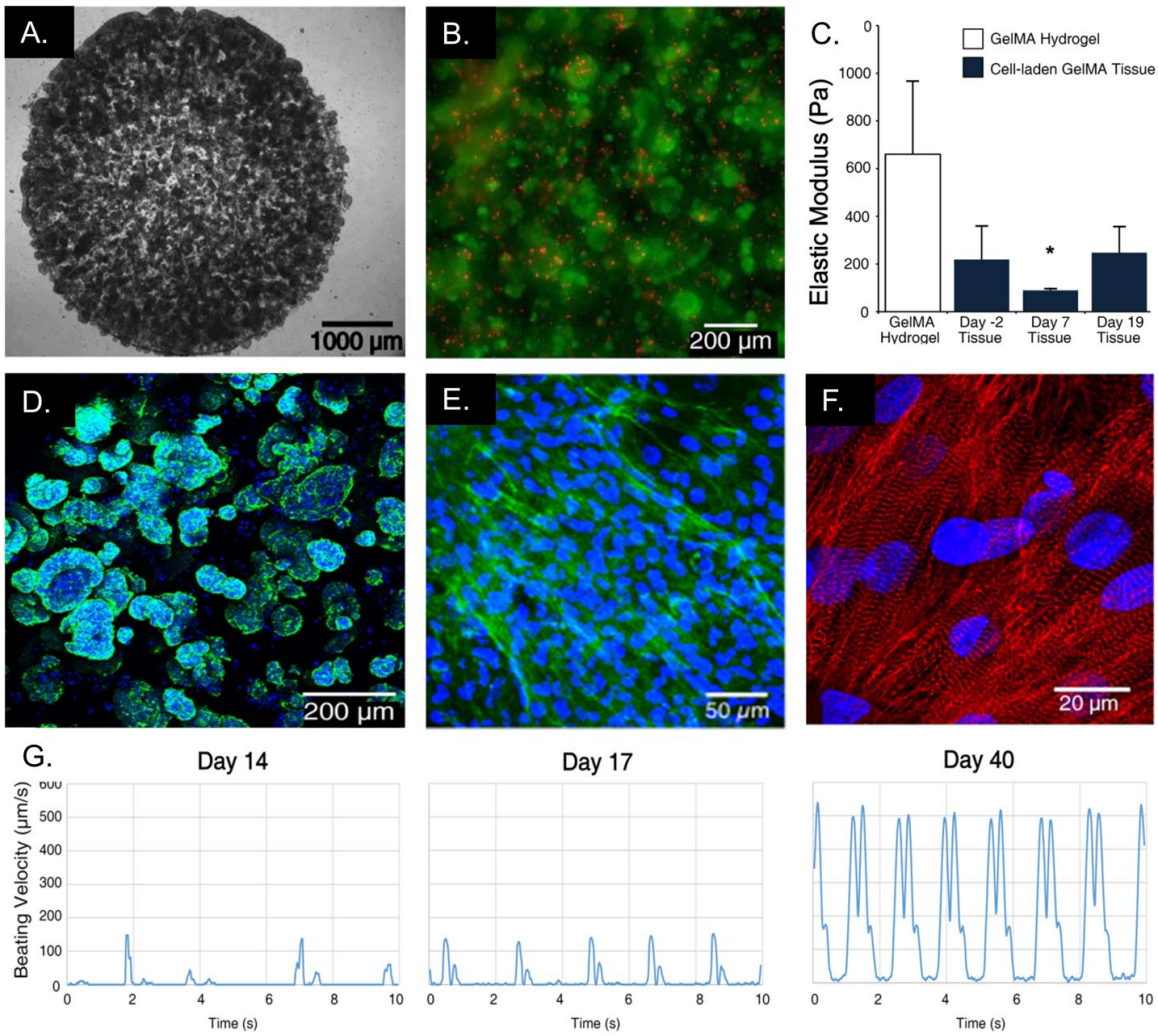

Figure A.4 HiPSCs survive encapsulation in GelMA to form soft, cell-laden hydrogels that are differentiated to produce GelMA human engineered cardiac tissues (GEhECTs).

(A) Phase contrast image showed circular 3D cell-laden hydrogel 24 h after encapsulation (day −2) with (B) the majority of hiPSCs surviving the encapsulation process (green = viable, red = dead). (C) Acellular GelMA hydrogels exhibited elastic modus of 660 ± 307 Pa; in comparison, cellular GelMA tissues 24 h after encapsulation (day −2) were softer, with an elastic modulus of 219 ± 140 Pa. Elastic modulus of the GEhECTs decreased to 90 ± 8.4 Pa by day 7. Later in the cardiac differentiation process (day 19), GEhECT elastic modulus was again higher at 248 ± 109

Pa. n = 3 tissues per group. Mean ± s.d. ANOVA P < 0.05, *vs GelMA hydrogel. (D) Three days after encapsulation (day 0), hiPSCs displayed a round cell morphology (F-actin filaments visualized by phalloidin, green) which transitioned to (E) elongated morphology by Day 22 of differentiation. (G) GEhECTs showed an increase of frequency of spontaneous contraction and contractile velocity over time shown in representative analyzed traces. n = 3−5 tissues. Mean ± s.d. ANOVA P < 0.05, *vs days 14, 17. (F) Following tissue dissociation, GEhECT-dissociated CMs locally self- aligned with each other, displaying defined and aligned sarcomeres (αSA, red). Reprinted with permission *ACS Biomater. Sci. Eng.* 3, 8, 1499-1509. Copyright 2017 American Chemical Society.

Closing Thoughts

Creating a physiologically relevant cardiac tissue engineering product for studying cardiac regeneration and disease modeling is a highly complex task. In recent years, significant research has been done in producing functional cardiomyocytes from human induced pluripotent stem cells (hiPSCs). The ability to study 3D cardiac tissues made with human cells has led to a paradigm shift in the study of cardiac disease modeling. The interactions both between the cells themselves and between the cells and the materials have been widely studied but determining appropriate materials to facilitate robust 3D cardiac differentiation and maturation has remained a challenge. In this study, we showed for the first time that the printable biomaterial gelatin methacryloyl (GelMA) can be successfully used to encapsulate and directly differentiate hiPSCs to form GelMA human engineered cardiac tissues (GEhECTs) (Kerscher, Kaczmarek, et al. 2016b). Our results show ability for GelMA to be used in a direct differentiation platform, eliminating

the need for differentiating and dissociating hiPSCs-cardiomyocytes prior to combination with a biomaterial. We can now look towards translating this direct differentiation platform to bioprinting applications for manufacturing reproducible human cardiac tissues using a single cell handling step approach.

The field of cardiac tissue engineering has made significant progress since the mid-1900s in creating a physiologically relevant tissue that mimic the native cardiac environment. However, several challenges remain including cardiomyocyte maturation and scalability. With advancements in human induced pluripotent stem cell technology and bioprinting, cardiac tissue engineering is progressing towards clinical relevance in drug discovery and cardiac regeneration.

Appendix B: Direct encapsulation and differentiation of human induced pluripotent stem cells in hybrid biomaterials to form engineered cardiac tissues

The protocol described here results in the production of 3D engineered cardiac tissue (3D-ECTs) using biomaterials and human induced pluripotent stem cells (hiPSCs). Encapsulated hiPSCs in hybrid biomaterials undergo efficient cardiac differentiation in a 3D microenvironment. Various characterization assays are described to quantify 3D-ECTs cell populations and functional properties and visualize features of maturing CMs. Resulting 3D-ECTs show 70-90% cardiomyocyte populations with increasing contraction frequency and velocity over time. 3D-ECTs produce using this protocol allow for the investigation of 3D cardiac development, disease formation and progression, and cardiac maturation over time without the need for pre-differentiated cardiomyocytes (CM).

B. 1 Introduction

Cardiovascular disease (CVD) is the leading cause of death worldwide, resulting in over 17 million deaths annually (Benjamin et al. 2017). Cardiac tissue engineering has provided significant insights for studying CVD disease mechanisms *in vitro* and has led to the production of therapeutic products for cardiac regeneration. While several methods currently exist for creating engineered cardiac tissue (ECT), these protocols often involve dissociating pre-differentiated cardiomyocytes and combining them with a biomaterial to form the resulting ECT. In these methods, important cell-cell junctions, required for

action potential propagation, are disrupted during the dissociation process resulting in 3D-ECTs that often do not mature beyond a fetal phenotype. Through direct differentiation of human induced pluripotent stem cells (hiPSCs) within 3D hydrogel constructs, a single cell-handling step platform is provided which avoids cardiomyocyte (CM) disruption and promotes formation of maturing cardiac features.

Methods for Creating Engineered Cardiac Tissues

When the heart experiences disease or damage, highly specialized CMs undergo apoptosis leaving breaches in the tightly aligned myocardium. These cells are unable to divide and regenerate, resulting in scar tissue formation that results in loss of myocardium functionality. The goal of cardiac tissue engineering is to produce tissue engineered products that aid in cardiac regeneration and provide a platform for testing therapeutics that promote regeneration. Over the years, several methods have been employed in both two-dimensional and three-dimensional platforms to produce ECT.

Due to the inability of adult CMs to replicate and be cultured long term, several methods have been employed to produce a physiologically relevant CM cell source. Early differentiation methods utilized embryoid bodies (EBs) to produce CMs from hiPSCs or human embryonic stem cells (hESCs). EBs can be formed using a variety of methods including hanging drop (M. Chen et al. 2011; Yoon et al. 2006), static suspension (Denning et al. ; Dahlmann et al.), forced aggregation (Ungrin et al. 2008; Pesl et al. 2014), and stirred suspension in bioreactors (He et al. ; Rungarunlert et al.). The hanging drop method utilizes hanging drops seeded with stem cells that are differentiated and left to form EBs which are then plated, cultured, and observed (Yoon et al. 2006). Although

this method produced contracting tissues as early as 4 days after differentiation, the resulting tissues had low differentiation efficiency (less than 50% CM populations) (Yoon et al. 2006). To form EBs from static suspension, hiPSCs are grown to confluency and dissociated into small clumps before being cultured in suspension for 7-10 days resulting in cell aggregates prior undergoing to cardiac differentiation (Kehat et al. 2001). This method produced very small percentages of spontaneously contracting CMs with only 5%-70% of EBs containing contracting CMs (Kehat et al. 2001; Batalov and Feinberg 2015). In both the hanging-drop and static suspension methods, there were size and morphology differences between the produced EBs (Hong et al.). In addition to low CM yield and experimental variability, the CMs also displayed properties consistent with immature fetal CMs (Kehat et al. 2001). Immature CMs have slower action potential propagation, weaker contractile force, and lack an extensive t-tubule network among other characteristics (Robertson, Tran, and George 2013; Batalov and Feinberg 2015). Unlike the hanging drop and static suspension methods, forced aggregation utilizes centrifugation to produce uniform EBs from single cell suspension (Ungrin et al. 2008; Hong et al. ; Pesl et al. 2014). CMs produced from this method saw contractions 14-20 days after differentiation with 33-46% of EBs contracting (Pesl et al. 2014). Recently, bioreactors have shown promise for forming uniform EBs on a larger scale with greater cardiac differentiation efficiency (Rungarunlert et al.). However, the low yield, high variability, and lack of mature CM phenotypes led to a transition towards a 2D platform for cell culture.

Currently, a majority of cardiac tissue engineering employs a 2D platform for producing CMs. Most of these protocols have hiPSCs grow to confluency on a well plate

or substrate in a 2D monolayer before inducing cardiac differentiation (Batalov and Feinberg 2015; Jeziorowska et al. 2017). 2D monolayer differentiation and culture has been shown to be a robust process for a variety of pluripotent stem cell lines with CM yields as high as 80%-95% (Batalov and Feinberg 2015; Burridge et al. 2014). However, 2D cardiac monolayers do not allow for the investigation of 3D cardiac development, tissue-level congenital heart disease formation, structural anomaly formation, and extracellular matrix-related diseases. Therefore, more physiologically relevant 3D-ECTs are desirable. Many 3D ECT protocols employ modified 2D differentiation techniques to produce CMs which are then dissociated and combined with a biomaterial to produce a 3D-ECT (Turnbull et al. 2014; Schaaf et al. 2011; Tulloch et al. 2011).

The 2D differentiated CMs used to produce 3D-ECTs displayed higher levels of maturity with larger sarcomere lengths as well as a larger percentage of bi-nucleation (average ranging from 20-35% of cells) compared to EBs (Jeziorowska et al. 2017; Herron et al. 2016). However, 2D differentiated CMs still tended to display fetal CMs characteristics such as low beat rates, altered Ca^{2+} handling, and immature sarcomeric protein content and organization (Batalov and Feinberg 2015; Jeziorowska et al. 2017). This lack of maturity may be the result of the multiple cell-handling steps associated with creating 3D-ECTs with pre-differentiated CMs, which must be dissociated before tissue formation, disrupting critical cell-cell junctions, and causing significant cell death. Therefore, a method for producing 3D-ECTs in a single cell handling step, minimizing disruption to developing CMs, could create cardiac models that more closely recapitulate native cardiac tissue.

Significant advancements have been made in the production of 3D engineered cardiac tissues since the first tissues were made over 100 years ago using dissociated embryonic chicken cardiomyocytes in a stirred flask to form beating cell aggregates (Eschenhagen and Zimmermann 2005).Since the initial cell aggregate ECT model, a variety of platforms have been implemented including: cardiac cell sheets (Shadrin et al. 2017), decellularized heart tissue (Ott et al. 2008), hydrogels (Eschenhagen et al. 1997) , and other engineered matrices (Lesman et al. 2010; Marsano et al. 2010). While these studies have provided significant advancements to the field of cardiac tissue engineering, the dissociation and reassembly of CMs disrupts important cell-cell interactions required for propagating action potentials along the cardiac tissue and prohibits the ability to study cardiac development and congenital heart disease formation in 3D. With our method, we sought to avoid CM dissociation post-differentiation and create a straightforward and robust method for producing 3D-ECTs using a variety of hiPSCs cell lines and biomaterials. This method can be used to produce uniform tissues by encapsulating hiPSCs in hydrogel materials and directly differentiating them to form 3D ECTs. The resulting 3D-ECTs show onset of spontaneous contractions on day 8 with contraction becoming more robust and synchronous by day 14. These 3D-ECTs show features of maturing CMs at late time points with highly aligned sarcomeres and T-tubules adjacent to z-lines. Additionally, these 3D-ECTs respond appropriately to pacing and drug treatment. Potential applications for these 3D-ECTs include studying cardiac development, cardiac disease modeling, extra cellular matrix disease modeling, biomanufacturing, and studying the influence of biomechanics during *in vitro* cardiac differentiation.

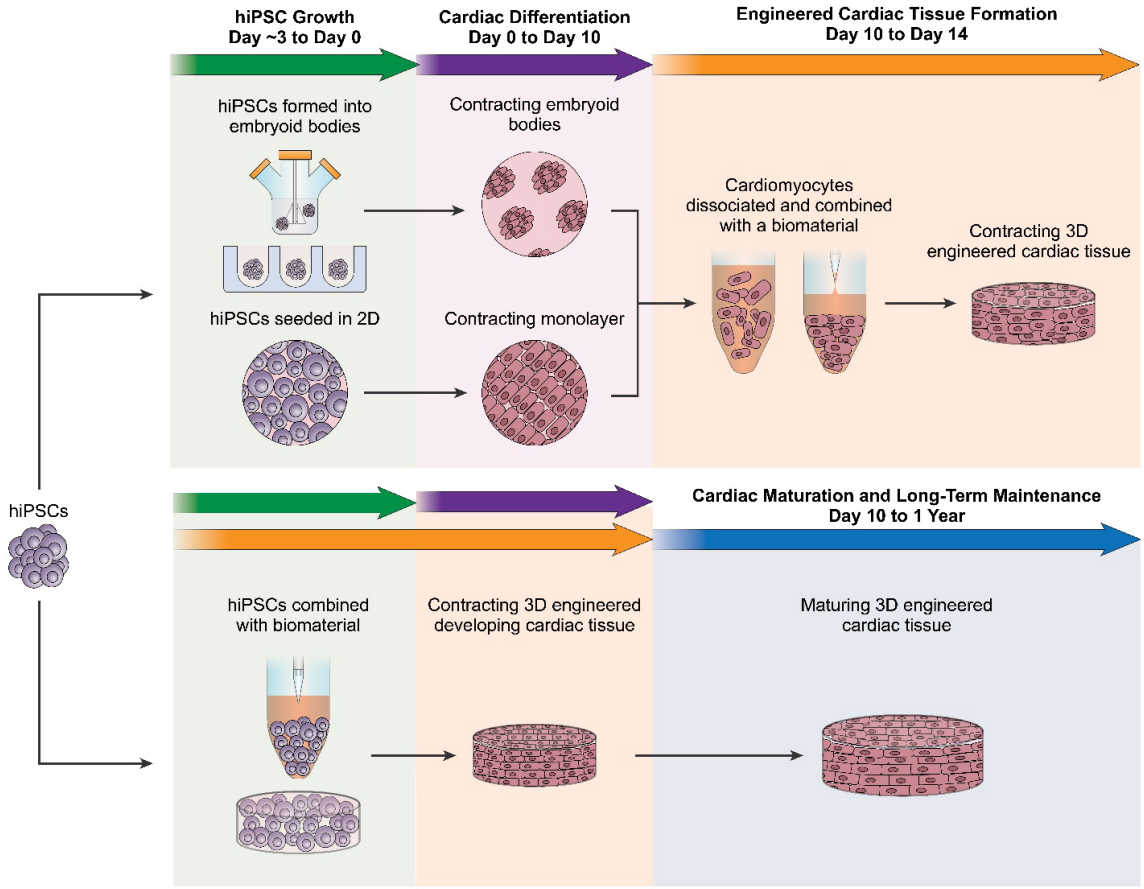

Potential applications and advantages	Cardiac tissues produced with a dissociation step following differentiation	Cardiac tissues produced through direct differentiation
Can be employed for disease modelling	+	+++
Can be used to study cardiac development	-	+++
Can be used to investigate ECM related diseases	+	+++
Can be used to study the Influence of 3D biomechanics during cardiac differentiation	-	++
Can be used for patient-specific studies (i.e. drug screening, disease mechanisms)	++	+++
Can undergo electrical and mechanical stimulation during cardiac differentiation	++	+++
Can be used for cell and tissue biomanufacturing	+	++
Can be used to support spontaneous tissue maturation without stimulation	+	+++

Figure B.1 | Direct differentiation of hiPSCs in 3D hydrogels decreases the number of cell handling steps required to produce 3D engineered cardiac tissues.

Traditionally, 2D sheets or EBs are differentiated then dissociated and combined with a biomaterial to produce an engineered cardiac tissue. This post-differentiation dissociation step disrupts important cell-cell junctions which are important for cardiac maturation. The direct differentiation method described here only requires one cell handling step which minimizes cell-cell junction interruption and enables the study of cardiac development, maturation, and disease progression in 3D tissues.

Experimental Design

Encapsulation Process

Here we present the protocol for the robust and straight-forward production of engineered cardiac tissues from hiPSCs using a single cell-handling step. HiPSCs are encapsulated within a biomaterial and directly differentiated to form contracting, functional cardiac tissues. For this process, hiPSCs are dissociated from monolayer culture and the resulting cell pellet is collected and combined with the biomaterial precursor solution. The biomaterial precursor solution consists of a photocrosslinkable biomaterial, photoinitiator, and co-initiator species (if needed). Because the biomaterial is photocrosslinkable, it can be used for rapid fabrication (less than 1 minute) of encapsulated hiPSCs. The biomaterials previously used can be photocrosslinked with visible light, which is less damaging than the traditional photocrosslinking methods using UV light. Following encapsulation, the hiPSCs maintain their pluripotency and continue

to proliferate and grow within the biomaterial microenvironment. The encapsulated hiPSCs are cultured for 3 days following encapsulation prior to initiation of cardiac differentiation. Cardiac differentiation occurs using the previously published method (Lian et al. 2013) in which Wnt signaling is activated and then inhibited using small molecules CHIR99021 and IWP-2. After cardiac differentiation, the mechanical properties of the engineered cardiac tissues can be determined, and analysis can be done for efficiency of cardiac differentiation using flow cytometry as well as gene and protein expression.

Biomaterial Selection

Biomaterials are used in cardiac tissue engineering to help recapitulate the complexities of the native 3D cardiac environment. Biomimetic materials aim to mimic the native extracellular matrix by sustaining cell viability, promoting cell proliferation and differentiation, and supporting proper cellular alignment and organization. Specific to cardiac tissue engineering, these biomaterials must be able to seamlessly integrate into the native tissue to prevent the onset of arrhythmias while withstanding constant mechanical contractions and electrical signaling as the heart beats. Cardiac biomaterials must support cardiac differentiation and maturation, and allow for vascularization to transport nutrients, oxygen, and waste.

Hybrid biomaterials combine both synthetic and natural components to create a material that is both tunable and biocompatible (Dunn, Hodge, and Lipke 2014). The synthetic portions of these materials are tunable allowing for a wide range for mechanical

properties. The natural components provide cell adhesion sites and enzymatically degradable regions that are cleaved as the cells produce their own ECM. Two hybrid biomaterials were tested in our single cell- handling hiPSC encapsulation technique: Poly (ethylene glycol) fibrinogen (PF) (Kerscher, Turnbull, et al. 2016) and Gelatin Methacryloyl (GelMA) (Kerscher, Kaczmarek, et al. 2016b). PF is synthesized by covalently coupling fibrinogen to the poly (ethylene glycol) diacrylate (PEGDA). GelMA is produced by functionalizing a gelatin backbone with methacrylate groups. Both biomaterials can be crosslinked to using visible light to form a 3D hydrogel network.

Process Robustness/Capability to vary process parameters

This hiPSC encapsulation process to produce cardiac tissues is inherently robust. Many parameters in the system are tunable based on the initial cell and material inputs as well as desired tissue characteristics. These parameters include tissue size, tissue shape, cell seeding density, biomaterial, mechanical properties, cell dissociation method, and day of induction of differentiation. The size and shape of the resulting tissues can be altered by adjusting the prefabricated PDMS mold used for holding the cell/material mixture during crosslinking. Alternatively, we have also developed a novel microfluidic system for the encapsulation of hiPSCs using a spheroidal platform (Seeto et al. 2019). Because of the advances in 3D printing, the positive caste of the desired PDMS mold can be easily printed with precision as little as 50 μm. The initial hiPSC density can be adjusted in the range of 25-75 million cells/mL for successful cardiac differentiation. This process has been successful using hybrid biomaterials PF and photoinitiator Eosin Y (Kerscher, Turnbull, et al. 2016), PF and photoinitiator LAP, printable GelMA

(Kerscher, Kaczmarek, et al. 2016b) and has the potential to be used with other biomaterials. Mechanical properties are known to influence cardiac differentiation; therefore, it is beneficial that the stiffness of the material can be adjusted during the encapsulation process to vary the microenvironment during differentiation. For this encapsulation process, initially hiPSCs are seeded in a monolayer and dissociated to be combined with the biomaterial. We have shown that this process is robust to the hiPSC dissociation method. We have used the enzymes Versene and Accutase as well as have varied the incubation temperature (37°C and RT) and resulting length of incubation (3-8 mins). Because the hiPSCs maintain their pluripotency and continue to proliferate within the biomaterial matrix, the day of induction of differentiation can be changed (from 2-5 days following encapsulation depending on initial cell density). Up to this point, the differentiation and resulting tissues have low variability between cell lines and numerous control and disease HiPSC cell lines have been used for the successful production of 3D-ECTs.

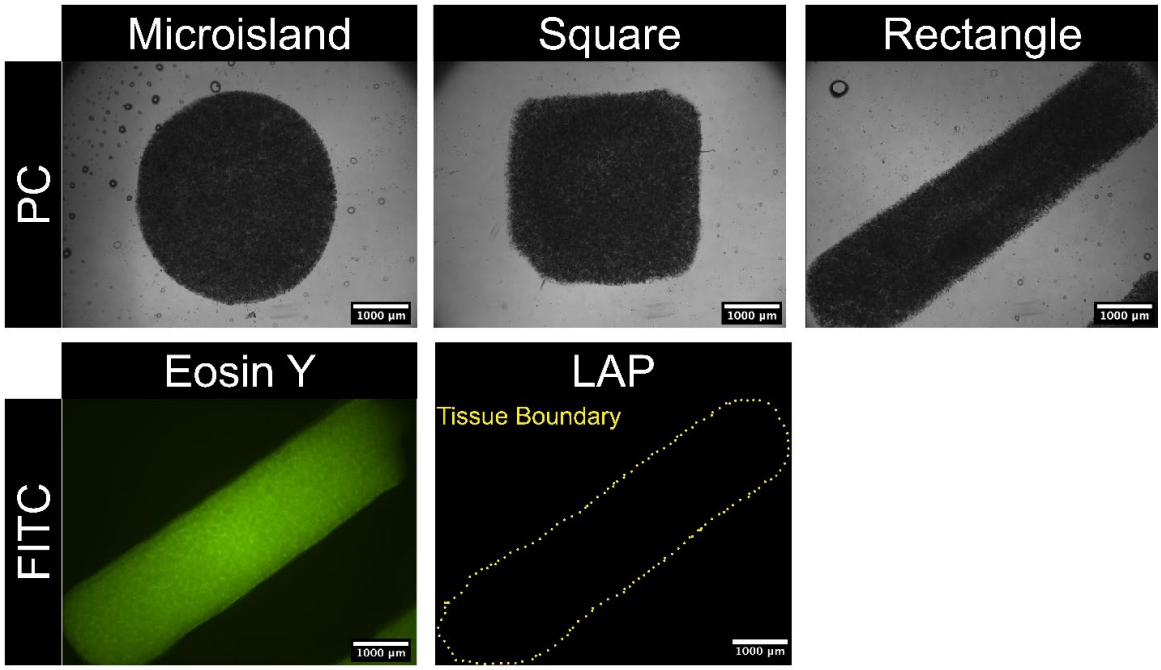

Figure B.2 | HiPSCs were encapsulated in PEG-fibrinogen hydrogels in various tissue geometries utilizing two different photoinitiators, Eosin Y and LAP.

Microisland, square, and rectangular molds and two different photoinitiators were used to test the robustness of our 3D direct differentiation method for producing engineered cardiac tissues. All three geometries were successfully differentiated 3D-ECTs. Additionally, both photoinitiators enabled successful photocrosslinking of the PEG-fibrinogen. The autofluorescence of the Eosin Y can be seen under the FITC channel while LAP displays no autofluorescence, enabling use of reporter cell lines.

Characterization of Engineered Cardiac Tissues

Following differentiation, the engineered cardiac tissues need to be characterized for efficiency of differentiation, maturity of resulting cardiomyocytes, and functionality of the tissues. To assess the efficiency of cardiac differentiation, flow cytometry was performed to quantify the percent yield of cardiomyocytes using cardiac markers cardiac

troponin T (cTnT) and MF20. For visualization of the cell distribution throughout the engineered tissues, immunofluorescence staining was performed with cardiac markers (cTnT and αSA) and functional proteins (Cx43 and Cav3). Immunostaining can be done using whole tissues as well as dissociated cells that have been re-plated for single cell analysis. Once single cells have been re-plated, the antibody αSA can be used to label CMs for analysis of sarcomere spacing and alignment, which can be compared to measurements from native tissue.

Cardiomyocytes change during development from a proliferative, fetal state and to a non-proliferative adult state shortly after birth. The differences occur in both phenotype (size, shape, and organization) and the functionality of the CMs. During maturation, CMs change their electrophysiology which impacts their resulting functionality. One of the main concerns with hiPSC derived CMs (hiPSC-CMs) is that hiPSC-CMs often maintain an immature phenotype. Using our encapsulation and differentiation protocol, we have seen features of maturing CMs, including the presence of t-tubules adjacent to Z-lines, caveolae adjacent to basement membranes, and mitochondria with well-defined cristae from TEM images as well as appropriate responses to electrical and physiological stimuli when plated on the multi-electrode array (MEA)(Kerscher, Turnbull, et al. 2016). Further assessment of the functionality can be assessed using an open-source MATLAB code (Huebsch et al. 2015a) for calculating the contraction and relaxation velocities as well as the time interval between contraction and relaxation using short (10 second) videos of contractions. Here we provide procedures for producing 3D-ECTs by directly differentiating hiPSCs in a hybrid biomaterial, including procedures for biomaterial synthesis, tissue formation, and 3D-ECTs characterization.

B.2 Materials

Reagents

- 1-vinyl-2-pryrrolidone (NVP) (Sigma-Aldrich, cat. no. V3409)
- 16% paraformaldehyde (EMS, cat. no. 15710)
- 3-(Trimethoxysilyl) Propyl methacrylate (Sigma-Aldrich, cat. no.M6514)
- Acetone
- Alexa Fluor 488 Goat Anti-Rabbit IgG Cross-Adsorbed Secondary Antibody (Thermo Fisher Scientific, cat. no. A11008)
- Alexa Fluor 569 Goat Anti-Mouse IgG Cross-Adsorbed Secondary Antibody (Thermo Fisher Scientific, cat. no. A11004)
- Alexa Fluor 647, Goat anti-mouse IgG Cross-Adsorbed Secondary Antibody (Thermo Fisher Scientific, cat. no. A-21235)
- Anti-Troponin T Cardiac Isoform (Thermo Fisher Scientific, cat. no. MA512960)
- B-27 minus insulin (Thermo Fisher Scientific, cat. no. A1895601)
- B-27 supplement (Thermo Fisher Scientific, cat. no. 17504044)
- Bisbenzimide H 33342 Fluorochrome, Trihydrochloride (Millipore Sigma, cat. no. 382065)
- Blebbistatin (VWR, cat. no. 80603-874)
- BSA (Sigma-Aldrich, cat. no. A2153)
- Calcium chloride dihydrate (Sigma-Aldrich, cat. no. C5080)
- CHIR 99021 (STEMCELL Technologies, cat. no. 72054)
- Collagenase type B (Sigma-Aldrich, cat. no. 11088815001)

- D-(+)-Glucose (Sigma-Aldrich, cat. no. G7021)
- DNAse
- DMEM/F12 (Life Technologies, cat. no. 10565018)
- Distilled Water
- DMSO
- eBioscience Foxp3 / Transcription Factor Fixation/Permeabilization Concentrate and Diluent (Invitrogen, cat. no. 00-5521-00)
- eBioscience Permeabilization Buffer (10X) (Invitrogen, cat. no. 00-8333-56)
- Eosin Y (Fisher Scientific, cat. no. E511-25)
- Ethanol solution, 70% vol/vol
- FBS (Sigma-Aldrich, cat. no. F2442)
- Fibrinogen from bovine plasma (Sigma Aldrich, cat. no. #F8630)
- Formamide
- Glacial Acetic Acid (Pharmco-Aaper, cat. no. 281000ACS)
- HEPES (Sigma-Aldrich, cat. no. H4034)
- Human pluripotent stem cell lines: IMR90 and 19-9-11 (WISC Bank) , UA16F2 (genetically encoded voltage indicator line from Gepstein Lab), T-3-5 (Timothy Syndrome Patient Line from Yazawa Lab)
- Hydrogen Peroxide (Macron fine Chemicals, cat. no. 5240-05)
- IWP-2 (STEMCELL Technologies, cat. no. 72122)
- Matrigel (Corning, cat. No. 354277)
- Magnesium Chloride hexahydrate (Sigma-Aldrich, cat. no. M0250)

- Mouse Monoclonal Alpha Sarcomeric Actinin (Sigma-Aldrich, cat. no. A7811-.2mL)
- Nucleospin RNA XS kit (Machery-Nagel)
- PBS (Lonza, cat. no. 17-517Q)
- PEG 8000MW
- PEGDA (10 kDa, Sigma-Aldrich, cat. No. 729094) (DeLong, Moon, and West 2005)
- Pierce BCA Kit (Life Technologies, cat. no. 23225)
- Potassium Chloride (Sigma-Aldrich, cat. no. P5405)
- Rabbit Anti-Connexin 43 (Sigma-Aldrich, cat. no. C6219)
- Rabbit Polyclonal to Ki67 (AbCam, cat. no. ab15580)
- Rhod-2 AM (Life Technologies, cat. no. R1245MP)
- RPMI 1640 (Life technologies, cat. no. 11875093)
- Sodium Chloride (Sigma-Aldrich, cat. no. S5886)
- Sodium Phosphate monobasic (Sigma-Aldrich, cat. no.S0751)
- Stem Cell Maintenance Media: Essential 8 (Thermo Fisher Scientific, cat. no. A157001) or mTeSR1 (STEMCELL Technologies, cat. no. 85850)
- Sulfuric Acid (J.T. Baker, cat. no. 9681-03)
- SuperScript III Platinum One-Step RT-qPCR kit (Thermo Fisher Scientific, 11732020)
- Sylgard 184 Silicone Elastomer Kit (Fisher Scientific, cat. no. NC9644388)
- Triethanolamine, 99+% (TEOA) (Acros Organics, cat. no. AC42163-0025)

- Tris(2-carboxyethyl) phosphine (TCEP) (Fisher Scientific, cat. no. AC363830010)
- Triton X-100 (Sigma-Aldrich, cat. no. X100)
- Trypsin EDTA 0.25% (Corning, cat. no. 25-053-CI)
- Urea (Sigma Aldrich, cat. no. 51456)
- Versene Solution (Thermo Fisher Scientific, cat. no. 15040066)
- Y-27632 (STEMCELL Technologies, cat. no. 72304)
- Zombie Green Fixable Viability Kit (Biolegend, cat. no. 423111)

Equipment

- Aluminum foil
- Automatic temperature controller (Warner Instrument Corporations, cat. no. TC-324B)
- Balance (Mettler Toledo, cat. no. MS204S)
- Beaker :1 liter
- Bottle: 1 liter
- Centrifuge 5702 (Eppendorf)
- Conical tubes (15 and 50 mL: VWR International cat. no. 21008-216 and 21008-242)
- Desiccator
- Dialysis Membrane Standard RC Tubing (MWCO12-14 kD; Spectrum Labs, cat. no. 132678)

- Disposable Serological pipets (5,10, and 25 mL; VWR International, cat no. 89130-896, 89130-898, 89130-900)
- Erlenmeyer Flask
- Flashlight (Ultra fire fitted with plug, Amazon)
- Flowmi Filter
- Flow Cytometer (Beckman Coulter, Cytoflex LX)
- Forceps
- Fume hood
- Glass rod
- Glass Serological Pipet (5 mL; VWR International, cat. no. 93000-696)
- Glass slides, Circular 21mm (Fischer Scientific supply store, Cat#12-544-3)
- Hemocytometer (Hausser Scientific)
- Homogenizer
- Inverted phase contrast microscope (Nikon, Eclipse Ti)
- iXon Ultra DU897 EMCCD camera (Andor)
- Microcentrifuge tube (1.5 mL; VWR International, cat.no. 87003-294)
- Microsquisher
- NanoDrop 1000 UV-Spectrophotometer (Thermo Fisher)
- Nikon A1R laser-scanning confocal microscope
- Optical mapping chamber
- Oven
- Pasteur pipet (VWR International, cat. no. 14672-380)

- Peristaltic pump (Masterflex, cat. no. 77202-60)
- Pipet Aid
- Pipet Tips (10,100, wide orifice 100, 1000, and wide orifice 1000 µL; VWR International, cat. no. 89079-464, 89079-476, 89079-464, 89079-486, 89079-486)
- Pipettor (P1000 µL, P100 µL, P10 µL; Eppendorf))
- Positive Caste for PDMS molds
- Separatory Funnel (500 mL)
- Staining Dish
- Sterile 6 Well Plate (Corning
- Sterile Biosafety Cabinet (Laconoco)
- Sterile Incubator (Humidified, 37°C, 5% CO_2)
- Sterile tissue paper
- Stimulator (Grass SD9)
- Stir bar
- Stir Plate
- Thermal cycler (Bio-Rad, cat. no. CFX96)
- Vacuum filter/storage systems (250 mL and 500mL, Corning, cat. no. 431096 and 431097)
- Vacuum Pump
- Vortex (VWR Scientific Products)
- Water Bath (Thermo Scientific)

Reagent Setup

20% PEG Solution Dissolve 2 grams of PEG 8000MW in 10mL of 37 °C DI water on a stir plate for 30 minutes.

40% PEG Solution Dissolve 4 grams of PEG 8000MW in 10mL of 37 °C DI water on a stir plate for 30 minutes.

50% Formamide Combine equal volumes of 100% Formamide and DI water.

50% Formamide/20% PEG clearing solution Combine equal volumes of 100% formamide and 40% PEG Solution.

25% Formamide/10% PEG clearing solution Combine equal volumes of 50% Formamide and 20% PEG Solution

Blocking Buffer (50 mL, 1% BSA and 10% FBS) Dissolve 50 mg of BSA in 4.5 mL of FBS and 41.5 mL of PBS. Sterile filter with a 0.2 μM filter. Store at 4 °C for 1 month.

CHIR99021 (36 mM) Add 596 μL of DMSO 10 mg of CHIR99021. Aliquot and store at -20 °C for 1 year.

Collagenase type B solution (50 mL, 1 mg/mL) Dissolve 50 mg Collagenase type B in 50 mL PBS (100 units/ml). Filter-sterilize using a 0.2 μm filter. Aliquot and store at 4 °C for a week or 20 °C for up to 1 year. Avoid freeze thaw cycles.

Day 0 Media: RPMI B-27 without insulin + 12 μM CHIR99021 (12 mL) Add 4 μL of 36 mM CHIR99021 into 12 mL of RPMI B-27 without insulin. Do not store longer term.

Day 3 Media: RPMI B-27 without insulin + IWP2 (12 mL) Add 12 μL of 5mM IWP2 to 6mL of fresh RPMI B-27 without insulin and 6 mL of RPMI B-27 without insulin from the well plate containing the tissues.

E8 + 5 μM Y27632 Add 10 μL of 5mM Y27632 to 10 mL of E8 for a final concentration of 5 μM Y27632. Store at 4 °C for 2 weeks.

FACS buffer (20 mL, 1% BSA and 10% FBS (vol/vol)) Dissolve 200 mg of BSA in 2 mL of FBS and 18 mL of Permeabilization buffer 1X. Sterile filter using a 0.2 μm filter. Store at 4°C for 1 month.

IWP2 (5 mM) Add 4.28 mL of DMSO to 10 mg of IWP2 and incubate at 37 °C for 10 minutes. Aliquot and store at -20 °C for 1 year.

Matrigel Aliquots Thaw Matrigel on ice at 4°C. Place sterile 1.5mL tubes and P1000 tips in the freezer for 1 hour prior to aliquoting. Aliquot Matrigel based on company provided dilution factor for producing 24mL of Matrigel/ DMEM/F12 suspension. Store at -80 °C for up to 2 years.

mTeSR1+5 μM Y27632 Add 10 μL of 5mM Y27632 to 10 mL of mTeSR1 for a final concentration of 5 μM Y27632. Store at 4 °C for 2 weeks.

Paraformaldehyde, 4% (vol/vol) Add 1 part 16% paraformaldehyde to 3 parts PBS. We do not recommend storing this solution.

Permeabilization buffer (1X) Add 5mL of Permeabilization buffer 10X to 45mL of distilled water. Sterile filter with 0.22 μm filter.

PBS-T (500 mL, 10% (vol/vol)) Add 5 grams of BSA and 1 mL of Triton X-100 to 500 mL of PBS. Filter using the 500mL Corning Vacuum filtration system. Store at 4°C for up to 6 months.

RPMI 20 (50 mL) In a sterile biosafety cabinet, add 10 mL of FBS to 40 mL of RPMI 1640. Sterile filter using a 0.22 μm filter. Store at 4°C for 1 month.

RPMI/B27 (510 mL) In a sterile biosafety cabinet, mix 10mL of B-27 supplement with 500mL of RPMI 1640. Store at 4°C for 1 month.

RPMI/B27 without insulin (510 mL) In a sterile biosafety cabinet, mix 10mL of B-27 without insulin supplement with 500mL of RPMI 1640. Store at 4°C for 1 month.

Tyrode's 5X Base Solution (1 Liter) Dissolve 5.9575 g/L of HEPES, 1.0165 g/L magnesium chloride hexahydrate, 2.0142 g/L of Potassium Chloride, 39.42 g/L sodium chloride, and 0.198 g/L sodium phosphate monobasic in 1 liter of ultrapure water. Store at 4 °C for 1 month.

Y27632 (5 mM) In a sterile biosafety cabinet, add 6.24mL of PBS to 10 mg of Y27632. Aliquot and store at -20 °C for 1 year.

Tyrode's 1X solution with blebbistatin (100 mL) Dissolve 90.1 mg of D-(+)- glucose in 20mL of Tyrode's 5X Base Solution, 10 mL of Calcium Chloride 10X solution, and 70 mL of ultrapure water in 100 mL bottle. Warm the solution to 37 °C on a heated stir plate. At 37 °C, pH the solution to 7.4. Add 100 μL of blebbistatin (10 μM) . Do not store long term.

Calcium Chloride Solution 10X (100 mL) Dissolve 265 mg of Calcium chloride dihydrate in 100 mL of ultrapure water. Store at 4 °C for 1 month.

Equipment Setup

Matrigel-coated plates and coverslips Resuspend one Matrigel aliquot in 1 mL of ice cold DMEM/F12. Add suspension into 23mL of ice cold DMEM/F12. Coat 6-well plates with 1mL/well of Matrigel solution. To coat glass coverslips, sterilize 21mm circular

glass coverslips under UV light overnight. Place coverslips in a 12 well plate. Add 500 µL of Matrigel solution to each coverslip. Allow solution to cure at room temperature for 30 minutes. After 30 minutes, add an equal volume of DMEM/F12 to each well. Store in sterile incubator at 37°C for up to two weeks.

PDMS molds (Sonicate in a 70% ethanol solution for 1 hour and allow to dry in the biosafety cabinet prior to encapsulation)

B.3 Procedure

Piranha cleaning and acrylation of glass coverslips • Timing: 24 hours

! CAUTION Piranha solution is highly corrosive and extremely exothermic. Double nitrile gloves, lab coat and face shield are recommended when working with this solution. Perform piranha cleaning in a chemical fume hood.

! CAUTION Organic solvents are highly reactive in Piranha solution.

CRITICAL Clean all glassware 24 hours prior to use and allow to dry in oven.

1) Prepare Piranha solution: 70% sulfuric acid, 30% hydrogen peroxide. Add 70 mL of sulfuric acid to the staining dish. Slowly add 30 mL of hydrogen peroxide to the staining dish while gently stirring with a glass rod. Allow to cool for 10 minutes.

2) Rinse circular glass slides with distilled water to remove excess debris prior to placing them in the staining dish. Submerge glass slides in Piranha solution and cover with lose fitting glass lid. Clean for approximately 20 minutes.

3) Remove glass slides from the Piranha solution and rinse with distilled water. Place the slides in a clean container to dry. Dispose of Piranha waste according to your institution's approved guidelines.

4) Prepare acrylation solution (100mL). Mix 0.26 mL glacial acetic acid in 2.64 mL of distilled water in a small beaker. Add 97 mL of ethanol 200-proof to the staining dish. Dilute 0.48 mL of 3-(Trimethoxysilyl) propyl methacrylate in the ethanol. Add the diluted acetic acid mixture. Stir for 2 minutes using a stir plate prior to adding glass slides.

5) Add the previously piranha cleaned glass slides to the staining dish. Seal the dish with parafilm. Acrylate for 12 hours or overnight while gently stirring.

6) Remove the slides from the acrylation solution and rinse with ethanol. Allow slides to dry and store at 4°C for up to 1 month. Prior to cell encapsulation, sterilize glass slides under UV in the biosafety cabinet.

PDMS Mold Preparation • *Timing: 2.5 hours*

CRITICAL Amount of Slygard 184 silicone elastomer base is determined by the number of molds being made at one time. Adjust volume accordingly.

7) Pour desired amount of Sylgard 184 silicone elastomer base into the weighing dish. Add the Sylgard 184 silicone elastomer curing agent in a 1:10 ratio to the base. Mix thoroughly for 4-5 minutes with the plastic spatula.

8) Place the weighing dish with the mixture in the desiccator and turn on the vacuum pump. This will degas the mixture and bring bubbles to the surface. Disconnect the pump after 10 minutes to allow pressure change to pop the bubbles. Reconnect pump to the desiccator and continue degassing. Repeat this process until all the bubbles are removed from the mixture.

9) Pour the mixture onto the desired positive mold. Cure at 70° C for 2 hours or room temperature for 8 hours. After curing, remove PDMS mold from cast and sterilize in 70% ethanol.

PF Synthesis (10mg/ml) • *Timing: 24 hours*

CRITICAL Clean all reaction vessels with acetone prior to use.

10) Prepare 4 liters of PBS. Prepare 8M PBS-Urea by adding 72.072 grams of urea and PBS to a final volume of 150mL. Adjust the pH to 7.4.

11) Dissolve 0.3 grams of fibrinogen in 42.86 mL PBS-urea in a 250mL Erlenmeyer flask. Stir slowing to avoid foaming. Filter the solution into a new reaction vessel using a 0.22 µm button filter. Add 0.002253 grams of TCEP. Adjust pH to 8

CRITICAL The protein concentration of denatured bovine fibrinogen varies. Protein concentration should be determined using Pierce BCA for each new bottle. The protocol requires 0.3 grams of 100% pure denatured bovine fibrinogen. For example, a bottle that contains 80% fibrinogen requires 0.375 grams to achieve the same concentration.

12) Combine 1.9392 grams of PEGDA 10 kDa(DeLong, Moon, and West 2005) and 6.93 mL of PBS-urea in a 50 mL centrifuge tube. Vortex on high for 2 to 3 minutes. Centrifuge for 3 minutes at 2500RPM until the solution is clear.

13) Add the PEGDA solution to the Fibrinogen solution in the 250 Erlenmeyer flask. Cover with foil and place on stir plate. Allow to react for 3 hours at room temperature. **CRITICAL** From this point forward, all steps should be performed in the dark.

14) Transfer the reaction solution to a 500mL flask and dilute with 49.78 mL of PBS-urea. Stir for 1 minute.

15) Transfer solution to a 500 mL separatory funnel. Add 398.26 mL of acetone, insert cork, and vigorously shake until uniform homogeneity is reached. Allow mixture to rest for 15-20 minutes. PEGylated Fibrinogen should precipitate to the bottom on the flask. **CRITICAL** Vent separatory funnel periodically during shaking to avoid pressure buildup.

16) Collect the precipitate in a 50 mL centrifuge tube. Centrifuge mixture for 2 minutes at 2500 RPM to separate the acetone from the product. Weigh the precipitate and dissolve in 2.6 mL of PBS-urea/gram of precipitate. Use the homogenizer to ensure complete dissolution.

CRITICAL Weigh the 50mL centrifuge tube prior to collecting precipitate.

17) Dialyze the product against 1L of PBS at 4°C for 24 hours, changing the PBS every 8 hours. Remove the product from the bag and store in 1 mL aliquots at -80°C for up to 1 year. Characterize the PF.

i) Crosslinking: Prepare the polymer precursor solution as described below. Crosslink the mixture using visible light for 30 seconds.

ii) BCA Assay: Perform Pierce BCA assay according to the company's instructions.

Bringing hiPSCs up from freeze • Timing: 15 minutes

18) Add 5 mL of mTeSR to a 15mL tube. Remove frozen vial of hiPSCs from cryostorage and gently rub between cryogenic glove covered hands. Spray the vial with 70% ethanol and place it in a sterile hood. Gently open the lid to release the pressure build-up. Re-seal the vial and gently swirl it in a 37 °C water bath until a small chunk of ice remains. Sterilize the vial and place it back in the biosafety cabinet.

19) Using a P1000 tip, add the cell suspension to the 5mL of mTeSR in the 15mL tube while gently swirling the tube. Centrifuge for 5 minutes at 200g.

20) Aspirate the supernatant form the hiPSC pellet. Remove the liquid from one well of a Matrigel-coated plate and add 2mL of mTeSR + 10µM Y27632 to the well. Resuspend the cell pellet in 500 µL of mTeSR + 10µM Y27632 and add to the well plate. Place the well plate into a 37°C, 5% CO_2 incubator and gently shake the well plate in all directions to evenly distribute the cells in the well.

21) On the following day, remove the spent media and add 2mL of fresh mTeSR to the well. Continue Step 21 for 3-4 days until hiPSCs are ready to passage at 70-

90% confluency. The number of days it takes to reach 70% confluency is highly dependent on the number of hiPSCs per frozen vial.

Passaging hiPSCs • Timing: 15 minutes

22) Passaging can be performed using a variety of dissociation enzymes, incubation times and temperatures. HiPSC dissociation method should be selected based on the cell line being used. Passaging should be performed when the cells are between 70-90% confluency.

(A) Passing hiPSCs with Versene

iii) Remove the old media and wash cells with 1mL of room temperature sterile PBS. Remove PBS and add 1mL of Versene to each well. Incubate for 4.5 minutes in a 37°C, 5% CO_2 incubator OR 7 minutes at room temperature in the sterile biosafety cabinet.

iv) Carefully aspirate Versene making sure not to touch the bottom of the well plate. Rinse cells off the well plate using 1mL of mTeSR + 10µM Y27632 in a P1000 tip. Collect cell suspension in a 15mL tube.

v) Remove excess solution from Matrigel-coated wells. Add 2mL of mTeSR + 10µM Y27632 to each well. Add cell suspension at desired split ratio. Typically, the split ratio ranges between 1:5 and 1:20 depending on the cell line. Here, this means between 50 to 200 µL of cell suspension should be added to each well.

(B) Passing hiPSCs with Accutase

i) Remove the old media and wash cells with 1mL of room temperature sterile PBS. Remove PBS and add 1mL of Accutase to each well. Incubate for 2.5 minutes in a 37°C, 5% CO2 incubator OR 4 minutes at room temperature in the sterile biosafety cabinet.

ii) Rinse cells off the well plate using 1mL of mTeSR + 10µM Y27632 in a P1000 tip. Collect cell suspension in a 15mL tube. Centrifuge for 5 minutes at 200g. Aspirate supernatant and resuspend cell pellet in 1 mL of mTeSR + 10µM Y27632.

iii) Remove excess solution from Matrigel-coated wells. Add 2mL of mTeSR + 10µM Y27632 to each well. Add cell suspension at desired split ratio. Typically, the split ratio ranges between 1:5 and 1:20 depending on the cell line. Here, this means between 50 to 200 µL of cell suspension should be added to each well.

Polymer Precursor Preparation: 100µL • Timing: 5 minutes

CRITICAL Polymer precursor volume can be scaled based on number of encapsulations. Allow materials to come to room temperature before using. Turn off lights in the biosafety cabinet.

23) Add 100 µL of PF to the microcentrifuge tube. Add 1.5 µL of TEOA to the PF.

CRITICAL This solution is very viscous. Be cognizant that it will move very slowly into and out of the pipet.

24) Add 0.39 µL of NVP to the mixture. Add 1 µL of 10mM Eosin Y for a final concentration of 0.1 mM. Cover with foil. Vortex for 20 seconds to mix.

HiPSC Encapsulation Technique • Timing: 30 minutes

25) Remove spent media from one well/flask of 80-90% confluent hiPSCs. Rinse the cells with 1 mL of Versene, gently shaking back and forth for about 20 seconds. Remove spent Versene. Add 1 mL of fresh Versene to the hiPSCs and place in the incubator for approximately 4.5 minutes.

26) After 4.5 minutes, remove the well plate from the incubator and aspirate the Versene. Remove the cells from the well plate by rinsing the surface with 2 mL of Stem Cell Maintenance media using 5 mL glass pipet. **CRITICAL** Choose which ever hiPSC dissociation protocol is bets for your cell line. **CRITICAL** Limit the amount of mixing to prevent the disruption of cell colonies. Small hiPSC colonies are desired for cardiac differentiation.

27) Collect the 2 mL cell suspension in a 15 mL centrifuge tube. Remove 10 µL of cell suspension for cell counting using the hemocytometer. Centrifuge the cell suspension for 5 mins at 200g.

28) During centrifugation, place the thick glass slide on the white sterile tissue. Place a PDMS mold on the acrylated circular glass coverslip and use the forceps to press the mold, forming a seal. Place the prepared mold and glass on top of the thick glass slide.

29) After centrifugation, there should be a cell pellet formed in the bottom of the tube. Carefully aspirate the media away using the thin glass aspirating pipet, leaving only the cell pellet in the tube. **CRITICAL** You may need to invert the tube to get every bit of media. Any media not removed from the pellet will disrupt crosslinking.

30) Gently tap to break up the cell pellet. Add required amount of polymer precursor solution for desired cell density using a wide orifice pipet. For example, if you have 2 million hiPSC, add 33µL of precursor solution to the cell pellet for a final cell density of 60 million cells per mL. Slowly pipet the mixture up and down approximately 3 times to evenly mix the cell in the polymer precursor. After mixing discard pipet tip and set the pipet to 8 µL.

31) Pipet 8 µL of cell suspension into each well of the PDMS mold. Apply visible light by shining the flashlight on the mold for 30 seconds approximately 0.5 cm from the mold. Make sure to have even coverage of light on all tissues. After 30 seconds, turn off the light and use two forceps to peel the PDMS mold off the acrylated glass, leaving the tissues on the glass. **?TROUBLESHOOTING**

32) Place the glass with the tissues into one well of a sterile 6 well plate using the forceps. Add 3 mL of Stem Cell Maintenance media to the tissues. **CRITICAL** Make sure the glass coverslip does not float on top of the media. This represents Day -3 of differentiation. On days -2 and -1 feed with 3 mL of Stem Cell Maintenance media. Start the differentiation process on Day 0. **?TROUBLESHOOTING**

Cardiac differentiation with CHIR99021 and IWP2 • Timing: 7 Days + long term culture

33) On Day 0 of differentiation, aspirate the Stem Cell Maintenance media from each well. Add room temperature RPMI/B27 w/o insulin supplemented with 12 μM CHIR99021 (4 mL/well for a 6 well plate). **CRITICAL** Note the time that the RPMI/B27 w/o insulin supplemented with 12 μM CHIR99021 was added. This should be the time that feedings on Day 1,3,5, and 7 should occur.

34) Exactly 24 hours after adding the day 0 media, remove the spent media and add 4 mL of RPMI/B27 w/o insulin to each well of a 6-well plate.

35) Exactly 72 hours after adding day 0 media, prepare day 3 media by removing 2 mL of media/well and combining it with 2 mL/well of fresh RPMI/B27 w/o insulin supplemented with 4 μL of 5 mM IWP2 for a final concentration of 5 μM IWP2.

36) On day 5 of differentiation, remove the spent media and add 4 mL/well of RPMI/B27 w/o insulin to each well.

37) Finally, on day 7 of differentiation remove the spent media and add 4 mL/well of RPMI/B27 to each well.

38) Perform media changes with 4 mL/well of fresh RPMI/B27 every 3-4 days for long term culture or use in characterization experiments.

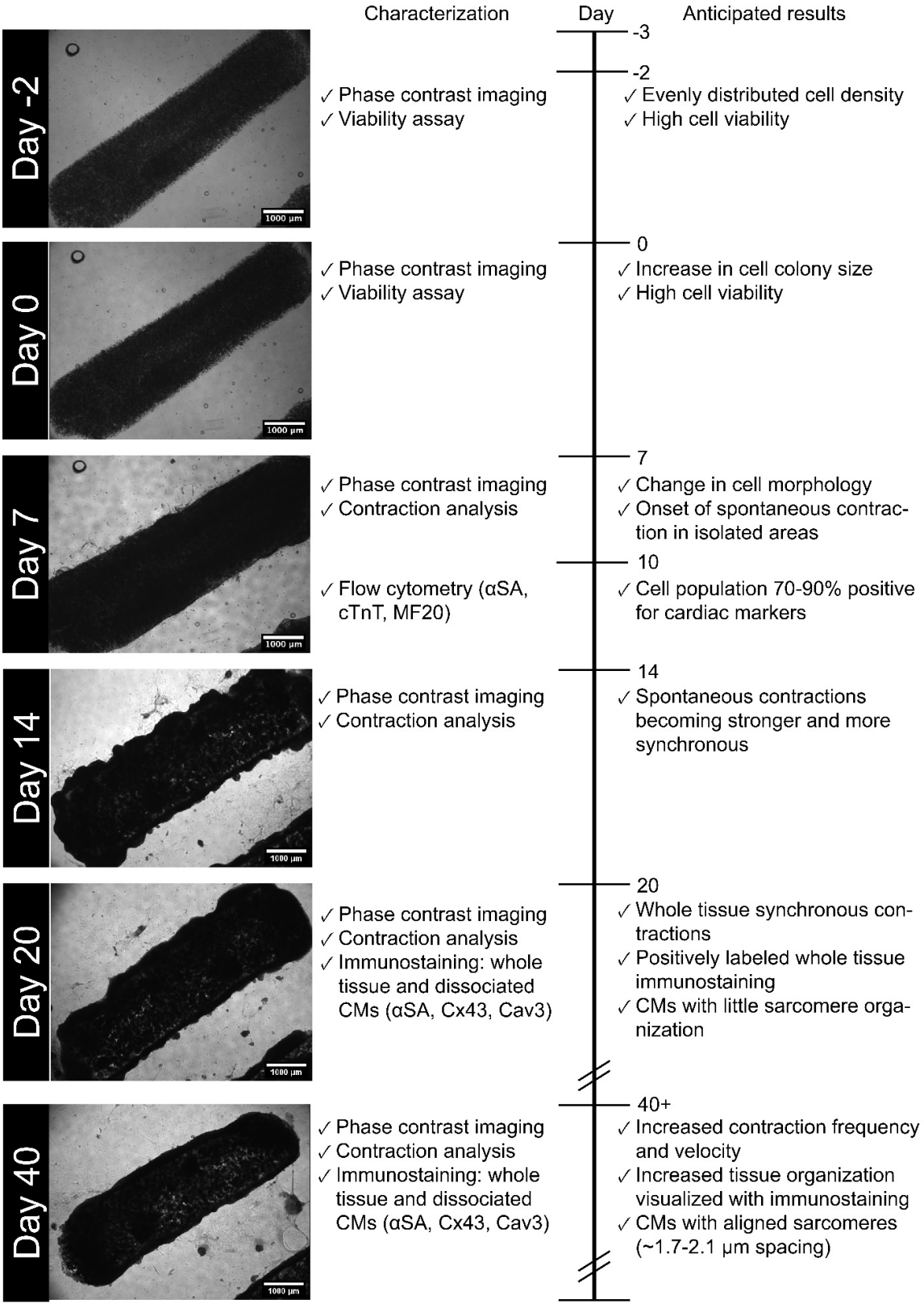
Characterization
Day
Anticipated results
Day -2
1000 µm
✓ Phase contrast imaging
✓ Viability assay
-3
-2
✓ Evenly distributed cell density
✓ High cell viability
Day 0
1000 µm
✓ Phase contrast imaging
✓ Viability assay
0
✓ Increase in cell colony size
✓ High cell viability
Day 7
1000 µm
✓ Phase contrast imaging
✓ Contraction analysis
7
✓ Change in cell morphology
✓ Onset of spontaneous contraction in isolated areas
✓ Flow cytometry (αSA, cTnT, MF20)
10
✓ Cell population 70-90% positive for cardiac markers
Day 14
1000 µm
✓ Phase contrast imaging
✓ Contraction analysis
14
✓ Spontaneous contractions becoming stronger and more synchronous
Day 20
1000 µm
✓ Phase contrast imaging
✓ Contraction analysis
✓ Immunostaining: whole tissue and dissociated CMs (αSA, Cx43, Cav3)
20
✓ Whole tissue synchronous contractions
✓ Positively labeled whole tissue immunostaining
✓ CMs with little sarcomere organization
Day 40
1000 µm
✓ Phase contrast imaging
✓ Contraction analysis
✓ Immunostaining: whole tissue and dissociated CMs (αSA, Cx43, Cav3)
40+
✓ Increased contraction frequency and velocity
✓ Increased tissue organization visualized with immunostaining
✓ CMs with aligned sarcomeres (~1.7-2.1 µm spacing)

Figure B.3 | Representative phase contrast images throughout cardiac differentiation and long-term culture (Day -2, 0, 7, 14, 20, and 40) show engineered cardiac tissue progression.

Differentiation timeline of the protocol including characterization and anticipated results of directly differentiated 3D cardiac tissue at key time points from day -3 to day 40+.

Characterization of Engineered Cardiac Tissues

39) On day 7-8 of cardiac differentiation, the 3D-ECTs should show onset of spontaneous contraction and express cardiac-specific markers. **?TROUBLESHOOTING** Tissue can be dissociated for immediate analysis or cultured long term for future analysis. To quantify the differentiation efficiency, dissociate the 3D-ECTs on between Day 10-12 and perform flow cytometry using cardiac markers alpha sarcomeric actinin and cardiac troponin T. To characterize the mechanical contractions of the tissue, perform video analysis and quantification using an open-source MATLAB code (Huebsch et al. 2015a). To visualize cardiac features, perform whole tissue and dissociated tissue immunostaining using cardiac-specific markers.

(A) Mechanical Properties • Timing: 15 minutes/sample

Parallel plate compression was used to determine the Young's Modulus of the 3D-ECTs using a micron-scale mechanical testing system referred to as the

Microsquisher (CellScale). All measurements occurred in 37°C PBS where the stress (σ) and strain (ε) were calculated from spheroid force, area, and compression height. The Young's modulus was determined from the linear range of the stress versus strain curve.

40) Set up Microsquisher system by first turning it on and calibrating the camera. Attach the cantilever to the compression plate using super glue and Loctite accelerator. The cantilever/compression plate apparatus should then be attached to the grip (glue side up). **CRITICAL** Be sure the grip and cantilever form a 90° angle and that the compression plate is completely flat. Measure the distance between the center of the grip and the center of the compression plate in mm and record information under "Equipment Settings. Finally, attach the grip and cantilever apparatus to the Microsquisher using the provided screws and push the stage against the wall of the chamber.

41) When preparing a sample for testing, use a micropipette or forceps to place the hydrogel sample (or microsphere) on the stage. Align and focus the camera so that the sample is in the middle of the screen.

42) After aligning the sample, "squish" the sample 2-3 times to remove media by bringing the compression plate down and moving it back up. After priming the sample, raise the compression plate so that it is resting on the top surface of the sample.

43) To initialize the software, first set the height of the sample by placing one target on the top at the level of the compression plate and the other on the bottom. Then right click on an area with a large light/dark contrast to set the tracker (green

rectangle). In “Equipment Settings”, set the compression speed to 2.5 µm/s and set the compression magnitude as at least half of the height of the sample (in µm). Finally, Adjust the loading duration by dividing the compression magnitude by the compression speed.

44) To test the sample, click the “Run” button and wait for the test to be complete. To perform another test, click File then Collect New and rename the test before repeating steps 41-43

(B) Tissue Dissociation for Flow Cytometry and Immunostaining • Timing: 20 minutes

45) Collect the tissues in a 15 mL centrifuge tube and remove all media using a P1000. Wash the sample with 1 mL PBS, allow the samples to settle, and remove PBS.

46) Next, add 1 mL Collagenase-B with DNAse solution to the sample and incubate at 37°C in a water bath for 10 minutes. While the sample is in the water bath, shake the test tube every 2 minutes in the warm water to break up the tissues. After 6 minutes, pipette the sample up and down up to 3 times using a P1000.

47) After 10 minutes in the water bath centrifuge the samples for 3 min at 300g. Remove the supernatant and resuspend in PBS. **?TROUBLESHOOTING**

48) If The sample is being used for flow cytometry, continue to the flow cytometry section. If it is being used for staining or other purposes, mix the cells with RPMI20 for further use.

(C) Flow Cytometry • Timing: 8 hours

49) Dissociate the 3D-ECTs according to the tissue dissociation protocol above. Remove a sample of unlabeled cells from the PBS cell suspension. Centrifuge the remaining samples at 300g for 3 min and remove the supernatant.

50) During centrifugation, dilute the zombie dye 1:1000 in PBS. After centrifugation, resuspend the samples in diluted 100 µl Zombie solution and incubate the samples at 2-8°C, in the dark, for 30 minutes. **CRITICAL** Do not use Tris buffer as a diluent and be sure that the PBS does not contain any other proteins like BSA or FBS. The amount of dye used can also influence the ability to detect apoptotic as well as live and dead cells.

51) After incubation, wash the samples by adding 1mL of blocking buffer for 10 minutes. Centrifuge the samples at 300 g for 3 minutes and remove the supernatant. Add 500 µL of Foxp3 Fixation/Permeabilization working solution and incubate for 30-60 minutes (or overnight) at 2-8°C **CRITICAL** Protect the samples from light.

52) After fixation, centrifuge the samples at 300g for 3 minutes and discard the supernatant. Add 1 mL of 1X Permeabilization Buffer to each sample, centrifuge at 300g for 3 minutes and remove the supernatant.

53) Add 500µL of FACS buffer to each sample and incubate at room temperature for 30 min. Filter samples through ## µm filters. Split the samples into multiple tubes for primary staining.

54) While the samples are incubating, prepare each primary antibody in FACS. Add cTnT, αSA, and MF20 in a 1:200 ratio of FACS and add IgG Isotype in a 1:1000 ratio of FACS. Then prepare the secondary antibody in a 1:300 ratio of FACS.

55) After incubation has been completed, centrifuge the samples at 300g for 3 minutes and remove the supernatant. Then add 100 μL of primary antibody to each tube, pipette the sample twice to mix, and incubate for 1 hour at room temperature. Protect the samples from the light.

56) Wash the samples with 1mL Permeabilization Buffer for 10 minutes. Centrifuge at 300g for 3 minutes, remove the supernatant and repeat this washing step.

57) Add 100 μL of the secondary antibody to the samples and incubate for 30-45 mins at 4°C. Protect the samples from the light.

58) Wash the samples with 1mL Permeabilization Buffer for 10 minutes. Centrifuge at 300g for 3 minutes, remove the supernatant, and repeat this washing step. After final wash, resuspend the cells in blocking buffer (1×10^6 - 10×10^6 cells/ml)

59) Analyze the sample using appropriate instrument parameters. Using the isotype controls to check for non-specific binding and making sure to collect 10,000 events inside the gate for live cells.

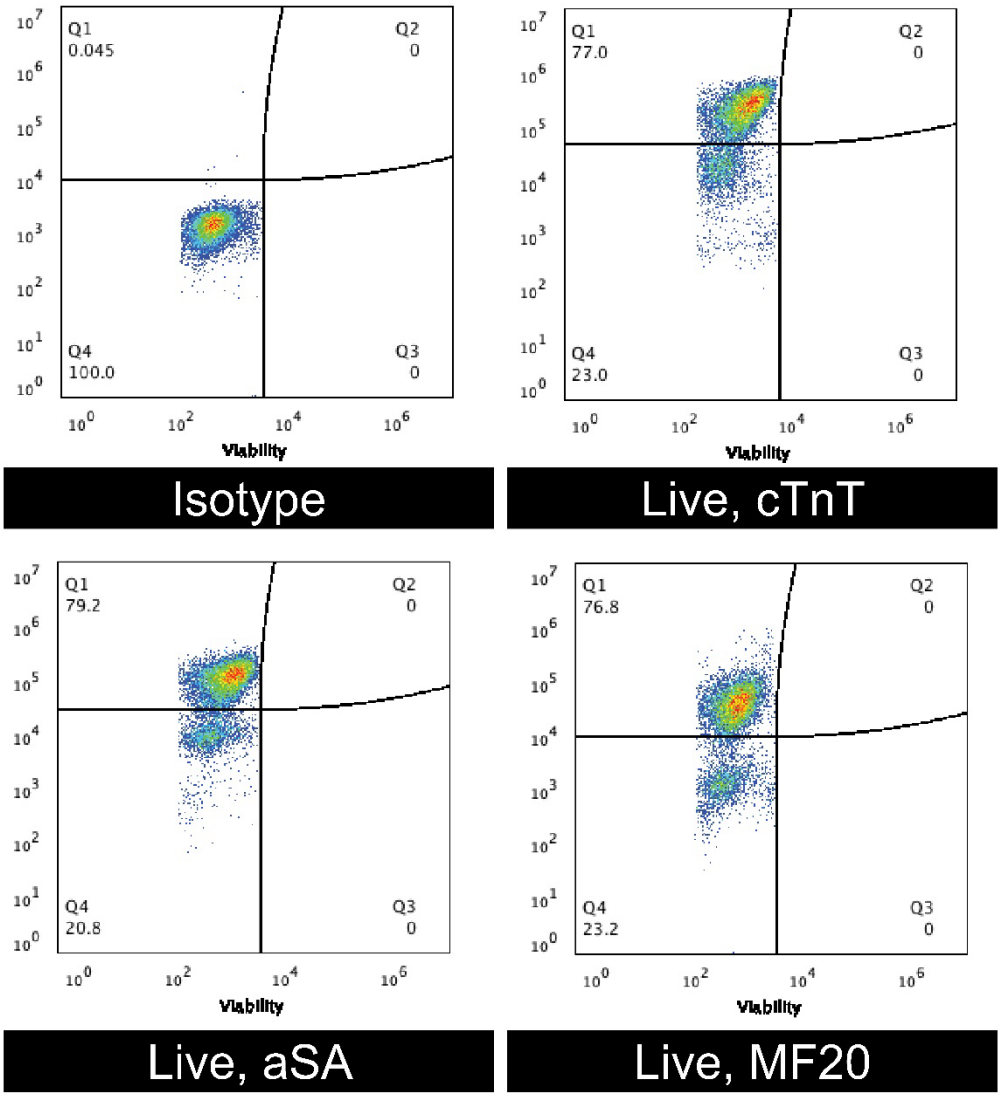

Figure B.4 | To quantify cell populations and asses cardiac differentiation, flow cytometry was performed on directly differentiated 3D-ECTs.

On day 10, the 3D-ECTs were dissociated and labeled with the cardiac markers cardiac troponin T (cTnT), alpha sarcomeric actinin (αSA), and MF20. An additional isotype control was also performed on day 10. Representative dot plots show that engineered cardiac tissues contained 77% cTnT positive populations, 79% αSA positive populations, and 77% MF20 positive populations.

(D) Contraction Analysis • Timing: 5 minutes per video

Contraction analysis was done using motion tracking software (Huebsch et al. 2015a) in which macroblocks were tracked between frames to determine the beat rate in beats per minute (BPM), maximum contraction velocity in μm/s, and maximum relaxation velocity in μm/s.

60) Record videos of tissue contraction. Upload contraction videos to computer separating each video into its own folder. Open each video in NIS Elements and export video as individual tiff files into the corresponding video specific folder.

61) Open MATLAB and load the motion tracking software[12]. Open the Motion GUI and click reset. Fill out fields necessary for contraction analysis including scale, framerate, and number of frames. When selecting area of interest, we split each tissue into quadrants. Run the code.

62) Click collect and evaluate contraction data. Find maximum peak and peak distance fields to highlight the contraction and relaxation peaks. Click find peaks and record results.

(E) Immunostaining of dissociated CMs • Timing: 3 days

63) Dissociate the 3D-ECTs according to the tissue dissociation protocol above. Plate the low cell density suspension on Matrigel-coated glass coverslips. Culture the cells for at least 48 hours in RPMI20 to allow the cells to recover from the dissociation process.

64) After 48 hours, gently wash the samples in PBS with KCl and fix with 2% paraformaldehyde in PBS for 20 min at room temperature.

65) After fixing the cells, wash the sample with PBS twice and permeabilize by incubating in PBS-T three times for 10 min each. Add blocking buffer for 30 minutes at room temperature or overnight at 4°C.

66) Prepare the primary antibodies in blocking buffer based on the pre-determined titrated concentrations. The primary antibodies: sarcomeric α-actinin (αSA, 1:200), cardiac troponin T (cTnT, 1:200), Connexin 43 (Cx43, 1:200), and/or Caveolin 3 (Cav3 1:200), were used for immunostaining.

67) Remove the blocking buffer from the samples. Add 500uL of primary antibody solution and allow to incubate for 1 hour at room temperature or overnight at 4°C.

68) Prepare the secondary antibodies in blocking buffer. The secondary antibodies used for immunostaining were 488-rabbit, 568-mouse (1:200), along with Hoechst 3342 (0.02 mg/mL). **CRITICAL** Protect the sample from light. All remaining steps should be done in the dark.

69) Wash the samples with PBS-T 4 times over a 10-minute period. Then add secondary antibody to the sample and allow to incubate for 40 minutes at room temperature. After 40 minutes, wash the sample gently with PBS-T three times for 5 minutes each.

70) To be prepare the slides for mounting remove the water from the samples by incubating in serial dilutions of ethanol as follows: 50% ethanol/ 50% deionized water for 15 minutes, 75% ethanol/ 25% deionized water for 15 minutes, 95% ethanol/ 5% deionized water for 15 minutes, and finally 100% ethanol for 15 minutes. After final dilution, remove the glass coverslip and allow to dry for 15 minutes.

71) After air drying, add a drop of Prolong Gold to a microscope slide and place the coverslip cell side facing down on to the mounting media. Allow to dry overnight. Seal the coverslip to the slide using clear nail polish. Image using confocal microscopy.

(F) Immunostaining of Whole Engineered Cardiac Tissues • Timing: 2 days

72) Remove media from 6 well plate and gently wash the 3D-ECTs in PBS with KCl and fix with 2mL of 2% paraformaldehyde in PBS for 2 hours at room temperature.

73) After fixing the cells, wash the sample with PBS twice for 5 minutes each and permeabilize by incubating in PBS-T three times for 10 min each. Add blocking buffer for 2hours at room temperature or overnight at 4°C.

74) Prepare the primary antibodies in blocking buffer based on the pre-determined titrated concentrations. The primary antibodies: sarcomeric α-actinin (αSA, 1:200), cardiac troponin T (cTnT, 1:200), Connexin 43 (Cx43, 1:200), and/or Caveolin 3 (Cav3 1:200), were used for immunostaining.

75) Remove the blocking buffer from the samples. Add 1 mL of primary antibody solution and allow to incubate for overnight at 4°C.

76) The next day, prepare the secondary antibodies in blocking buffer. The secondary antibodies used for immunostaining were 488-rabbit, 568-mouse (1:200), along with Hoechst 3342 (0.02 mg/mL). **CRITICAL** Protect the sample from light. All remaining steps should be done in the dark.

77) Wash the samples with PBS-T 4 times over a 10-minute period. Then add secondary antibody to the sample and allow to incubate for 2 hours at room temperature. After 2 hours, wash the sample gently with PBS-T three times for 5 minutes each. Wash the samples with PBS twice for two minutes each.

78) To clear the samples, remove the PBS and incubate in 25% formamide and 10% PEG solution for 10 minutes. Remove solution and add 50% formamide/20% PEG solution for 5 minutes. Remove solution and add fresh 50% formamide/20% PEG solution for one hour. Image in final clearing solution.

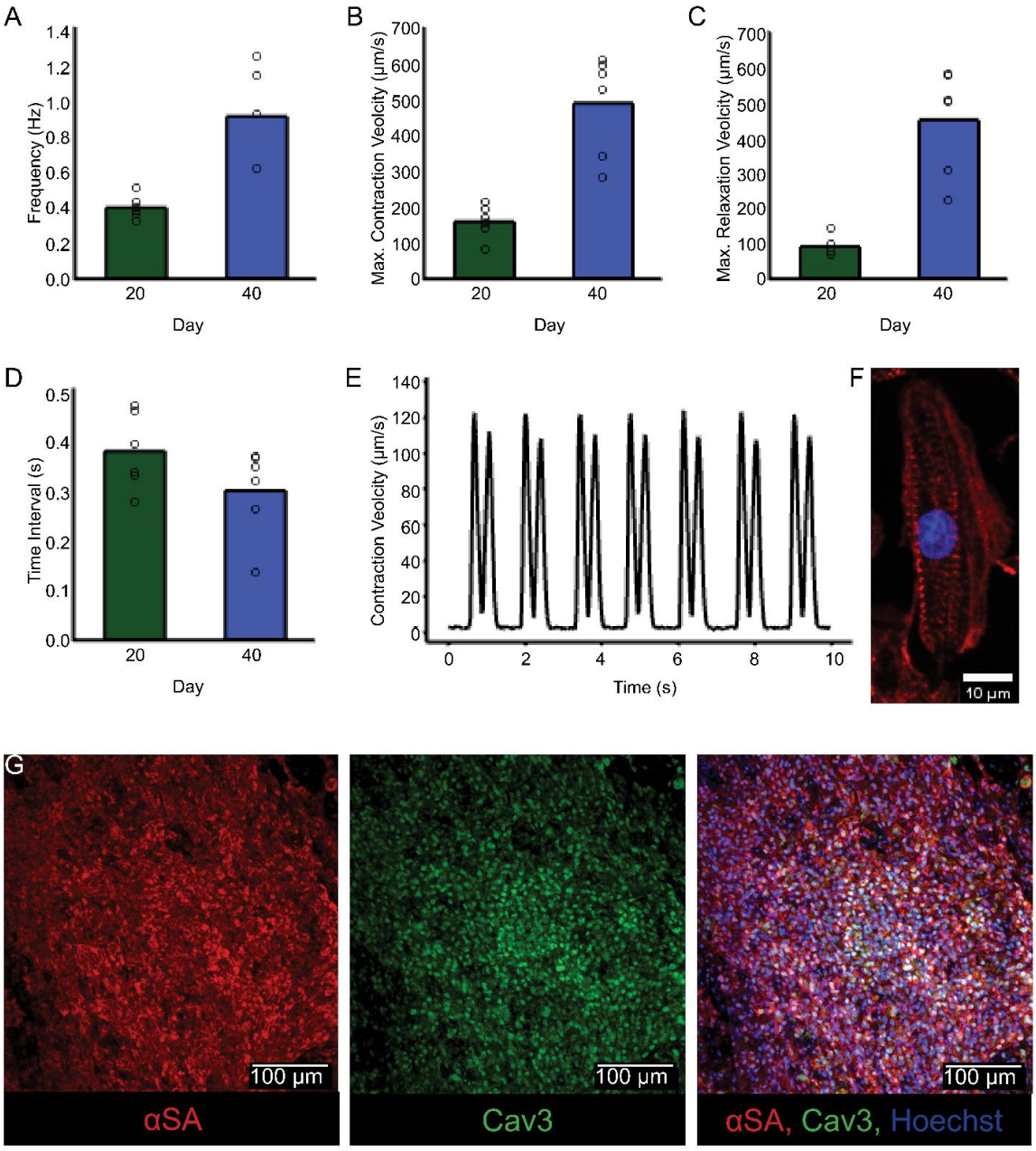

Figure B.5 | To further characterize the 3D-ECTs, contraction analysis (A-E), sarcomere staining (F), and whole tissue staining (G) was performed according to this protocol.

On day 20 and day 40, the frequency of contraction (A), maximum contraction velocity (B), maximum relaxation velocity (C), and time interval (D) were quantified. Confocal images of dissociated cardiomyocytes were taken at 40X to evaluate sarcomere spacing and alignment (F).

Additionally, confocal images of whole 3D-ECTs were taken at 20X to visualize expression of αSA, Cav3, and Hoechst.

Table B.1| Troubleshooting table

Step	Problem	Possible reasons	Solution
31	Material does not crosslink after 30 seconds of visible light exposure	One of the components in the polymer precursor solution is bad.	Try crosslinking the material without cells. If the material does not crosslink, make new polymer precursor components including TEOA, NVP, and Eosin Y. Remake the polymer precursor solution and test again.
		The flashlight is too far away from the PDMS mold set up.	Test the distance of the light source from the PDMS mold setup by crosslinking materials without cells for 30 seconds.
32	HiPSCs have not grown in the 3D hydrogel microenvironment	Initial seeding density was too low or hiPSC did not survive the encapsulation process	Increase the initial hiPSC encapsulation density; increase the number of days before initiation of cardiac differentiation (Day -4 to 0)
39	3D-ECTs are not spontaneously contracting on Day 7-8	3D-ECTs did not differentiate efficiently	Optimize the initial hiPSC encapsulation density; optimize CHIR99021 concentration (step 33) (cell line dependent); optimize timing of small molecules (step 33,35)
46	3D-ECTs are not dissociating to single cells	Cells are dead and are sticking together. Collagenase type B solution was not properly aliquoted and stored	Minimize the mechanical pipetting; make fresh Collagenase B solution; If material has dissociated but cells remain in small clusters, resuspend the samples in Trypsin for 2 minutes in the water bath. After 2 minutes, add 3X the volume of RPMI20 to the sample to deactivate the trypsin. Then centrifuge the sample for 3 min at 300g for 3 minutes.

• Timing

Steps 1-6, Piranha cleaning and acrylation of glass coverslips**:** 24 hours

Step 7-9 PDMS Mold Preparation: 2.5 hours

Step 10-17 PF Synthesis (10mg/ml): 24 hours

Step 18-21 Bringing hiPSCs up from freeze: 15 minutes

Step 22 Passaging hiPSCs: 15 minutes

Step 23-24 Polymer Precursor Preparation: 100μL: 5 minutes

Step 25-32 HiPSC Encapsulation Technique: 30 minutes

Step 33-38 Cardiac differentiation with CHIR99021 and IWP2: 7 Days +long term culture

Step 40-44 Mechanical Properties: 15 minutes/sample

Step 45-48 Tissue Dissociation for Flow Cytometry and Immunostaining: 20 minutes

Step 49-59 Flow Cytometry: 8 hours

Step 60-62 Contraction Analysis: 5 minutes/video

Step 63- 71 Immunostaining of dissociated CMs: 3 days

Step 72-78 Immunostaining of Whole Engineered Cardiac Tissues • Timing: 2 days

B.4 Anticipated results

This protocol describes the process of producing viable, contracting 3D-ECTs (60-80% CMs) using a single cell handling step. Before encapsulation, biomaterials should be synthesized, and glass coverslips should be piranha cleaned and acrylated. hiPSC encapsulations should take place when hiPSCs have reach 70-80% confluency and stem cells should continue to proliferate in the biomaterial construct. When initiating

differentiation (day 0), phase contrast images of the encapsulated hiPSCs should appear denser and darker than day -2 following encapsulation. Following differentiation, in contractions can be seen as early as day 7 with synchronous contractions occurring by day 14. Cardiac markers αSA, cTnT, and MF20 will be expressed in 60-80% of cells from dissociated 3D-ECTs on day 10, quantified using flow cytometry. When characterizing contractile properties of the 3D-ECTs, frequency and velocity should increase from Day 20 to Day 40 as the 3D-ECTs contract against the acrylated glass coverslip. Lastly, sarcomere organization will be visualized in whole 3D-ECTs and dissociated CMs using αSA.